UNIVERSITAT DE BARCELONA

Target Therapy in Rhabdomyosarcoma: Discovering new targets and apportunities

Estela Maria Prada Varela

Universitat de Barcelona

Facultat de Medicina

Doctoral Program in Biomedicine

Target Therapy in Rhabdomyosarcoma: Discovering new targets and opportunities

Dissertation submitted by:

Estela Maria Prada Varela

This work was performed at the Developmental Tumor Biology Laboratory of Institut de Recerca Sant Joan de Déu (IRSJD). Hospital Sant Joan de Déu, Barcelona.

Thesis directors:

Jaume Mora, M.D. Ph.D.

Inmaculada Hernández, Ph.D.

Thesis tutor:

Neus Agell Jané, Ph.D.

The author:

Estela Maria Prada Varela

Barcelona, 14 September 2021

“A loita nobre e leal das ideas é o único que asegura o progreso”

A.R. Castelao

A Cristina y a Emma

Acknowledgements

I would like to begin by thanking the family of Cristina Casanovas, especially her mother Laura Abella, who with her perseverance and strength has decided that we will change the course of RMS. I would also like to thank with special affection the trust placed in me from the beginning. This work is also yours.

I have been lucky to have two directors who have given me different but complementary scientific visions. I want to thank my thesis director, Dr. Jaume Mora, for trusting me and my work, which has allowed me to grow as a scientist but also as a person. I feel really privileged to be part of this nice team. Thanks to my director Dr. Inma Hernandez, for pushing me to develop tools that allow me to be a critical and determinded scientist, and for guiding me in questioning and perseverance with science. Thank you both for sharing your inspiring discussions and scientific knowledge.

Aos meus pais, que sempre me impulsaron para chegar ata onde eu queira, como eles mesmos me dixeron alguna vez: “Nós queremos que tí cambies o mundo”. Aínda estando lonxe estes anos, sentinvos cada día animandome para chegar ao final, por todo, moitas gracias!

Special affection to Pablo Taboas, my great colleague, friend and my partner in RMS—with your arrival to the lab, my work gained a lot. You are going to be a great scientist. The beginnings are always complicated, but thanks to Evelyn Andrades, it has been easier, I really learned a lot from you at the IMIM!

Thanks to Álvaro, who every day when I get home in pieces, has been able to rebuild me to face the next day with strength and joy. My brother Alex and my sister Adela, thank you for always being there for me. Nazaret and Carolina, loyal, strong and capable of everything, I am simply lucky to have the best friends.

Gracias Nuria por ser a miña compi de aventuras na gran cidade. A mis tíos y primos de Montornés, que me acogieron desde el primer día. A los más “guays”: Espe, Manu, Jokin, Anna, Óscar, Ferran, Cora, Jordi, Laia, Montse, Paula; y las alegrías de mi huerta, Judith y David. A mis amigas Sandra y Yolanda gracias por vuesta paciencia y apoyo mientras esta tesis se gestaba. A tots ells moltes gràcies per ser la meva família a Barcelona.

Dr. Laura García and Dr. Guillem Pascual, always with their helpful suggestions and opened discussions, have gone from good companions to best friends. Dr. Eliana Gonçalves, partner in the hard beginnings, always loyal collegue and friend. Monica, a born hard worker and Dr. Gaia Botteri, thank you for your help and support. Thank you, Dr. Silvia Mateo, always ready to help with a friendly word. Also, I would like to thank all my colleagues in the sarcomas team who have contributed to my project and have offered their time and knowledge: Dr. Elisabet Figuerola, Dr. Sara Sanchez, Maria Sanchez, and Jara Martin. Also thanks all my collegues in this big lab, specially AMC team and Sara Perez, the nicest mathematician and the first colleague I met in SJD.

I would especially like to thank Dr. Angel Montero, Dr. Cinzia Lavarino and Dr. Alex Avgustinova for their kindness and scientific education.

I was very lucky for having met such clever people over these years—many thanks to all of them.

Table of Contents

I. INTRODUCTION 19
1 Introduction to rhabdomyosarcoma 21
1.1 General overview: pediatric rhabdomyosarcoma 21
1.2 Defining rhabdomyosarcoma 21
1.3 Clinical presentation and epidemiology 22
1.3.1 Clinical presentation 22
1.3.2 Epidemiology 24
1.3.2.1 Genetic predisposition 24
1.3.3 Risk stratification 25
1.3.4 Clinical management 27
1.4 Biology of rhabdomyosarcoma 31
1.4.1 RMS cell of origin 31
1.4.1.1 Ontogeny of the skeletal muscle 31
1.4.1.2 Origins of RMS 34
1.4.2 Fusion oncoproteins in Rhabdomyosarcoma 35
1.4.3 Genetic and epigenetic alterations in RMS beyond the translocation 39
1.4.4 Targeted therapies and innovative treatments 41
2 The insulin-like growth factor axis 46
2.1 Components of the IGF axis 46
2.1.1 The ligands: IGFs 46
2.1.2 The receptors: IGF1R, IGF2R and IRs 48
2.2 IGF1R signaling 50
2.3 The IGF axis in RMS 52
2.4 Pharmacological inhibition of the IGF axis 54
2.5 The dual-specific anti-IGF-1/IGF-2 human monoclonal antibody 56
3 AKT signaling in RMS 57
3.1 AKT signaling 58
3.1.1 The mTOR complex 61
3.2 AKT functions 62
3.2.1 AKT functions in cell growth and metabolism 63
3.2.2 AKT effects in muscle differentiation 65
3.2.3 AKT modulation of cell survival. 65
3.3 AKT as a therapeutic target in RMS 66
3.4 AKT inhibitors: Mechanism of action 67
3.4.1 Ipatasertib 67
3.4.2 Miransertib 70
4 The PI3K/AKT and RAS/MEK/ERK pathways: cross-talk and compensation mechanism. 72
4.1 Trametinib, the MEK inhibition in RMS 73

II. HYPOTHESIS AND OBJECTIVES 77

III. MATERIALS AND METHODS 81
1 Pharmacological treatments 83
2 Cell culture 83
2.1 Cell lines 83
2.2 Establishment and characterization of primary cultures 84
2.2.1 Establishment of RMS primary cultures 84
2.2.2 Characterization of RMS primary culture 85
2.3 siRNA oligofection to knockdown PRKG1 in the RH4 cell line 86
2.4 Knock-Out of PRKG1 in the RH4 cell line using CRISPR-Cas9 technology 87
2.5 Cell viability studies by MTS assay 88
3 Flow cytometry: 88
3.1 Apoptosis analysis 88
3.2 Cell cycle analysis by BrdU staining and flow cytometry detection. 89
3.3 Detection of the expression of IGF-1R at the cell membrane. 90
4 Molecular biology techniques 91
4.1 RNA techniques 91
4.1.1 RNA extraction and Reverse transcription quantitative polymerase chain reaction (RT-qPCR) 91
4.1.2 Gene expression detection by microarray analysis 92
4.2 DNA techniques 94
4.2.1 DNA extraction 94
4.2.2 Droplet digital PCR (ddPCR) from paraffin-embedded tissue 94
4.2.3 Sanger sequencing 96
4.2.4 Clustering of PRKG1 peaks with epigenomic marks 96
4.3 Protein techniques 97
4.3.1 Protein extraction 97
4.3.2 Western blotting 97
4.3.3 Human phospho-kinase array 99
4.3.4 Immunofluorescence (IF) 99
4.3.4.1 IF of adherent cells 99
4.3.4.2 IF on primary culture cells 99
4.3.4.3 Image acquisition and processing 100
4.3.5 Immunohistochemistry (IHQ) 100
5 *In vivo* experiments 101
5.1 Ethical statement and animal experimentation 101
5.2 Antitumoral efficacy studies 101
5.2.1 Antitumoral activity of ipatasertib (GDC-0068) 102
5.2.2 Antitumoral activity of miransertib (ARQ-092.2MSA) 103
5.2.3 Subcutaneous inoculation of A006_s cells 103
5.3 Pharmacokinetic analysis 104
5.3.1 Ipatasertib methodology detection 104
6 Gene expression analyses in pediatric tumor public data bases 105
6.1 Supervised PRKG1 expression in pediatric databases 105
6.2 Prognostic value of PRKG1 gene expression in RMS 106

IV. RESULTS 109
1 Targeting the IGF axis with the dual anti-human IGF1/2 monoclonal antibody m708.5 in RMS cell lines 111
1.1 Functional and molecular characterization of m708.5 effects in RMS cell lines 111
2 Characterization of the AKT/mTOR and MEK/ERK pathways in RMS 120
3 AKT blockade by ipatasertib (GDC-0068) as a therapeutic approach for RMS. 123
3.1 Anti-proliferative activity of the AKT inhibitor ipatasertib in RMS patient-derived models. 123
3.2 Ipatasertib treatment induces tumor regression in vivo in a subgroup of RMS patient-derived xenografts. 125
3.3 Ipatasertib pharmacokinetics (PK) and pharmacodynamics (PD) in mice harboring FP- or FN-RMS PDX models 132
3.4 Dual blockade of the AKT/mTOR and MEK/ERK signaling in in vitro RMS culture models. 136
3.5 Dual pharmacological inhibition of the AKT/mTOR and MEK/ERK pathways in RMS models in vivo. 141
4 The AKT inhibitors ipatasertib (GDC-0068) and miransertib (ARQ-092): different anti-tumor activity against RMS. 143
4.1 Antiproliferative effects of two different AKT inhibitors 143
4.2 Inactivation of the AKT/mTOR pathway in RH4 cells by subcytotoxic concentrations of miransertib or ipatasertib. 144
4.3 Antitumoral activity of miransertib and ipatasertib in vivo 147
5 Ipatasertib targets PRKG1 in RMS. 149
5.1 Ipatasertib-sensitive RMSs express high PRKG1 levels. 149
5.2 The transcriptional profiles of RMS with high PRKG1 expression levels are enriched in cell cycle and impoverished in myogenic genes 154
5.3 PRKG1 silencing induces a transcriptional myogenic pattern and cell cycle arrest in RMS. 158
6 Expression and prognostic value of PRKG1 in RMS 164
6.1 PRKG1 is highly expressed in RMS tumors 164
6.2 PRKG1 prognostic value in RMS tumors 165

V. DISCUSSION 171
1 Therapies targeting IGF1R and AKT in combination with MEK/ERK inhibition in pediatric RMS 175
1.1 The dual specific anti-IGF1/IGF2 human monoclonal antibody m708.5 in pediatric RMS 175
1.2 Combination of AKT and MEK inhibitors 177
2 Ipatasertib as effective treatment in RMS tumors with high PRKG1 levels 178
2.1 Ipatasertib activity in RMS models 178
2.2 Antitumoral effects of ipatasertib in RMS in comparison to other AKT inhibitors ... 182
2.3 PRKG1 expression and role in RMS. 183
2.3.1 PRKG1 is differentially expressed in RMS. 184
2.3.2 High PRKG1 expression identifies ipatasertib-sensitive RMS. 184
2.3.3 Depletion of PRKG1 in RMS cells induces myogenic differentiation. 186

2.3.4 Prognostic value of PRKG1 188
3 Open questions for future research 189

VI. CONCLUSIONS 195

VII. BIBLIOGRAPHY 199

List of Figures

I. INTRODUCTION

Figure I. 1. Characteristic MRI images of RMS. 23
Figure I. 2. New cases of pediatric cancer at Hospital Sant Joan de Deu in Barcelona distributed by tumor types. 24
Figure I. 3. Origins of the muscles. 33
Figure I. 4. PAX-3/7-FOXO1 driver of RMS formation. 36
Figure I. 5. PAX3-FOXO1 binding sites in the MyoD1 enhancer region are marked by H3K27acetilation. 38
Figure I. 6. Genomic landscape of pediatric RMS across 147 rhabdomyosarcoma cases. 40
Figure I. 7. Overview of RMS targeted therapies organized by pathway. 44
Figure I. 8. Homology of the folded protein structures of Insulin (blue), IGF1 (green) and IGF2 (gray). Overlay shows the comparative structure. 47
Figure I. 9. Comparative relevance of IGF1 *vs.* IGF2 at different tissues and life stages. 47
Figure I. 10. The IGF/INS axis is a complex multilayer interacting molecular network. 49
Figure I. 11. Substrates and functions of the IGF1R signaling network. 51
Figure I. 12. mRNA expression levels for IGF2 and IGF1R in a panel of tissue and tumor samples. 53
Figure I. 13. High IGF1R expression level predicts worse survival in RMS patients. 54
Figure I. 14. The IGF-target therapies in clinical development. 55
Figure I. 15. The Class IA PI3K signaling. 59
Figure I. 16. From inactive to active AKT conformation. 60
Figure I. 17. Overview of mTORC1 and mTORC2 function and structure. 62
Figure I. 18. Functional AKT isoforms specificity. 63
Figure I. 19. Graphical abstract of AKT/mTOR pathways and functions described in previous section. 64
Figure I. 20. Regulation of cell cycle progression by FOXOs. 66
Figure I. 21. Model of AKT inhibition. 68
Figure I. 22. Cross talk between AKT and MEK pathways. 74

III. MATERIALS AND METHODS

Figure III. 1. Primary cultures expressed RMS and human markers. 86
Figure III. 2. Examples of gating selection for apoptosis detection by flow cytometry. 89
Figure III. 3. Cytometric analysis of BrdU incorporation. 90
Figure III. 4. RT-qPCR quantification of the expression levels of PAX3-FOXO1 fusion gene in HSJD-ARMS PDXS. 92
Figure III. 5. Analysis of MYCN amplification by droplet digital PCR in FN RMS PDX. 95

IV. RESULTS

Figure IV. 1. Effect of m708.5 in RMS cell viability. 112
Figure IV. 2. Effect of m708.5 treatment in RH4 cells on apoptosis and cell cycle. 113
Figure IV. 3. Subcellular localization of IGF1R in RMS cell lines. 114
Figure IV. 4. IGF1R levels at the plasma membrane are modulated by m708.5 treatment in CW9019 and RH30 cell lines. 115

Figure IV. 5. Regulation of IGF1R expression and activation by ligand binding and m708.5 treatment. 116
Figure IV. 6. Inhibition of the IGF1R signaling pathway by m708.5. 117
Figure IV. 7. Long-term exposure to m708.5 restores AKT activation in RH4 cells. 117
Figure IV. 8. Identification of active RTKs in RMS cell lines. 118
Figure IV. 9. Characterization of active RTK signaling pathways in RMS cell lines. 120
Figure IV 10. Identification of active proteins of the AKT and MAPK signaling pathways in RMS samples. 122
Figure IV. 11. Ipatasertib activity in a panel of RMS models. 124
Figure IV. 12. Early changes in MEK/ERK phosphorylation in cells exposed to ipatasertib. 125
Figure IV. 13. Immunohistochemistry of human nuclei, MYOD1, and Hematoxylin/eosin in HSJD-RMS PDX included in this thesis. 126
Figure IV. 14. Efficacy of ipatasertib administrated at 100 mg/kg orally (PO) and daily (QD) in eight RMS-PDX. 128
Figure IV. 15. Percentage of tumor response, evaluated after 10 doses of ipatasertib at 100 mg/kg administered orally, once a day (PO and QD). 129
Figure IV. 16. Ipatasertib dose dependent effects in RMS models. 130
Figure IV. 17. Ipatasertib re-challenge in regrowing tumors of the ERMS-011 model. 131
Figure IV. 18. In vivo ipatasertib pharmacokinetics in HSJD-ERMS-011 and HSJD-ARMS-006 tumor-bearing mice. 133
Figure IV. 19. Pharmacodynamic changes at 3 h and 24 h after a single ipatasertib dose. 135
Figure IV. 20. Phosphorylation of proteins in the AKT and MEK pathways and c-PARP in RMS cultures treated with ipatasertib (AKT inhibitor) and trametinib (MEK inhibitor). 138
Figure IV. 21. Anti-proliferative effects of trametinib in RMS cell lines and A010_S primary culture. 139
Figure IV. 22. Effect of combined ipatasertib and trametinib treatments for 72 h on RMS cell viability. 140
Figure IV. 23. Effect of ipatasertib and trametinib in the tumoral growth of RMS primary model *in vivo*. 142
Figure IV. 24. Comparison of miransertib and ipatasertib activities in RMS cell lines and primary culture models. 144
Figure IV. 25. AKT signaling inhibition and transcriptional changes in ipatasertib and miransertib RH4-treated cells. 146
Figure IV. 26. Antitumoral effectiveness of miransertib and ipatasertib *in vivo*. 148
Figure IV. 27. Ipatasertib, but not Miransertib, affects PRKG1 activity. 150
Figure IV. 28. PRKG1 levels in A006_S, RH4 and E024_S cells in basal culture conditions or upon 1 µM ipatasertib or miransertib treatments for 24 h, assessed by western blot analysis. 151
Figure IV. 29. Gene expression analysis of the RMS samples included in the study. 152
Figure IV. 30. PRKG1 mRNA levels correlate with RMS responsiveness to ipatasertib *in vivo*. 153
Figure IV. 31. Supervised analysis of gene expression in RMS experimental models. 155
Figure IV. 32. Functional pathways associated with high PRKG1 levels in RMS. 156
Figure IV. 33. Transcriptional changes upon PRKG1 knockdown in RH4 cells. 159
Figure IV. 34. Transcriptional effects of PRKG1 knock-out in RH4 cells. 161
Figure IV. 35. Histone marks at PRKG1 transcription start site 163
Figure IV. 36. PRKG1 expression levels in developmental tumors, from *in silico* databases. 165
Figure IV.37. High PRKG1 expression levels predict enhanced overall survival in RMS patients. 167

List of Tables

I. INTRODUCTION

Table I. 1. Syndromes associated with an increased risk of RMS. 25
Table I. 2. Staging classification system for RMS 25
Table I. 3. Clinical group classification system for RMS 26
Table I. 4. Risk stratification for patients with RMS 28
Table I. 5. Summary of target therapies with supporting preclinical data in RMS already in clinical trials open for pediatric cancer in North America. 45
Table I. 6. Comparison of the IGF axis components in pediatric sarcomas. 52
Table I. 7. Binding affinities of MEDI-573 and m708.5. 56
Table I. 8. Biochemical selectivity of ipatasertib or miransertib to AKT isoforms and other kinases.71

III.MATERIALS AND METHODS

Table III. 1. RMS cell lines features. 83
Table III. 2. Summary of molecular, biological and clinical features of each RMS primary culture generated in this thesis. 84
Table III. 3. Small interfering RNA (siRNA) knockdown sequences 87
Table III. 4. sgRNA guide used for CRISPR-Cas9 experiments 88
Table III. 5. cDNA primers used for qPCR 91
Table III. 6. Primer sequences for PRKG1 sequencing. 96
Table III. 7. All the antibodies used along this thesis. 98

IV. RESULTS

Table IV. 1. IC50 values for m708.5 in established cell lines from pediatric tumors. 112
Table IV. 2. IC50 values of each RTK axis inhibitor. 119
Table IV. 3. Ipatasertib IC50 values in RMS models. 124
Table IV. 4. PK parameters of ipatasertib following a single dose in RMS PDX bearing mice. 133
Table IV. 5. Trametinib IC50 values in RMS models 139

List of abbreviations

AGC-KINASES	**Protein Kinases family comprising PKA, PKG and PKC**
ARMS	Alveolar Rhabdomyosarcoma
ATRT	Atypical Teratoid/Rhabdoid Tumors
CG	Clinical Group
ChIPseq	Chromatin Immunoprecipitation Sequencing
CNS	Central Nervous System
COG	Childrens Oncology Group
CR	Complete Response
CRISPR/CAS9	Clustered Regularly Interspaced Short Palindromic Repeats /CRISPR-associated protein 9
DEG	Differentially Expressed Genes
DIPG	Diffuse Intrinsic Pontine Glioma
EC50	Half maximal effective concentration
EFS	Event-free survival
hESC	Human Embryonic Stem Cells
EP	Ependymoma
EpSSG	European Pediatric Soft Tissue Sarcoma Study Group
ERMS	Embryonal Rhabdomyosarcoma
ESC	Embryonic Stem Cells
EW	Ewing Sarcoma
FDR	False Discovery Rate
FFS	Failure-free survival
FKHR	Forkhead Transcription Factor
FN	Fusion-Negative
FP	Fusion Positive
GO	Gene Ontology
GSEA	Gene Set Enrichment Analysis
HGG	High-Grade Glioma
hSMM	Human Skeletal Muscle Myoblasts
hSMPC	Human Skeletal Muscle Precursor cells
IC50	Half maximal inhibitory concentration
iPS	Induced Pluripotent Stem Cells
IRSG	Intergroup Rhabdomyosarcoma Study Group
KD	Kinase Domain or Kinetic dissociation
KM	Kaplan-Meier
KO	Knock Out
LC-MS/MS	Liquid Chromatography with tandem mass spectrometry
LOH	Loss of Heterozygosity
LOI	Loss of Imprinting
LGG	Low-Grade glioma
MB	Medulloblastoma

MRI	Magnetic Resonance Imaging
MSC	Mesenchymal Stem Cells
MSigDB	Molecular Signatures Database
MRF	Myogenic Regulatory Factors
MSC	Mesenchymal Stem Cell
MTD	Maximum Tolerated Doses
NB	Neuroblastoma
OS	Osteosarcoma
PARP	Poly (ADP-ribose) Polymerases
PD	Pharmacodynamics
PDB	Protein Data Bank
PDX	Patient Derived Xenografts
PH	Pleckstrin Homology
PA	Pilocytic Astrocytoma
PK	Pharmacokinetics
PR	Partial response
PRKG1	Protein Kinase CGMP-Dependent 1
CT	Chemotherapy
RECIST	Response Evaluation Criteria in Solid Tumors
RMS	Rhabdomyosarcoma
RNP	Ribonucleoprotein
RT	Radiation Therapy
RTK	Receptor Tyrosine Kinase
_S	_Spheres
SD	Stable Disease
SEM	Standard error of mean
SE	Super-enhancer
sgRNA	Single Guide RNA
SIOP	International Society of Paediatric Oncology
siRNA	Small interfering RNA
SkMC	Skeletal muscle cells
SNP	Single Nucleotide Polymorphisms
STS	Soft Tissue Sarcomas
SS	Synovial sarcoma
_T	Tumors
TF	Transcription Factor
VA	Vincristine-Actinomicine
VAC	Vincristine-Actinomicine-Cyclophosphamide
VI	Vincristine-Irinotecan
_X	Xenografts

SUMMARY

Pediatric RMS is a developmental tumor that affects patients from birth to late adolescence. RMS tumorigenesis involves the stalk of embryological myogenic processes. Classically, two main subgroups of RMS have been defined based on the histopathological features: Embryonal (ERMS) and Alveolar (ARMS). However, the molecular classification refines the subgrouping into Fusion Positive or Fusion Negative based on the occurrence of FOXO1 oncogenic translocations. The recent genetic and epigenetic landscapes of those subgroups have identified few potential druggable targets. Nowadays, the outcome of children with relapsed/refractory RMS remains very poor. In order to find new opportunities for these patients this thesis focuses on the identification of new therapeutic targets effective for RMS treatment as well as on characterizing biomarkers of response for the new targeted treatment.

We initially performed a functional approach starting from IGF1R target therapies to main downstream pathways including PI3K/AKT/mTOR and MEK/ERK that we found active in primary samples as well as in patient derived models. The new IGF1/2 monoclonal antibody m708.5 was found active in a subset of RMS particularly dependent on the IGF/AKT/mTOR pathway. Interestingly, we found that the ATP-competitive pan-AKT inhibitor ipatasertib was highly active causing tumor regression in a subset of patient derived models. We were able to classify RMS primary models and their parental samples into two subgroups: ipatasertib-dependent and ipatasertib non-dependent. Moreover, preclinical pharmacology corroborated the dose-dependent response of RMS to this inhibitor. Most interesting, those tumors particularly sensitive to ipatasertib were shown to be resistant to the MEK inhibitor trametinib. Surprisingly, the study of a mechanistically different AKT inhibitor did not recapitulate ipatasertib efficacy *in vivo*. We discovered that ipatasertib sensitivity correlated with high PRKG1 levels. We described for the first time *PRKG1* gene expression as RMS specific and predictive of ipatasertib response *in vivo*. The genetic signature of P*RKG1* depleted RMS cells is enriched in the expression of myogenic genes, positioning for the first time PRKG1 in the landscape of RMS tumorigenesis. The potential of PRKG1 as a prognostic marker was evaluated. Ongoing studies will determine the mechanism of myogenic blocking dependent on PRKG1.

I. INTRODUCTION

1 Introduction to rhabdomyosarcoma

1.1 General overview: pediatric rhabdomyosarcoma

Rhabdomyosarcoma (RMS) is the most common soft tissue sarcoma in children, comprising about half of all pediatric soft tissue sarcomas [1]. RMS is a high-grade malignant tumor with an annual incidence of about 4.5 cases per 1 million children in the USA and Europe, as international cooperative groups have recently reported [1-3].

Pediatric RMSs have been traditionally classified in two different subgroups, the alveolar and the embryonal RMS, based on histological criteria. Most alveolar RMS (ARMS) tumors harbor a chromosomal translocation, the most frequent of which involves the paired box transcription factors *PAX3* or *PAX7* genes and the forkhead transcription factor (FKHR) *FOXO1* gene. In contrast, embryonal RMSs (ERMS) lack this chromosomal aberration. The presence or absence of the fusion gene (fusion-positive [FP-RMS] or fusion-negative [FN-RMS], respectively) define two main RMS subgroups with prognostic implications. Despite ultrastructure divergence, both FP- and FN-RMS cells share myogenic features and propensity for skeletal muscle differentiation.

Clinical management of RMS requires a multidisciplinary approach integrating surgery, chemotherapy, and radiology, and is aimed to eradicate the primary tumor and the disseminated disease. Even so, patients with high-risk or recurrent disease present a reduced 5-year survival.

1.2 Defining rhabdomyosarcoma

RMS is a malignant **developmental tumor** whose cells display a **myogenic lineage phenotype**. The definition of developmental (pediatric) tumors refer to their embryological origin; in contrast, in adults, these are the result of ageing and the mutational accumulation over time in differentiated cells. RMS is a paradigmatic example of a **developmental tumor,** since it recapitulates specific early embryogenic programs; in some RMS tumor cells, typical puberty signaling pathways are also altered [4, 5]. RMS belongs to the **soft tissue sarcomas**

(STS) category, a heterogeneous group of tumors that can originate in any part of the human body, since they arise in the connective tissues. All STSs have one common feature: their cells mimic tissues derived from the mesenchymal embryonic layer. The most primitive cell of mesenchymal origin is the mesenchymal stem cell (MSC), which bears the capacity to differentiate at least into three lineages: osteogenic, adipogenic, and chondrogenic. RMS is postulated to originate from MSCs or muscle satellite cells. Indeed, RMS cells have a propensity for **myogenic differentiation**, and MyoD is a myogenic master transcription factor (TF) for RMS cells [6, 7]. Early myogenic expression markers such as MyoD, myogenin, and desmin are critical for the histological diagnosis of RMS [8].

1.3 Clinical presentation and epidemiology

1.3.1 Clinical presentation

The diagnosis of RMS has been classically based on the detection of skeletal myoblast-like tumor cells in the tumor mass and the use of immunohistochemical staining to detect the expression of myogenic proteins (e.g, myosin, desmin, MyoD1, and MyoG) [9]. RMS can appear in multiple anatomic locations, but each tumor type presents a preferential localization. ERMS appears most frequently in the head and neck regions, and the genitourinary areas, whereas ARMS affects mainly the extremities and (less frequently) torso [10]. The age at diagnosis is also differential: ERMS mostly affects young children, infants and children under 10 years of age, while ARMS is more frequent in adolescents [11].

The signs and symptoms associated with RMS are unspecific and are typical of an asymptomatic mass associated with soft tissues [12]. When symptoms are present, they frequently reflect the regions affected by the mass, the neovascular tissue, or the involvement of adjacent organs.

For primary tumor evaluation, magnetic resonance imaging (MRI) with contrast must be used to visualize the anatomical tumor region and lymph nodes. In addition, high-resolution computed tomography scan with contrast administration

of the chest helps for detecting metastasis, characterizing the mediastinal involvement, and distinguishing masses from pleural effusion.

Metastatic disease in bone and bone marrow should be studied in all cases with bone scintigraphy and at least two bone marrow aspirates and biopsies. Notably, the use of fluorodeoxyglucose (FDG)-positron emission tomography (PET) for disease evaluation is very sensitive for MS detection.

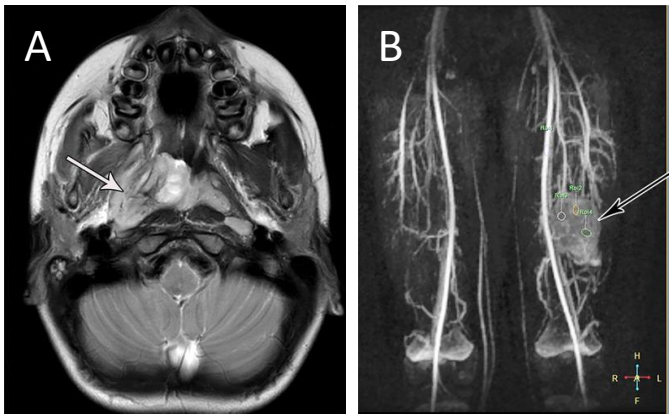

Figure I. 1. Characteristic MRI images of RMS. A) Axial T2-weighted MRI image of an ERMS involving the parapharyngeal space in a 7-year-old boy in which the tumor mass and its relationship with the adjacent tissues are distinguished. Of note, T1 images optimally show normal anatomy of soft tissue and fat, while T2 images optimally show fluid and alterations (e.g., tumors, inflammation, trauma). **B)** Alveolar rhabdomyosarcoma in an 11-year-old boy with a left thigh mass. Dynamic contrast-enhanced MRI image shows diffuse early enhancement of the tumor (black arrow). Note that dynamic contrast enhanced (DCE) imaging measures T1 changes in tissues over time after bolus administration of contrast medium (which is frequently gadolinium). Images taken from reference [13].

In general, patients with metastases have a worse prognosis. The most frequent sites of metastasis are lungs (20-40%), lymph nodes (30-50%), bone (30%), or bone marrow (35%) [14]. Within the metastatic patient population, ARMS patients have the worst life expectancy, of less than 5% chance of a 3-year-survival, and their prognosis has not changed in any of the studies performed to date [15]. It is therefore imperative to conduct an extent of disease work-up at the time of diagnosis to determine the degree of tumor infiltration and its relationship to adjacent organs. A multidisciplinary approach is always required for the correct orientation and management of RMS.

1.3.2 Epidemiology

RMS is the most common STS of childhood, with an estimated annual incidence of 4.5 cases per million children, making it the third most common extracranial solid tumor of childhood, after neuroblastoma and Wilms tumor.

By subgroups, ERMS is 2.5 times more prevalent than ARMS. By age, the peak of incidence for embryonal RMS is around 2–6 years of life, and for ARMS, at the beginning of adolescence[1]. By sex, there is a slightly higher incidence in boys than in girls. Distribution ratios of pediatric tumors diagnosed at Hospital Sant Joan de Deu in Barcelona between 1994 to 2020 show that pediatric RMSs (in red) represent 23.6% of all soft tissue tumors (**Figure I. 2**).

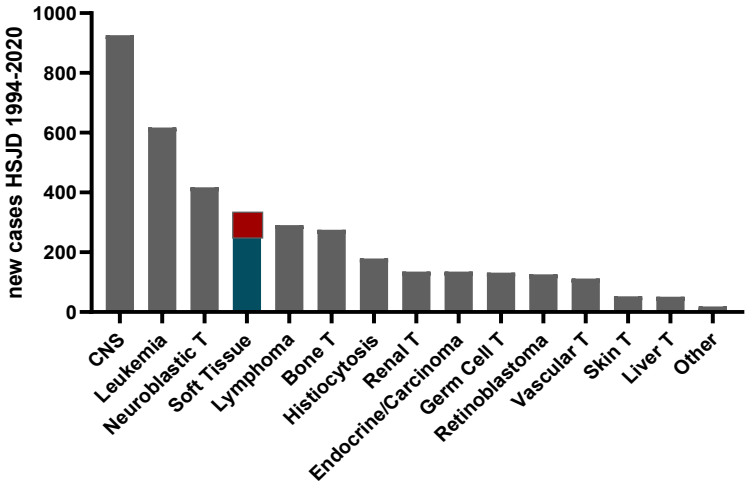

Figure I. 2. New cases of pediatric cancer at Hospital Sant Joan de Deu in Barcelona distributed by tumor types. Patient ages range from newborns to 18 years old. CNS: central nervous system. Soft tissue include RMS, Synovial sarcomas, and Ewing sarcomas located in soft tissues. Bone tumors include osteosarcoma and Ewing sarcoma.

1.3.2.1 Genetic predisposition

Diverse somatic mutations in tumors have been identified, but there are no studies on how germline DNA alterations could predispose for RMS. Some genetic syndromes found mainly in ERMS include the Li-Fraumeni syndrome (germline mutation of TP53), neurofibromatosis (deletions in the NF1 gene), Noonan syndrome (germline genetic variants activating the RAS-MAPK

pathway), Beckwith-Wiedemann syndrome (overgrowth disorder, with the insulin-like growth factor 2 [IGF2] or the H19 gene affected), Costello syndrome (HRAS mutation), and the DICER1 syndrome (germline DICER1 mutations). However, only 5% of all RMS patients present a cancer predisposition syndrome.

Table I. 1. Syndromes associated with an increased risk of RMS.

Syndrome	*Associated gene(s)*	*Refs*
Li–Fraumeni	***TP53***	[16]
Neurofibromatosis type 1	***NF1***	[17]
DICER1	***DICER1***	[18]
Costello	***HRAS***	[19]
Noonan	***BRAF*, *KRAS*, *NRAS*, *PTPN11*, *RAF1* and *SOS1***	[20]
Beckwith–Wiedemann	***IGF2*, *CDKN1C*, *H19* and *KCNQ1OT1***	[21]

Taken from [22].

1.3.3 Risk stratification

The Intergroup Rhabdomyosarcoma Study Group (IRSG), a U.S. and Canadian clinical trial cooperative group, stratifies RMS based on the stage and the clinical group (CG). Anatomical site and size of the primary tumor, together with the presence or absence of lymph nodes, and distal metastasis, define stage ranging from 1 to 4. The clinical groups range from I to IV and take into account surgical and pathological criteria such as tumor resection and existence of distal metastasis. **Tables I. 2 and I. 3** summarize relevant criteria for RMS classification according to the IRSG.

Table I. 2. Staging classification system for RMS.

Stage	Sites	Invasiveness	Size primary tumour	Nodes	Metastasis
1	**Orbit, head and neck (non-PM), genitourinary (non-B/P) and biliary**	**T1 or T2**	**<5 cm or >5 cm**	**N0, N1 or Nx**	**No distant metastasis**
2	**B/P, extremity, PM and other**	**T1 or T2**	**<5 cm**	**N0 or Nx**	**No distant metastasis**
3	**B/P, extremity, PM and other**	**T1 or T2**	**<5 cm**	**N1**	**No distant metastasis**
			>5 cm	**N0, N1 or Nx**	
4	**Any**	**T1 or T2**	**<5 cm or >5 cm**	**N0, N1 or Nx**	**Metastasis present (CSF, pleural or peritoneal)**

PM, Parameningeal; B/P, bladder/prostate; CSF, Cerobrospinal fluid. N0, regional nodes not involved; N1, regional nodes involved; Nx, status of regional nodes not known; T1, primary tumour confined to anatomical site of origin; T2, primary tumour with extension and/or fixation to surrounding tissue. Adapted from [1]

Table I. 3. Clinical group classification system for RMS

Clinical group	Subgroup	Definition
I	NA	Localized disease, completely resected
II	NA	Total gross resection with evidence for regional spread
	A	Grossly resected tumour with microscopic residual
	B	Involved regional lymph nodes, completely resected with no microscopic residual
	C	Involved regional lymph nodes, grossly resected with microscopic residual
III	NA	Biopsy only or partial resection with gross residual
IV	NA	Distant metastatic disease

NA: not applicable. Adapted from [1]

Williamson D. et al. (2010) reported that RMS with alveolar histology, but without the *FOXO* fusion gene, showed the same clinical outcome as ERMS [23]. In 2019 the Childrens Oncology Group (COG) in the USA re-examined the prognostic value of the **fusion gene status** and determined that it was the second most **important prognostic factor** after the metastasis status [24]. Therefore, the fusion gene status (FN-RMS or FP-RMS) has been recently incorporated as a criteria to refine RMS stratification and thereby improve outcome prediction [25, 26]. Although some novel non-FOXO1 fusions have been identified, their clinical significance is not yet fully understood. A recently recognized subtype, spindle cell and sclerosing RMS (SRMS), is a rare variant of RMS characterized by recurring fusions of *VGLL2* or *NOCA2* and has a favorable prognosis. This subtype does not require aggressive multimodal treatments as used for ARMS or ERMS. SRMS-RMS harbors *MyoD1* mutations in a subset of adult cases in association with poor prognosis. Despite the fact that pediatric RMS infrequently present MyoD1 gene mutations, a lack of MyoD1 staining is associated with poor prognosis in non-ARMS [27].

It is noteworthy that, based on these clinical parameters, the European RMS study group classifies RMS into four groups: ***low-***, ***standard-***, ***high-*** and ***very high risk RMS***, while the North American RMS study group defines only three stratification groups of risk: ***low***, ***intermediate***, and ***high***. Thus, there are many discrepancies between the two classifications, with patients classified as

intermediate by the COG that could be classified as very high risk by the European criteria.

The **high risk stratification** is assigned based on the **metastatic status**, irrespectively of the histology or fusion gene, both in the European and North American classifications.

1.3.4 Clinical management

The standard treatment for all RMS patients is chemotherapy (CT). The first randomized clinical trial to demonstrate the effectiveness of CT as compared to isolated local treatment, conducted in the USA (1967 to 1971), randomized patients with localized RMS after surgical resection to receive vincristine and actinomycin D (VA) versus observation [28]. The event-free survival (EFS) at 4 years was 82% for the group of patients that received CT, as compared to 47% for the control group. This study highlighted two findings: 1) CT drastically improves the outcome of RMS patients; and 2) a subgroup of patients can be cured with only local treatment. Local treatment with surgery, radiotherapy (RT) or a combination of the two is imperative for the cure of RMS. However, surgery as the only local control approach is not always feasible due to the invasiveness or anatomical difficulty of RMS. For the treatment of the clinical groups II–IV, the COG recommends RT. Notably, until the clinical trial *Mesenchymal malignant tumors protocol* 1989 (MMT 89) [29], the European Cooperative Group SIOP studies avoided RT for patients who achieved a complete response with CT regardless of surgery. The EFS was reduced to 57% for non-metastasic RMS patients in the MMT89 study. However, some of these patents were cured using rescue treatments, indicated that the differences in overall survival (OS) were also reduced as compared to the Intergroup Rhabdomyosarcoma Study Group (IRSG) IRS-IV study, which compares risk-based regimens of surgery, radiotherapy (RT) and chemotherapy [30, 31].

In the following, I discuss the results of recent studies according to the risk stratification definitions from the US **Children´s Oncology Group (COG)** and the **European Pediatric Soft Tissue Sarcoma Study Group (EpSSG)**.

Treatment for low-risk RMS patients

COG: Low Risk

EpSSG: Low /Standard Risk

In general, patients grouped as CG-I receive only CT of vincristine and actinomycin D (VA), while CG-II and CG-III patients (residual disease) receive VA and cyclophosphamide (VAC) together with RT at week 13 (COG D9602 protocol). The COG ARST0331 study evaluated the extent to which the length of therapy could be reduced without compromising the failure-free survival (FFS) for low-risk patients by (i) reducing the CT (VA) treatment to 22 weeks (using VA) treatment; (ii) using lower doses of cyclophosphamide for CG-II and CG-III; and (iii) reducing radiation dose to 36 or 41.4 Gy for patients of the CG-IIA [32]. COG investigators concluded that shorter therapy, including a lower cyclophosphamide and RT dose, did not compromise the FFS for patients with subset-one low-risk ERMS (Table I. 4).

Table I. 4. Risk stratification for patients with RMS

COG-Risk group	Stage	Clinical Group	Histology	COG study	Therapy
Low, subset 1	1	I or II	ERMS	ARST0331	VACx4, VAx4; 24 weeks
	1	III (orbit)			
	2	I or II			
Low, subset 2	1	III (non-orbit)	ERMS	ARST0331	VACx4, VAx12; 48 weeks
	3	I or II			
Intermediate	2 or 3	III	ERMS	ARST0531	VAC vs VAC/VI; 42 weeks
	1, 2, or 3	I, II, or III	ARMS		
High	4	IV	ERMS or ARMS	ARST08P1	VI / VDC / IE / VAC with Cixutumumab or Temozolomide

Adapted from [1].

The **EpSSG-RMS2005** study recommends 8 weeks of VA only for **low-risk patients**. For **standard risk patients** (CG-I, CG-II and CG-III without lymph node involvement and tumor size < 5 cm under 10 years of age for unfavorable tumor site), treatment consists of ifosfamide plus VA (IVA), followed by cycles of VA. CG-I patients in complete remission after initial surgery do not receive local

treatment. However, patients in CG-II and CG-III in remission after IVA and VA treatment receive 41.4 Gy radiotherapy.

Treatment for intermediate-risk RMS patients

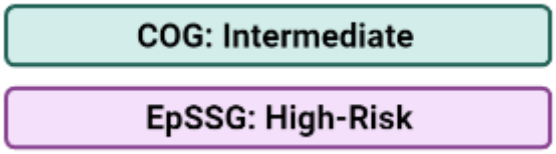

All recent attempts by cooperative groups to improve the survival of this group of patients have failed. The addition of doxorubicin, ifosfamide, or ifosfamide with etoposide to VAC scheme failed to improve in EFS [33] [31]. The COG evaluated the addition of topotecan to vincristine and cyclophosphamide in intermediate-risk RMS alternating with VAC, but this protocol failed to show any improvement in patient survival [34]. The antitumor activity and toxicity of vincristine in combination with irinotecan (VI), when administered as window therapy, was evaluated in pediatric patients with newly diagnosed metastatic RMS. The VI combination is highly active in metastatic RMS with a complete response/partial response (CR/PR) rate of 70% [35]. These data support the rational for the COG protocol ARST0531 for intermediate risk RMS. This study randomized patients to receive VAC compared to VAC alternating with VI for 43 weeks. The study D9803 study focused on second look surgery for initially unresectable tumors and evaluated radiation dose reduction to 36 Gy after salvage surgery. Despite interventions designed to enhance local control in ARST0531 compared to D9803, local failure was higher in ARST0531 than D9803 (27.9% *vs.* 19.4%). The reduced cyclophosphamide dose is entertained as a potential explanation [36].
With the goal of improving local control, the IRS-IV study compared hyperfractionated radiotherapy (2/day) versus conventionally fractionated radiotherapy (daily) in children of the CG III RMS with no improvement in local/regional control, FFS, or OS [37]. The D9803 study focused on *second look* surgery for initially unresectable tumors and evaluated radiation dose reduction until 36 Gy after rescue surgery. The ARST0531 study aims to evaluate the benefit of RT administered early (week 4). As for radiotherapy, it is now accepted that brachytherapy and proton radiation reduce treatment-associated toxicities.

Treatment for high-risk RMS patients

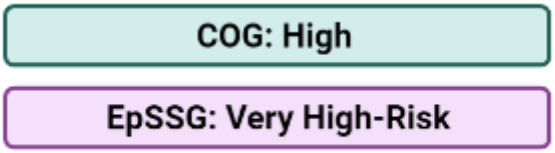

The outcome of children with metastatic disease remains very poor. Despite the high-intensity of systemic therapy, the overall survival at 3 years is 25-30%. The COG recently conducted the ARST0431 study, an intense multidrug combination of therapy. Patients received 54 weeks of VI therapy, an interval compressed of vincristine/doxorubicin/cyclophosphamide alternating with etoposide/Ifosfamide and vincristine/ dactinomycin/ cyclophosphamide. In addition, radiation therapy in weeks 20 to 25 or weeks 1 to 6 was applied in patients with intracranial or paraspinal RMS extension. Unfortunately, the use of this dose-intensive multiagent regimen resulted in a 3-year EFS of 38% and OS of 56% for all patients with stage 4 RMS, not improving the prior IRSG/COG phase II window study that reported a 3-year EFS of 30% and 3-year OS of 43% [38]. Thereafter,the addition of cixutumumab (an anti-insulin-like growth factor-1-IGF1-monoclonal antibody) or temozolomide (a DNA alkylating agent) to the ARST0431 intensive chemotherapy backbone was evaluated in the ARST08P1 study. Despite being safe, neither cixutumumab nor temozolomide improved survival outcome compared to single chemotherapy [39]. Recently, the European randomized phase II VIT-0910 trial also evaluated the combination of temozolomide with vincristine and irinotecan (VIT). They observed better outcomes on VIT than in the ARST08P1- COG trial. However, the European group reported a significant increase in toxicity, mainly related to the increased dose [40].

The combination of gemcitabine and docetaxel has been demonstrated to be active in relapsed RMS [41]. Since response of RMS to chemotherapy is initially linear, myeloablative chemotherapy with stem cell rescue was proposed following the thought that “the higher the dose, the greater the response”. However, several studies have shown that there is no survival advantage [42].

One of the major obstacles for success in high-risk RMS is the control of minimal residual disease (MRD). To approach MRD, an alternative strategy is the use of maintenance therapy or metronomic CT, the continued administration of low doses of drugs with the aim of blocking the growth of residual tumor cells. Several studies suggest that prolonged and continued use of low-dose CT has a different mechanism of action than maximal tolerated cytotoxic doses. The oral maintenance CT study of the German group with trofosfamide and etoposide alternating with trofosfamide and idarubicin showed promising results [43]. This data were the basis for the EpSSG study where they propose maintenance therapy for 6 months with vinorelbine and low doses of cyclophosphamide [44].

1.4 Biology of rhabdomyosarcoma

1.4.1 RMS cell of origin

RMS can arise in the limbs, trunk, head and neck, and pelvis. Muscles at each of these regions are generated from distinct mesodermal pathways. In addition, although RMS frequently arise in muscle-skeletal tissues, some ERMS originate in regions such as the genitourinary tract or parameningeal sites, which are devoid of skeletal muscle.

1.4.1.1 Ontogeny of the skeletal muscle

Understanding the origin and development of the skeletal muscle is fundamental to characterize the RMS cell (or cells) of origin, due to the high number of parallelisms observed between the myogenic program and overall RMS features.

After neural tube formation (22-23 embryonic days) in the ectoderm, mesoderm is disposed adjacent to the neural tube and starts to segment into somites. Most anterior somites are the first to enter into a myogenic program. At embryonic days 26-30, branchial arches generate muscles of the facies and jaw. By the time posterior somites start early stages of muscle differentiation, anterior somites are already in advanced stage of differentiation. At this time, myoblasts start to migrate into the limb buds and to generate the limb muscles [45].

Limbs and trunk muscle derive from somites (**Figure I. 3)**. The somite substructure unit, the dermatomyotome, is where the first myogenic precursors appear, which are characterized by the expression of *PAX3* and *PAX7*. These genes are the upstream myogenic regulatory genes that, unlike the myogenic regulatory factors (MRFs), are not tissue-specific. As such, *PAX3* and *PAX7* are expressed in the neuroectoderm and neural crest. *PAX3*, rather than promoting proliferation or tumor formation, is responsible for maintaining a progenitor state in the cell, and its deregulation allows the tumor-initiating process to take place [46] [47].

Myogenic differentiation requires the expression of a core gene set which includes *MYF5 or MRF4, MyoD and MyoG*. Moreover, lineage-specific TFs reflect differences in muscle subgroups. Limb and trunk muscles derived from somites differ in the set of transcriptional factor activators. In the limbs, sine oculis homeobox homologue (SIX) and eyes absent (EYA) proteins regulate PAX3, which in turn control the proliferative myogenic cell pool acting through MYF5 or MRF4 to regulate MyoD and myogenin expression. For limb muscles, the migrating progenitor cells that develop the limb buds expressed PAX3. In the trunk muscles, PAX3 acts directly upstream of MyoD. It is worth noting that jaw and extraocular muscle differentiation is not controlled by early expression of the TFs PAX3 or PAX7, but by other TFs such as PTX2 and TBX1 that regulate the expression of MRFs in these muscle progenitor cells [45, 48, 49] (**Figure I. 3 B).**

The expression of the b-Helix-Loop-Helix (bHLH) MRFs as *MYF5* and *MyoD* indicates early commitment of the cells into the myogenic program. Here, cells exit the cell cycle and begin to express muscle-specific markers while *PAX3* is down-regulated [45]. Later, terminal differentiation is characterized by *MyoG* and *MRF4* gene expression. To successfully complete the normal myogenic process, sequential expression of different MRFs must occur [50]. The expression of these regulatory factors increase at the same time as *PAX3* and *PAX7* gene expression decrease in cells undergoing the myogenic specialization program [50].

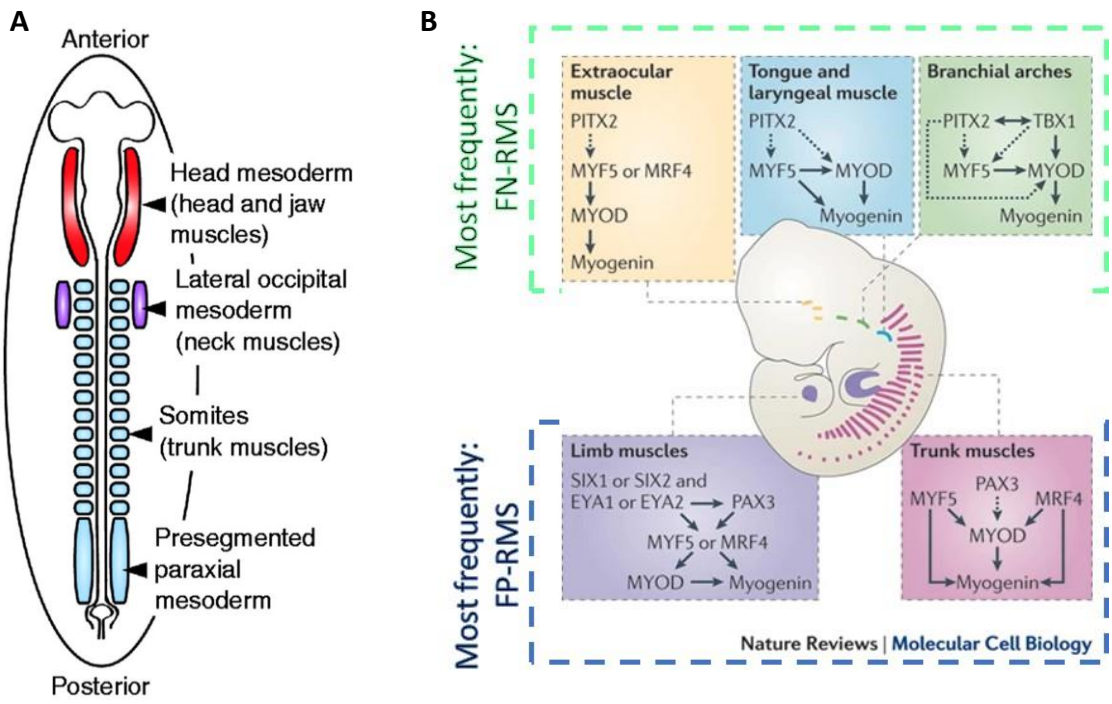

Figure I. 3. Origins of the muscles. A) Schematic of 13 somite amniotic embryo corresponding to Carnegie stage 11 in human (~24 days) showing location of myogenic regions. Carnegie stages are a standardized system of 23 stages used to provide a unified developmental chronology of the vertebrate embryo. Figure taken from [45] **B)** Distinct genetic networks regulate the differentiation of specific muscle lineages Figure taken from [48] and modified from [51].

According to the literature, some signaling pathways are implicated in the positive regulation of myogenic differentiation. Sonic Hedgehog signaling (SHH) and WNT family are described to increase the expression of pro-myogenic regulatory factors, such as MyoD and Myf5, and downregulate the expression of the stem regulatory factors PAX3 and PAX7 [52, 53]. The hepatocyte growth factor (HGF) was described to stimulate limb bud formation, and HGF and its receptor c-MET are involved in the migration of PAX3-positive myoblasts. Also, the Fibroblast Growth Factor (FGF), whose expression is under PAX3 regulation, promotes myogenic differentiation [54]. In contrast, a subgroup of cytokines of the transforming growth factor β (TGFβ) family, such as the Bone Morphogenetic Protein (BMP), were described to favor the stemness of muscle progenitor cells, which would retain an undifferentiated state [55].

1.4.1.2 Origins of RMS

Based on its anatomical location and the characteristic expression of MRFs, such as *MyoD1, MYF5, MyoG* and *MYF6*, RMS is a tumor resulting from the blockage of the myogenic program of muscle lineage committed precursor cells. This hypothesis fits well with FP-RMS tumorigenesis, in which the aberrant oncoprotein PAX3-FOXO1 maintains the expression of *MyoD1*, *MyoG*, *SIX1* and *IGF2* upregulated, and tumor cells retain an undifferentiated, proliferative, and mitogenic state. However, the blockade in a myogenic progenitor state would not explain the origin for those RMSs (especially FN-RMSs) that arise in muscles whose embryological regulation depends on non-canonical muscle TFs, common for limb and trunk muscles, or those RMSs that arise in regions that lack skeletal muscle. In those RMS, the tumor cell of origin has been postulated to be a mesenchymal progenitor, or even a non-myogenic precursor cell. Furthermore, some reports have proposed the hypothesis of different cells of origin in RMS, based on the existence of an early mesenchymal precursor shared by myogenic and endothelial lineages [56].

Currently, the most widely accepted theory for RMS origin is a myoblast or myocyte cell in fetal stages (embryonic origin) or a post-natal satellite muscle cell. To recapitulate the molecular events required to drive RMS initiation from a muscle progenitor cell, genome engineering models have shed light on multiple potential RMS cells of origin. In 2004 Keller et al. generated the first model using a conditional *PAX3-FOXO1* knock-in allele activated in MYF6-positive cells in late embryogenesis. No other genetic alteration was required in this model to replicate FP-RMS features [57]. In 2007, Linardic et al. ectopically expressed PAX3-FOXO1 in fetal and postnatal human skeletal muscle cells (SkMCs) cultured *in vitro* [58]. Unlike non-muscle cells, SkMCs not only tolerated the fusion oncogene, but they were effectively converted into tumorigenic RMS-like cells. In contrast, Ren Y.X. et al. found that, after inducing the expression of PAX-FOXO1 in murine mesenchymal stem cells, these cells failed to form tumors when inoculated into mice [59].

Of particular interest for this thesis is the report by Abraham et al. (2014), in which they addressed the relationship between cell lineage origin and sensitivity to

targeted therapies [60]. Using conditional murine models, they expressed the *PAX3-FOXO1* fusion oncogene and inactivated *p53* at different stages of the myogenic lineage. They described that the characteristics of the tumors changed during myogenic development, and that the tumors responded differently to HDAC inhibitors (SAHA and entinostat).

Other attempts to identify the RMS cell of origin included mimicking the most frequent alterations found in FN-RMS [3]. RMS formation driven by RAS gene expression was attempted in 2004 by Hettmer et al. They ectopically expressed KRAS-G12V in murine satellite cells to recapitulate the oncogenic signature of human ERMS and ARMS [61]. Also, the relevant timing for cell transformation along the myogenic lineage continuum was reported by Linardic et al (2005) [62] They showed tumorigenesis in mouse xenograft models by stably expressing the oncoproteins T/t-Ag, hTERT and HRAS-G12V in transformed postnatal human skeletal muscle myoblasts (hSkMM) but not in human fetal skeletal muscle precursor cells (hSkMPC) [62]. Langenau and colleagues generated tumors in zebra fish transgenic lines expressing the human KRAS-G12D oncogene, which exhibited ERMS histology [63]

In addition, progenitor cells different from the SkMCs were postulated as cell of origin of RMS, including an adipogenic progenitor, dependent on constitutive SHH [64], and endothelial progenitor driven by the Hedgehog pathway in FN-RMS [56].

1.4.2 Fusion oncoproteins in Rhabdomyosarcoma

In 1993, the fusion of the FKHR gene (or FOXO1) to PAX3 was first described in ARMS [65]. The chromosomal rearrangement, in which the *PAX*3 gene on chromosome 2 juxtaposes to the 3′ end of the *FOXO1* locus on chromosome 13, generating the PAX3-FOXO1 fusion oncogene t(2;13)(q35;q14), is found in approximately 60% of ARMS cases. Less frequently, in about 20% of ARMS cases, another chromosomal translocation occurs between *PAX7* (on chromosome 1) and *FOXO1*, leading to the *PAX7-FOXO1* oncogene t(1;13)(p36;q14) (**Figure I. 4**). Patients with the *PAX7-FOXO1* rearrangement

have superior overall survival compared to patients with the *PAX3-FOXO1* rearrangement [26, 66].

These new transcripts are translated into chimeric oncoproteins that work as bona fide TFs. The regions of PAX3 or PAX7 compounding the oncoproteins conserve the DNA binding domain in the amino terminal region, while FOXO1 harbors the transcriptional activation domain fully functional in the carboxy-terminal region. Moreover, these fusion proteins are highly expressed and are more potent transcriptional activators than the wild type PAX and FOXO1 proteins [67-69]. Of note, the mechanisms for the high PAX3-FOXO1 expression rates differ from PAX7-FOXO1 [70]. In the latter, the high levels of transcription are the result of gene copy number amplification that leads to enhanced mRNA levels. In contrast, the increased expression of PAX3-FOXO1 is a copy number-independent process [70]. The stabilization of the fusion oncoprotein occurs by post-translational modifications such as the phosphorylation of S503 mediated by PLK1 (Polo-like kinase 1) or the acetylation of the K426 and K429 residues in PAX3-FOXO1 [71, 72]

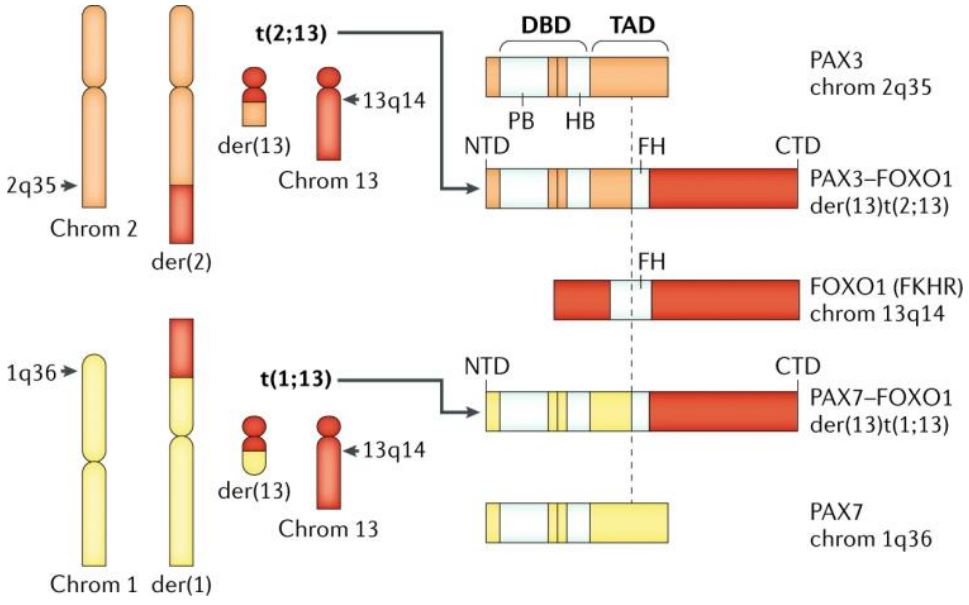

Figure I. 4. PAX-3/7-FOXO1 driver of RMS formation. Balanced translocations between PAX3 in the long arm (q) of chromosome 2 (2q35) and PAX7 in chromosome 1 (1q36), with the FOXO1 gene in chromosome 13 (13q14), generate the fusion proteins characteristic of FP-RMS. The coding fusion proteins contain the amino-terminal domain (NTD) of PAX3 or, less commonly, PAX7, and the carboxy-terminal domain (CTD) of FOXO1. The PAX region retains the DNA-

binding motifs in the amino-terminal region of the wild type PAX3. Of note, some of the activation domains of the wild type FOXO1 CTD are altered in the translocated form of FOXO1. In this region there are acetylation and phosphorylation sites. For example, AKT-dependent phosphorylation sites regulate the subcellular localization and degradation of wild type FOXO1 but not PAX3-FOXO1. On the other hand, involvement of alternative chromosomes in the pathogenesis of RMS has not been described. DBD, DNA-binding domain; HB, homeobox domain; FH, forkhead-related domain; FKHR, forkhead homologue in RMS (initial FOXO1 gene designation); PB, paired box domain. Adapted from[1]

PAX3/7-FOXO1 targets have recently been identified by immunoprecipitation studies [73]. PAX3-FOXO1 binds to chromatin regions enriched in histone marks associated to active transcription [7]. Mechanistically, PAX3-FOXO1 binds to DNA regions enriched in enhancer box (E box-domains) elements (DNA specific sequence CAGCTG) recognized by myogenic master TFs (such as MyoD) to activate muscle differentiation [74].

By studying the regions of the genome that control the expression of muscle cell identity genes, defined as super-enhancers and characterized by an enrichment in acetylated H3K27 (H3K27Ac), Gryder et al.[7] found that MyoD1 expression levels are under the control of super-enhancers (SE) during normal muscle development as well as in the PAX3-FOXO1-bearing cell line RH4, but not in other lineage tissues (**Figure I. 5**). Mechanistically, PAX3-FOXO1 cooperates with MyoD, MyoG, and MYCN, which in turn generate SEs in their target genes. Interestingly, like the PAX3 wild type, PAX3-FOXO1 does not directly bind to the *MyoG* gene, therefore *MyoG* expression is regulated indirectly by MyoD1 and by PAX3-FOXO1. PAX3-FOXO1 directly interacts with the BRD4 protein (chromatin protein remodeling bromo domain 4), allowing the redistribution of chromatin regulatory marks in RMS and forming 3D-loops in the promoters of those target genes that will result in the generation of new SEs.

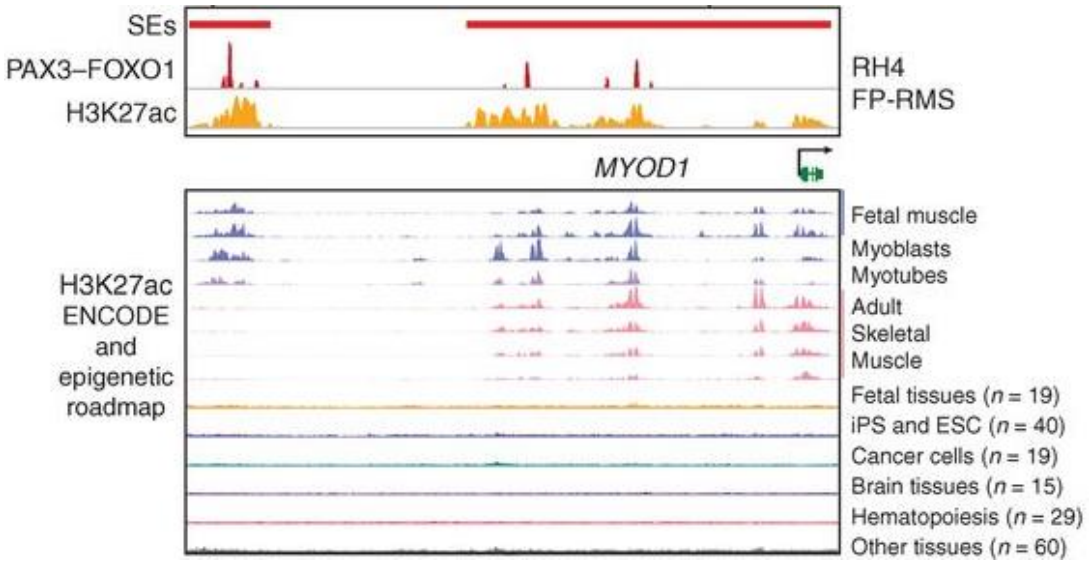

Figure I. 5. PAX3-FOXO1 binding sites in the MyoD1 enhancer region are marked by H3K27acetilation. Histone 3 acetylation in lysine 27 (H3K27ac), mark for active enhancers, is present in MyoD1 enhancers in myogenic precursor cells. Through myogenic differentiation (middle) H3K27acetylation in MyoD1 enhancers and super-enhancers is reduced, while this mark is absent in MyoD1 in other cells and tissue types (overlapping plots, bottom). iPS, induced pluripotent stem cells; ESC, embryonic stem cells. Taken From Gryder et al[7] .

The fusion gene generates SEs near a subset of target genes. In this study, along with four other major studies [73, 75], 1010 target genes of the oncoprotein were defined, including: *MYCN, FGFR2, FGFR4, MET, ALK, FOXF1, EYA1, PITX2 or BMP5. MYCN* is amplified frequently in ERMS. Some genes such as *MET* [76], *ALK* [77], *FGFR4* [78], and *FGF8* [79] have central roles in the growth and differentiation of muscle progenitor cells, and validated therapeutic targets in both FP and FN-RMS. The relevance of *FOXF1* in PAX3-FOXO1-mediated tumorigenesis *in vivo* has recently been demonstrated [80]. E*YA1* have previously been described involved, together with SIX in normal myogenesis and tumorigenesis [81]. The BMP phosphoprotein signaling is differentially expressed in myoblasts and myotubes when compared to RMS [82]. PITX2 is involved in SHH signaling pathways during myogenesis [40]. These genes are examples of the plethora of fundamental myogenesis cascades affected directly by the fusion gene.

1.4.3 Genetic and epigenetic alterations in RMS beyond the translocation

Tumors that bear FOXO1 translocations have an exceptionally low mutational rate, although focal genomic amplifications are frequently observed in these tumors [83] (**Figure I. 6**). The most frequently amplified regions are 2p24, containing the *MYCN* oncogene, and 12q13-q14, containing *CDK4*. *MYCN* amplification involves less than 1 Mb and corresponds to the amplified region also found in neuroblastoma [2]. Amplification involving *MYCN* occurred predominantly in FP-RMS [83]. Whereas *MYCN* amplification is relevant for neuroblastoma clinical outcome, it has not been correlated with prognostic significance in RMS [84]. In contrast, the 12q13-q14 amplification involving *CDK4* has been associated with worse survival [85]

ERMSs exhibit a more complex genetic pattern: loss of heterozygosity (LOH), chromosomal alterations, increase of single nucleotide polymorphisms (SNPs), and several other causal gene mutations have been reported [1, 2, 83].

LOH of the chromosomal region 11p15.5 is due to loss of the maternal allele and duplication of the paternal allele, resulting in paternal isodisomy. Genes such as *H19*, *IGF2* and *CDKN1C* are found in this region [83]. The loss of monoallelic gene regulation by DNA methylation, or loss of imprinting (LOI), of 11p15.5 is associated with IGF2 overexpression, which is one of the most universal RMS hallmarks [86, 87]. IGF2 has an autocrine mitogenic effect through its binding to IGF1R. The IGF2/IGF1/IGF1R axis constitutes a central part of this work, and details of this pathway will be exposed in the following sections.

Gains or losses of whole chromosomes or chromosome arms also occur more frequently in FN-RMS than in FP-RMS. In a cohort of 147 RMS, gains of chromosomes 2, 7, 8, 12 and 13 were found mainly in FN-RMS. Copy number gains of the 12q14-15 locus, which involves the *MDM2* gene occurred predominantly in FN-RMS [83]. MDM2 inactivates the tumor suppressor protein TP53, and MDM2 protein overexpression has been described in 10% of RMS patients [88]. In addition, *TP53* mutations could be found in up to 12% RMS, as inferred by a study with 631 RMS samples [89]

The most frequent mutations affect genes of the RAS pathway, the receptor tyrosine kinase FGFR4 (fibroblast growth factor receptor 4) gene, and the catalytic subunit of the phosphatidylinositol-4,5-bisphosphate 3-kinase (PI3KCA), of the PI3K complex [2]. Activating mutations in the RAS family genes are frequently observed in FN-RMS. KRAS and *HRAS* mutations are mainly found in infants less than 1 year, while *NRAS* mutations are preferably found in adolescents [89]. Mutations in genes coding proteins involved in RAS signaling have also been described (such as NF1, BRAF and PIK3CA), and all of these mutations result in aberrant RAS signaling. Of note, most FN-RMS cell lines used in the laboratory harbor oncogenic mutations in some RAS isoforms.

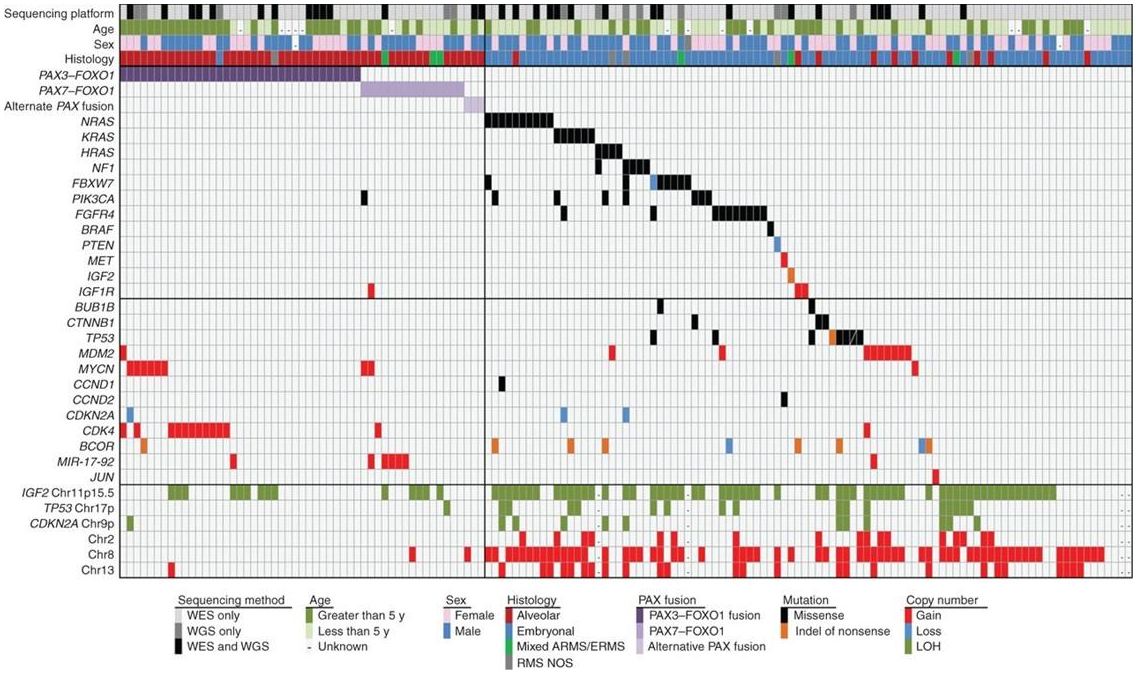

Figure I. 6. Genomic landscape of pediatric RMS across 147 rhabdomyosarcoma cases. The image displays two distinct RMS genotypes defined by the presence or absence of a PAX gene fusion and recurrent mutations in RAS pathway genes in fusion-negative tumors. Note the low prevalence of mutations especially in the FP-RMS. Adapted from [83].

Another alteration frequently found in FN-RMS is a mutation in the *FGFR4* receptor gene. FGFR4 plays a role in the normal process of muscle development, but its expression declines along skeletal muscle maturation [45, 90]. Activating *FGFR4* mutations, or increased expression of the wild type form of *FGFR4*

sustained by PAX3-FOXO1 in FP-RMS, result in increased signaling through RAS or STAT signaling pathways, affecting RMS growth and metastasis [91].

Another frequent genetic alteration found mainly in FN-RMS is the mutation of the *PTEN* gene, which regulates PI3K. PTEN (Phosphatase and tensin homologue deleted on chromosome 10) expression can also be silenced by promoter DNA methylation. In addition, the expression of the tumor suppressor gene *CDKN2A* is found deleted 2% of RMS [83], by mechanisms involving promoter methylation, LOH and mutations [1].

MYOD1 mutation of the L122R codon have been described for a subgroup of FN-RMS with distinctive clinico-pathological features and outcome, and involves alterations in the PI3K–AKT pathway [92]. Recently in a cohort of 641 patients, the COG reported MYOD1 mutation in 3% (n = 17 of 515) of all FN-RMS cases and no FP-RMS cases [93]. Mutation of MYOD1 was associated with dismal survival and head and neck or parameningeal location for primary tumor.

The integration of the molecular features into a functional RMS signature has shown that the genes regulated by the PAX3-FOXO1 fusion, and the genetic and epigenetic alterations found in FN-RMS converge at the same receptor kinase signaling axes: the PI3K/AKT/mTOR and the RAS/RAF/MAPK pathways. Therefore, alterations in these two key RMS pathways will be responsible for tumor growth and proliferation of the RMS tumor cell [94].

1.4.4 Targeted therapies and innovative treatments

To date, promising preclinical candidates brought to clinical trials have not resulted in significant improvement in the survival of high-risk RMS patients. Examples of these failures include the great efforts invested in the development of inhibitors for IGF1R (insulin-like growth factor receptor 1) and other tyrosine kinases (TKs), which showed promising results in preclinical assays but did not bring compelling improvements in the overall survival of RMS patients [95]. Similarly, haploidentical allogenic hematopoietic stem cell transplantation failed to achieve improvement in overall survival of metastatic RMS patients, and behaved an increased toxicity [96]. Given the limited therapeutic options for

patients with metastatic or recurrent RMS, the search for new treatments and clinical trials in this group of patients is currently a priority in RMS research.

Targeting the chimeric TF PAX3/7-FOXO1 would be conceptually the most effective approach in the case of FP-RMS: it should be highly specific against tumor cells since fusion oncogene is not found in healthy cells. However, pharmacological inhibition of a TF is challenging, since any enzymatic region is easily targetable. Although there are currently techniques that would allow the intracellular/intranuclear delivery of antisense oligonucleotides to silence genes of interest, these tools are still far from clinical implementation[97]. With the aim of targeting PAX3/7-FOXO1, other strategies have been investigated, like PLK1 inhibitors which would drive the fusion oncoprotein to proteasomal degradation and therefore reduce PAX3/7-FOXO1 stabilization [72].

A new therapeutic approach is derived from the recent description of the RMS oncogenic core regulatory circuit. The core regulatory circuit is a set of master TFs governing cell identity program. The groups of regulatory enhancers occupied by master TFs are called SEs. SEs and TFs interact to orchestrate transcriptional lineage in normal and malignant cells. Therapeutic approaches aimed to SE disassemble by small molecule inhibitors are now being explored in RMS. In 2017, Gryder et al. were the first to demonstrate the vulnerability of RMS cells to the inhibition of the Bromodomain and Extra-Terminal Domain (BET) family of proteins, which interferes with RMS-specific SE stabilization [7].

In the epigenetic field, members of the histone deacetylase (HDAC) family of proteins were shown to play a relevant role in the transcription of the core regulatory circuits in RMS. Several HDAC inhibitors have already been approved for hematological diseases, but early clinical data have shown reduced efficacy in solid tumors, probably due to issues related with drug bioavailability [98]. Also, potential side effects must be taken into account due to the plethora of key roles that histone deacetylases play in normal non-transformed cells. Currently, a clinical trial of entinostat (HDAC1/2/3 inhibitor) is ongoing for sarcomas including RMS.

The receptor tyrosine kinase (RTK)/RAS/PI3K-driven axis is aberrantly activated in many human malignancies. IGF1R is one of the fundamental targets in

childhood sarcoma and has been extensively studied. There is multitude of studies analyzing the role of IGF1R in sarcomas. Overexpression of the IGF1R itself, deregulation of ligands/ligand-binding proteins or constitutive activation of downstream effectors account for the aberrant IGF1R kinase activation in RMS. Regarding other RTKs, FGFR4 has a direct impact on both FP- and FN-RMS biology by different mechanisms. In FP-RMS, FGFR4 is a transcriptional target of the PAX3-FOXO1 fusion gene, whereas mutations or amplifications activating FGFR4 are described in FN-RMS. FGF receptors activate multiple effectors, including the RAS/RAF/MEK/ERK and PI3K/AKT/mTOR pathways, and sensitivity to PI3K/mTOR inhibitors was observed in preclinical models of FGFR4-dependent RMS [99]. Erdafitinib, which inhibits FGFR and was originally designed to treat bladder cancer, is currently being tested for recurrent childhood RMS (NCT03210714). The c-MET receptor and its ligand HGF have been also preclinically evaluated in pediatric RMS based on their role in muscle development. However, the c-MET inhibitors tested did not prove active in pediatric RMS. The vascular endothelial growth factor receptor (VEGFR), a critical regulator of angiogenesis, was inhibited by different approaches including small molecules and neutralization antibodies. Bevacizumab (Avastin), which binds VEGF and thereby blocks its binding to VEGFR, is well tolerated in children and has been tested in clinical trials for sarcomas, unsuccessfully (BERNIE study, EJC 2017). Similarly, apatinib, a small molecule selective for VEGFR2 inhibition, has been tested in a clinical trial for pediatric sarcomas [100].

The RTK inhibitors are the group of compounds where more development has occurred. Although early clinical trials of many TK inhibitors included RMS patients, very few if any, were designed specifically for RMS [97]. Only the clinical trial of the IGF1R monoclonal antibody Ganitumab in combination with Dasatinib (inhibitor of SRC kinases) was developed for refractory RMS patients (Clinical Trial NCT03041701). This combination is based on preclinical evidence of by-pass resistance to IGF1R inhibitors when used in monotherapy [101].

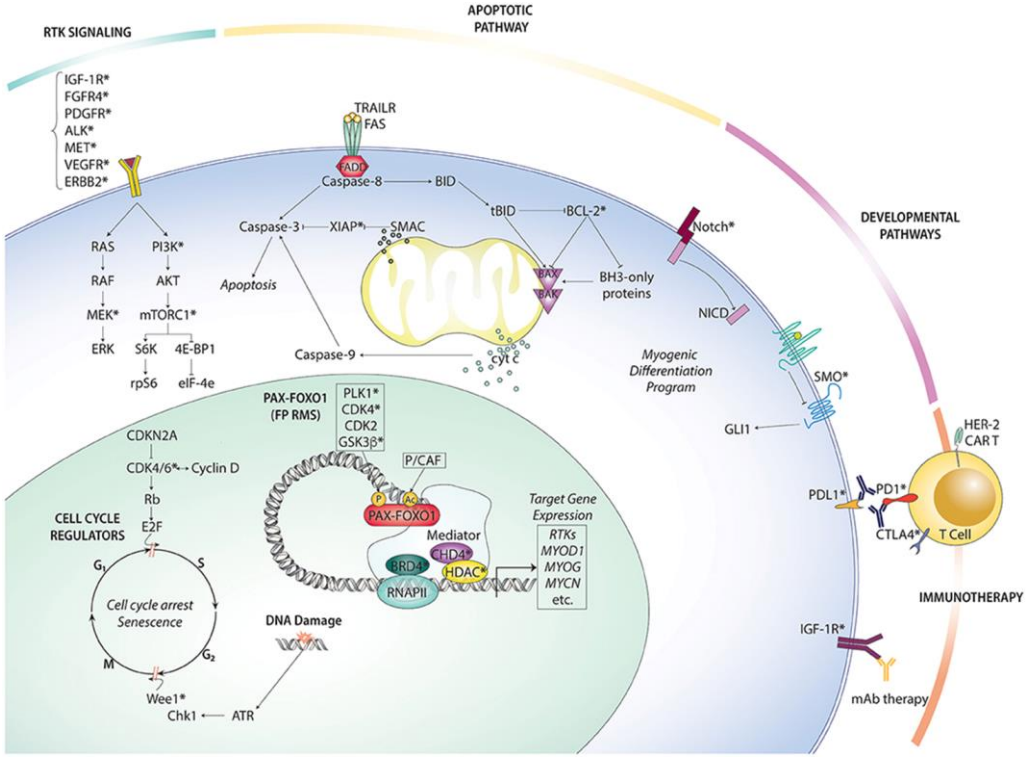

Figure I. 7. Overview of RMS targeted therapies organized by pathway. Therapeutically actionable targets are indicated with an asterisk (*) Taken from [97].

Developmental pathways such as Hedgehog (HH) and Notch have been frequently found aberrantly activated in RMS [102]. Therefore, pharmacological strategies to target these pathways have also been investigated, especially in the subset of embryonal RMS harboring mutations in PTCH1 (the receptor for SHH) or GLI1 amplifications. For other pediatric malignancies the Vismodegib was tested in clinical trials [103]. This drug inhibits Smoothened (SMO), a G protein-coupled receptor that interacts with PTCH1.

As in other solid tumors, cell cycle regulators have also been pharmacologically targeted. Mutations in CDK4 (cyclin-dependent kinase 4) have been described in a subgroup of FP-RMS. The CDK4/9 inhibitor Palbociclib has demonstrated active inducing G1 cell cycle arrest in RMS models. Palbociclib is currently being tested in clinical trials for pediatric tumors, including RMS [82].

The poly (ADP-ribose) polymerases (PARP) bind to DNA single-strand breaks and force DNA homologous repair. PARP inhibitors drive cells to apoptosis by preventing proper DNA repair. Drugs such as olaparib are currently in clinical development also for RMS [104].

Anti-apoptotic inhibitors like venetoclax (a BCL-2 inhibitor) and S63845 (MCL-1 inhibitor) are now being evaluated in the clinic [105, 106]. For childhood RMS, we recently published that selective MCL-1 inhibitors such as S64315 prime RMS to undergo cell death when combined with chemotherapy [107]. These anti-apoptotic inhibitors are particularly relevant for overcoming acquired chemoresistance in RMS.

Table I. 5. Summary of target therapies with supporting preclinical data in RMS already in clinical trials open for pediatric cancer in North America.

Note that the reference from the European clinical trial is indicated if that from North America is not available.

Molecular target	Drug	Phase	clinical trial
Bromodomain and extra-terminal (BET) proteins	**BMS-986158**	**Clinical (I)**	**NCT03936465**
HDAC	**Entinostat/Vorinostat**	**Clinical (I/II)**	**NCT02780804**
ALK	**Crizotinib**	**Clinical (II)**	**EU: 2011-001988-52**
PLK1	**Volasertib**	**Clinical ***	**Withdrawn**
GSK3β	**9-ING-41**	**Clinical (I)**	**NCT04239092**
PI3K/mTOR	**Temsirolimus, Omipalisib**	**Clinical (I/II)**	**NCT00106353**
MEK1	**Cobimetinib**	**Clinical (I/II)**	**EU: 2014-004685-25**
FGFR	**Erdafinitib**	**Clinical (II)**	**NCT03210714**
IGF1R	**Ganitumab**	**Clinical (II)**	**NCT00642941**
CHEK1/CHEK2	**Prexasertib**	**Clinical (I)**	**NCT04095221**
VEGF	**Bevacizumab/ Apatinib**	**Clinical (II)**	**NCT01222715/ NCT03121846**
Multi-RTK	**Regorafenib**	**Clinical (II)**	**NCT01900743**
CDK4/CDK6	**Palbociclib**	**Clinical (II)**	**NCT03242382**
PARP	**Olaparib**	**Clinical (II)**	**NCT03155620**
Immunotherapy			
B7/H3	**B7H3 CAR T Cell Immunotherapy**	**Clinical (I)**	**NCT02982941. Completed**
EGFR	**EGFR806 CAR T Cell Immunotherapy**	**Clinical (I)**	**NCT03618381**
PD-1/PD-L1	**Nivolumab/ Ipilimumab**	**Clinical(I/II)**	**NCT02304458**

Finally, immunotherapy has revolutionized oncology therapy. One example is the clinical efficacy of anti-GD2 (dinutuximab or naxitamab) monoclonal antibodies in neuroblastoma. However, immunotherapy is still in its infancy for RMS treatment. Phase I clinical trials are ongoing with enoblituzumab, an Fc optimized B7-H3 humanized IgG1 monoclonal antibody, engineered for enhancing antibody-dependent cellular cytotoxicity (ADCC) [108]. Similarly, overexpressed surface antigens that drive RMS biology (e.g. IGF1R or EGFR) may support potential for a cancer vaccine or T cell therapy (chimeric antigen receptor T cell, or CAR T cell, therapy).

2 The insulin-like growth factor axis

2.1 Components of the IGF axis

The IGF axis consists of three different ligands (**IGF1**, **IGF2** and **insulin**), three cell-membrane receptors **(IGF1R**, **IGF2R** and the insulin receptor or **IR**), and six high-affinity IGF binding proteins (**IGFBPs 1-6**).

2.1.1 The ligands: IGFs

At the organism level, the release of IGF1 and IGF2 is controlled by the central nervous system, which regulates the endocrine secretion of the growth hormone (GH). GH stimulates IGF1 and IGF2 production in the liver. Unlike insulin, whose release is systemic, IGF1 and IGF2 are secreted by paracrine or autocrine mechanisms. IGF ligands in circulation are bound by IGFBPs, 90% of which bind to IGFBP3. IGFBPs are responsible for the bioavailability of the IGF1 and IGF2 ligands. The role of IGFBPs is defined mostly by the amount of IGF1 and IGF2 released by the cells and ability to bind to the receptor [109].

The IGF1 gene is located in the chromosome region 12q23, comprises six exons, two different promoters, and encodes for a 70aa protein. The *IGF2* human gene, also called somatomedin A, is located in the chromosome region 11p15.5, has four promoters and ten exons, but only the last three exons contain coding

sequences. Both ligands share high homology between these and with the insulin peptide.

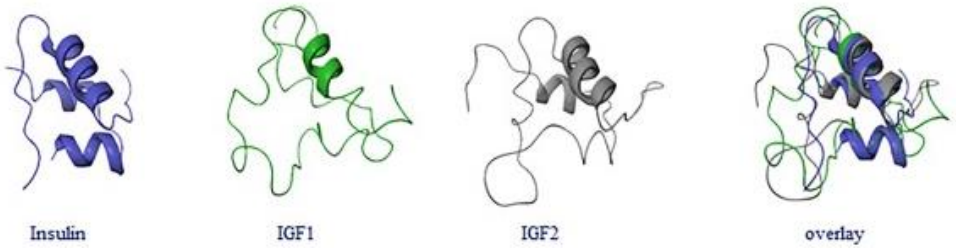

Figure I. 8. Homology of the folded protein structures of Insulin (blue), IGF1 (green) and IGF2 (gray). Overlay shows the comparative structure. Adapted from [110]

IGF1 and IGF2 levels change along fetal and postnatal life. IGF2 plasma concentrations are several folds higher than IGF1 levels during fetal life. IGF2 plays a central role in embryogenesis. n mammals, IGF2 is the major growth promoting hormone during gestation. Interestingly, IGF2 positively regulates the MyoD1 function by facilitating the recruitment of transcriptional coactivators, thereby controlling muscle terminal differentiation. At birth, IGF2 serum concentrations decline and IGF1 levels rise concomitantly, induced by GH secretion. In adults, and in contrast to IGF1, IGF2 ligand is sec reted in the liver and is no longer regulated by GH.

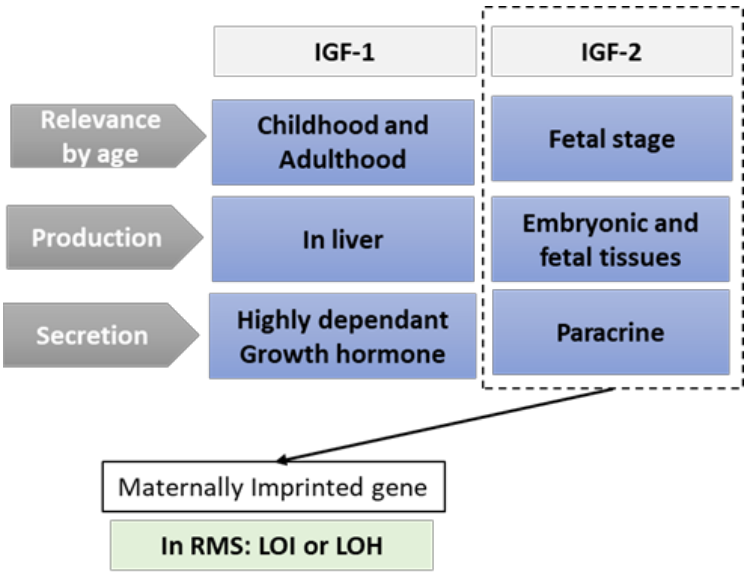

Figure I. 9. Comparative relevance of IGF1 *vs.* IGF2 at different tissues and life stages. More information can be found in detail in the previous section.

Especially relevant for this work is the fact that IGF2 plasma levels in humans are different to those in the postnatal life of mice. IGF2 levels in the serum of adult mice are undetectable while IGF2 is secreted beyond birth in humans. Nevertheless, in adult life, both human and mice express high amounts of IGF1.

In normal skeletal muscle, IGF promotes proliferation, survival and differentiation [111]. In RMS, IGF1 clearly promotes cell proliferation and has anti-apoptotic effects. IGF1 inhibition suppresses the growth of RMS cells *in vivo*. The role of IGF2 in pediatric tumors has been extensively analyzed. Overproduction of IGF2 is a mechanism intimately implicated in the proliferation and survival of tumor cells from RMS, Wilms tumor, and Ewing sarcoma. Due to its relevance in embryonic development and in pediatric tumors, it is of capital importance to understand the regulatory mechanisms of *IGF2* gene expression.

The *IGF2* gene is maternally imprinted, which means that the expression of the inherited maternal *IGF2* allele is silenced by epigenetic mechanisms, assuring the precise control of IGF2 levels. Therefore, only the paternal allele is expressed in the embryo. LOI of the maternal allele, which results from a break in the methylation pattern of the regions associated with its monoallelic specific expression, or the LOH and duplication of the paternal allele, result in IGF2 overexpression. Beckwith-Widemann syndrome is an example of overproduction of IGF2 by LOI [112].

2.1.2 The receptors: IGF1R, IGF2R and IRs

In addition to the complex regulation of ligands, the IGF signaling pathway is modulated by receptors IGF type 1 and type 2 (IGF1R and IGF2R) and the Insulin receptors A and B (IR-A, IR-B). IGF1R and IR exist as homodimers while IGF2R is a monomer. IGF1 as well as IGF2 peptides can activate IGF1R. However IGF2 binds to IGF1R with 2- to 15-fold lower affinities than IGF1 [113]. Of note, although Insulin can also bind IGF1R, its affinity is much lower than IGF1 or IGF2 binding. When IGF1 or IGF2 bind IGF1R or their hybrid receptors, they preferentially support IGF signaling rather than IR signaling [114, 115].

The IGF-1R is mainly involved in the regulation of cell proliferation, anti-apoptosis, differentiation, and cell motility, whereas IR is mostly involved in the control of glucose uptake and metabolism [116]. Details on the role of IGF1R and its ligands in tumor cell growth, differentiation, metastasis, and chemotherapy resistance have been extensively characterized (reviewed [117-119]).

Besides the archetypal structure, heterodimer receptors can exist as hybrids of IGF1R with IR (IGF1R/IR-A and IGF1R/IR-B). Additional data indicate that IGF-1R/IR hybrid receptors have higher affinity to IGF1. The IGF1 ability to bind to multiple receptors confers its tumorigenic property in many types of cancer. On the other side, the IR is not the only RTK associated with IGF1R; other plasma-membrane molecules have been described to have a “cross-talk” with IGF1R. For example, IGF1R/EGFR heterodimers have been identified in cancer cells [120].

IGF2 is the only ligand that binds to IGF2R (or mannose-6-phosphate receptor). However, this binding does not elicit a downstream signaling since IGF2 is immediately internalized and degraded. This reduction in IGF2 bioavailability to bind IGF1R has led to consider IGF2R as a tumor suppressor gene in many tumors. However, in other cancers an active role in proliferation and apoptosis inhibition has been described for IGF2R [109].

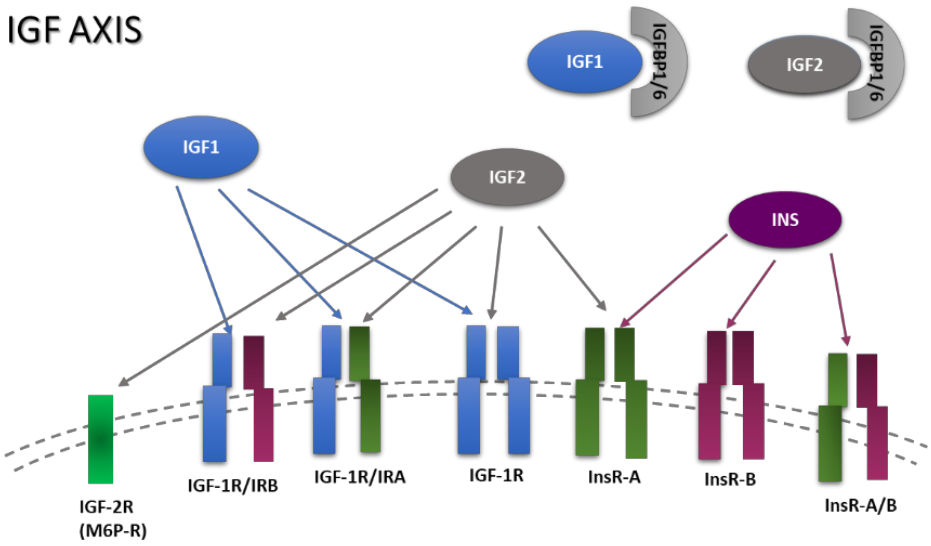

Figure I. 10. The IGF/INS axis is a complex multilayer interacting molecular network. See Section 2.1.2 for details.

2.2 IGF1R signaling

IGF1R is a transmembrane tetrameric glycoprotein formed by two extracellular α-chains linked to two β-chains respectively by disulfide bridges. The β-chain comprises three domains: an extra cellular domain, a transmembrane domain, and a kinase-containing intracellular domain [114, 121]. Binding of IGF1 and IGF2 to the extracellular α-globe (rich in cysteines region) triggers a conformational change that activates the catalytic domain in the β subunit. The IGF1R activation A-loop segment contains the three principal autophosphorylation sites—Tyr1135, Tyr1131, and Tyr1136—, which are sequentially phosphorylated in the kinase domain. After the autophosphorylation of these three residues, IGF1R is fully active and recruits scaffold proteins, particularly the IR substrates IRS1 and IRS2. The adaptor protein SHC1 binds to the juxtamembrane Tyr950 residue when phosphorylated, and IRS1, IRS2 and SHC1 also result phosphorylated. This phosphorylation cascade results in the recruitment of new signaling molecules that contain the Scr homology 2 (SH2) domain, such as the 85kDa regulatory subunit (p85) of PI3K and GRB2 to mediate IGF bioactivities. Alternatively, IGF1R can signal through the Janus kinase (JAK) and phosphorylate STAT3. In summary, IGF1R can signal through three main kinase cascades: 1) IRS1/PI3K/AKT/mTOR; 2) IRS or SHC/GRB2/RAS/MAPK, and 3) JAK/STAT3. It is noteworthy that IGFIR can send contradictory signals depending on the type of signal. In this thesis, we focus on the growth and proliferative functions dependent on the IRS1/PI3K/AKT/mTOR signaling. In RMS, this is the main pathway implicated in activating the expression of growth and cell cycle progression genes (e.g., Myc and cyclin D1). Moreover, the downstream IRS1/PI3K/AKT/mTORC1 signaling is the dominantly activated pathway having prognostic significance in RMS [113, 122].

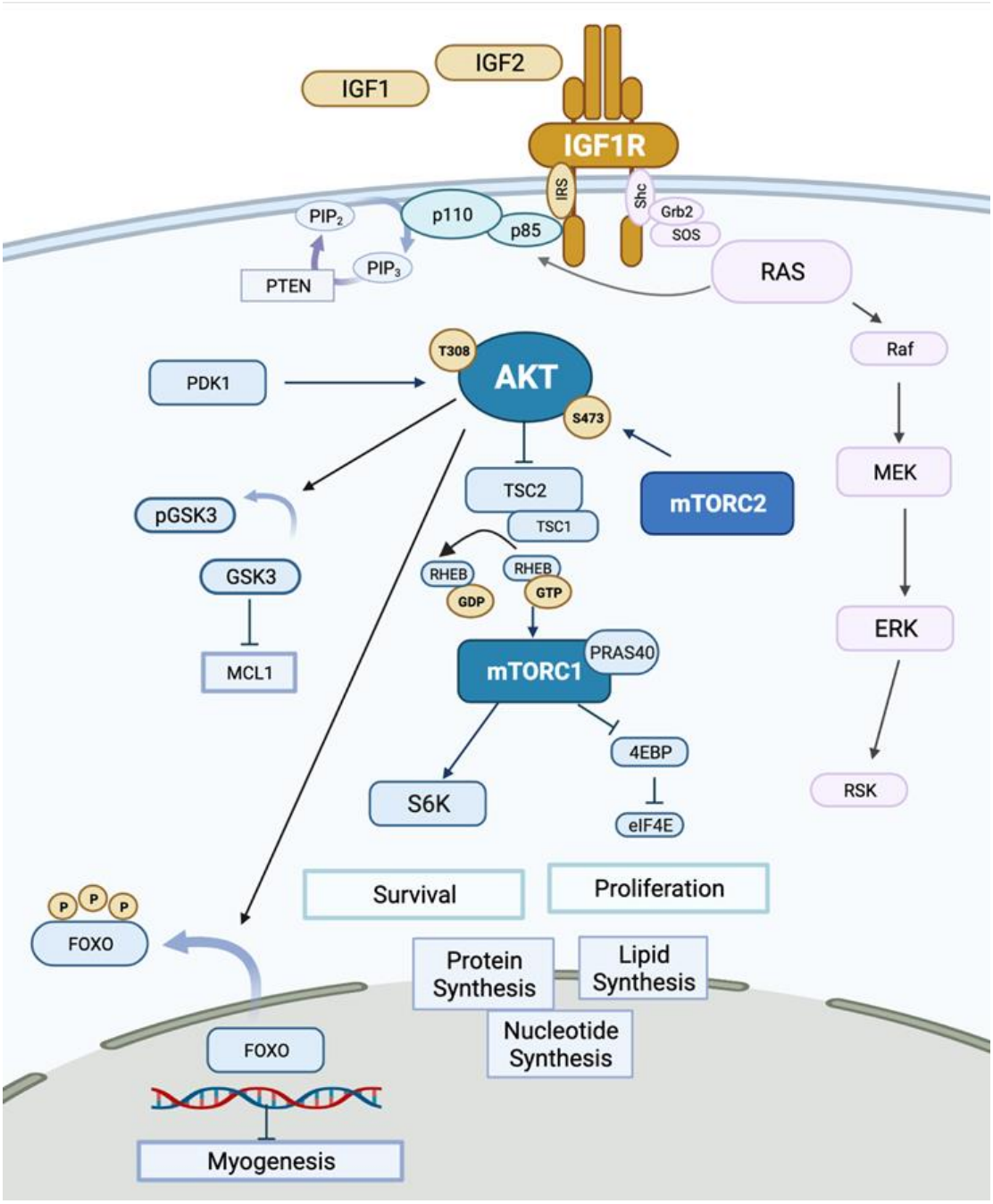

Figure I. 11. Substrates and functions of the IGF1R signaling network. The major signaling pathways activated by the IGF1R are the PI3K/AKT/mTOR and RAS/RAF/MEK/ERK. IGF1R is activated by binding of either IGF1 or IGF2. Ligand binding induces a conformational change and autophosphorylation of key residues in the β subunits of the receptor, and docking proteins then interact with the phosphorylated residues of the activated receptor. Activation of the receptor and transduction of the intracellular signaling kinase cascades culminates in cell proliferation and anti-apoptotic effects. Detailed descriptions of the regulation of IGF1R activation and of these signaling pathways can be found in Sections II.2 and III.1

2.3 The IGF axis in RMS

In contrast to other pediatric sarcomas, IGF2 and IGF1R are the two most relevant components of the IGF axis for RMS oncogenesis [73]. Fazenbaker et al. (2014) showed that IGF2 protein levels in RMS cells were significantly higher than in Ewing sarcoma, in which IGF1 is the predominant ligand of the IGF axis [123] (**Table I. 6**). Moreover, IGF2 is overexpressed in RMS regardless of the presence of the fusion oncogene, both in RMS cell lines [124] as well as in primary tumor samples [23, 87]. As mentioned above, LOI and LOH are two of the mechanisms responsible for the IGF2 overexpression in RMS [83, 86]. In 1990, the Lee Helman´s lab demonstrated the autocrine effect of IGF2 in RMS tumors [125]. In addition, the oncofusion TF PAX3-FOXO1 can induce the upregulation of IGF2, thus enhancing the activation of IGF signaling pathway in FP-RMS [126] [127] [128].

Table I. 6. Comparison of the IGF axis components in pediatric sarcomas.

Tumour type	Cytogenetic characteristics*most comom	Fusion gene	Ligand expression	Receptor expression	Relevance
Fusion Positive RMS	t(2;13)(q35;q14) or t(1;13)(p36;q14)	PAX3–FKHR, PAX7–FKHR	IGF-II	IGF-1R	IGF-II functions as an autocrine growth factor. IGF-II/IGF-1R signalling provides a second hit after PAX–FKHR-induced transformation
Embryonal RMS	Complex karyotype, often LOH of 11p15.5	-	IGF-II	IGF-1R	IGF-II functions as an autocrine growth factor. IGF-II/IGF-1R signalling is involved in the pathogenesis amongst other oncogenic events
Synovial sarcoma	t(X;18)(p11;q11)	SS18–SSX1, SS18–SSX2	IGF-II	IGF-1R	IGF-II/IGF-1R is involved in SS18–SSX-induced transformation and tumour progression
Ewing's sarcoma	t(11;22)(q24;q12)	EWS–FLI1	IGF-I	IGF-1R	IGF-1R is required for EWS–FLI1-induced transformation. Ewing sarcoma cells are highly dependent on IGF-1R signalling both in vitro and in vivo
Osteosarcoma	Complex karyotype		IGF-I, IGF-II	IGF-1R	Activation of IGF -1R by IGF-I stimulates osteosarcoma cell growth in vitro and in vivo

Table Adapted from [129].

On the other hand, analyses of ChIP-seq data have shown that IGF1R and IGFBP2 are directly upregulated by PAX3-FOXO1 [73] [7] and ectopic PAX3–FOXO1 expression was able to transactivate the IGF-I-R promoter in RMS cells [130]. In FP-RMS cells, IGF1R is expressed on the cell surface but also localizes

in the cell nuclei, whereby nuclear expression is associated with increased tumorigenesis *in vivo* [131].

Of note, IGF1R is expressed in almost all cases of RMS, irrespective of subtype, as shown by immunohistochemistry studies [132]. IGF1R mRNA quantification revealed a broad range of IGF1R expression levels in RMS primary tumor samples and cell lines [133] (**Figure I. 12**). A vast amount of information connects the function of the IGF axis with RMS proliferation [134] and myogenic differentiation [135].

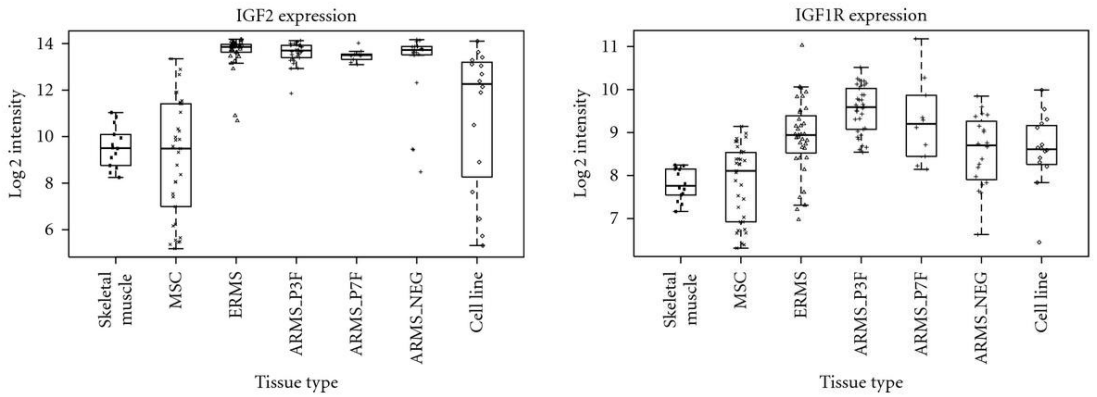

Figure I. 12. mRNA expression levels for IGF2 and IGF1R in a panel of tissue and tumor samples. These databases include normal skeletal muscle (skeletal muscle), mesenchymal stem cells (MSC), ERMS, ARMS (PAX3-FOXO1 and PAX7-FOXO1 fusion positive and fusion negative ARMS_NEG). They also include cell lines (RH3, SCMC, RMS, RH30, RD, RMS-YM, RH18, Ruch3, T91-95, RH41, TE617T, Hs729T, T174, TE441T, Ruch2, and RH4). Expression profile data from Williamson, Missiaglia et al. 2010 [23] and from Missiaglia, Selfe et al. 2009[136]. Figures taken from Martins, Olmos et al. 2011[87].

IGF1R is a prognostic biomarker for overall survival in RMS. Indeed, high IGF1R levels inversely correlate with survival in RMS, even in a subgroup of PAX3-FOXO1-positive patients (**Figure I. 13**) [137]. Furthermore, in basal conditions, IRS1 receives negative feedback from the mTORC1 target p70S6, self-limiting signaling stimulation [122]. In RMS, however, the IRS1 activation appears refractory to physiological negative feedback signals, thus contributing to increased tumorigenesis and poor survival in these patients [122].

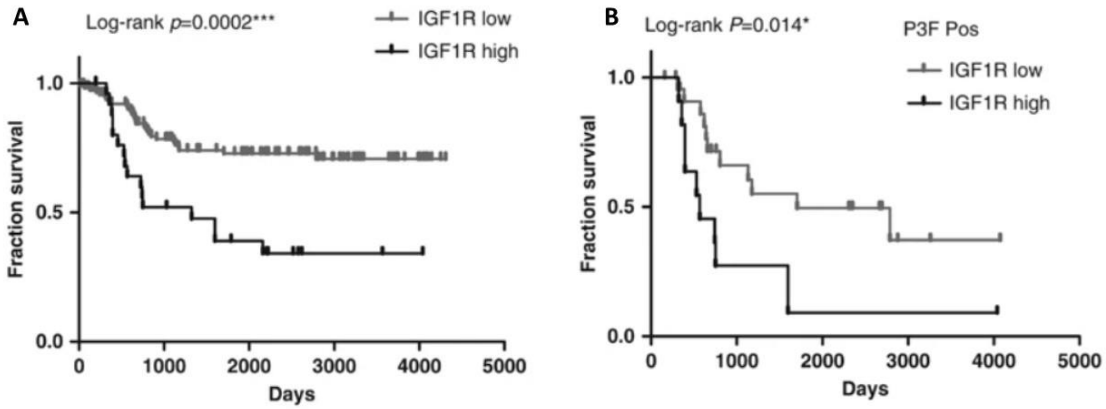

Figure I. 13. High IGF1R expression level predicts worse survival in RMS patients. A) Kaplan–Meier survival analysis of 146 RMS patients grouped by IGF1R level. High IGF1R levels correlate with poor overall survival. **B)** Kaplan–Meier survival analysis of based on IGF1R expression levels in PAX3-FOXO1-positive RMS patients (n=35). Combination of high IGF1R expression and PAX3-FOXO1 presence predicts the worst survival outcome. Graphs taken from [137], and original data taken from [138].

2.4 Pharmacological inhibition of the IGF axis

Since the first inhibitors were developed and tested in RMS experimental models back in the 1990s [25], the efficacy of dozens of inhibitors of the IGF pathway has been evaluated in preclinical models and clinical trials. Different strategies have been developed to inhibit the IGF axis: i) small molecules inhibiting the RTK; ii) antibodies blocking ligand binding to the receptor, and iii) antibodies capturing free ligands and preventing their binding to the receptor.

In reference to the first strategy, in the COG preclinical testing program (PPTP), the IGF1R inhibitors effectively and specifically displayed cytotoxic activity in RMS cells [139, 140]. Different trials have used IGF1R inhibitors in preclinical models of ERMS or ARMS [141]. Briefly, some of the IGF1R inhibitors preclinically tested include i) **BMS-754807,** a small molecule that blocks the tyrosine kinase domain; ii) **MEDI-573**, an IGF1/2 blocking monoclonal antibody; and iii) **R1507 (Teprotumumab),** an IGF1R blocking monoclonal antibody. These were preclinically tested as single therapy or in combination with specific inhibitors of SRC, YES, PDGFR, PI3K, mTOR, ALK or multi-kinase inhibitors.

Particularly relevant for this thesis are anti-IGF1R antibodies that achieved phase I/II in clinical assays for pediatric sarcomas, of **cixutumumab** (IMC-A12)

combined with the mTOR inhibitor temsirolimus [95]; **teprotumumab** (R1507) [142]; and **ganitumab** in combination with the SRC inhibitor **dasatinib**. However, despite multiple pharmacological approaches to inhibit the IGF1R signaling, their effectiveness in the clinic proved limited.

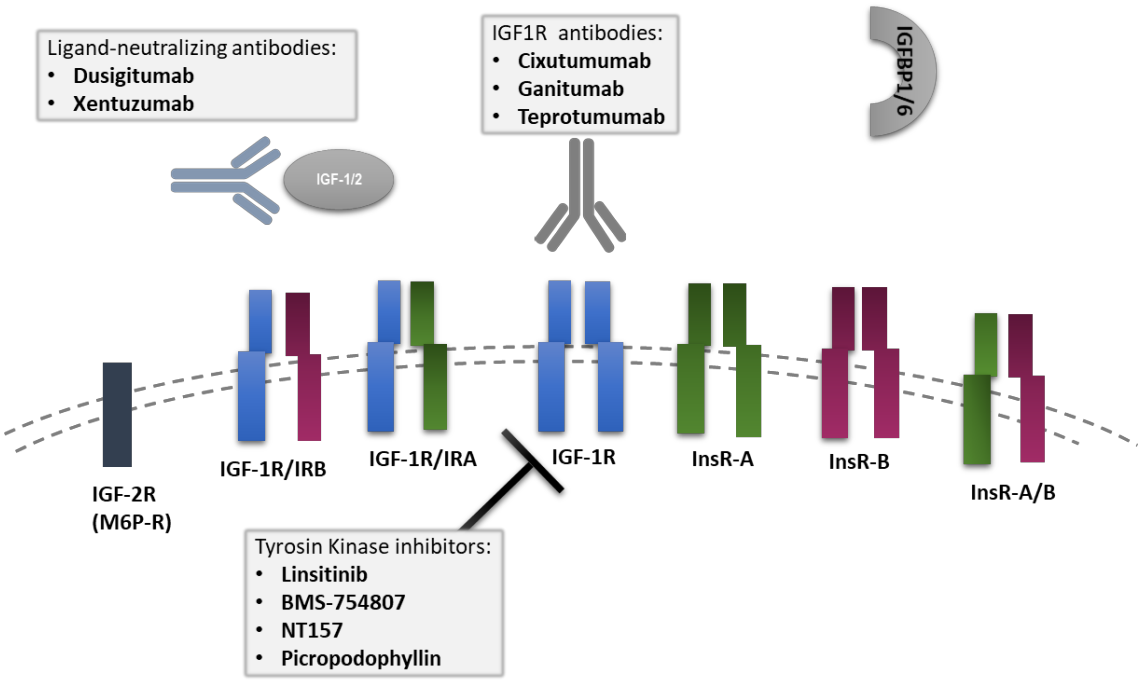

Figure I. 14. The IGF-target therapies in clinical development. IGF-targeted therapies block ligand receptor interactions and induce receptor internalization and degradation. The ligand-receptor interaction can be blocked with different strategies: i) anti-IGF1R monoclonal antibodies; ii) IGF ligand neutralizing monoclonal antibodies; and iii) small molecules that bind the receptor tyrosine kinase domain and block signaling downstream of IGF1R and IR. mAb monoclonal antibody. TKI tyrosine kinase inhibitor. Data from [143].

Failed attempts to block the IGF pathway at the receptor level suggested that specific biomarkers are necessary to identify cases of RMS that are potentially sensitive to IGF inhibition, which would increase the efficacy in clinical trials. On the other hand, many intracellular compensatory mechanisms previously described are involved in adaptive strategies that overcome IGF inhibitory monotherapy and confer resistance to these treatments: formation of heterodimers with other membrane receptors [144], transcriptional activation by the PAX3/7-FOXO1 oncoprotein [130], or the nuclear expression of IGF1R [131].

2.5 The dual-specific anti-IGF-1/IGF-2 human monoclonal antibody

Remarkably, even though IGF1 and IGF2 share 62% protein sequence, only IGF2 can bind IR and enhance tumor proliferation. The ability of IGF2 to signal through IR-A homodimers, thereby promoting tumor cell proliferation, is a potential mechanism of resistance to IGF1R inhibition. Although many IGF1R inhibitors also block hybrid IGF1R/IR-A signaling, IR-A signaling escapes IGF1R inhibition. However inhibitors developed to block both receptors display a significant side effect, namely hyperglycemia, which is a significant clinical deterrent.

The development of IGF ligand inhibitors stems from the need to mitigate the side effects triggered from IR blockade, possible IR-dependent escape mechanisms, and the very likely ability of IGF1/2 ligands to bind (albeit with lower affinity) and signal through other membrane RTKs.

The synthesis of the dual-specific anti-IGF1/IGF2 human monoclonal antibody m708.5 was described in 2011 [145]. The *in vitro* and *in vivo* cytotoxic activity of m708.5 in neuroblastoma models has been tested [146]. The antibody m708.5 binds human IGF1 and IGF2 with high affinity, as was determined by surface plasmon resonance, and has also the ability to bind murine IGF1 and IGF2 [146, 147].

Table I. 7. Binding affinities of MEDI-573 and m708.5.

	MEDI-573	m708.5
Target	Human IGF-I and IGF-II	Human IGF-I and IGF-II
Antibody type	IgG2λ	IgG1
Binding affinity for hIGF-I (K_D pmol/L)	K_D = 294	K_D = 15
Binding affinity for hIGF-II (K_D pmol/L)	K_D = 2	K_D = 9
Binding affinity for mIGF-I (K_D pmol/L)	K_D = 2,000	K_D = 9,500
Binding affinity for mIGF-II (K_D pmol/L)	K_D = 4	K_D = 1,900
Binding to insulin	No significant binding detected	No binding to insulin

Adapted from [146, 147].

Coincidently, another IGF-ligand-inhibitor has been developed, namely, dusigitumab (MEDI-573), which exhibits a worse KD for hIGF than m708.5, but similar affinity for hIGF-2 (see **Table I. 7**). However, m708.5 has lower avidity for murine ligands than MEDI-573. This poor ability to bind murine IGF1/2 must be taken into account, since it will very likely have an impact on efficacy in xenograft models. Note also that murine ligands may activate the human IGF1R receptor on tumor cells, further reducing any anti-tumor effect.

Despite these caveats, experiments testing m708.5 efficacy demonstrated its antitumoral activity *in vitro* and *in vivo* in neuroblastoma experimental models [146]. They also showed the special sensitivity of neuroblastoma cells to this antibody when used as a single agent, due to the high IGF1R and/or IR-A expression levels in neuroblastoma. *In vivo*, m708.5 delayed tumor growth in two neuroblastoma xenograft models, LAN1 and SK-N-MM, at doses as low as 4 mg/kg. Moreover, the mTOR inhibitor, Temsirolimus, had a synergistic effect when combined with this anti-IGF1/2 [146]

The expected anti-tumoral effect of m708.5 in RMS cells or tumors is predicted to be worse than in neuroblastoma, based on the high EC50 for m708.5 in RMS cell cultures (EC50 (µg/ml): Rh30=8.84; Rh41~30; Rh48>30). On the other hand, MEDI-573 lacks *in vivo* antitumoral response in RMS and EW models [123, 146]. The intracellular signaling following m708.5 treatment has not been explored in any pediatric tumor model.

3 AKT signaling in RMS

Genomic and transcriptomic approaches do not always fully explain regulation at the functional level of the cell. In this regard, proteomic studies have shed light in the search for clinically translatable biomarkers of kinase inhibitors, also in RMS models[82, 122]. It has been shown that disparate upstream genomic events can end up in similar downstream pathway modifications.

Some kinases only modify a specific and defined group of substrates, while others are more promiscuous in phosphorylating their effector proteins which often converge phosphorylating the same substrate or substrate complexes. The

preferential activation of one or the other pathway often depends on the type and amount of the initial agonist, as well as the time during which it is exerting its effect. For example, in the case of RMS, the prevalent agonist IGF preferentially signals through the PI3K/AKT/mTOR cascade.

Many studies indicate that the antitumoral efficacy of IGF inhibitors in RMS is conditioned by the activation state of AKT [133]. Moreover, AKT-dependent regulation defines possible intracellular escape mechanisms to IGF1R inhibitors in RMS tumors [122]. Indeed, it has been proposed the existence of two different clusters of RMS tumors based on the phosphoproteomic network analysis of the AKT/mTOR pathway [122]. Furthermore, correlation analysis aimed to find possible links between the levels of protein phosphorylation in tumor samples and short-term survival of patients suggest that protein status could be useful as biomarker for RMS sensitive to IGF/AKT/mTOR inhibitors.

3.1 AKT signaling

AKT (or protein kinase B, PKB) is a serine/threonine kinase that belongs to the AGC family of kinases (the PKA, PKG and PKC kinases). Its three isoforms of AKT1 (PKBα), AKT2 (PKBβ) and AKT3 (PKBγ) share a structure that consists of three functional domains: an N-terminal fragment with a pleckstrin-homology (AKT-PH) domain, a central kinase domain (AKT-KD), and a C-terminal fragment with a regulatory region (AKT-RR) containing a hydrophobic motif [148, 149].

Under basal conditions, without stimulation, AKT is localized in the cytoplasm in an inactive conformation (PH-in), in which the intramolecular structure is maintained by interactions between the AKT-PH and AKT-KD domains. Ligand binding to RTKs or G-protein-coupled receptors (GPCRa) initiates the canonical signaling at the cell membrane level, leading to the activation of different isoforms of class I PI3K kinases. Equally important is PI3K regulation by small Ras-related GTPases [150].

Mechanistically, **RTK**-triggered signaling, such as that initiated by IGF binding to IGF1R in RMS, recruits the PI3K class IA regulatory subunit **p85** to the cell membrane. This recruitment occurs by interaction of the phosphorylated YXXM

motifs in the RTKs or their adaptor proteins (primarily **IRS1** in the case of IGF1R) and the p85 SH2 domain [151, 152]. This interaction results in the release of PI3K class IA catalytic subunit **p110,** which phosphorylates phosphatidylinositol (PtdIns) 4,5-bisphosphate [**PI(4,5)P$_2$**] to generate PtdIns-3,4,5-triphosphate [**PI(3,4,5)P$_3$**][150]. Class IA PI3K catalytic subunits **p110α**, **p110β** and **p110δ** have p85 binding domains (p85-BD) (**Figure I. 15**), and the isoforms p110α, p110δ and p110γ (Class IB) bear RAS-binding domains (RBDs). In addition, p110β can also bind to the RHO family GTPases **RAC1** and **CDC42**. There are two others PI3K catalytic classes (Class II and Class III) [see review; 60]

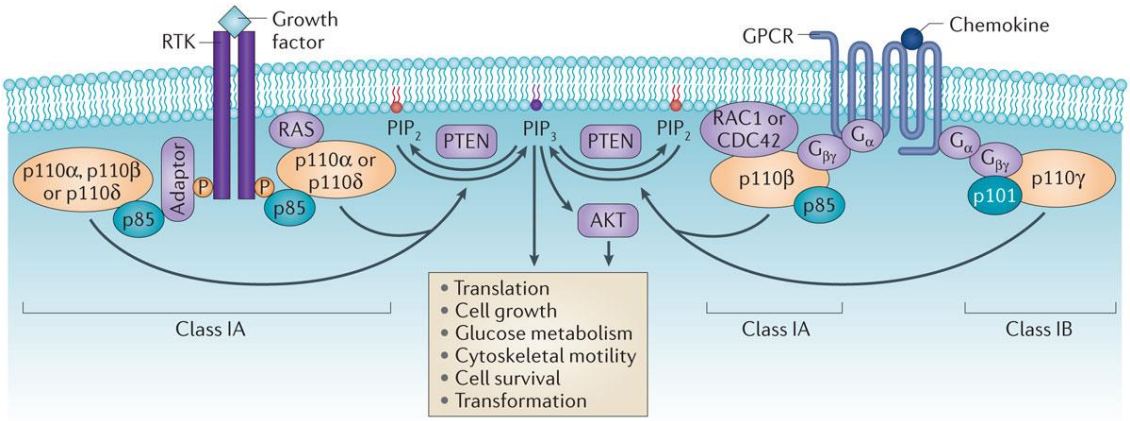

Figure I. 15. The Class IA PI3K signaling. Following growth factor stimulation and subsequent activation of RTKs, class IA phosphoinositide 3-kinases (PI3Ks), consisting of p110α–p85, p110β–p85 and p110δ–p85, are recruited to the membrane by direct interaction of the p85 subunit with the activated receptors or by interaction with adaptor proteins such IRS1. The class IB PI3K (p110γ) can be activated directly by G protein-coupled receptors (GPCRs) through interaction with the Gβγ subunit of trimeric G proteins. The p110β subunits can also be activated by GPCRs. The activated mechanism by p110 catalytic subunit is further analyzed in section III1.1. [150].

Class I PI3K proteins predominantly phosphorylate **PI(4,5)P$_2$**, thereby producing **PI(3,4,5)P$_3$**, the main recruiter of inactive AKT. **PTEN** is the phosphatase responsible for returning **PI(3,4,5)P$_3$** to **PI(4,5)P$_2$**, working as negative regulator of the signaling pathway. In addition, AKT can also be recruited by **PI(3,4)P$_2$**, generated by specific PI3K isoforms in different cellular contexts. Of note, recent studies identified PI(3,4,5)P$_3$ and **PI(4,5)P$_2$** at endomembranes directly activating AKT. Regardless of the activation mechanism, the ultimate output is AKT

recruitment to the cell membrane, specifically recognized by the AKT-PH domain [149].

After **PI(3,4,5)P$_3$** binding to the AKT-PH domain, AKT translocation causes a conformational change from the auto-inhibited **PH-in** to de-inhibited **PH-out** conformation. At this point AKT substrates can bind to the kinase with high affinity, because both the kinase and the regulatory domains are accessible. **PDK1** phosphorylates the activation loop of the AKT-KD at the **T308 residue,** while the mTOR/Rictor complex (**mTORC2**) phosphorylates the **Ser473** residue in the AKT-RR domain, leading to AKT1 activation [149]. Similarly, T309 and S473 residues in AKT2 and T308 and S472 residues in AKT3 can also be phosphorylated [153]. To reach a full activation state, AKT must be phosphorylated at S473, while single T308 phosphorylation results in a reduced AKT activation state.

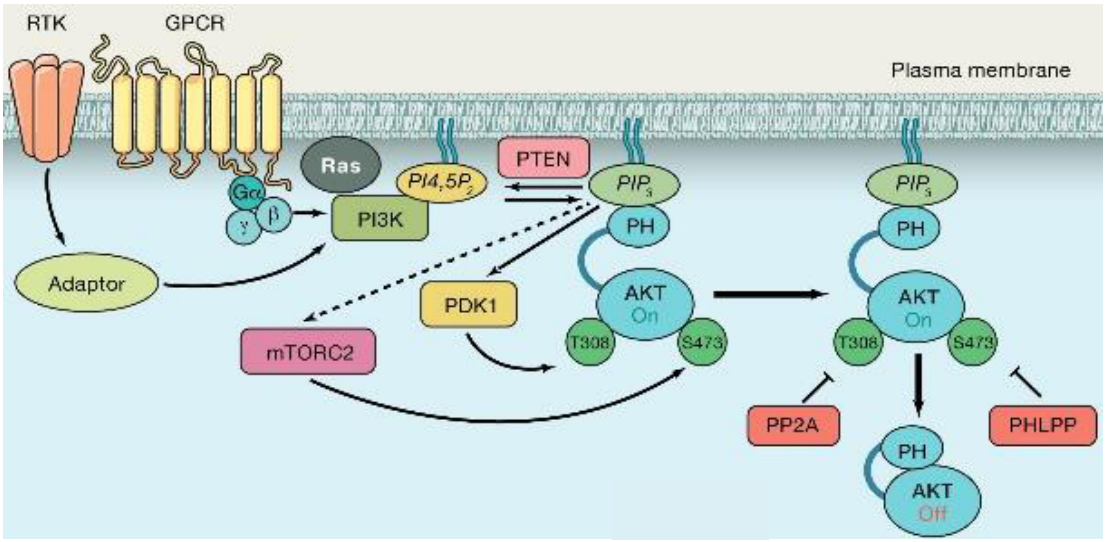

Figure I. 16. From inactive to active AKT conformation. Stimulation of RTKs or GPCRs leads to activation of PI3K, resulting in PIP3 production at the plasma membrane. Through its pleckstrin homology (PH) domain, cytosolic inactive AKT is recruited to the membrane by PI (3,4,5)P3 and is phosphorylated at T308 in the kinase domain (T308 in AKT1), which is critical for activation of the enzyme. The C-terminal hydrophobic domain (HD) contains a serine residue (S473 in AKT1) important for full activation by mTORC2, which contributes to the stability of the molecule. AKT signaling is negatively regulated by the PIP3 phosphatase PTEN and the PP2A protein phosphatase. Taken from [149]

AKT can be inactivated by **PTEN, PP2A** or PHLPP1 phosphatases. PP2A (protein phosphatase 2A) can dephosphorylate the AKT residue T308, while

PHLPP1 (PH domain leucine-rich repeat protein phosphatase) specifically dephosphorylates S473, in both cases leading to kinase inactivation. Finally, PTEN inhibits AKT through NDRG1 (N-myc downstream regulated gene 1)[154]. AKT phosphorylation of NDRG1 can be direct [155] or mediated by **SGK1** and other AGC kinases [156, 157]. PTEN is a recognized tumor suppressor that can be mutated in RMS tumors, while **NDRG1** is intimately involved in multiple stages of embryogenesis.

3.1.1 The mTOR complex

Of particular interest in the AKT signaling is the mTOR complex or mammalian Target Of Rapamycin, in reference to its canonical inhibitor. There are two subtypes, the mTOR complex 1 (mTORC1) mTORC2, which share the same mTOR catalytic subunit but differ in their regulatory protein associated with the scaffold. The RAPTOR (Regulatory-associated protein of mTOR) subunit is found in mTORC1, while RICTOR (Rapamycin-insensitive companion of mTOR) is present in mTORC2. The differential core architecture defines their substrates and functions. mTORC1 enhances anabolic synthesis of proteins, lipids, and nucleotides. In addition, mTORC1 favors glycolysis over oxidative phosphorylation providing energy molecules (such as NADPH) for anabolic synthesis[149, 158] .

Both mTORC1 and mTORC2 complexes work on promoting proliferation and survival in cancer cells, and mTORC2 is specifically involved in cell motility and metastasis via actin cytoskeletal organization. In the oncogenic context, and also in RMS, the regulatory feedback present in non-transformed cells that inhibits mTORC1 is lost, which results in constitutive mTORC1 activity. Through eIF4E-binding protein 1 (4E-BP1) and S6 ribosomal protein phosphorylation, mTORC1 upregulates translation, cell growth, and metabolism. Unlike mTORC1, S6K1 phosphorylation is not affected by mTORC2 knockdown. Although the relationship between mTORC2 and AKT is incompletely understood, it is known that AKT requires mTORC2 kinase activity for FOXO1/3A phosphorylation [158, 159].

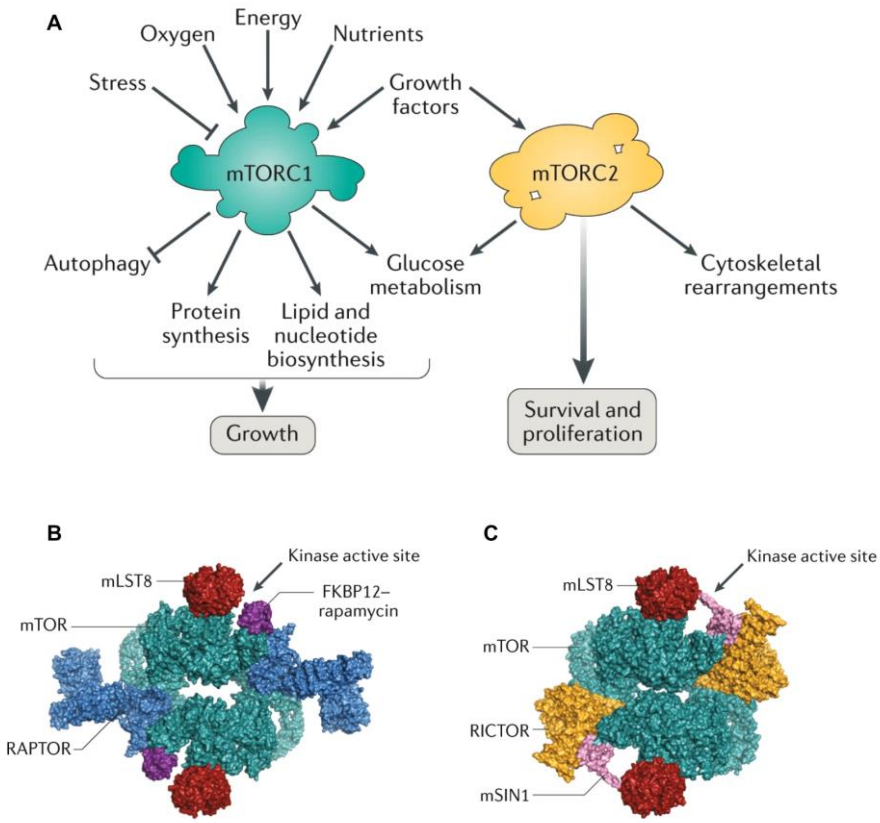

Figure I. 17. Overview of mTORC1 and mTORC2 function and structure. **A)** Summary of different roles of mTORC1 and mTORC2, described in detail in section III.1.2. **B)** Cryogenic electron microscopy (cryo-EM) reconstruction of human mTOR complex 1 (PDB identification code 5FLC) and **(C)** mTOR complex 2 structures (PDB identification code 5ZCS) (right). The FKBP12–rapamycin binding (FRB) domain of the mTORC1 complex is indicated in purple. Adapted from [158]

3.2 AKT functions

AKT has functions in a multitude of cell types and tissues, and it is the convergent signaling node for multiple hormones, growth factors, cytokines, and diverse trophic factors. To date, a large number of studies indicate that the different AKT isoforms have redundant functions, and that most AKT substrates are functionally regulated and phosphorylated by the three AKT isoforms. However, it has also been reported that a limited number of substrates can be targeted by only one of the three isoforms, suggesting AKT specific functions. It is important to note that these non-redundant functions are context-dependent and must be validated in each cell type.

The different AKT isoforms have a preferential tissue expression: AKT1 is the most ubiquitously expressed, while AKT2 is mainly expressed in insulin-responsive and high metabolic tissues and AKT3 is specially expressed in brain. Notably, the specific AKT functions depend on the main targets affected in each specific tissue [149, 160] (**Figure I. 18**).

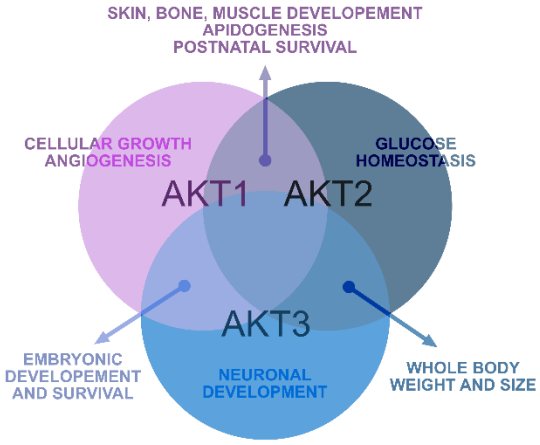

Figure I. 18. Functional AKT isoforms specificity Adapted from [160].

Intracellularly, AKT controls the activation of many signaling pathways depending on the phosphorylation of different downstream substrates. The best studied signaling cascades modulated by AKT are: 1) **TSC2/mTORC1/PRAS40/S6K cascade**; 2) **FOXO transcriptional targets**, such as the cyclin family of proteins, and 3) **GSK3/MCL1,** which constitute the central nodes that allow AKT regulation of metabolism and growth, proliferation, and apoptosis, respectively [149].

3.2.1 AKT functions in cell growth and metabolism

AKT phosphorylation at **T308** residue results in the activation of mTOR/RAPTOR complex1 (**mTORC1**), which is mediated by **TSC2** (Tuberin sclerosis complex 2, or Tuberin) and its targets **70S6K** and **4E-BP1** [149, 151].Going deeper, the main mechanism by which AKT activates mTORC1 is through TSC2 inhibition by phosphorylation. TSC2 is a GTPase-activating protein and the most important intrinsic regulator of mTORC1. In addition, mTORC1 activity can also be

regulated by multiple signaling kinases that inhibit or stimulate mTORC1 activity (AMPK and GSK-3β or AKT, ERK and RSK-1, respectively).

PRAS40 (Proline-rich AKT substrate of 40kDa) is a component of the mTORC1 complex, which is phosphorylated by AKT at **T246** and is frequently used as readout for AKT activity in tissues.

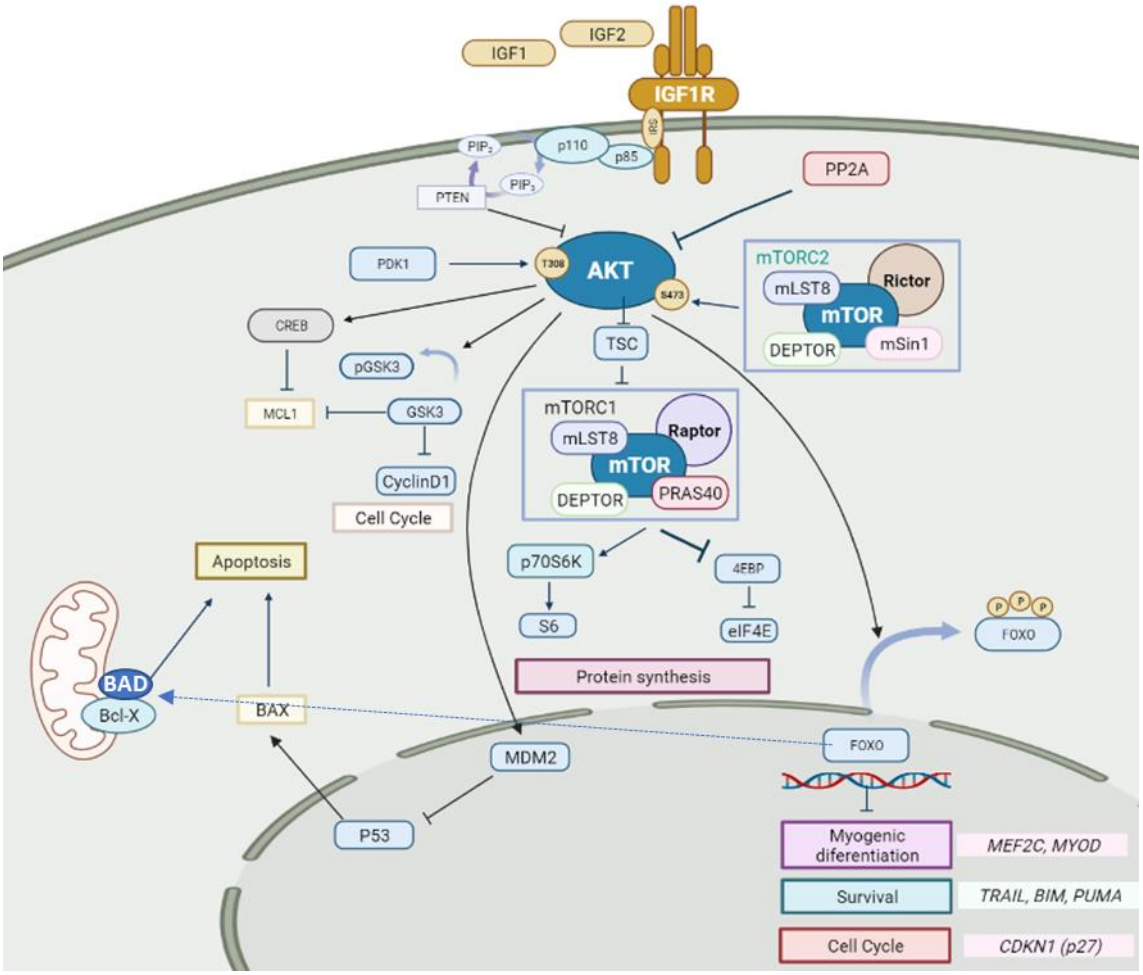

Figure I. 19. Graphical summary of AKT/mTOR pathways and functions described in this section.

In regards to negative signals, **70S6K** can phosphorylate an inhibitory residue of **IRS1**, causing a **negative feedback** that inhibits IGF signaling through PI3K/AKT. In addition, AKT can be phosphorylated by mTORC2 at the residue S473 [161]. Although the mechanism of mTORC2 regulation remains unclear in

RMS, IRS1 signaling could be involved in feedback loops that control growth factor stimuli [162].

AKT can **reprogram the cellular metabolism in order to enhance** cell survival and proliferation. One of the cancer hallmarks described decades ago, the Warburg effect or aerobic glycolysis, can be regulated, at least partially, by AKT signaling. Some of the transcriptional changes in the tumor cell implicated in **glycolysis**, **lipid synthesis** and **nucleotide synthesis,** are regulated by AKT.

3.2.2 AKT effects in muscle differentiation

Activation of PI3K-AKT signaling leads to phosphorylation and translocation out of the nucleus of the TF family FOXO (FOXO1a, FOXO4 and FOXO3a). Wild type FOXO1 regulates the function of the skeletal muscle, counteracting the effects of insulin and IGF1 during the normal process of muscle development. [163]. The regulation of FOXO proteins by an AKT-dependent mechanism has been described to be involved in **myoblast differentiation** [164]. FOXO can also be phosphorylated and regulated by other members of the AGC kinase family [165, 166]

3.2.3 AKT modulation of cell survival.

AKT activation also has implications for cell survival and apoptosis. Mechanistically, phosphorylated AKT in turn phosphorylates **GSK3,** stabilizing anti-apoptotic proteins such as **MCL-1** in RMS cells [167, 168]. Anti-apoptotic proteins such as BCL-2, or MCL-1 are frequently expressed at high levels in RMS contributing to the evasion of chemoresistance. Investigation of the BCL-2 family of proteins in RMS have revealed a role of the MCL-1 anti-apoptotic protein in response to chemotherapy in preclinical models [169, 170]. Interestingly, synthetic lethal interactions of the combination of inhibitors against PI3K and MEK pathway occur through mechanisms involving the downregulation of several anti-apoptotic proteins such as XIAP, Bcl-xL and MCL-1. Moreover, direct interactions have been described between the AKT-PH domain and MCL1 in adult cancer

models [171]. Recently, we reported the molecular mechanism for the synergistic effect of vincristine in combination with the MLC-1 Inhibitor, S63845, in RMS models [107]

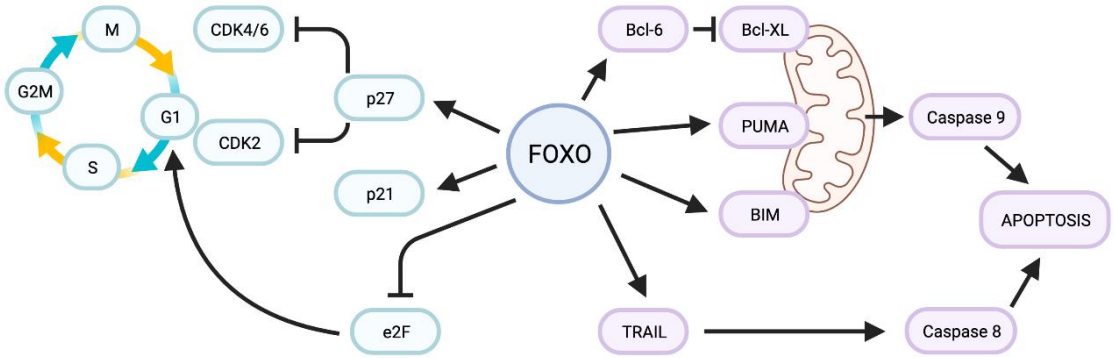

Figure I. 20. Regulation of cell cycle progression by FOXOs. FOXOs can inhibit distinct phases of the cell cycle and induce apoptosis when activated. Some FOXOs targets responsible of inhibiting cell cycle include p21, and p27. When active, p27 and p21 inhibit CDK4/6 and CDK2 causing cell cycle arrest. FOXOs upregulate pro-apoptotic proteins and inhibit anti-apoptotic proteins. FOXOs can induce TRAIL upregulation, inducing the activation of the extrinsic apoptotic pathway, while regulation of the expression of BIM, PUMA, and BCL-6 can induce apoptosis via the mitochondria-dependent intrinsic pathway. Adapted from [172].

On the other hand, AKT can also mediate the inhibition of apoptosis through FOXO phosphorylation. FOXO ceases its functions as TF when it translocate to the cytoplasm after being phosphorylated by AKT. Currently, four orthologs of FOXO have been identified: FOXO1, FOXO3, FOXO4 and FOXO6. FOXO targets are involved in apoptosis induction (BCL-6, BIM) and cell cycle arrest (p27, p21), among others (**Figure I. 20**). The balance of pro-apoptotic BAD proteins and anti-apoptotic proteins of the BCL-2 family are also affected by FOXO phosphorylation.

3.3 AKT as a therapeutic target in RMS

AKT hyperactivation is a common feature in pediatric solid tumors. The function of aberrantly generated oncogenic proteins such as the PAX-FOXO1 fusion protein, the functional loss of tumor suppressors (such as PTEN) or the

hyperactivation of IGF cascade, are some examples that result in high AKT signaling in RMS [83, 133, 173]. Since the diverse mechanisms leading to the sustained AKT activation in RMS are not equivalent, it is important to determine the group of patients who could, potentially, benefit from AKT inhibition and to find reliable **biomarkers for each drug** in each tumor subtype.

3.4 AKT inhibitors: Mechanism of action

In recent years, many small molecule inhibitors of AKT have been developed and are currently in clinical trials [174, 175]. These inhibitors can be divided into two major groups: ATP-competitive and allosteric inhibitors [148, 174]

ATP-competitive inhibitors target the ATP pocket of the AKT-KD, whereas allosteric inhibitors bind to a different pocket located between the AKT-PH and AKT-KD domains. ATP-competitive inhibitors thus prevent phosphorylation of AKT subtracts by binding to the AKT PH-out conformation, whereas allosteric inhibitors retain AKT in its PH-in conformation, causing a reduction in the phosphorylation of AKT regulatory regions and in the phosphorylation of its substrates [148, 149].

Of note, after cell treatment with ATP-competitive inhibitors, a paradoxical increase in AKT phosphorylation is observed in both S473 and T308 [176]. This accumulation of the phosphorylated AKT forms is thought to be due to a membrane retention effect, binding to $PI(3,4,5)P_3$, and a shielded conformation that prevents dephosphorylation by the AKT phosphatases PP2A and PHLPP1 [149, 177]. AKT hyperphosphorylation due to ATP-competitive inhibitors is functionally inactive. However, since AKT, like other kinases, could display catalytic-independent functions, it is possible that AKT hyperphosphorylation might retain some yet unknown functions.

3.4.1 Ipatasertib

Ipatasertib (GDC-0068) is a pan-AKT inhibitor, therefore, it inhibits the three AKT isoforms. The design and chemical optimization of this compound was based on X-ray structure studies of inhibitors forming complexes with AKT1 and PKA.

ipatasertib strongly binds to the three AKT isoforms and weakly to the kinases of the AGC family[178] (**Figure I. 21**).

Mechanistically, ipatasertib binds to the ATP pocket in the active AKT conformation PH-out (T308 and S473 phosphorylated), interfering with the ATP binding ability of AKT [174]. Thus, its phosphorylated conformation is maintained, while the AKT enzymatic function is blocked, and downstream signals are (likely) not transmitted [179].

The antitumoral activity of ipatasertib has been evaluated in experimental models (cell cultures and xenografts) from common cancers in adults, where mutations or genetic alterations in the PI3K/AKT pathway are found [180]. In addition, using reverse-phase protein array studies, clinically translational biomarkers were described that allow the treatment response in models of breast, prostate and glioblastoma to be tracked [179]. Some of the downstream AKT markers affected by ipatasertib treatment are the phosphorylation of PRAS40, GSK3b, mTOR, eIF4G, and FOXO3a. ipatasertib is orally bioavailable and pharmacokinetic studies in xenograft models showed that the effect on the AKT-downstream markers was maximal three hours following ipatasertib oral administration [180].

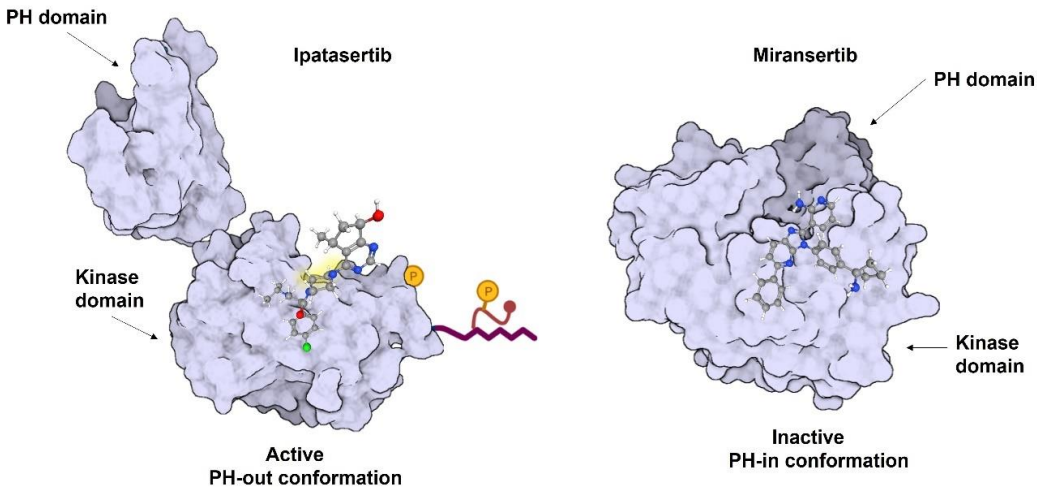

Figure I. 21. Model of AKT inhibition. The ATP competitive inhibitor ipatasertib binds to the active form of the enzyme, phosphorylated at T308 and S473, in the more extended conformation called "PH-out". Meanwhile the allosteric inhibitor stabilizes the PH-in form of the inactive enzyme. Surfaces representations derived. A) Crystal structure of the AKT kinase domain with ipatasertib (PDB accession code 4EKL) and the AKT-PH domain (PDB 1UNQ). B) Crystal structure

of the allosteric inhibitor miransertib, in complex with the autoinhibited form of AKT1 (PDB accession code 5KCV). Phosphorylated T308 and S473 are indicated as yellow balls. The chemical compounds are shown as ball and stick models on the protein surfaces colored by atom type.

In adult tumor models, ipatasertib showed differential activity in models with high basal AKT activation [180]. This suggested that stratification of potential ipatasertib patients based on AKT activation levels is necessary [181].

Compared to previously reported ATP-competitors, ipatasertib displays lower off-target binding to AGC kinases, although its binding to AGC kinases such us PKG and p70S6K has been described. Affinity of ipatasertib binding to AGC kinases is much lower than to AKT [178].

Ipatasertib is currently being tested in clinical trials. The first human phase I study in solid tumors (mostly breast, colorectal, and prostate cancers) demonstrated that ipatasertib administered as monotherapy was well tolerated, with maximum tolerated doses (MTD) of 600 mg [182]. AKT downstream biomarkers were shown to be inhibited at doses as low as 100 mg. Adverse events of ipatasertib (AEs) are mainly diarrhea, nausea, fatigue, and rash, all of which can be controlled and resolved with supportive care [183]. Compared with other AKT or PI3K inhibitors, ipatasertib AEs of hyperglycemia or rash are less intense [174]. In terms of clinical efficacy, decreases in AKT downstream markers in biopsies of treated patients are not accompanied by objective radiographic RECIST (Response Evaluation Criteria in Solid Tumours) responses. The best response observed is stabilization of the disease [182]. The addition of ipatasertib to Paclitaxel as first-line therapy for triple-negative breast cancer increases progression-free survival for patients who received ipatasertib as compared to those who received placebo[184].

Currently, ipatasertib efficacy is being evaluated in a phase II/III trial in combination with conventional chemotherapy or other target therapies in different adult cancers (reviewed in [148]). Particularly well developed is the therapy with ipatasertib for treating metastatic triple-negative breast cancer that use PIK3CA/AKT1/PTEN alteration as predictable biomarker [183-186]. Also in 2021,

phase III clinical trial data were published for ipatasertib in castration-resistant prostate tumors (CRPCs) with functional PTEN-loss status [187].

To date, only one report on ipatasertib treatment in pediatrics has been published: a 12-year-old girl diagnosed with an epithelioid neoplasm that harbors a novel fusion between the LAMTOR1 and AKT1 genes was treated with ipatasertib for four weeks [188]. This treatment resulted in significant tumor regression, as evaluated by PET-CT. Despite the initial favorable response, after ten weeks of ipatasertib, the tumor mass regrew, and the girl eventually died. Since the end of 2020, there is an open clinical trial for participants aged 12 to 17 years with metastatic or advanced AKT1/2/3-mutant positive tumors (clinical trial NCT04589845).

3.4.2 Miransertib

Miransertib (ARQ092) is a highly selective allosteric inhibitor of the three AKT isoforms. It binds to the unphosphorylated form of AKT at PH-in conformation, in an allosteric pocket pleckstrin homology (PH) and kinase domain. Like ipatasertib, the design of miransertib was based on studies aiming to identify structure-activity relationships [189]. Based on biochemical assays, the half maximal inhibitory concentration (IC50) of miransertib to inhibit AKT1, AKT2 and AKT3 is 5 nM, 4.5 nM and 16nM, respectively.

Apart from AKT isoforms, only six kinases (from a panel of 303 kinases) have also been described to be inhibited by miransertib: MARK1, 3 and 4, DYRK2, IRAK1, and HASPIN [190].

Table I. 8. Biochemical selectivity of ipatasertib or miransertib to AKT isoforms and other kinases.

Miransertib (ARQ-092)	IC50 (nM)	Ipatasertib (GDC-0068)	IC50 (nM)
AKT1	5	Akt1	5
AKT2	4,5	Akt2	18
AKT3	16	Akt3	8
MARK4	129	PKG1α	98
MARK3	173	PKG1β	69
MARK1	180	p70S6K	860
DYRK1	386	PKA	3100
IRAK1	806		
HASPIN	1160		

Data taken from [178, 190].

The antiproliferative activity of miransertib was tested in several adult tumor cell lines harboring mutations in PI3K/AKT signaling, as single agents or in combination with FGFR inhibitors[191]. These studies revealed their effectiveness in cells harboring PI3K/AKT mutations. Further, miransertib shows higher potency than other ATP-competitive AKT inhibitors (such as ipatasertib) in inhibiting cell viability and inducing cell death in adult tumor cell lines [174]. In addition, other differences in the phosphoproteomic signatures induced by allosteric AKT inhibitors versus by ATP-competitive AKT inhibitors were described [174].

miransertib is currently being tested in phase I clinical trials for patients with proteus syndrome and PIK3CA-related overgrowth spectrum (PROS) diseases, including pediatric patients. Treatment of two children with PROS led to improvement in key qualitative outcomes, with no significant associated toxicities [192]. Moreover, miransertib has been evaluated in phase I/II clinical trial in combination with chemotherapy (carboplatin ± paclitaxel) for solid adult cancer (NCT02476955) with particularly good results tumors harboring AKT mutations [193].

4 The PI3K/AKT and RAS/MEK/ERK pathways: cross-talk and compensation mechanism.

PI3K/AKT is probably the most interconnected cellular signaling pathway, with **points of cross-regulation** with all major signal transduction pathways. There are three fundamental features that confer PI3K/AKT pathway the ability to interconnect: i) redundant substrate regulation, that is, the phosphorylation sites of a particular protein respond to more than one upstream stimulus; ii) the ability to regulate different subsets of proteins depending on the stimulus; and iii) in parallel to AKT, other kinases are activated after an external stimuli. The mechanism(s) that directs AKT signaling toward one protein subset or another is not fully understood. The only parameter that we know defines the target selectivity is the differential expression of substrates. Nevertheless, the duration of AKT activation might influence which substrates get phosphorylated.

In a physiological context, the integration of cellular signaling pathways is essential as it allows, for example, nutrient sensing or cellular stress signaling to be prioritized over growth signals. However, in a tumor context, this dynamically changing cellular state may define potential escape mechanisms for targeted therapies.

Especially interesting for its complexity and therapeutic implication in cancer is the cross-regulation between **PI3K/AKT** and the **RAS/MEK/ERK** MAPK pathway. The **RAS/MEK/ERK** pathway together with PI3K/mTOR are two central nodes of cell signaling that regulate survival, differentiation, metabolism, proliferation, and motility through the integration of extracellular signals.

High levels of phosphorylated AKT in RMS cell lines and primary tumors indicate a constitutive activation of the PI3K/AKT/mTOR pathway, suggesting that RMS may be sensitive to targeted inhibition of this pathway. However, a growing number of cross-talk, feedback, and feed-forward loops link the PI3K/AKT/mTOR and Ras/MEK/ERK signaling pathways [194], which provide insights into the compensatory responses observed when targeting each pathway. Some examples are graphically summarized in **Figure I. 21.**

The prevalence of simultaneous activation of PI3K/AKT/mTOR and RAS/RAF/MAPK was shown for 25 ARMS and 54 ERMS primary tumors [195] Interestingly, almost 60% of ARMS (but only 29% of ERMS) were positive only for phospho-AKT and not for ERK.

Therefore, a rational of **combining MEK inhibitors** with **PI3K/AKT/mTOR inhibitors** emerged for pediatric RMS, particularly in NRAS mutated tumors [195]. Further, pharmacological or genetic knockdown of MEK and PI3K simultaneously trigger apoptosis in RAS mutated RMS models [196].

4.1 Trametinib, the MEK inhibition in RMS

Trametinib is an orally bioavailable allosteric MEK1 and MEK2 inhibitor approved by the FDA and EMA in combination with Dabrafenib for metastatic melanoma with BRAF(V600E/K) mutation. In pediatric patients, low-grade gliomas (PLGG) as well as plexiform neurofibromas (PNs) frequently present activation of the MAPK/ERK pathway. In those diseases, trametinib in clinical trials has resulted in significant responses in most patients [197].

As an allosteric inhibitor, it binds to unphosphorylated MEK1/2 and prevents RAF-dependent MEK phosphorylation and activation. ERK1/2 phosphorylation on both T202 and Y204 is the main response biomarker. Across a wide range of tumor cell lines, activating mutations in RAS or BRAFV600E mutation define the most sensitive cell [198, 199].

In contrast to the IGF-dependent AKT signaling pathway, RAS/MEK/ERK, signaling has a not well defined role in the process of myogenic differentiation. There is strong evidence and detailed mechanisms of how AKT promote differentiation in normal muscles cells, while the ERK targets in the myogenic process are unknown. The MEK-ERK pathway is thought to play a different role in the early versus late stages of differentiation. Briefly, ERK translocation from nucleus to cytoplasm promotes early differentiation of muscle progenitor cells [200]. On the other hand, myoblast fusion into myotubes is impaired by the lack of ERK2, confirming its role in late myoblasts differentiation. MEK1 bind to the MyoD complex and inhibits its transcriptional activity [201].

Whether oncogenic RAS affects differentiation is incompletely understood. However, Yohe et al. (2018) confirmed that the myogenic transcription factor MyoG is repressed by RAS/MAPK oncogenic activity in FN-RMS [202]. Furthermore, in contrast to previous results of MEK inhibitors efficacy in FN-RMS [203, 204], they showed favorable and promising efficacy data in FN-RMS for trametinib [202].

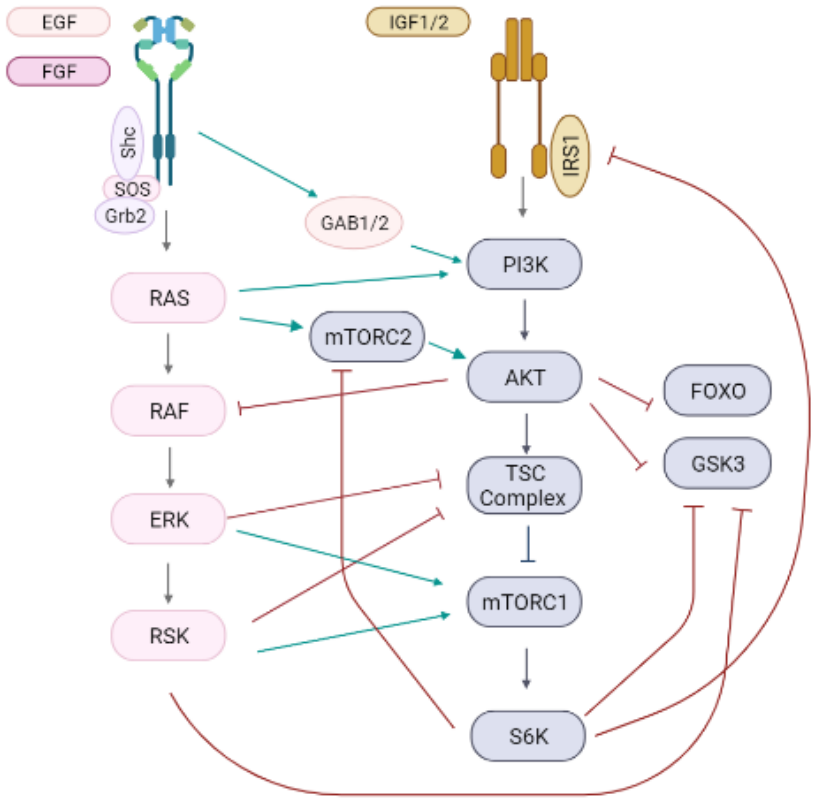

Figure I. 22. Cross talk between AKT and MEK pathways. Epidermal growth factor (EGF), FGF or IGF can stimulate their corresponding tyrosine kinase receptor (RTK). Each RTK present a preferential adaptor protein triggering differential downstream cascades. The adaptor complex, through Src homology 2 (SH2) domain, activates MAPK cascade. In SH2 complexes, GRB2 allows SOS to catalyze GTP exchange and activation of the RAS family of small GTPases. RAS activates RAF, which subsequently phosphorylates and activates MEK. MEK, in turn, phosphorylates and activates ERK1/2. By other side, IGF1 signaling though IRS1/PI3K/AKT/mTOR has been previously described in detail. The main positive interactions between PI3K/AKT/mTOR and RAS/MEK/ERK pathways are in green: i) RAS activates PI3K, and ii) ERK/RSK activates the mTOR complex. Negative feedback regulations (indicated in red) are: i) ERK/RSK inhibition of TSC complex and GSK3, and ii) S6K inhibition of IRS1 and GSK3. ERK, mitogen-activated protein kinase; GSK3β, glycogen synthase kinase 3 beta; IRS, insulin receptor substrate; MEK, mitogen-activated protein kinase kinase; mTOR, mammalian target of rapamycin; mTORC1/2, mTOR complexes 1 and 2; RAF, Rapidly accelerated fibrosarcoma; S6K, p70 ribosomal S6 kinase; TSC1, Tuberous sclerosis complex.

II. HYPOTHESIS and OBJECTIVES

Pediatric rhabdomyosarcoma (RMS) is a developmental tumor with low survival rates (below 30%) and has high-risk for metastatic and relapsed disease. These low rates of survival make developing new and effective therapies an urgent need.

In this thesis, we **hypothesize** that a comprehensive pharmacological targeting of the IGF axis and the AKT/mTOR signaling cascades might represent a therapeutically active strategy for pediatric RMS. Moreover, we postulate that identification of predictable biomarkers of this pharmacological inhibition is a key strength to target the particularities of each RMS.

Overall, to accomplish our **objectives**, the specific aims were:

Aim 1. Test the antitumoral activity of IGF1/2 inhibition by the antibody m708.5 in RMS models;

Aim 2. Evaluate preclinical pharmacology and antitumoral activity of the novel, highly selective, ATP-competitive pan-AKT inhibitor ipatasertib in RMS models *in vitro* and *in vivo;*

Aim 3. Identify functional AKT or MEK signaling dependencies in RMS models upon pharmacological inhibition;

Aim 4. Compare the antitumoral and target effects of the AKT inhibitors ipatasertib and miransertib in RMS models;

Aim 5. Define and describe predictive biomarkers of ipatasertib response in RMS.

III. MATERIALS AND METHODS

1 Pharmacological treatments

The novel human monoclonal antibody **m708.5**, which binds with high (pM) affinity to both human IGF-1 and IGF-2, was produced by (and kindly provided by) the Dr. Nai-Kong Cheung-Laboratory (Memorial Sloan Kettering Center, New York) [1]. The ERK Inhibitor **trametinib** (GSK1120212) was purchased from Selleck Chemicals. **Ipatasertib** (GDC-0068) was provided by Genentech (affiliated to Roche), and **miransertib** (ARQ-092-2MSD) was provided by Arqule (recently affiliated to MSD); the use of both inhibitors were under material transfer agreements (MTA).

2 Cell culture

2.1 Cell lines

The RMS commercial cell lines RH4, CW9019, RH30 and RD were kindly provided by Dr. Martinez-Tirado (IDIBELL). They were cultured in RPMI 1640 medium supplemented with 10% fetal bovine serum (FBS) (Hyclone, Lonza), 5 mM of L-glutamine, and 10,000 U/ml of penicillin-streptomycin (Gibco) and were grown in monolayer conditions. All cell cultures were maintained at 37^0C in a humidified atmosphere containing 5% CO_2. For long term storage, stock cultures were cryopreserved in FBS with 10% DMSO. **Table III. 1** summarizes molecular features and anatomical origin of each RMS cell line used in this thesis [205].

Table III. 1. RMS cell lines features.

RMS cell line	Fusion Oncogene	*TP53*	Other genetic alteration	Origin
RH4	*PAX3-FOXO1*	mut	-	Lung metastasis
RH30	*PAX3-FOXO1*	mut	*CDK4* amp	Bone marrow metástasis
CW9019	*PAX7-FOXO1*	-	-	Unknown
RD	FN-RMS	mut	*MYC* amp, *NRAS* mut	Pelvic mass

2.2 Establishment and characterization of primary cultures

2.2.1 Establishment of RMS primary cultures

Two types of primary cultures were generated from: (i) fresh patient surgical biopsies, immediately after removal; or (ii) patient-derived xenografts (PDX). First and second relapsed biopsies from the same RMS patient, identified as E001_T and E024_T respectively, were used to generate primary cultures named as E001_s and E024_s. Also, RMS-PDX tissues were collected to generate A001_s, A006_s, A007_s and A010_s primary cultures, from their corresponding fresh tissue. All human samples used to generate our RMS models came from fresh biopsies of patients at Hospital Sant Joan de Déu, Barcelona (HSJD). Molecular and clinical features are listed in **Table III. 2**. All patients were diagnosed based on imaging, clinic-pathological features and molecular diagnosis confirmation. All patient material was collected after informed consent, and the procedure was approved by the institutional ethics committee. Newly primary cultures were named as **_S** in reference to tumor sphere forming culture. Alveolar or embryonal subtypes are indicated as "A" or "E", respectively, at the starting ID followed by correlative numbers.

Table III. 2. Summary of molecular, biological and clinical features of each RMS primary culture generated in this thesis.

Tumor biopsy ID	Tumor_biopsy Site	Primary Site	Debut/ Relapse	Age (years)	Histology	Molecular features validated	PDX	In vitro primary culture
ERMS_T	Occipital lesion (arising from meninges)	Leptomeningeal	Relapse	3,5	ERMS	↑MYCN	-	E001_S
ERMS24_T	Temporal (intraparenchymal Brain)	Leptomeningeal	Relapse	4,5	ERMS	↑MYCN	HSJD-ERMS-024	E024_S
ERMS3_T	cervical lymph node	Head and Neck	Relapse	8	ERMS	↑MYCN MDM2 mut *others	HSJD-ERMS-003	-
ERMS11_T	Abdominal	Abdominal	Debut	12	ERMS	KDR mut	HSJD-ERMS-011	-
ARMS1_T	Pleura	Chest	Relapse	13	ARMS	PAX3-FOXO1	HSJD-ARMS-001	A001_S
ARMS6_T	cervical lymph node	Limb	Relapse	16	ARMS	PAX3-FOXO1	HSJD-ARMS-006	A006_S
ARMS7_T	Limb	Limb	Debut	11	ARMS	PAX7-FOXO1	HSJD-ARMS-007	A007_S
MO010	Bone Marrow	Muscle	Relapse	13	ARMS	PAX7-FOXO1	HSJD-ARMS-010	A010_S

Tumor samples were mechanically dissociated using two scalpels and then filtered with 0.45µm Corning™ Sterile Cell Strainers (Fisher scientific). After collected for centrifugation at 0.4 g for 3 min, tumors were cultured in tumor stem media (TSM) consisting of a 50:50 mixture of DMEM/F12 (Dulbecco's Modified Eagle Medium/Nutrient Mixture F-12) and Neurobasal medium (Invitrogen), HEPES buffer solution 10 mM, 1% Sodium pyruvate MEM 100mM, 1% MEM non-essential aminoacids 10 mM, 1% glutamax-I supplement and antibiotic and antimycotic (Ref 15240096), all purchased from Fisher™ [206]. In addition, the medium also contained the following factors: B-27™ Supplement minus vitamin A (Gibco™), heparin (2 µg/ml) (H3149-10KU, Sigma), H-EGF (20 ng/ml), H-FGF (20 ng/ml), H-PDGF-AA (10ng/ml) and H-PDGF-BB (10 ng/ml). All the human recombinant growth factors were purchased from PeproTech. The cultures were incubated at 37^0C, 5% CO_2 and 95% humidity. The media was refreshed every 2-3 days. Further details on media composition can be found in [207, 208].

After 3-4 days, cultures reach on confluency, and they need to be transferred to new flask for maintenance. Of note, a mixture of cells growing attached and in suspension was observed. Cells were mechanically dissociated collected for centrifugation at 0.4 g for 3 min. The pellet was resuspended in fresh medium and splitted into new flasks. For future uses, a stock of cells were frozen in freezing medium (Synth-a-Freeze cryopreservation medium, ThermoFisher).

2.2.2 Characterization of RMS primary culture

After establishing each primary culture, the presence of RMS and human tissue-specific markers was analyzed. To this end, the expression of human nucleus antigen, MyoG, MyoD1, and the fusion genes when applicable, were routinely checked in primary cultures *in vitro*.

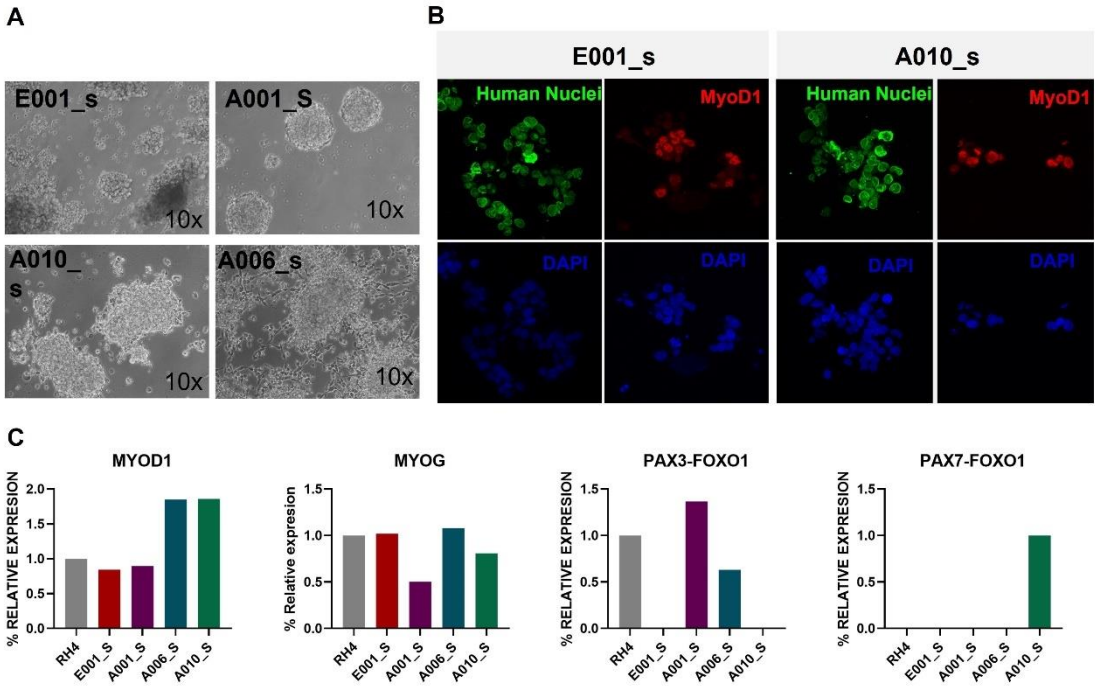

Figure III. 1. Primary cultures expressed RMS and human markers. A) Representative phase-contrast images showing RMS primary cultures. All images were captured at 10× magnification. **B)** Immunofluorescence of MYOD1 (red) and human-nuclei (green) in E001_s, and A010_s as representative examples of staining in primary cultures (x40 magnification). Cell nuclei were stained with DAPI (blue). **C)** *ΔΔCt* values form RT-qPCR for RMS markers in primary cultures relative to RH4 cell lines

2.3 siRNA oligofection to knockdown PRKG1 in the RH4 cell line

Transient transfection of siRNA to knockdown PRKG1 was performed as follows. Briefly, 2.5 × 10^5 cells/well were seeded in 6-well dishes, and 24 h later were transfected with four different siRNAs targeting PRKG1 (**Table III. 3**), or with a luciferase siRNA as a negative control. The siRNA-lipid complex was produced by diluting 25 pmol of each siRNA duplex in OPTIMEM media with 7µL of Lipofectamine™ RNAiMAX reagent (Thermo Fisher Scientific, CA, USA) following the protocol guidelines of the manufacturer. Cells were harvested at 72 h after transfection and subjected to transcriptional and proteomic analysis.

Interference RNA oligonucleotides

Table III. 3. Small interfering RNA (siRNA) knockdown sequences

Primer		Sequence	Source
luciferase control		CUUACGCUGAGUACUUCGA	Sigma Aldrich
PRKG1_seq#j14		GGAUUGACAUGAUAGAAUU	Dharmacon
PRKG1_seq#j15		GGAUAGAGGUUCGUUUGAA	Dharmacon
PRKG1_seq#j16		CAUGGAAGAUGGUAAGGUU	Dharmacon
PRKG1_seq#j17		AGACUGUACAGAACAUUUA	Dharmacon

2.4 Knock-Out of PRKG1 in the RH4 cell line using CRISPR-Cas9 technology

Genome knockout (KO) of PRKG1 in RH4 cells was performed using a ribonucleoprotein (RNP) complex that consists of purified Cas 9 nuclease duplexed with chemically modified synthetic single guide RNA (sgRNA). For RNP formation, a sgRNA/Cas9 ratio 1.3:1 was used. Therefore, the reaction comprised 3.9 pmoles sgRNA and 3 pmoles recombinant Cas9. In the same tube, Lipofectamine TM Cas9 Plus reagent was added and incubated for 10 min to generate Cas9/sgRNA RNP, following Synthego guidelines. For the RNP delivery into cells, LipofectamineTM CRISPRMAX was used as transfection reagent in a ratio 1.5 per reaction. The RNP-transfection solution was mixed with cells ($1x10^5$) prior to plating and divided into 24-well plates. After 72 h, transfected cells were used for banking and single-cell cloning. Individual clones were sequenced and clones with confirmed knockout were expanded for further experiments. Amplified fragments were Sanger sequenced and indel frequency was calculated using the ICE tool.

A multi-sgRNA strategy was used here in which multiple sgRNAs are designed to jointly knockout PRKG1 gene. When cotransfected, the sgRNA includes a large fragment deletion, resulting in a robust knockout. Cas9 complexed was as a negative control, and a human TRAC multi-guide sgRNA (included in the Transfection Optimization Kit Multi-guide; Synthego) as positive control. Mock conditions with parental (untransfected) cells were routinely included as an additional negative control.

Table III. 4. sgRNA guide used for CRISPR-Cas9 experiments

sgRNA		Sequence 5'—3'	Source
PRKG1_guide_#1		GAAGCGGCUGUCAGAGAAGG	SYNTHEGO
PRKG1_guide_#2		AGGGCACUGGGAGCACCGAC	SYNTHEGO
PRKG1_guide_#3		GUCCUUCCACGACCUCCGAC	SYNTHEGO
TRAC_guide_#1		CUCUCAGCUGGUACACGGCA	SYNTHEGO
TRAC_guide_#2		GAGAAUCAAAAUCGGUGAAU	SYNTHEGO
TRAC_guide_#3		ACAAAACUGUGCUAGACAUG	SYNTHEGO

2.5 Cell viability studies by MTS assay

IC50 calculation

Cells were seeded in 96-well plates in a proportion of 3,000 cells/well (RH4, RD, CW9010 and RH30) or 10.000 cells/well (E001_s, A006_s, A007_s, A010_s, and E024_s) 24h prior to treatment (37^0C, 5% CO_2). They were treated with each drug at 1:2 or 1:10 serial dilutions into final concentration ranges starting from 10µM. After 72h, 10% MTS was added, and absorbance at 490 nm was read using a Tecan microplate reader. Percent viability was calculated by normalizing absorbance values to those from cells grown in media with vehicle treatment, after background subtraction. IC50 was determined with log(inhibitor) *vs.* response. Variable slope (four parameters) curves were top (100%) and bottom (0%) constrained to determine the right value using Prism 8 Software (GraphPad).

3 Flow cytometry:

3.1 Apoptosis analysis

To determine apoptosis, RH4 cells were treated with 10 µg/ml of m708.5 and 48 h later cell death was measured with the FITC Annexin V Apoptosis Detection Kit (556547, BD Pharmingen™), according to manufacturer instructions. Cells were collected from a 6-well plate by pipetting up and down. After centrifugation, 1 x 10^6 cells/ml were resuspended in Annexin-binding buffer and, 15 min prior to

analysis, Annexin V antibody and PI were added. Unlike cell cycle analysis, in which cells are fixed, cells to detect Annexin V staining are alive. Sample acquisition was performed in a BD FACScanto cytometer (BD Biosciences) and all channels were previously compensated for fluorescence spillover. Data analysis was performed with BD FACSDiva™ Software. These analyses were performed at the Flow Cytometry Core Facility (UPF-PRBB). Experiments with m708.5 were performed in a reduced serum condition (2.5% FBS).

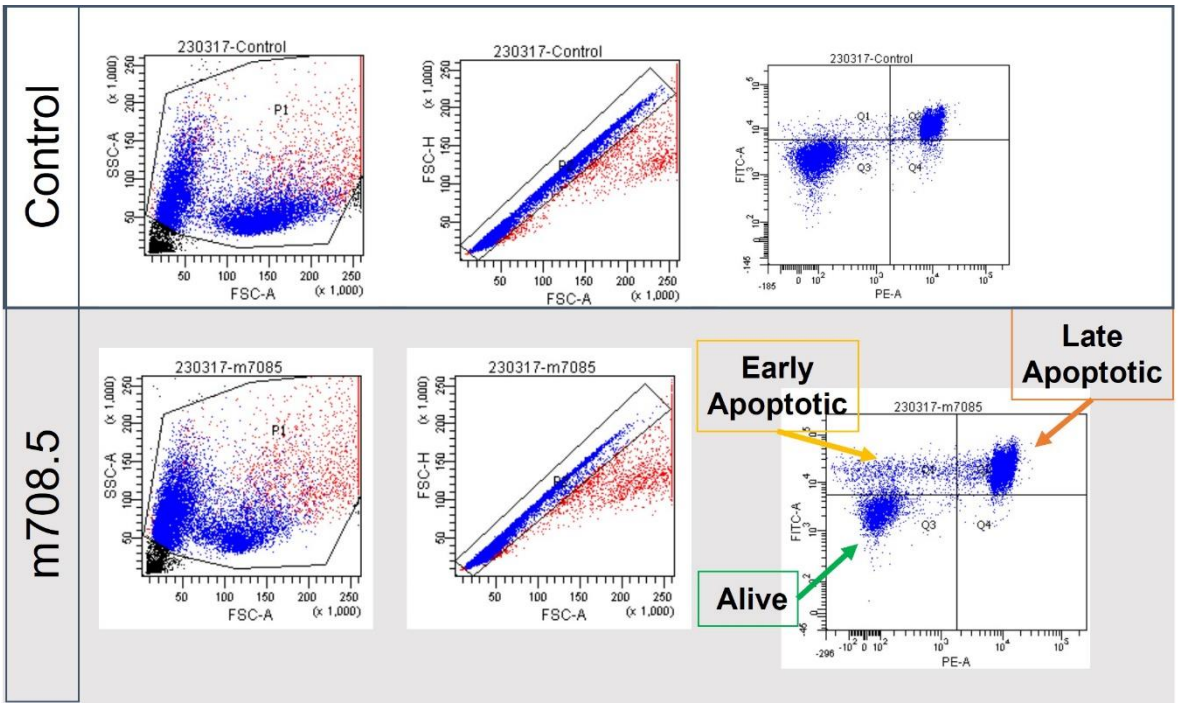

Figure III. 2. Examples of gating selection for apoptosis detection by flow cytometry. Externalization of phospholipid phosphatidylserine (PS) is the hallmark for the earliest stages of apoptosis, before loss of membrane integrity and DNA fragmentation. The combination with propidium iodide (PI) allows to distinguish early apoptotic cells from dead cells, permeable to PI. Thus, early apoptotic cells are Annexin V positive and PI negative. Alive cells are negative for both markers. The positivity for both markers, Annexin and PI, indicates that cells have undergone a complete apoptosis process .

3.2 Cell cycle analysis by BrdU staining and flow cytometry detection.

To evaluate the effects of m708.5 on cell cycle, cells were incubated with 10 µM BrdU for 30 min. Cells were then fixed and permeabilized with BD Cytofix/ Cytoperm buffer and labeled with an APC-conjugated antibody to detect incorporated BrdU. Fluorescence was determined by flow cytometric analysis.

The 7-aminoactinomycin D (7-AAD) was used to label total DNA. With this combination, two-color flow cytometric analysis allowed quantification of those cells that are actively synthesizing DNA (BrdU incorporation) in terms of their cell cycle position (i.e., G_0/1, S, or G_2/M phase defined by 7-AAD staining intensities).

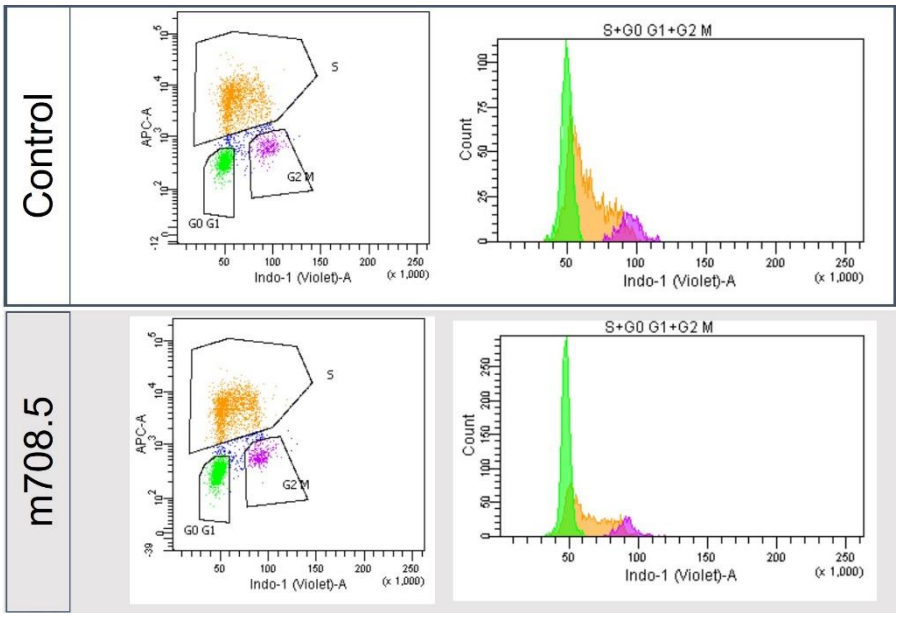

Figure III. 3. Cytometric analysis of BrdU incorporation. Cytometric analysis of BrdU incorporation. The incorporation of BrdU was used to analyze cell cycle phases by flow cytometry. In this representative figure, biparametric dot plots of control or 1 µg/ml of m708.5 treated RH4 cells are shown. The number of cells in G_0/G_1 cycle phase, labeled with green dots, increases when cells were treated with m708.5.

3.3 Detection of the expression of IGF-1R at the cell membrane.

To evaluate the presence of IGF1R at the cell membrane and alterations in this localization induced by m708.5, we performed cell immunolabeling followed by flow cytometry analysis. RMS cells (1 x 10^5) were collected from each experimental condition by scraping with ice-cold PBS. Detached cells were washed once with blocking buffer before being stained with the fluorescent conjugated primary antibody IGF-1R-PE (1:65, **Table III. 7**) for 45 min at room temperature and protected from light exposure. After incubation, samples were washed with blocking buffer and stained with 4′,6-diamidine-2′-phenylindole dihydrochloride (DAPI) (Sigma-Aldrich) at a non-toxic concentration of 0.2 µg/mL to dismiss technic-induced cell death. Samples were analyzed with the flow

cytometer ACEA Novocyte 3000 (Acea Bioscience Inc.) and results processed with NovoExpress Software (Acea Bioscience Inc.).

4 Molecular biology techniques

4.1 RNA techniques

4.1.1 RNA extraction and Reverse transcription quantitative polymerase chain reaction (RT-qPCR)

RNA was isolated and purified with the RNA easy Mini kit (Qiagen) following manufacturer instructions. For *in vivo* or human tissue samples, RNA was isolated with Trizol reagent (Sigma-Aldrich) (composed by a phenol solution), followed by the addition of chloroform. Finally, the RNA in the aqueous phase was precipitated by isopropanol and ethanol. RNA was quantified using Nanodrop One C (Thermo Fisher). The retrotranscription of RNA to cDNA was performed with 1 µg RNA with Applied Biosystems™ GeneAmp™ dNTP Blend (2.5 mM each), Fisher Random Hexamers (50 uM), and M-MLV Reverse Transcriptase (200 u/µL) (Promega, Fitchburg, WI, USA). The quantitative analysis of gene expression was performed with Syber Green PCR Master Mix (Applied Biosystems) and specific forward and reverse primer pairs (primer sequences listed **Table III. 5**). The qPCR was accomplished on Applied Biosystems Quant Studio 6 Real-Time PCR system (Thermo Fisher), using the ΔΔCT relative quantification method. GAPDH or TBP were used as housekeeping genes.

Table III. 5. cDNA primers used for qPCR

Gene	Seq	Fw (5'→3')	Rv (5'→3')
PAX3-FKHR	s1	AGGCATGGATTTTCCAGCTATA	GGGACAGATTATGACGAATTGAATT
PAX7-FKHR	s1	TCTGCCTACGGAGCCCG	GGGACAGATTATGACGAATTGAATT
PRKG1	S1	AAAATATGAAGCTGAAGCGG	CAACTCCAAGGGTATCAATG
PRKG1	S2	ATCATATTGAGGGGGATTGAC	TCTTTCTGATGGATTGTCCC
PRKG1	S3	GGTCCAAGGATCTTATAAAGG	CATCTTCCATGACATACACC
MYOD1	S1	AATAAGAGTTGCTTTGCCAG	GTACAAATTCCCTGTAGCAC
MYOG	S1	AATTGAGAGAGAAGAAGGGG	AACAACACACGAAACAAAAC

Characterization of patient-derived xenografts

To verify the presence of the gene translocations PAX3-FOXO1 or PAX7-FOXO1, when applicable, in RMS PDX, a RT-qPCR was performed in tissue samples in parallel with their original patient tumor biopsies. Fig. 4 shows the relative value compared to their primary biopsy.

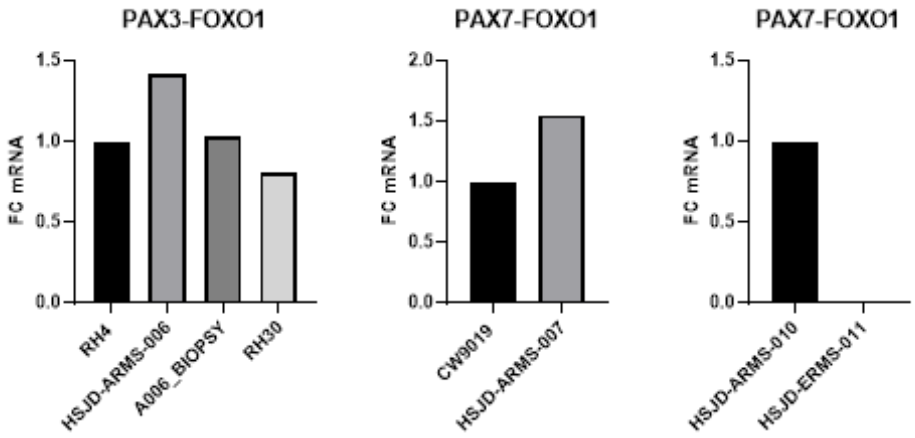

Figure III. 4. RT-qPCR quantification of the expression levels of PAX3-FOXO1 fusion gene in HSJD-ARMS PDXS. (a) PAX3-FOXO1 levels in PDXs and in the PAX3-FOXO1 RMS cell line RH4. (b) PAX7-FOXO1 expression levels in HSJD-ARMS-0007 and the PAX7-FOXO1 RMS cell line CW9019, and (c) in HSJD-ARMS-010 but not in the HSJD-ARMS-011 PDX.

4.1.2 Gene expression detection by microarray analysis

To study transcriptomic differences between RMS tumors with high and low PRKG1 gene expression, RNA was summited to microarray hybridization at the IDIBAPS Genomic Service following standard procedures after the 3'IVT Pico method. Quality and integrity RNA sample were analyzed using bioanalyzer, and the GeneChip™ HT HG-U133 Plus PM Array Plate 24-array format (Thermo Fisher Scientific) was used. Data were quality controlled and normalized using the robust multi-array average (RMA) [24]. Unsupervised analyzes were performed based on the distribution density of standard deviations probes and taking the SD> 1. PRKG1 expression values were analyzed to choose a cut-off point and the median corresponding to the value 5.187 of the PRKG1 probe 11740294_a_at (cell lines or bone marrow were not included in the analysis). The supervised analyzes were performed using the R limma package [25] Probes were considered significantly differentially expressed when the adjusted false discovery rate (FDR) was <0.05. To functionally compare High-PRKG1 samples

to Low PRKG1 samples gene we performed gene set enrichment analysis (GSEA)(67) on High-PRKG1 RMS samples. Gene expression from each model system was ranked according to absolute fold change expression over the corresponding control. GSEA analysis (http://www.broadinstitute.org/gsea/index.jsp) was performed using default parameter settings. By default, FDR <0.25 is significant in GSEA.

To study the effects of ipatasertib, miransertib and PRKG1 gene silencing in RH4 cells at the transcriptional level, a Clariom S Human microarray (WT Plus, Affymetrix) gene expression analysis was performed. Samples were processed at MARGenomics IMIM's core facility. RNA samples were amplified and labelled according to GeneChip manufacturing protocol. For the statistical analysis, R programming (Version 4.0.3) was used, together with different packages from Bioconductor [209] and the Comprehensive R Archive Network (CRAN 2019). After quality control of raw data, samples were background corrected, quantile-normalized and summarized to a gene-level using the robust multi-chip average (RMA) [210], obtaining a total of 20893 transcript clusters. Clustering methods were used. An empirical Bayes moderated t-statistics model (LIMMA) [211] was built to detect differentially expressed genes between the studied conditions. Correction for multiple comparisons was performed using FDR [212], and adjusted p-values were obtained. **Pre-ranked** GSEA [213] implemented in Cluster Profiler [214] package version 3.18.0 was used in order to retrieve enriched functional pathways. The ranked list of genes was generated using the -log(p.val)*signFC for each gene from the statistics obtained in the DE analysis with limma (ME.Ritchie and GK.Smyth 2015). Functional annotation was obtained based on the enrichment of gene sets belonging to gene set collections in Molecular Signatures Database (MSigDB). The collections used in this project are Hallmark Gene sets generated by a computational methodology and summarize and represent specific well-defined biological states or processes and display coherent expression. The specific analyses performed are detailed in the following subsections. Together with the Hallmark Gene sets, a selected list of gene sets derived from the Gene Ontology (GO) Biological Process ontology C2 and C5_GO_BP was analyzed. Moreover, the upregulated gene signature in

CRISPR_KO RH4 cells was intersected with two human myogenic differentiation signatures defined by Yohe et al. [202] and identified as hSMMdiff_UP. In addition, they also defined the gene signature associated with myogenically induced super-enhancers named as Myogenic_SE_UP.

4.2 DNA techniques

4.2.1 DNA extraction

To sequence the isolated CRISPR-KO clones, DNA was extracted from RMS cells. Cell lysis buffer (Cat. Nº 158908, Qiagen) was added to cell pellets, which were incubated at room temperature for 72 h, and then Protein Precipitation Solution (Cat. Nº 158912 Qiagen) was added following manufacturer's instructions. After centrifugation, the supernatant was transferred to a new tube containing isopropanol, and precipitated DNA was obtained by centrifugation and washed with 70% ethanol. After removing ethanol, the DNA pellet was rehydrated with DNA hydration solution (Qiagen). DNA was quantified using a Nanodrop machine.

To check the presence of MYCN amplification in RMS PDX when required, DNA from formalin-fixed paraffin-embedded tissues- PDX was extracted. After an initial deparaffination step with xylol and subsequently ethanol solutions, DNA was extracted from tissues using the QIAamp DNA FFPE Tissue Kit following the manufacturer instructions.

4.2.2 Droplet digital PCR (ddPCR) from paraffin-embedded tissue

To confirm NMYC amplification present in some primary patient samples, DNA of HSJD-ERMS-E001 xenograft, HSJD-ERMS-003 and HSJD-ERMS-024 PDXs was analyzed by Droplet Digital PCR technology. MYCN copy number variation (CNV) was assessed using 10 µl of ddPCR™ Supermix for probes (BioRad, Hercules, CA) for 5 ng of DNA per sample and 1 µl of primer to a final reaction volume of 20 µL. Primer for MYCN was detected in FAM channel (Unique ID dHsaCP2500435, bioRad) and HEX channel for AP3B1 (Unique ID dHsaCP2500348, bioRad) gene used as reference gene. To generate droplets,

individual reaction mixtures were then loaded into a Droplet Generator Cartridge (Bio-Rad) with 70 µL of droplet generation oil (Bio-Rad). The droplets from each well were transferred into a 96-well PCR plate, heat-sealed, and subjected to PCR: 95 °C for 10 min, followed by 40 cycles of 94 °C for 30 s, 60 °C for 1 min, and 98 °C for 10 min. The droplets of each well were then analyzed in a QX100 droplet reader (Bio-Rad) and were quantified using target DNA. The outcome data were analyzed using QuantaSoft version 1.7.4.0917 (Bio-Rad), and the copy number variation was determined.

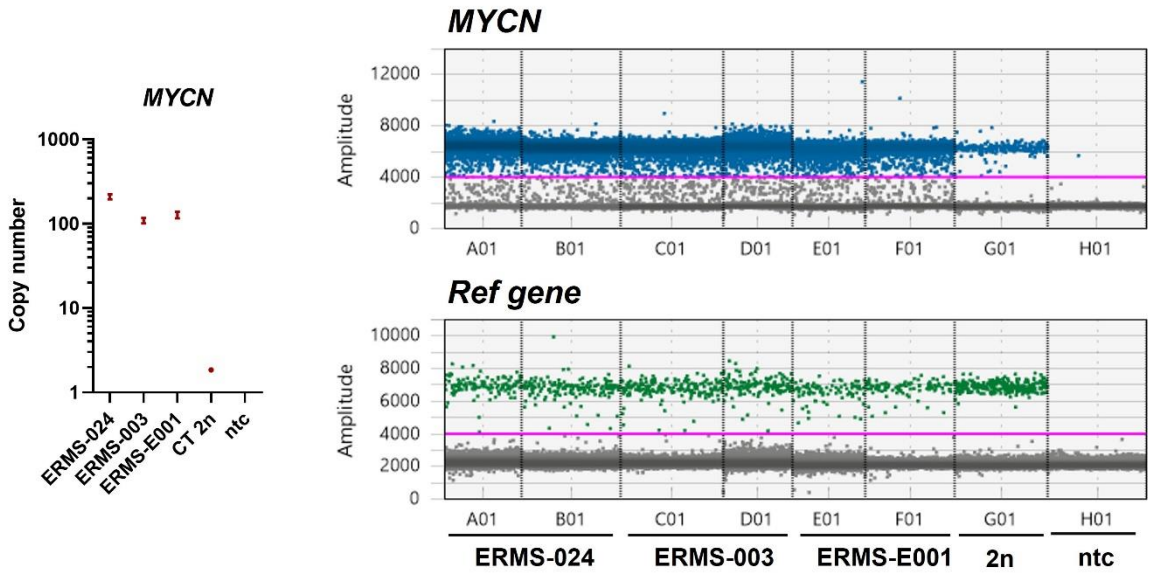

Figure III. 5. Analysis of MYCN amplification by droplet digital PCR in FN RMS PDX. MYCN amplification gene in three FN-RMS PDX. Representative figure for one dimensional ddPCR plots for MYCN and Reference gene, showing MYCN amplification in RMS PDX compared to blood normal control (2n, non-amplified) samples. MYCN was read in blue (FAM) channel, while reference gene was read in green (HEX) channel. Each point represents a single droplet, which is scored as positive (colored and above the threshold intensity, as indicated by the pink line) or negative (grey, below the threshold line), depending on the fluorescent amplitude.

4.2.3 Sanger sequencing

To check editing efficiency on RH4 CRISPR-KO clones, the PRKG1 gene was sequenced by conventional Sanger sequencing at the sgRNA-target-region in control or CRISPR-edited cells. Primer sequences were custom designed based on the gene sequences obtained from the Ensemble database NM_001098512.3. Briefly, amplification of the template was performed in the GeneAmp PCR System 9700 (Applied Biosystems). The melting temperature was 60^0. After running an agarose gel to verify DNA amplification, the PCR product was cleaned with ExoSAP-IT™ PCR Product Cleanup Reagent (Cat nº 78205, Applied Biosystems). Then, for sequencing reaction, we used the same primers used for amplification, but performed in two different reactions, one for the forward and other for the reverse sequences. The DNA product was purified by Sephadex G-50 (GE17-0573-01, Merck) gel filtration. The eluted DNA was place in a MicroAmp 96 well plate and analyzed in the genetic sequencing unit of the HSJD. Sequencing results were visualized with the ICE CRISPR Analysis Tool (https://ice.synthego.com).

Table III. 6. Primer sequences for PRKG1 sequencing.

PRKG1	Sequence 5'—3'	Source
FW1	AGGCTCTCTGATCCAACCCT	Sigma-Aldrich
RV1	AGGTCGTGGAAGGACCTGTA	Sigma-Aldrich

4.2.4 Clustering of PRKG1 peaks with epigenomic marks

For visualization of ChIP-seq data from public databases, the UCSC genome browser was used to generate the screenshots presented in this thesis. Publicly available ChIP-seq tracks were obtained from the accession numbers GSM2214114 (MYOD1), GSE140115 (PAX3-FOXO1), GSE83725 (H3K27 acetylation), GSM2214109 (H3K4me3), GSM2214107 (H3K4me1), GSM2214105 (H3K27m3).

4.3 Protein techniques

4.3.1 Protein extraction

Cultured cells were scraped and collected by centrifugation. For whole cell protein extracts, cells were lysed with RIPA 1X buffer (50 mM Tris pH 8.8, 150 mM NaCl, 0.1% SDS, 0.5% sodium deoxycholate and 1% NP40) completed with Proteases Inhibitor Cocktail Tablets (Roche). To detect phosphorylated proteins, cells were lysed with Tris-HCl pH 7.4; 5 mM NaCl, Triton X-100, 1%, EDTA, Na3VO4 (1 mM), NaF (2,5mM), sodium pyrophosphate (4 mM), free-protease inhibitor (Roche) and milli-Q water. This buffer ensures the inhibition of phosphatases and proteases. In both cases, cell lysates were incubated 15 min on ice and centrifugated 12000 rpm for 10 min at 4ºC.

For protein isolation from tissues, tumor samples were homogenized in 0.5% Igepal, 0.5% sodium deoxycholate 0.1% sodium dodecyl sulfate, 50 mM TRIS-HCl (pH 7.5) and 150 mM NaCl with stainless-steel beads (0.2 mm diameter) in the bullet blender at 12,000 rpm for 2-5 min until a homogeneous mixture was obtained..

4.3.2 Western blotting

Protein extracts were quantified with Bradford Reagent (BioRad), and about 35-50 ug of protein extracts were boiled for 3 min at 95ºC and loaded in 8-12% polyacrylamide gels for electrophoresis. Proteins were then transferred into nitrocellulose membranes (GE Healthcare Life Science). Membranes were blocked in 3% BSA or 5% milk powder solved in TBS-T (Tris-buffered saline, 0.1% Tween 20) for 1 h. In general, membranes were incubated overnight at 4^0C with the primary antibodies and 1 h at room temperature with fluorescently labeled secondary antibodies. Fluorescence was detected using LI-COR Odyssey Classic Infrared Imaging System (LI-COR Inc.). Relative levels of protein expression were measured by Image J software.

Table III. 7. All the antibodies used along this thesis.

Protein	Technique	Working dilution	Reference	Company
Phospho-IGF-I Receptor β (Tyr1135)	WB	1:1000	3918	Cell Signalling
IGF-I Receptor β (D23H3) XP®	WB/ IF	1:1000/ 1:200	9750	Cell Signalling
Phospho-Akt (Ser473)	WB	1:1000	4060s	Cell Signalling
Phospho-Akt (Thr308)	WB	1:1000	4056	Cell Signalling
AKT_total	WB	1:1000	9272	Cell Signalling
Phospho-S6 Ribosomal Protein (Ser240/244)	WB/IHQ	1:1000	5364	Cell Signalling
Phospho-S6 Ribosomal Protein (Ser235/236)	WB	1:1000	2211	Cell Signalling
S6 Ribosomal Protein (5G10)	WB	1:1000	2217	Cell Signalling
Phospho-GSK-3β (Ser9) (5B3)	WB	1:1000	9323	Cell Signalling
GSK-3β (D5C5Z) XP®	WB	1:1000	12456	Cell Signalling
Phospho-FoxO1 (Thr24)/FoxO3a (Thr32)	WB	1:1000	9464	Cell Signalling
Cleaved PARP (Asp214) (D64E10) XP®	WB/ IHQ	1:1000/ 1:50	5625	Cell Signalling
Phospho-PRAS40 (Thr246)	WB	1:1000	2997	Cell Signalling
PRKG1 (C8A4)	WB	1:1000	3248	Cell Signalling
Phospho-p44/42 MAPK (ERK1/2)	WB	1:1000	4370	Cell Signalling
ERK1/2	WB	1:1000	4695	Cell Signalling
Phospho-Stat3 (Tyr705)	WB	1:2000	9145	Cell Signalling
STAT3	WB	1:2000	68153	Abcam
Actin	WB	1:30000	A2228	Sigma Aldrich
α-Tubulin	WB	1:30000	T6199	Sigma Aldrich
Lamin B1	WB	1:2000	Ab16048	Abcam
MyoD1	IHQ	1:20	M3512	Dako, Agilent Technologies
MyoD1 (D8G3)	IF	1:400	13812	Cell Signalling
Anti-human Nuclei	IHQ/ IF	1:200	MAB4383	Millipore
Human IGF-IR/IGFIR PE-conjugated	FC	1:65	FAB391P-025	Bio-Techne

Fluorescent Western blots were imaged using the Odyssey Infrared Imaging System (LI-COR Biosciences). Secondary antibodies used were IRDye 680LT donkey anti-rabbit (925-68023), IRDye 800CW donkey anti-mouse (926-32212), IRDye 800 CW goat anti-rabbit IgG (926-32211), and IRDye 680RD goat anti-mouse IgG (926-68070). For chemiluminescent detection, secondary HRP-conjugated antibodies were obtained from Dako and Immobilon Western Chemiluminescent HRP substrate for detection.

4.3.3 Human phospho-kinase array

In order to detect phosphorylation of intracellular kinases in RMS samples, the Human phosphokinase array kit (Proteome Profiler Kit ARY001B, ARY002B and Kit ARY003B) was used according to the manufacturer's protocols. Briefly, after blocking for 1 h using Array Buffer 1, membranes were incubated with 350 µg of protein lysates overnight at 4°C, and then washed and incubated with a streptavidin-HRP detection antibody (1:5000). Membranes were developed using ECL Western blotting detection reagents (Chemi reagent A and Chemi reagent B) provided by the manufacturer. Chemiluminiscent signal of each membrane was detected with iBright Imagine System (Thermo Fisher) and the expression levels were densitometrically quantified using HLImage++ Western Vision software.

4.3.4 Immunofluorescence (IF)

4.3.4.1 IF of adherent cells

To detect the expression of IGF1R and to label the plasma membrane for confocal microscopy analysis, RMS adherent cells were grown over a slide, and fixed with 4% formaldehyde for 15 min at 37^0C. Previous to permeabilization, cells were labeled with Wheat Germ Agglutinin conjugated to Alexa Fluor® 647 at a concentration of 5.0 µg/ml. After 10 min of incubation at room temperature, cells were washed and permeabilized with 0.2% Triton X-100. Then, cells were incubated with blocking solution (3% BSA) for 30 min and with IGF1R primary antibody for 1 h. Cells were washed and labeled with a secondary antibody conjugated with green Alexa 488. Nuclei were counterstained with DAPI, and samples mounted with ProLong Gold (Thermo Fisher Scientific)

4.3.4.2 IF on primary culture cells

Pellets from primary cultured cells were embedded in OCT and placed into slides for fixation with 4%PFA for 10 min and permeabilization with 0.1× Triton. MyoD1 and anti-human nuclei were used as primary antibodies. As corresponding

secondary antibodies, Alexa Fluor® 594 conjugate goat anti-mouse (1:400, A-11012, Applied Biosystems) and Alexa Fluor® 488 goat anti-mouse (1:400, 15626746, Thermo Fisher Scientific) were used. Samples were incubated with secondary labeled antibodies for 1.5 h at room temperature.

4.3.4.3 Image acquisition and processing

Super-resolution images were acquired with a Leica TCS SP8 X White Light Laser confocal microscope with Hybrid spectral detectors and HyVolution (Leica Microsystems, Wetzlar, Germany) using the Leica LAS X software (version 3.1.5). Images were acquired using a HC x PL APO 100×/1.4 oil immersion objective. Optimized emission detectors bandwidths were configured to avoid inter-channel crosstalk. Appropriate negative controls were used to adjust confocal settings to avoid non-specific fluorescence artifacts. For IGF1R signal six different fields were quantified. Confocal images were processed and analyzed with Image J software.

4.3.5 Immunohistochemistry (IHQ)

PDX engraftments as well as successive mouse-to-mouse transplantation tumors were characterized by immunohistological detection of MyoD1 (1:20, M3512; DAKO Agilent Technologies, Santa Clara, CA, USA) and anti-human nuclei antigen (1:200, MAB4383; Merck Millipore, Burlington, MA, USA), and counterstained with hematoxylin and eosin. Pharmacodynamic analysis were performed by immunohistochemistry detection of p-s6 (Ser240/244) (1:1000) and Cleaved-PARP (1:50, #5625S, Cell signaling). Briefly, tumor samples were fixed in 10% formalin and embedded in paraffin. Paraffin block samples were cut into sections of 3 µm with the microtome and deparaffined at 60˚C for 45 min. Then, sections were rehydrated and transferred to xylol and ethanol standard baths. This protocol was followed by heat-induced antigen retrieval in sodium citrate (pH 6.0) buffer and, subsequently, endogenous peroxidase action was inhibited with hydrogen peroxide and 0.1% sodium azide, following manufacturer's instructions. The staining was carried out using the corresponding primary antibodies. The

DAB (Polymer) Kit (Buffer + Chromogen) Novocastra (Leica Biosystems) was used. Slides were finally cover slipped with dibutyl phthalate polystyrene xylene (DPX) and dried at room temperature.

5 *In vivo* experiments

5.1 Ethical statement and animal experimentation

All *in vivo* studies were accomplished according to the institutional and European guidelines (EU Directive 2010/63/EU) on the principle of the 3R; that is to replace, reduce and refine the use of animal for scientific purposes. Animal procedures have been approved by the animal experimental ethics committee. (Comité de Ética de Experimentación Animal of University of Barcelona).

5.2 Antitumoral efficacy studies

The antitumoral efficacy of all therapies tested was studied in three-to six-week-old NOD/SCID female mice subcutaneously implanted in both flanks' with a 3 $\times$3 mm^3 fresh PDX tumor. PDXs HSJD-ARMS-001, ERMS-003, ARMS-006, ARMS-007, ARMS-010 and ERMS-011 were previously established and provided by Dr. Montero's group in our lab. HSJD-ERMS-E001 and HSJD-ERMS-024 PDX models were generated from the same patient at different stages of disease. ERMS-024 model was directly generated from a primary biopsy like the rest of the PDX models. ERMS-E001 model was generated in our lab by culturing primary biopsy in sphere-forming conditions. All *in vivo* studies were performed between F1 and F8 passages. Mice were weighed and tumors measured with a caliper three times per week during treatment and after treatment. The specific number of animals in each experimental group is indicated in the graphs.

Tumor volume was calculated as follows: (longer measurement x (shorter measurement) ^2) / 2. Animals were euthanized when the tumor volume exceeded 2000 mm3 or if body weight loss was more than 20% of the starting weight. To analyze efficacy, percentage of tumor volume regression was calculated as: ((Tumor volume at 10 doses) – (initial tumor volume))/ (initial tumor

volume) *100. Defined parameters were Complete Response (CR): volume < 100 mm3 and > 50% reduction; Partial Response (PR): volume ≥ 100 mm3 and regression ≥ 50%; SD: volumen ≤25% increase or < 50% regression; and PD: volume > 25% increase or < 50% regression.

5.2.1 Antitumoral activity of ipatasertib (GDC-0068)

Ipatasertib was diluted in water and freshly prepared every day before administration. When tumor volumes reached 150-350 mm^3, mice were randomized into different groups (5-10 animals per group) and divided into four different groups: saline (control), ipatasertib (100 mg/kg), ipatasertib (50 mg/kg) and ipatasertib (25 mg/kg) when applicable. Ipatasertib treatments or control vehicle were orally administrated five times per week with 2 days off each week, during four consecutive weeks, (dx5) $\times 4$.

The regimen of 100 mg/kg of ipatasertib group was the Maximal Tolerated Dose (MTD). Note that doses of 25 or 50 mg/kg, below the MTD, were only included in graphs of dose-dependent effect.

A second experiment to study dose dependent effect of ipatasertib in E001 xenograft model was performed (**Figure IV. 16**). Like the previous experiments, 2 $\times 10^6$ cells were inoculated in each flank of mice. However, this second experiment included some technical differences: (i) ipatasertib treatment initiation was started at 300-500 mm3 tumor volume and (ii) mice were male, instead of the previously groups that only included female mice. Animals were divided in three different groups: control (5 mice); ipatasertib (100 mg/kg; 5 mice); and ipatasertib (50 mg/kg; 10 mice).

Survival curves of mice bearing HSJD-ARMS-010 and ERMS-024 PDX, treated with 100 mg/kg or 25 mg/kg of ipatasertib were calculated by Kaplan-Meier Method. Survival event was reported at 1500 mm^3 tumor size. Log-rank statistic with Bonferroni correction test was used to compare statistical significances between treated groups, and performed with GraphPad Prism 8 software.

5.2.2 Antitumoral activity of miransertib (ARQ-092.2MSA)

To test miransertib (**ARQ-092)** efficacy on tumoral reduction, *in vivo* experiments were carried out following the published instructions: a solution of 10 mg/ml of **ARQ-092.2MSA** was prepared in 0.01 M phosphoric acid and freshly prepared every day before administration. The compound amount weight was corrected by a Potency Correction Factor (free-base content) of 0.649. For a dose of 100 mg/kg, 200 µl were administrated per 20 g weight (by oral gavage) for the mouse. This volume was corrected by the animal weight. Tumor volume criteria were the same as for ipatasertib-treated mice.

Here we present data from an HSJD-ERMS-011 model. When tumor volumes reached 150-450 mm^3, mice were randomized into five groups (n range between 4-9 animals per group): (i) only water (vehicle), (ii) 0.01 M phosphoric acid (vehicle), (iii) **miransertib** dissolved in 0.01 M phosphoric acid; and (iv) two groups of **ipatasertib** at high and low doses dissolved in water. Treatment started on a regimen of 5-days-on/ 2-days-off for 2 weeks for all groups in order to compare toxicities and responses. However, due to the high toxicity seen in **ARQ-092** after 10 doses, we switched the administration protocol to 3-days-off between cycles of **ARQ-0.92-phosphoric acid** to avoid this high toxicity.

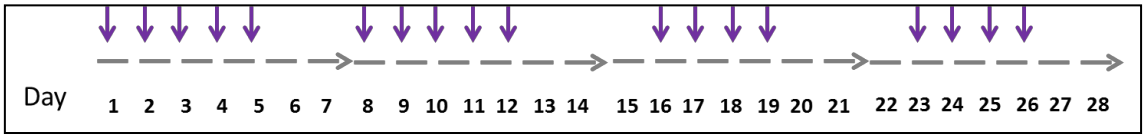

Diagram of posology followed for ARQ-092·2MSA animal group. Purple arrows indicate oral administration.

5.2.3 Subcutaneous inoculation of A006_s cells

Rhabdomyosarcoma cells coming from cultures were suspended in 1:1 TSM - Matrigel (Corning® Basement Membrane Matrix, Cultek) and these suspensions were inoculated in each flank of every mouse. When tumor volumes reached **150-350 mm3**, mice were divided into four different groups: vehicle (control); ipatasertib (100 mg/kg); ipatasertib (100 mg/kg) plus trametinib (3mg/Kg) and trametinib (3mg/Kg). Ipatasertib was administrated at 100 mg/kg diluted in water and freshly prepared every day before administration. trametinib was

administrated as suspension in vehicle (0.5% hydroxypropylmethylcellulose/0.2% Tween 80/5% sucrose). It was prepared weekly and stored at 4ºC until use. In the ipatasertib+trametinib group, independent drug administration was separated by at least 1 hour. Treatments were administered to animals **during three weeks** in the A006 model. As in previous experiments, daily administration was maintained for **3 weeks**, with 2 days off each week. Survival statistical analysis used log-rank test corrected by Bonferroni method in four group comparison (0.0125). The criteria for the end of the study, which was based on tumor volume, was the same as previously described for ipatasertib and miransertib experiments.

5.3 Pharmacokinetic analysis

5.3.1 Ipatasertib methodology detection

To investigate the pharmacokinetics (PK) of ipatasertib, we used female NOD/SCID mice bearing bilateral subcutaneous HSJD-ARMS-006 and HSJD-ERMS-011 PDX. Mice received ipatasertib oral administration at a dose of 100 mg/kg or 25 mg/kg, when tumors reached >250 mm^3. Blood and tumor samples were collected at 0, 1, 3, 8, and 24 h after a single dose of ipatasertib. Blood samples (approximately 800 µL) were collected from each animal at the scheduled sample collection time by terminal cardiac puncture into tubes containing Heparin as an anticoagulant and centrifuged at 1500–2000 g to isolate plasma. In each time condition, 4 animals were included for each dose tested, and therefore, 8 tumors and 4 plasma samples were analyzed for each condition and time. A total of 32 animals were included for the ERMS-011 PK and 25 animals for the PDX HSJD-ARMS-006 PK. Plasma and tumor tissues were snap-frozen in liquid nitrogen and stored at −80 °C.

The concentration of ipatasertib in each plasma ant tumor sample was determined by an internally validated Liquid Chromatography with tandem mass spectrometry (LC-MS-MS) assay in the Department of Pharmacology, Therapeutics and Toxicology, Universitat Autonoma de Barcelona (UAB). For PK studies of a small molecule such as ipatasertib, using an LC-MS/MS instrument

provide much higher sensitivity and specify than UV detectors commonly used on HPLC units. Chromatography was performed using Zorbax Eclipse Plus C18 (2.1x50, 1.8 µm) (Agilent Technologies) with a mobile phase of 0.1% formic acid in acetonitrile and with a flow rate of 0.4ml/min. Lincomycin was used as internal standard. The drug and the internal standard were extracted by liquid–liquid extraction and analyzed by mass spectrometry. The Autosampler model Agilent 1260 Infinity together with the detector model Agilent 6420 mass spectrometer were used for the analysis.

6 Gene expression analyses in pediatric tumor public data bases

6.1 Supervised PRKG1 expression in pediatric databases

Thirty public GO_datasets for pediatric tumor transcriptomes, generated with the platform U133 plus2.0, Affymetrix were identified, in collaboration with FSJD genomic group. A dataset of 783 pediatric tumors plus human mesenchymal (hMSC), embryonic stem cells (hESC), and human Skeletal Muscle Precursor cells (hSMPs), was generated. Tumors represented include medulloblastoma (MB), osteosarcoma (OS), neuroblastoma (NB), EW (EW), synovial sarcoma (SS), diffuse intrinsic pontine glioma (DIPG), low-grade glioma (LGG), high-grade glioma (HGG), ependymoma, pilocytic astrocytoma (PA) and RMS. Importantly, 58 RMS samples are included. Gene expression data normalization was performed using RMA algorithm included in the oligo R-package (R/Bioconductor) [210, 215]. Quality control was done using oligo and limma R-packages (R/Bioconductor) [211]. There were three probes associated with PRKG1 gene. For our analysis, the PRKG1 207119_at, 211380_s_at, 228396_at probes were analyzed. Datasets included in this study have been previously reported and were obtained from the NCBI Gene Expression Omnibus (GEO) data repository. Reference Accession Numbers GSE67851, GSE70678, GSE44971, GSE26576, GSE74195, GSE13828, GSE7896, GSE8884, GSE9440, GSE9510, GSE17679, GSE34620, GSE37371, GSE34824, GSE36245, GSE26576, GSE10327, GSE37418, GSE49243, GSE67851,

GSE74195, GSE10315, GSE13604, GSE6460, GSE7637, GSE9520, GSE9451, GSE9593, GSE16254, GSE73537, GSE14827, GSE44971, GSE26576, GSE66533, GSE20196 and GSE44227. All microarray analysis was performed by Dr. Soledad Gómez (HSJD DAI-Omics unit).

6.2 Prognostic value of PRKG1 gene expression in RMS

Here we studied PRKG1 as prognostic factor along FP and FN RMS, therefore the cut-off point was maintained for both subgroups.

In order to perform survival analysis, we used data from the gene expression data set GSE92689. Overall Survival (OS) probabilities were calculated with the Kaplan-Meier Method [216]. OS determined the time from biopsy until patient's death or last contact. To estimate the cut-off point of PRKG1 expression levels the Contal-O'Quigley method was used [217].

IV. RESULTS

1 Targeting the IGF axis with the dual anti-human IGF1/2 monoclonal antibody m708.5 in RMS cell lines

Studying the IGF axis and its pharmacological inhibition as a therapeutic approach in cancer has been of great interest for many years, also for RMS. The monoclonal antibody m708.5 targets the human IGF1 and IGF2 and has shown anti-proliferative effects when used as single agent in cell cultures of pediatric cancers such as neuroblastoma and EW. *In vivo*, m708.5 treatment prolonged the survival of mice carrying the neuroblastoma LAN1 xenografts. In RMS, studies are limited to the establishment of the m708.5 IC50 in RH30 and RH41 cell cultures [146]. Besides these preliminary studies, neither the systematic analysis of the IGF1R/IRS/AKT pathway nor the biological effects of m708.5 treatment in RMS models had been analyzed.

1.1 Functional and molecular characterization of m708.5 effects in RMS cell lines

The antibody m708.5 (kindly provided by Dr. N.K. Cheung's lab) was first used to evaluate m708.5 anti-proliferative activity in four different RMS cell culture models (RH4, CW9019, RH30 and RD), to determine m708.5 specificity in RMS by comparing its cytotoxicity to neuroblastoma and EW cell lines (LAN1 and A4573, respectively). Cells were exposed to m708.5 at concentration ranges of 0.01 to 100 µg/ml for 48 h. MTS viability assays confirmed previous data reporting the high sensitivity of LAN1 and A4573 cells to m708.5 [146]. Of the RMS lines, the RH4 cell line was the most sensitive to m708.5 cytotoxic effects, with a similar range as the LAN1 cells. In contrast, the other RMS cell lines showed a cell viability reduction of less than 50% even at the maximum dose tested (**Figure IV. 1**).

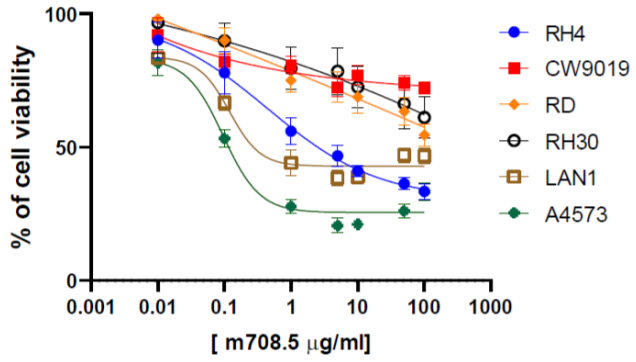

Cell line	IC50 µg/ml (95% Confidence interval)
RH4	0,44 (0,07 – 0,88)
CW9019	n.s.
RD	n.s.
RH30	n.s.
LAN1	0,12 (0,07-0,20)
A4573	0,09 (0,06-0,12)

Figure IV. 1. Effect of m708.5 in RMS cell viability. Cell viability analysis by MTS assays showing the percentage of viable RH4, CW9019, RD and RH30 cells treated with different m708.5 concentrations for 48 h. Neuroblastoma (LAN1) and EW (A4573) cell lines were used as positive controls. **Table IV.1. IC50 values for m708.5 in established cell lines from pediatric tumors.** n.s., not significant. Observe that m708.5 exhibited cytotoxicity in the fusion positive-RMS cell line RH4 at similar concentration range as LAN1 and A4573 cells.

To discriminate between the cytostatic and cytotoxic effects of m708.5, we subsequently studied apoptosis by annexin V staining in the most m708.5 sensitive cell line. At 48 h after treatment, m708.5 reduced the fraction of viable RH4 cells (black bar) (38.6% in the m708.5-treated group compared with 65.5% in the control group). Moreover, late apoptosis increased to 49% in treated cells as compared to 27% in control cultures (**Figure IV. 2A**). Therefore, m708.5 treatment slightly increased early and late apoptosis in RH4 cells, although this was not statistically significant.

To explore the potential cytostatic effect of m708.5, the RH4 cell cycle profile was analyzed by flow cytometry after BrdU labeling. As observed in **Figure IV. 2B**, m708.5 (1 µg/ml) treatment for 24 h induced a slight increase in the percentage of cells in G_0/G_1 phase, which however was not statistically significant.

We conclude that RH4 sensitivity to m708.5 could be due to mechanisms involving both apoptosis and cell cycle arrest. In addition, these results suggested that m708.5 treatment as single agent lacks the potency to reduce the viability of RMS cells *in vitro*.

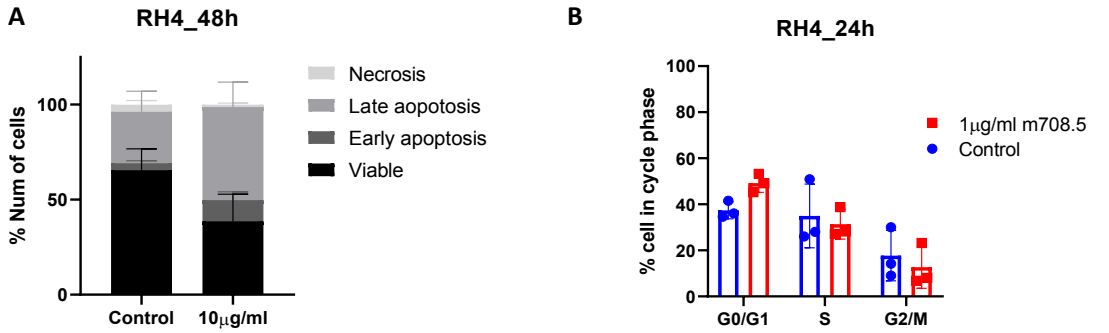

Figure IV. 2. Effect of m708.5 treatment in RH4 cells on apoptosis and cell cycle. A) Bar charts representing percentages of viable, early, and late apoptotic and necrotic RH4 cells upon 10µg/ml m708.5 treatment for 48h. Cells were stained with annexin V and analyzed by flow cytometry. Data represent mean of three biological replicates for each experimental condition. Mann Whitney test was performed in control *vs.* treated group cells for viable (n.s.) and late apoptotic cells (n.s). **B)** RH4 cells treated at 1 µg/ml m708.5 for 24h were pulsed with BrdU. Cells were then labeled with a FITC-conjugated anti-BrdU antibody and with 7-AAD to label DNA and analyzed by flow cytometry. Bar graph shows the proportion of cells at G_0 /G_1, S, and G_2 /M phases of the cell cycle. Data represents mean of three different experiments. Mann-Whitney test was performed in control *vs.* treated group cells for each cell cycle phase (n.s.). Note that m708.5 treatments induced moderate increases in the number of apoptotic cells and the number of cells at G_0 /G_1.

We next asked whether differences in IGF1R subcellular localization could predict the differential sensitivity displayed by the four RMS cell lines to m708.5. IGF1R detection by immunofluorescence in a sensitive (RH4) and resistant (CW9019) cell line, revealed a differential expression pattern in these two cell lines. Confocal microscopy revealed that RH4 cells expressed high levels of IGF1R localized at the cell membrane, while CW9019 cells expressed low IGF1R levels with a cytoplasmic distribution (**Figure IV. 3**). These data correlate with the observed RH4 sensitivity to m708.5 and provide an explanation for the resistance observed in CW9019. Therefore, on the basis of this preliminary observation, the expression of IGF1R at the cell membrane evaluated by immunofluorescence could predict responsiveness to m708.5 treatment.

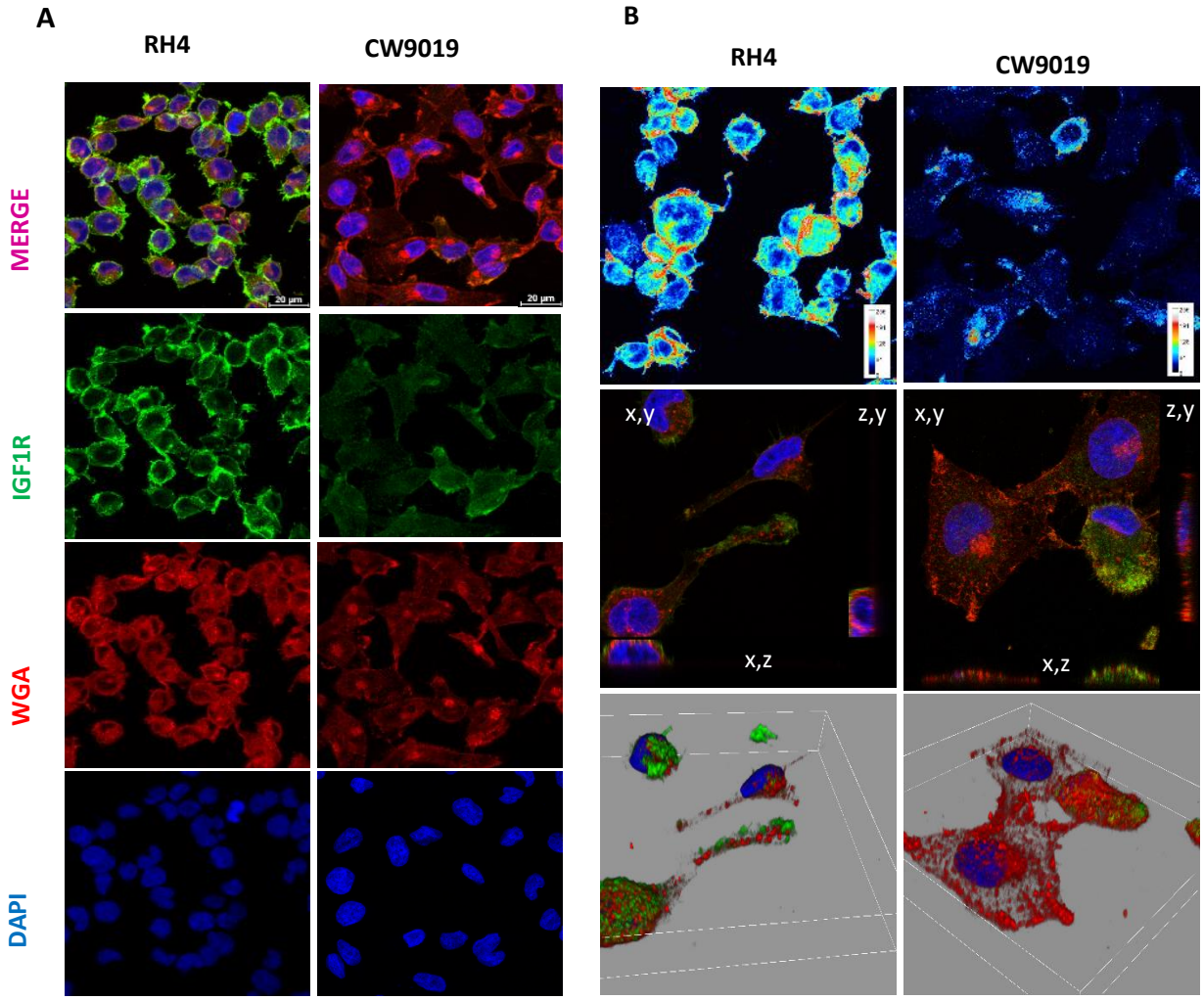

Figure IV. 3. Subcellular localization of IGF1R in RMS cell lines. A) Confocal imaging of IGF1R (in green) distribution in RH4 and CW9019 cells was performed across the plasma membrane, which was stained with wheat germ agglutinin (WGA; in red). In blue, nuclear counterstain with DAPI. Observe the pronounced IGF1R localization at the plasma membrane in RH4 cells. **B)** First-row panels, analysis of IGF1R intensity in RMS cells lines. Second- and third-row panels show immunofluorescence images for 3D reconstruction projections across the confocal z-stack; projections on x,y, x,z, and z,y planes are indicated. Note (at high resolution) that IGF1R localizes to the plasma membrane (labeled in red) in RH4 cells.

To investigate whether neutralization of IGF1/2 ligands by m708.5 affects IGF1R levels at the plasma membrane, cells treated with the antibody were analyzed by flow cytometry. The highest IGF1R membrane levels in basal conditions corresponded to the RH4 cell line, according to the IGF1R signal detected by confocal microscopy. Cell treatment with m708.5 slightly increased IGF1R levels

in RH30 and CW9019 (**Figure IV. 4**). Therefore, in these cells, ligand deprivation by m708.5 results in an enhancement in IGF1R protein expression at the cell membrane that can sustain the activation of the IGF1R signaling pathway, suggesting a positive feedback mechanism. This effect constitutes a potential escape mechanism that could impair the therapeutic efficacy of m708.5. Importantly, this mechanism does not seem to be active in the RH4 cell line, in which m708.5 treatment did not affect IGF1R expression levels, in accordance with its high sensitivity to the antibody.

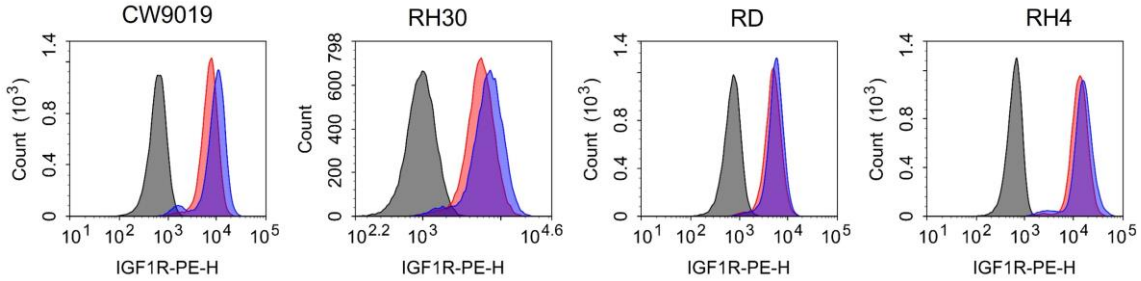

Figure IV. 4. IGF1R levels at the plasma membrane are modulated by m708.5 treatment in CW9019 and RH30 cell lines. Flow cytometry histogram of membrane expression of IGF1R in RMS cells untreated (in red) or treated with 10 µg/ml of m708.5 (in blue) for 48 h cultures in 2.5% FBS. Isotype control antibody, in grey.

To better understand receptor regulation, RMS cells were treated for 48h with m708.5 (10 µg/ml), IGF1 (75 ng/ml), or IGF2 (50 ng/ml), and IGF1R expression and activation was evaluated by Western blot analysis. Receptor expression levels were reduced upon ligand treatment, while total IGF1R was upregulated upon m708.5 treatment in RMS cells (**Figure IV. 5**).

We also wished to determine IGF1R activity by measuring the phosphorylation levels of the residues Tyr1135/Tyr1136, the first phosphorylation triggered during IGF1R activation [114]. As expected, IGF1 activated its receptor, except in RD cells, while IGF2 increased IGF1R phosphorylation only in RH4 cell lines. Conversely, m708.5 reduced IGF1R phosphorylation in RMS cell lines (except for RD cells) despite the enhanced total IGF1R levels (**Figure IV. 5**). Therefore, m708.5 is able to functionally inhibit IGF1R activation in RH4, CW9019 and RH30. In RD cells, m708.5 reduced IGF1R phosphorylation at a short time point

(of 3 h) (**Figure IV. 6**), although IGF1R phosphorylation was restored at 48 h (**Figure IV. 5**).

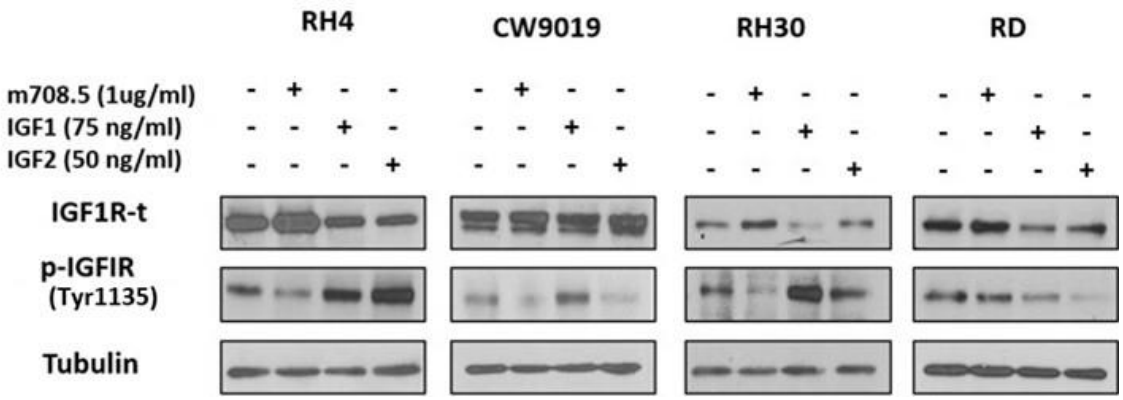

Figure IV. 5. Regulation of IGF1R expression and activation by ligand binding and m708.5 treatment. Western blot analysis of one representative experiment showing protein levels of IGF1R and p-IGF1R (Tyr1135) upon IGF1, IGF2 and m708.5 treatments for 48 h in RMS cell lines. Tubulin was used as loading control.

We then analyzed the effects of m708.5 on the IGF1R signaling cascade. AKT and FOXO3a/O1 phosphorylation levels, determined by Western blot, were analyzed as a readout for IGF1R pathway activation. The effects of m708.5 treatment on intracellular signaling directly correlated with the biological responses observed by the MTS viability assays: those cells highly sensitive to m708.5 were also those that showed the greatest reduction in AKT and FOXO3a/O1 phosphorylation. In particular, and in contrast to the other RMS cell lines, the RH4 cell line showed an inhibition of the IGF1R pathway similar to LAN1 (neuroblastoma) or A4573 (EW) cells (**Figure IV. 6**).

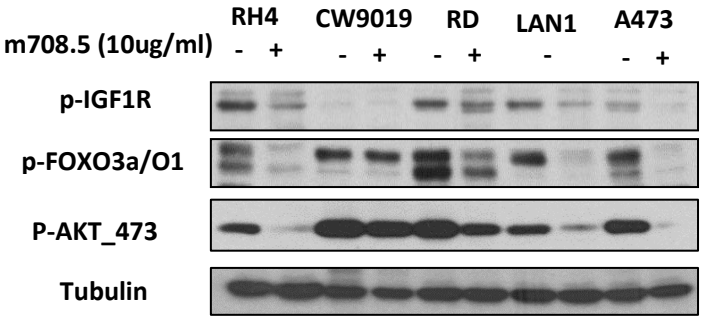

Figure IV. 6. Inhibition of the IGF1R signaling pathway by m708.5. Cells were treated with m708.5 (10 µg/ml) for 3 h and total extracts were analyzed by Western blot to detect phosphorylation levels of IGF1R (Tyr1135), FOXO3a (Thr32)/FOXO1 (Thr24) and AKT (S473). Tubulin was used as loading control.

We observed that m708.5 effectively reduced IGF1R phosphorylation, but this effect disappeared at 48 h in RD cells. Therefore, we investigated whether this adaptation mechanism, which results in a cascade of intracellular phosphorylation, also takes place in the most m708.5 sensitive cell line. Protein extracts from RH4 long-term cultures treated with m708.5 and control were immunoblotted using the proteome profiler phospho-kinase array. The most significant change was the reactivation of AKT activity, which was reflected by the restoration of Ser473-phosphorylation levels after 7 days of m708.5 treatment (10µg/ml) (**Figure IV. 7**). This result highlights the relevance of AKT in RMS cell survival and unveils the capacity of RMS to restore AKT activity independent of IGF1/IGF2 signaling.

Coordinate	Target protein
A1-A2	Reference spot
A3-A4	p38α
A5-A6	ERK 1/2
A7-A8	JNK1/2/3
A9-A10	GSK3-3α/β
A13-A14	p53
A15-16	-
A17-18	Reference spot
B3-B4	EGFR
B5-B6	MSK1/2
B7-B8	AMPKα1
B9-B10	AKT1/2/3
B11-B12	AKT1/2/3
B13-B14	p53
C1-C2	TOR
C3-C4	CREB
C5-C6	HSP27
C7-C8	AMPKα2
C9-C10	β-Catenin
C11-C12	p70 S6 kinase
C13-C14	p53
C15-C16	c-Jun
D1-D2	Src
D3-D4	Lyn
D5-D6	Ldk
D7-D8	STAT2

Coordinate	Target protein
D9-D10	STAT5a
D11-D12	p70 s6 kinase
D13-D14	RSK1/2/3
D15-D16	Enos
E1-E2	Fyn
E3-E4	Yes
E5-E6	Fgr
E7-E8	STAT6
E9-E10	STAT5b
E11-E12	STAT3
E13-E14	p27
E15-E16	PLC-γ1
F1-F2	Hck
F3-F4	Chk-2
F5-F6	FAK
F7-F8	PDGF Rβ
F9-F10	STAT5a/b
F11-F12	STAT3
F13-F14	WNK1
F15-F16	PYK2
G1-G2	Reference spot
G3-G4	PRAS40
G9-G10	Negative Control
G11-G12	HSP60
G17-G18	Negative Control

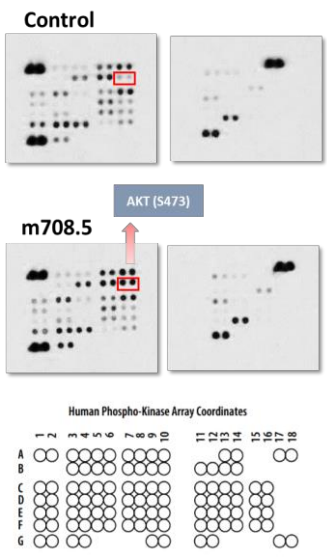

Figure IV. 7. Long-term exposure to m708.5 restores AKT activation in RH4 cells. Phospho-proteome profile of RH4 cell treated for 7 days with 10µg/ml of m708.5 (media was changed every 3 days, refreshing m708.5). Left panels: full legend of each protein in the proteome profiler.

Experimental evidence has shown that the IGF1R network is interconnected with other receptor tyrosine-kinase (RTK) axes [144], and that these networks could explain restoration of AKT phosphorylation in long-term m708.5 treatments, and the modest efficacy of m708.5 to inhibit cell proliferation or effectively induce cell death. Therefore, we hypothesized that combination of drugs targeting different RTK axes could be a promising alternative to inhibiting IGF1R signaling and related bypass networks.

To dissect the IGF1R signaling crosslinked networks, we used RH4 and CW9019 to represent the two extreme outcomes of RMS regarding IGF1R axis activation. Protein extracts collected from these cells treated with m708.5 for 48 h were used to determine the phosphorylation status of forty-nine RTKs, corresponding to their active state, by using phospho-RTK arrays. At basal conditions, the strongest phosphorylation signal corresponded to IGF1R and HGFR in RH4 cells and to HGFR, EGFR and Axl in CW9019 cells. In the latter, IGF1R phosphorylation was not detected. These data confirm the non-dependence of CW9019 on the IGF1R axis. Interestingly, m708.5 reduced HGFR phosphorylation in both cell lines (**Figure IV. 8**). This indirect inhibition of HGFR activation by m708.5 suggested that autocrine/paracrine IGF1/2 could be promiscuously signaling through HGFR or, alternatively and less likely, that m708.5 was able to neutralize the HGF ligand.

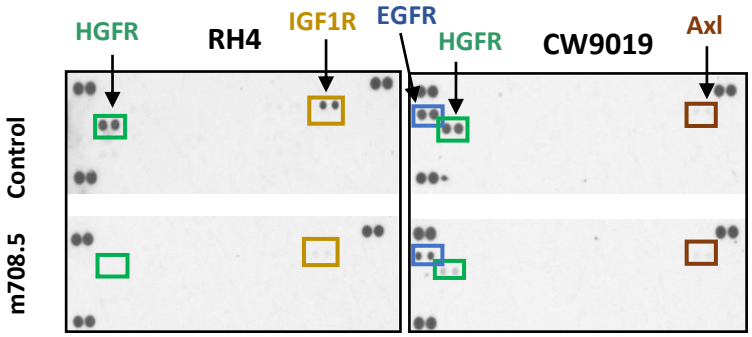

Figure IV. 8. Identification of active RTKs in RMS cell lines. RTK phosphorylation levels (measured by a human phospho-RTK array) in RH4 and CW9019 cells, in basal culture conditions and after m708.5 treatment at 10 µg/ml for 48 h. Note the steady state of HGFR activation in both RMS cell models, and the inhibition of HGFR phosphorylation by m708.5.

To investigate the crosstalk between the IGF and HGF cascades, two different strategies were used to block IGF1R signaling at different levels: m708.5, which blocks the axis at the ligand level, and BMS-754087, which inhibits IGF1R tyrosine kinase activity, while the HGFR axis was inhibited with Tivantinib, a selective drug now in clinical trials. As shown in **Table IV. 2**, the IC50 values for each inhibitor differed between RH4 and CW9019 cell lines.

Target	Inhibitor	RH4 IC50 (95%CI)	CW9019 IC50 (95%CI)
IGF1/2	m708.5	0,44 µg/ml (0,07 to 0,88)	n.a.
IGF1R	BMS-754807	4,2 nM* (0,23 to 1,11)	434 nM* (186 to 738)
HGFR	Tivantinib	510 nM* (0,47 to 0,56)	130 nM* (very wide)

Table IV. 2. IC50 values of each RTK axis inhibitor, calculated by best-fit curves with non-linear regression, four parameters variable slope. * indicates data calculated with constraints after normalization. Not applicable n.a.

We then tested the kinase phosphorylation status in RH4 and CW9019 cells that had been treated with these inhibitors by Western blot. In accordance with the IC50, the inhibition of the IGF1R signaling resulted in stronger inactivation of AKT in RH4 as compared with CW9019 (**Figure IV. 9**). Phosphoprotein levels showed that IGF1R axis inhibition, at either the ligand (m708.5) or the receptor (BMS-754807) level, resulted in AKT and S6 inactivation in RH4 cells. In line with our previous data, RH4 cells display a functional canonical IGF signaling pathway. In contrast, IGF1R inhibition at the tyrosine kinase level (with BMS-754807) inhibited ERK phosphorylation in CW9019, but not in RH4 (**Figure IV. 9**) This result indicates that, in contrast to RH4 cells, IGF1R signals through both ERK and AKT in CW9019 cells. Finally, Tivantinib treatment indicated that HGFR signals through STAT3 and ERK in CW9019, whereas it mainly activates AKT in RH4 (**Figure IV. 9**).

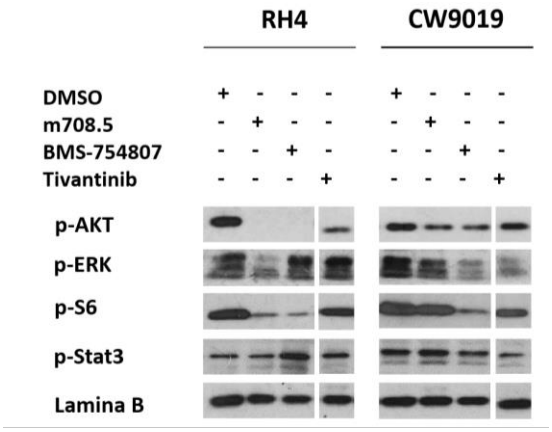

Figure IV. 9. Characterization of active RTK signaling pathways in RMS cell lines. Western blot showing phosphorylation status of AKT (S473), ERK (T202/Y204 T185/Y187), S6 (S240/244) and STAT3 (Y705) in cells treated for 2 h with the signaling inhibitors. RH4 and CW9019 were treated with 10μg/ml m708.5, 500nM BMS-754807 or 500nM Tivantinib (HGFR). Lamin β was used as loading control.

In summary, our data demonstrate that blockade of IGF1 and IGF2 ligands with the m708.5 antibody displayed differential responses in the four RMS cell line models tested. Further, we demonstrated that the elevated IGF1R expression at the cell membrane together with the strong dependency on the IGF1R/AKT pathway explain the exquisite sensitivity of the RH4 cell line among the RMS cell lines to m708.5 treatment.

2 Characterization of the AKT/mTOR and MEK/ERK pathways in RMS

The specificity of m708.5 effects in RH4, but not in other RMS cell line models, together with the steady RTK activation in RMS cell lines, prompted us to the study of downstream signaling molecules in these cell lines, in primary RMS tumors (_T) and their corresponding patient-derived xenografts (_X), and in primary cultures growing as spheres (_S). AKT and MEK are two central nodes for RTK signaling in RMS cells; thus, to characterize the preferential activation of each of these pathways in RMS cell lines and primary cultures, we used proteome profiler human phospho-kinase arrays. This allowed us to study basal activation of 43 proteins kinases in RMS cell lines, primary cultures, and primary tumors.

We selected three cell lines (RD, RH4, and CW9019), three primary cultures (E001_S, A006_S and A001_S) and three primary tumors (E001_T, ERMS24_T, ARMS007_T). RMS samples represented FN-RMS, PAX3-FP-RMS and PAX7-FP-RMS among the nine samples selected. Briefly, E001_T and ERMS24_T samples correspond to the first and second relapse from the same patient, respectively. E001_S primary culture was derived from E001_T. The RH4, A006_S and A001_S cells harbor the PAX3-FOXO1 fusion oncogene. The PAX7-FOXO1 translocation was present in the ARMS007_T primary tumor and CW9019 cells. Further details on the molecular alterations of each of the models described are summarized in the M&M section (**Table III. 2**).

After quantification, only the most representative phosphorylated proteins from the AKT/mTOR, MEK/ERK, and STAT3 pathways were selected for graphical representation in **Figure IV. 10A**. The highest phosphorylation signal in all RMS samples corresponded to **PRAS40** (AKT pathway), indicating **mTORC1 complex activation**. Interestingly, PRAS40 and **JNK1/2/3** show high intense signal across all cell lines and primary cultures as well as in tumors. JNK1/2/3 is a protein that integrates signals from different upstream pathways, including PI3K/AKT and MAPK pathways.

Phosphorylation on S473-AKT has been classically interpreted as readout of AKT activation by mTORC2. RD and E001_S samples displayed high pS473-S473 levels. Of the primary tumors, E001_T presented the highest phosphorylation levels of **S473-AKT** and **TOR**, indicating a strong AKT/mTOR complex activation in this tumor. Moreover, **GSK3 phosphorylation** levels were particularly high in RD and RMS primary models. In regard to the MAPK pathway, **ERK1/2** was substantially **phosphorylated** in RD and the three RMS primary cultures. Of the tumor samples, ARMS007_T presented the lowest level of phospho-ERK1/2. (**Figure IV. 10A**). **Phosphorylated STAT3** was particularly high at PAX7-FOXO1-bearing samples (CW9019 and ARMS7_T). Of note, these cells showed low levels of p-CREB compared to FN-RMS and PAX3-FP-RMS (**Figure IV. 10A**).

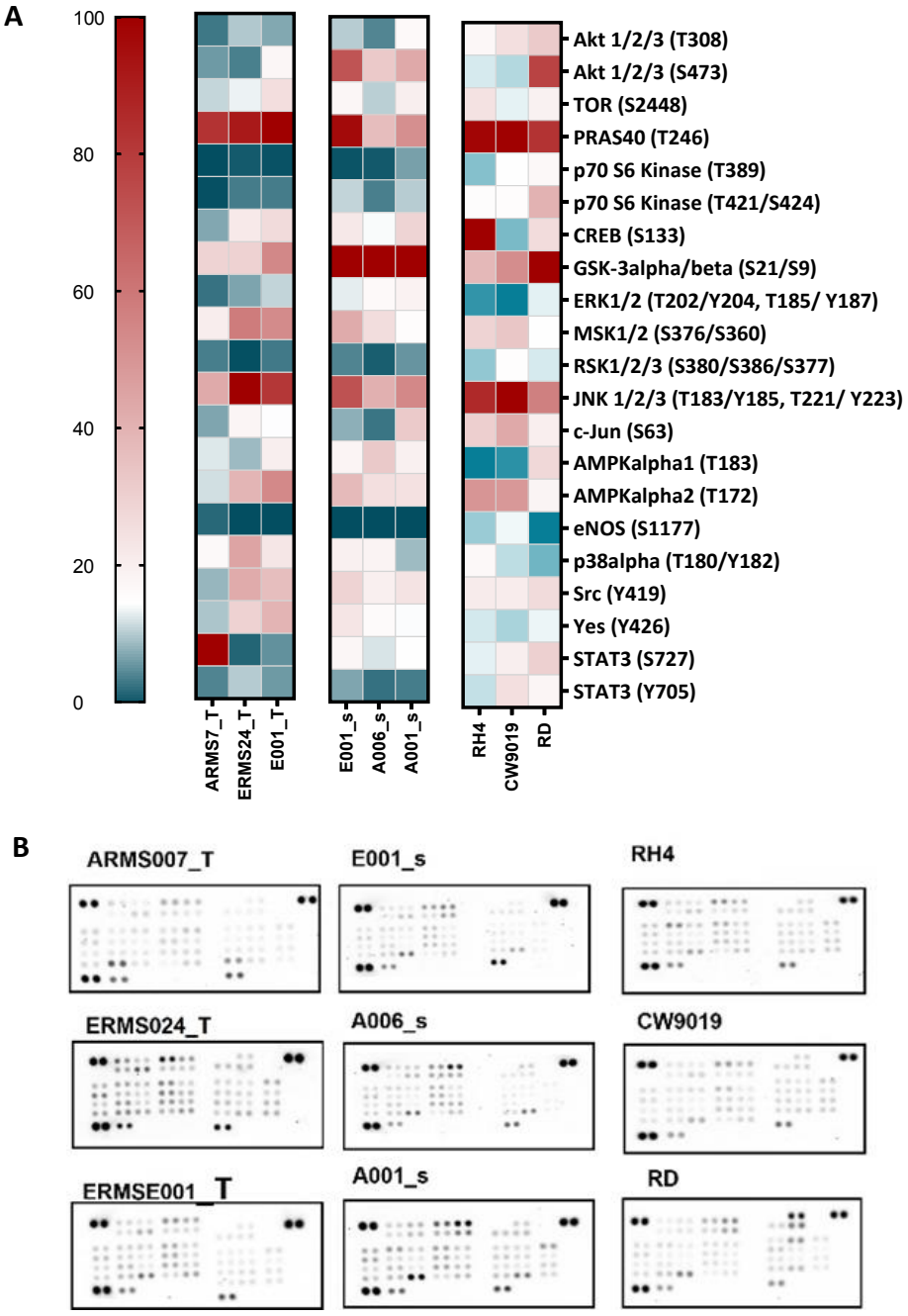

Figure IV 10. Identification of active proteins of the AKT and MAPK signaling pathways in RMS samples. A) Phospho-protein analysis of RMS cell lines and primary cultures and tumors. Heat-maps represent signal quantification of the corresponding blot. Quantitative pixel densities were internally normalized for each sample. For each RMS sample, the highest value is assigned to the most phosphorylated protein and is graphically represented in dark red, whereas poorly phosphorylated proteins for each particular sample are indicated in dark blue. **B)** Membranes of fourty-three human phospho-kinase protein, each one corresponding to a single RMS sample.

In brief, despite the lack of uniformity in AKT activation along RMS samples, proteins from the AKT/mTOR pathway were found constitutively activated in all cell lines, primary cultures, and tumors, as exemplified by the homogenously high signal corresponding to PRAS40 phosphorylation. This result, together with the restoration of the phosphorylation levels of IGF1R signaling molecules after prolonged m708.5 treatments, indicated that the AKT/mTOR pathway is critical for RMS cell survival.

3 AKT blockade by ipatasertib (GDC-0068) as a therapeutic approach for RMS.

3.1 Anti-proliferative activity of the AKT inhibitor ipatasertib in RMS patient-derived models.

To explore the sensibility of the different RMS models to the AKT inhibitor ipatasertib as single therapeutic agent, we used RMS cell lines and RMS patient-derived models. We exposed four RMS cell lines (RH4, CW9019, RD and RH30) and five primary RMS derived from patient-derived xenografts (PDX) (A001_S, A006_S, A007_S and A010_S) and one primary biopsy culture (E001_S) to ipatasertib at concentration range of 0.01 to 10 μM (**Figure IV. 11**). Ipatasertib showed anti-proliferative effects at low sub micromolar range in RH4 cells and A010_S, A006_S, E001_S and A001_S models. Ipatasertib IC50 values for A007_S, and E020_S models were close to 1 μM. **Table IV. 3** displays ipatasertib IC50 values for each RMS model. Cells derived from the neuroblastoma PDX-HSJD-NB-005 (cultured in the same conditions as RMS spheres) were included as negative control since they were completely insensitive to ipatasertib cytotoxic effects.

As previously described, the RH4 cells were sensitive to anti-IGF treatment; here we show that they were also sensitive to the AKT inhibitor, highlighting the relevance of the IGF1R/AKT pathway in this RMS cellular model.

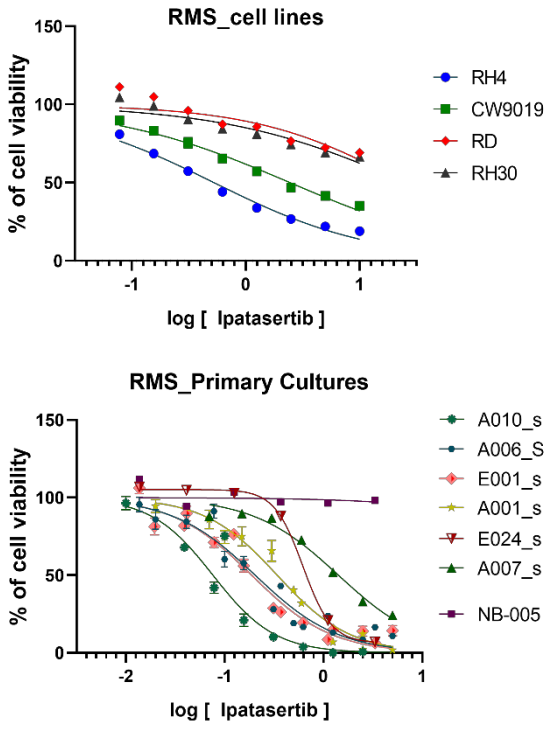

RMS model	Ipatasertib IC50 [95% CI (IC50)]	Molecular characteristics
RH4	0,45 µM [0,41 to 0,50]	PAX3-FOXO1, TP53 mut
CW9019	2,45 µM [2,13 to 2,83]	PAX7-FOXO1
RD	24,63 µM [17,76 to 38,12]	↑NMYC NRAS mut, TP53 mut
RH30	25,68 µM [19,48 to 36,17]	TP53 mut CDK4↑
HSJD-ARMS-001	0,41 µM [0,31 to 0,55]	PAX3-FOXO1
HSJD-ERMS-E001	0,17 µM [0,15 to 0,20]	↑NMYC
HSJD-ARMS-006	0,18 µM [0,15 to 0,22]	PAX3-FOXO1
HSJD-ARMS-010	0,079µM [0,031 to 0,08]	PAX7-FOXO1
HSJD-ARMS-007	1,42 µM [1,08 to 1,90]	PAX7-FOXO1
HSJD-ERMS-024	0,72 µM [0,57 to -]	↑NMYC

Figure IV. 11. Ipatasertib activity in a panel of RMS models. Ipatasertib anti-proliferative effects on primary cultures (upper panel) and cell lines (lower panel). **Table IV. 3. Ipatasertib IC50 values in RMS models** (micromolar range). Cell viability was measured at 72 h by a MTS assay, and IC50s were calculated using Graphpad Prism version 7.

Constitutive ERK activation has been previously observed in some RMS cell models [195, 218]**.** ERK pathway, among other pathways, crosstalks with AKT signaling at more than one node to regulate cell survival. We therefore investigated changes in kinase phosphorylation that could be triggered by ipatasertib blockade. Protein extracts from E001_S cultures treated with ipatasertib for 6h were evaluated for the phosphorylation of twenty-four phosphorylated (active) kinases. According to the expected ipatasertib-induced blockade of AKT in the phosphorylated (although inactive) form, AKT isoforms were the most phosphorylated kinases in ipatasertib treated cells. In addition, an incipient phosphorylation of RSK and ERK (red arrow) was observed (**Figure IV. 12**), although ERK phosphorylation was not maintained past 24h of ipatasertib treatment (see below **PK studies, Results Section 2.3**).

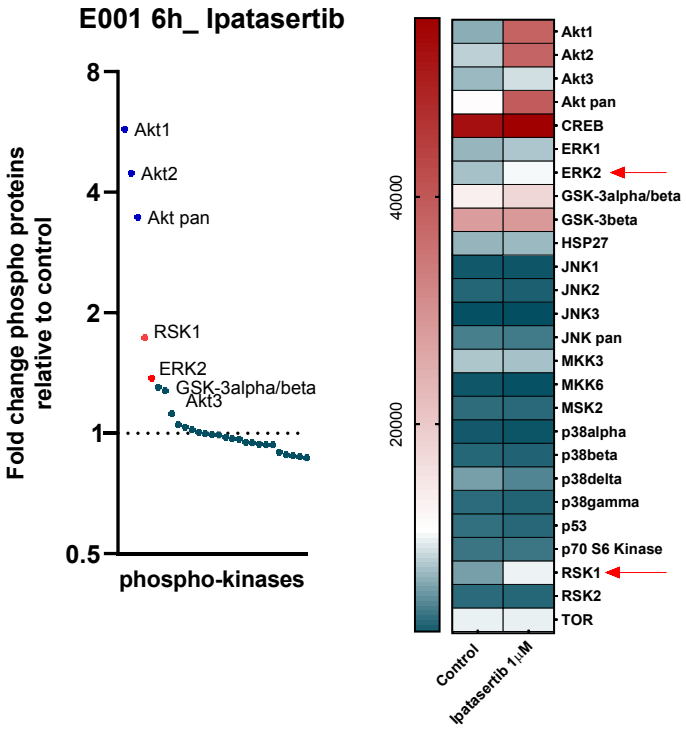

Figure IV. 12. Early changes in MEK/ERK phosphorylation in cells exposed to ipatasertib. E001_S cells were treated with ipatasertib (1 µM) for 6h. Protein extracts were analyzed for phosphorylated proteins of the MEK/ERK pathway included in the array ARY002B. Observe the activation of ERK2 and RSK1. Left panel, paired fold-change analysis of treated *vs.* control cells. In grey, phosphorylated proteins not affected by ipatasertib treatment at this time point.

Therefore, the brief activation of ERK and RSK induced by ipatasertib suggested the existence of compensatory mechanisms in the treated cell to overcome AKT inhibition.

3.2 Ipatasertib treatment induces tumor regression *in vivo* in a subgroup of RMS patient-derived xenografts.

Next, ipatasertib efficiency was tested *in vivo* in eight different RMS-PDXs from our institution. Briefly, PDX models from our institution were generated by subcutaneous implantation of freshly resected tumor biopsies as tumor pieces, or tumoral cell suspensions injection, in case of liquid biopsies (pleura or bone marrow) in immunodeficient NOD/SCID mice. Tumor tissues were expanded and maintained *in vivo* until implantation.

To validate the genetic and transcriptomic characteristics as well as the histopathological features of the human biopsy, we performed the corresponding validation by qPCR to detect the fusion gene when proceeds and copy number variants (CNVs) analysis of NMYC in the corresponding models (see M&M). We also used RNA sequencing approaches to confirm concordance of gene expression profiles between tumor donor and PDX and immunohistochemistry analysis to detect lineage-specific markers (see **Figure IV. 29**).

The expression of human tissue marker and MYOD1 was checked in the tumors studied, both treated and controls, with each pass to a new individual or when collecting the tumors at the end of the study. Example images of the different control tumors included in this study are shown in **Figure IV. 13**. The histological comparison study of some of these PDX with their original patient sample was studied by Dr. Angel Montero's team [219].

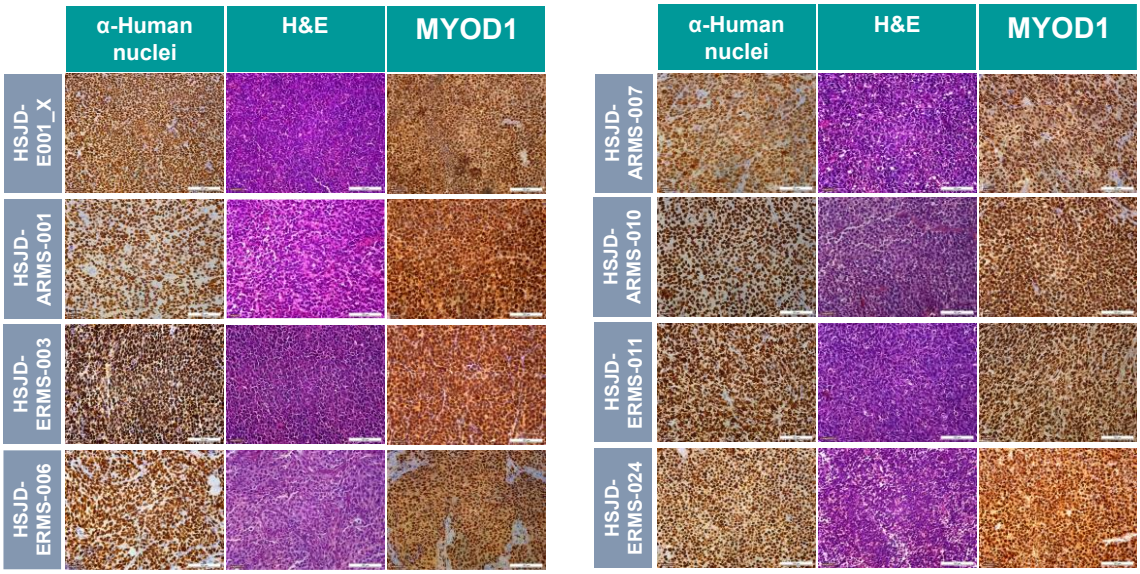

Figure IV. 13. Immunohistochemistry of human nuclei, MYOD1, and Hematoxylin/eosin in HSJD-RMS PDX included in this thesis. White bar indicates the scale bar of 100µm. Observe nuclear positiveness for MYOD1 and anti-human nuclei in all RMS PDX.

For ipatasertib efficacy in *in vivo* studies, 4-6–week-old mice were subcutaneously implanted with 3 × 3 mm^3 of fresh tumor pieces from the tumor sample or the established PDX. When tumors reached 150-350 mm^3, they were

randomly divided into control and treated groups. At the maximum tolerated dose (MTD, 100 mg/kg/day), ipatasertib significantly reduced or delayed the subcutaneous tumor growth in all tested PDX models (**Figure IV. 14**). However, we could differentiate two subgroups of RMS-PDXs based on their responsiveness to ipatasertib *in vivo*. One group, which includes E001 xenograft, ERMS-011, ARMS-010 and ARMS-006 RMS-PDX, was characterized by tumors reduced by more than 50% from the tumor-initiating-volume at two weeks of treatment (ten doses) (**Figure IV. 15**). The second group was characterized by continued growth on ipatasertib treatment (ERMS-024, ARMS-007 and ARMS-001), or reduction in tumor volume inferior to 50% from initial tumor volume (ERMS-003).

After completing four weeks of treatment, treatment was discontinued and animals were maintained until tumors reached 2000 mm^3. In some models, like ERMS-E001 and ERMS-011, we administered only two weeks treatment for two reasons: (i) tumors were almost completely eradicated, and (ii) we aimed to study whether recurrent tumors responded to a new cycle of ipatasertib. In all RMS-PDX, drug discontinuation resulted in tumor regrowth, even in the best ipatasertib-responsive models. By the end of treatment, ipatasertib slowed tumor growth in all the treated mice, even in those RMS models less sensitive to ipatasertib, when compared to control -untreated- group. Note that ERMS-003 control tumors did not grow following an exponential growth phase, suggesting a problem in tumor initial engraftment. Therefore, ERMS-003 data should be taken with caution.

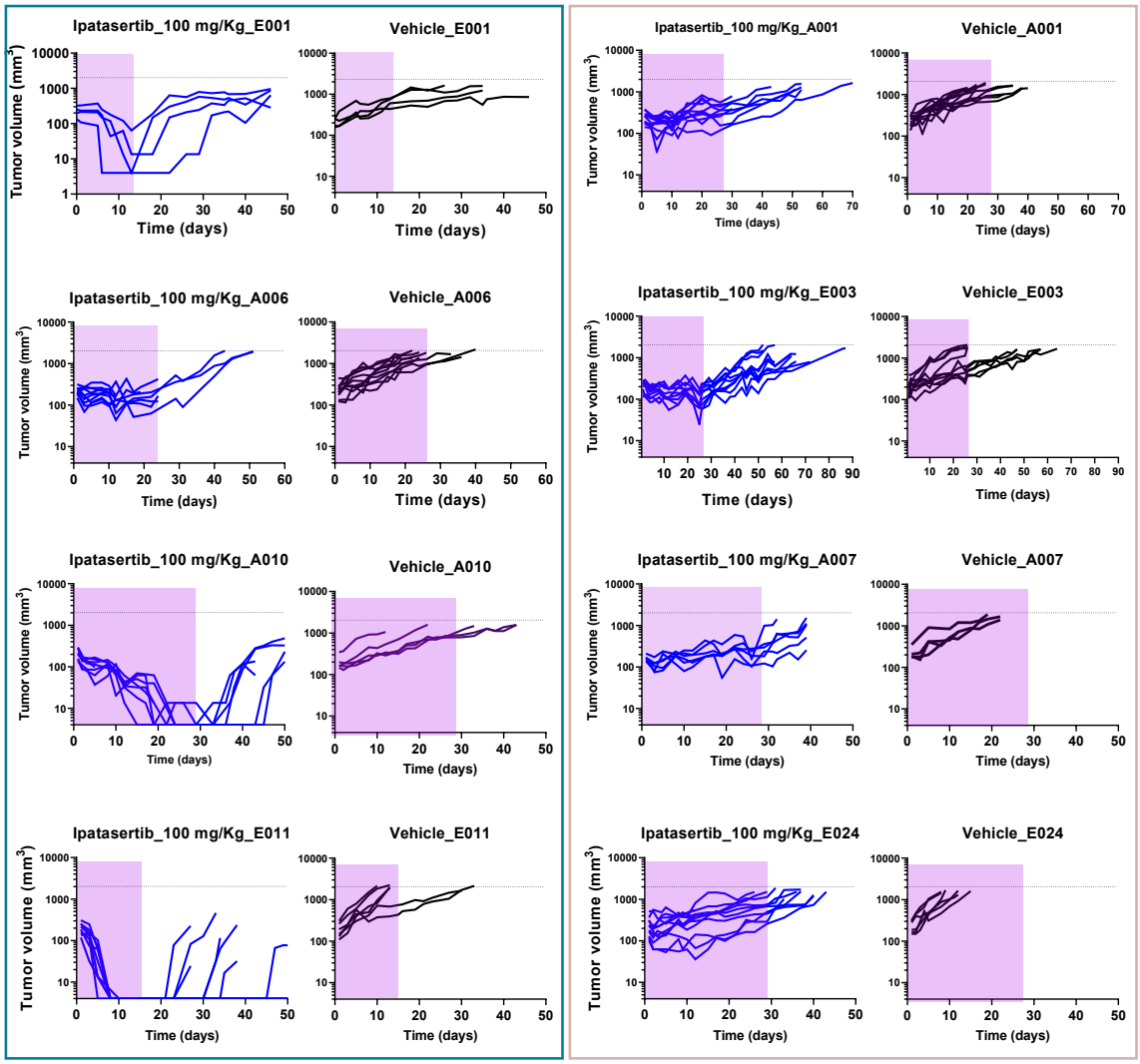

Figure IV. 14. Efficacy of ipatasertib administrated at 100 mg/kg orally (PO) and daily (QD) in eight RMS-PDX. Tumor growth curves of individual tumors are shown for vehicle and ipatasertib groups. Highlighted in purple the time when animals were receiving treatment. Data came from one single experiment for each model, except for ARMS-006, in which two independent experiments were performed. Number of treated animals: E001_xenograft, n = 4; ARMS-A001, n = 8; ERMS-003, n = 7; ARMS-006 n = 10; ARMS-007, n = 8; ARMS-010, n = 6; ERMS-011 n = 6; and ERMS-E024, n = 6.

After ten doses of ipatasetib at 100 mg/kg/day, a complete response was observed in E001_xenograft, ERMS-011 and ARMS-010 mouse models (**Figure IV. 15**). In ARMS-006 mice, the tumor volume was reduced by more than 50% in half of the ipatasertib-treated mice, while the other half reached stable disease. In contrast, none of the ipatasertib-treated mice of the ERMS-003, ARMS-001, ARMS-007 or ERMS-024 models achieved complete response. The *in vivo*

efficacy data of ipatasertib were consistent with their corresponding *in vitro* IC50 data, and RMS cells with lower IC50 predicted a better response *in vivo*. The agreement between *in vitro* and *in vivo* data confers robustness to the predictive capacity of the *in vitro* models in this system.

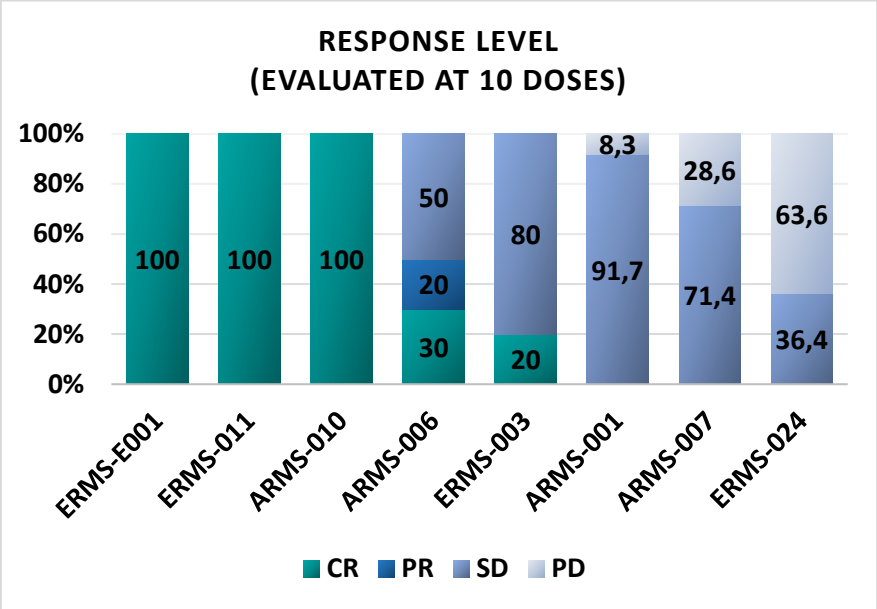

Figure IV. 15. Percentage of tumor response, evaluated after 10 doses of ipatasertib at 100 mg/kg administered orally, once a day (PO and QD). Response was classified as: complete remission (CR: tumor volume: <100 mm^3 + reduction >50%), partial response (PR: tumor volume ≥100 mm3 + reduction ≥ 50%), stable disease (SD: reduction < 50% o increase ≤ 25%) and progressive disease (PD: reduction <50% o increase >25%). ERMS-E001 (n=10, from two independent experiments), ARMS-001 (n=12), ERMS-003 (n=10), ARMS-006 (n=10, from two independent experiments), ARMS-010 (n=7), ARMS-007 (n=7), ERMS-011 (n=9), and ERMS-E024 (n=11); n indicates number of treated tumors in each PDX.

In order to explore the potential clinical translation of this study, we explored more feasible dosing, lower than MTD. With this aim, and to reduce potential toxicities, one-half and one-quarter of the MTD dose were tested in five RMS PDXs. Indeed, 25 mg/kg is a feasible dose to translate into the clinic. Ipatasertib presented a dose-dependent effect in RMS models. As shown in **Figure IV. 16A**, dose reduction conditioned the response in many RMS tumors: at 50 mg/kg and 25 mg/kg ipatasetib slowed down the growth rate of E001_xenograft, ARMS-006, ARMS-010, and ERMS-011 PDXs. Moreover, at feasible clinical doses, ipatasetib treatment achieved complete response in 80% ERMS-011 tumors (see

next section, **Figure IV. 26**). Also, in this particular PDX, re-challenge administration of ipatasertib after tumor regrowth demonstrated activity (see below **Figure IV. 17**). Therefore, ipatasertib is effective in blocking tumor progression in a dose-dependent manner. Kaplan-Meier survival curves for ARMS-010 and ERMS-024 models are shown in **Figure IV. 16B**, as representative examples among the different RMS models tested. At 100 and 25 mg/kg doses, ipatasertib significantly slowed tumor growth and increased survival time in both models. At the highest ipatasertib doses, the mean survival time for ARMS-010 mice was extended 71 days (mean survival time for control mice, 38 days), and to 35 days for the mice carrying the aggressive ERMS-024 PDXs (versus 10 days of the control group).

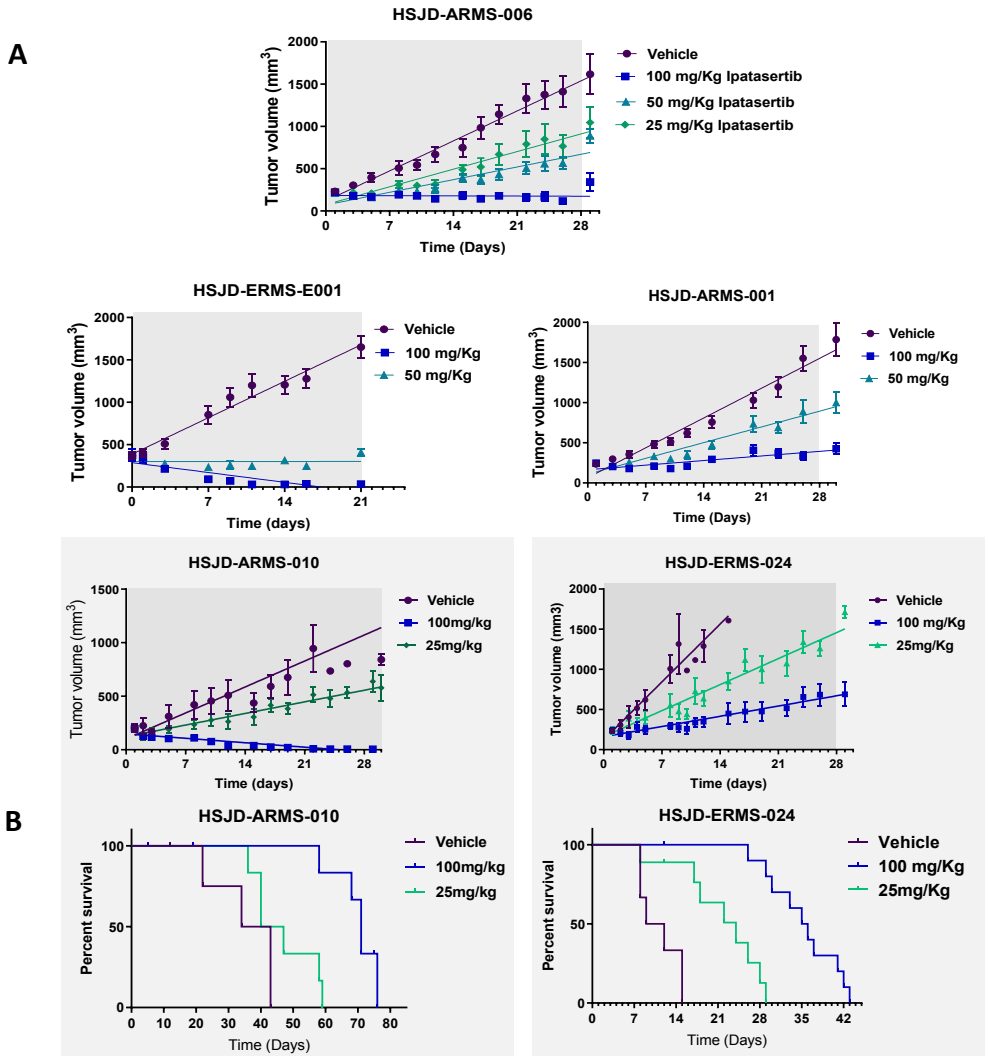

Figure IV. 16. Ipatasertib dose dependent effects in RMS models A) Dose-response plots for tumor volumes in HSJD-RMS-PDX models. Fitted tumor volume to a simple linear regression for

each PDX model comparing vehicle group (in dark purple) and ipatasertib-treated tumors (100mg/kg in dark blue, 50mg/kg in light blue and 25mg/kg in turquoise). Tumor volume is shown until the end of treatment. Data from vehicle and 100mg/kg treated tumors came from previous graph except for E001_s, in which a new independent experiment is represented. Note that doses of 25 or 50 are below the maximum dose tolerated. **B)** Kaplan-Meier survival curves for tumor-bearing HSJD-ARMS-010 and ERMS-024 PDXs after each treatment, with 100mg/kg or 25 mg/kg of ipatasertib. Log-rank statistic with Bonferroni correction test was used to compare statistical significance between treatment groups (p= 0,4704 and p= 0,0126* in Vehicle *vs.* 25mg/kg, and p=0,0054* and p=<0,0001* in Vehicle *vs.* 100mg/kg, in ARMS-010 and ERMS-024, respectively). Survival event was reported at 1500 mm^3 tumor size.

As described above, tumor regression required ipatasertib sustained administration, otherwise tumors re-emerged. To investigate possible tumor escape mechanisms, ipatasertib was re-administered to ERMS-011 mice in which the tumor regrew up to 150-300 mm^3. As seen in **Figure IV. 17**, re-challenge with ipatasertib reduced the tumor volume two more times after the initial treatment, extending the survival of the ipatasertib-treated mice to 100 days.

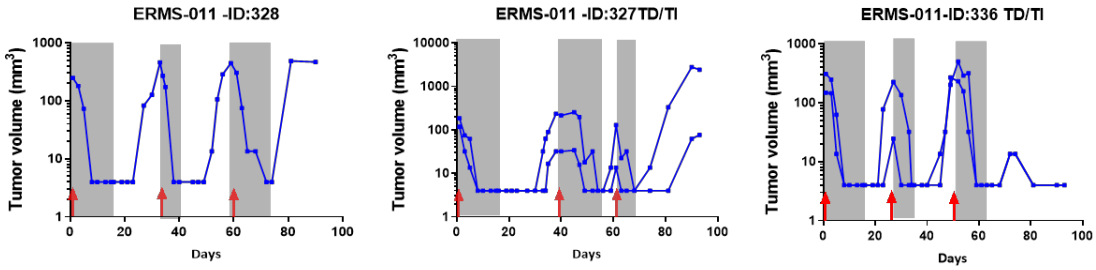

Figure IV. 17. Ipatasertib re-challenge in regrowing tumors of the ERMS-011 model. Individual tumor volume in ipatasertib-treated mice (blue). Each plot represents an individual mouse with tumors in the right (TD) and left (TI) flanks. The first plot indicates an animal with only one subcutaneous tumor, whereas second and third plots show one animal with tumors in each flank. ID is the identification for mouse.

It is important to note that side effects of ipatasertib were mainly observed at the highest dose, of 100mg/kg. Animal weight loss, evaluated as a readout of toxicity, was observed in 5-10% treated mice (≥15% of weight loss), particularly during the first week of ipatasertib administration. More infrequently, at maximal and

sequential ipatasertib doses, abdominal distension was also observed in treated mice. Necropsy of these animals revealed that this effect was due to air retained in the intestine. No or one mouse out of the total animals treated with MTD in each experiment were excluded because of ipatasertib-associated toxicities.

3.3 Ipatasertib pharmacokinetics (PK) and pharmacodynamics (PD) in mice harboring FP- or FN-RMS PDX models

The observed differential anti-tumor efficacy of ipatasertib in the eight RMS models tested could be related to drug bioavailability. To test this hypothesis, ipatasertib pharmacokinetics in plasma and tumor samples was studied in embryonal (HSJD-ERMS-E011; complete remission upon ipatasertib treatment) and alveolar (HSJD-ARMS-006; partial responses to ipatasertib) RMS-PDXs. After a single ipatasertib administration, either at 100 mg/kg or at 25 mg/kg, samples were collected at different time points up to and analyzed by LC-MS/MS by the core facility at the Universitat Autònoma of Barcelona.

Concentration–time curves showed that ipatasertib arrived at the tumor site at concentrations high enough to inhibit AKT signaling and to effectively slow tumor growth (**Figure IV. 18**). Ipatasertib was rapidly distributed and accumulated in the tumor tissue. This data confirms the oral availability of ipatasertib, which reached intratumoral active concentrations, in agreement with efficacy results observed *in vivo*. Ipatasertib concentrations in plasma suffered a rapid decay corresponding to the elimination phase after reaching the peak concentration. At 24 h after administration of the 25 mg/kg dose, ipatasertib intratumoral concentrations were close to 1µM at 100 mg/kg dose, ipatasertib concentrations remained high (above 1 µM) in both PDX models (**Figure IV. 18**). These differences in sustained concentrations paralleled the ipatasertib dose-dependent effects observed in efficacy studies.

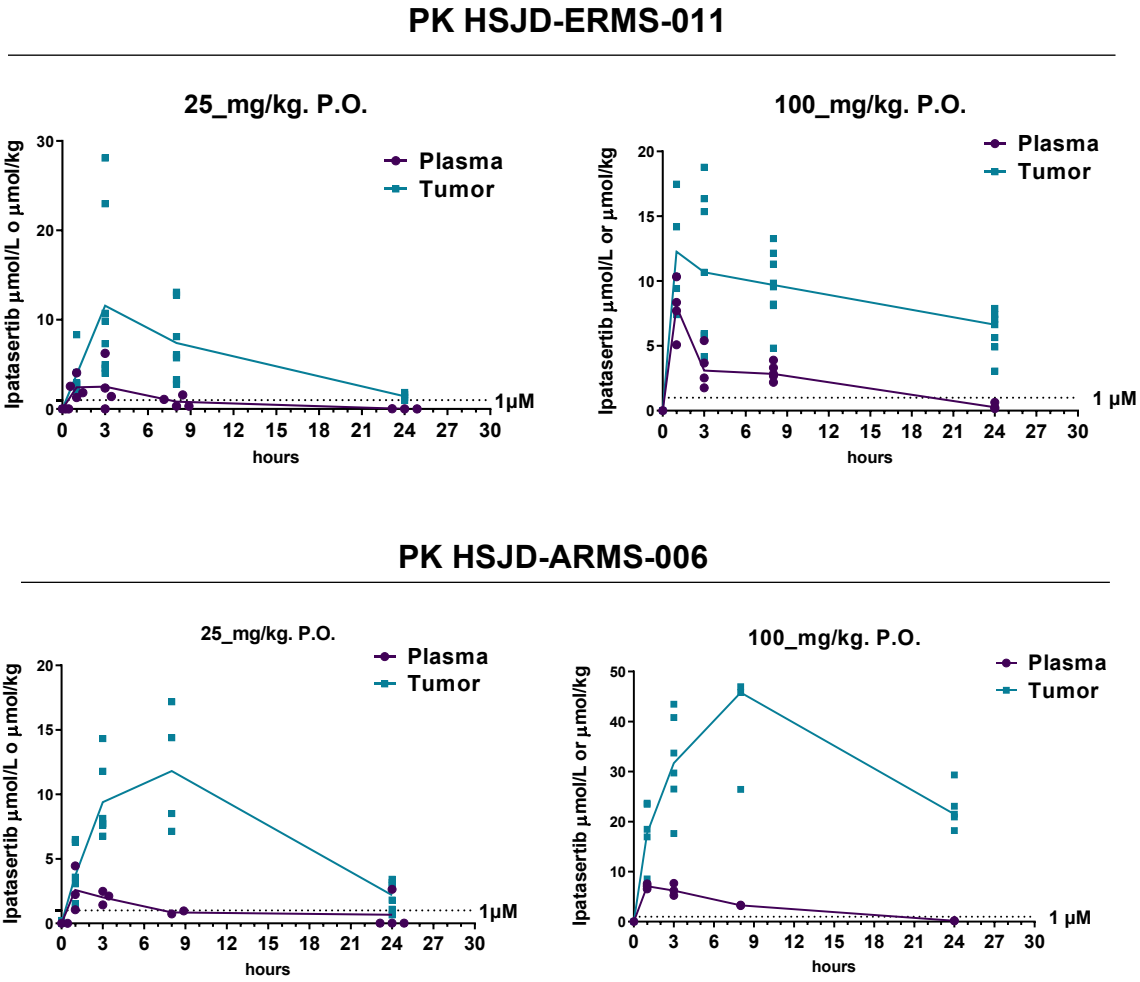

Figure IV. 18. In vivo ipatasertib pharmacokinetics in HSJD-ERMS-011 and HSJD-ARMS-006 tumor-bearing mice. Plasma and tumor ipatasertib concentrations in RMS PDX over time (0-24 h). For reference, the value of 1 uM is indicated in all graphs. AUC (area under the curve), Cmax (maximum observed concentration) and Tmax (the time of Cmax) in plasma and tumor are shown in **Table IV. 4** for ERMS-011 and ARMS-006 bearing mice.

Table IV. 4. PK parameters of ipatasertib following a single dose in RMS PDX bearing mice.

HSJD-ERMS-011	specimen	AUC 0–24 (µmol•h/L) or (µmol•h/Kg) ± Std.Error	Cmax (µM)	Tmax (h)
25 mg/kg	Plasma	21 ± 8,9	3,32	3
	Tumor	135 ± 43	11,56	3
100 mg/kg	Plasma	57,48 ± 7,5	7,87	1
	Tumor	207,8 ± 30,9	12,72	1

HSJD-ARMS-006	specimen	AUC 0–24 (µmol•h/L) or (µmol•h/Kg) ± Std.Error	Cmax (µM)	Tmax (h)
25 mg/kg	Plasma	25 ± 11	2,58	1
	Tumor	180 ± 42	11,8	8
100 mg/kg	Plasma	69 ± 3,4	7,06	1
	Tumor	735 ± 106	39,74	8

The area under curve (AUC) is an indicator of total drug exposure over time. As expected, both AUC and the maximum observed concentration (Cmax) were higher at 100 mg/kg than at 25 mg/kg in both PDXs (**Figure IV. 18**). Drug accumulation phase was longer in ARMS-006 mice, in which the time corresponding for peak concentration, or Tmax, in the tumor was 8 h, while in ERMS-011 Tmax was at 1 h (25 mg/kg dose) and 3 h (100 mg/kg dose), thus showing an earlier decay phase. This curve profile allowed maintaining intra-tumoral levels in the HSJD-ARMS-006 model much higher than its corresponding IC50 (0.18 µM), both at 25 and 100 mg/kg ipatasertib doses within 24 h after administration, ensuring prolonged ipatasertib activity.

Phospho-S6 measured by immunohistochemistry (IHC) was used as a pharmacodynamic marker in HSJD-ERMS-011 (**Figure IV.19B**) and HSJD-ARMS-006 tumors (**Figure IV. 19A**) from mice treated with one single dose of ipatasertib. Compared to untreated controls, the strongest reduction in phospho-S6 signal was observed three hours after ipatasertib treatment, and phospho-S6 levels were restored at 24 h. Moreover, **cleaved PARP levels**, a readout of the apoptotic effect, significantly increased 24 h after single dose of 100 mg/kg ipatasertib in ERMS-011 (**Figure IV. 19B**) and ARMS-006 (**Figure IV. 19A**) tumor samples. In addition, ERMS-011 PDX tumors collected at 3 and 24 h after single dose of ipatasertib were analyzed for phosphoprotein levels by a phosphokinase array. Of the forty-three different intracellular kinases, ERK1/2 and AKT were the only ones upregulated (as phosphorylated proteins) upon treatment (**Figure IV. 19C**). As mentioned before, AKT phosphorylation upon ipatasertib treatment does not reflect AKT activation, given the ipatasertib mechanism of action that retains the phosphorylated but kinase inactive form of the AKT protein. Indeed, ipatasertib treatment induces downregulation of CREB phosphorylation at both 3h and 24h after treatment, reflecting effective AKT/mTOR signaling pathway inhibition. In contrast, ERK1/2 activation confirms the existence of an emerging escape mechanism that could be triggered early, as shown by the *in vitro* results of E001_S cells treated with ipatasertib for 6 h.

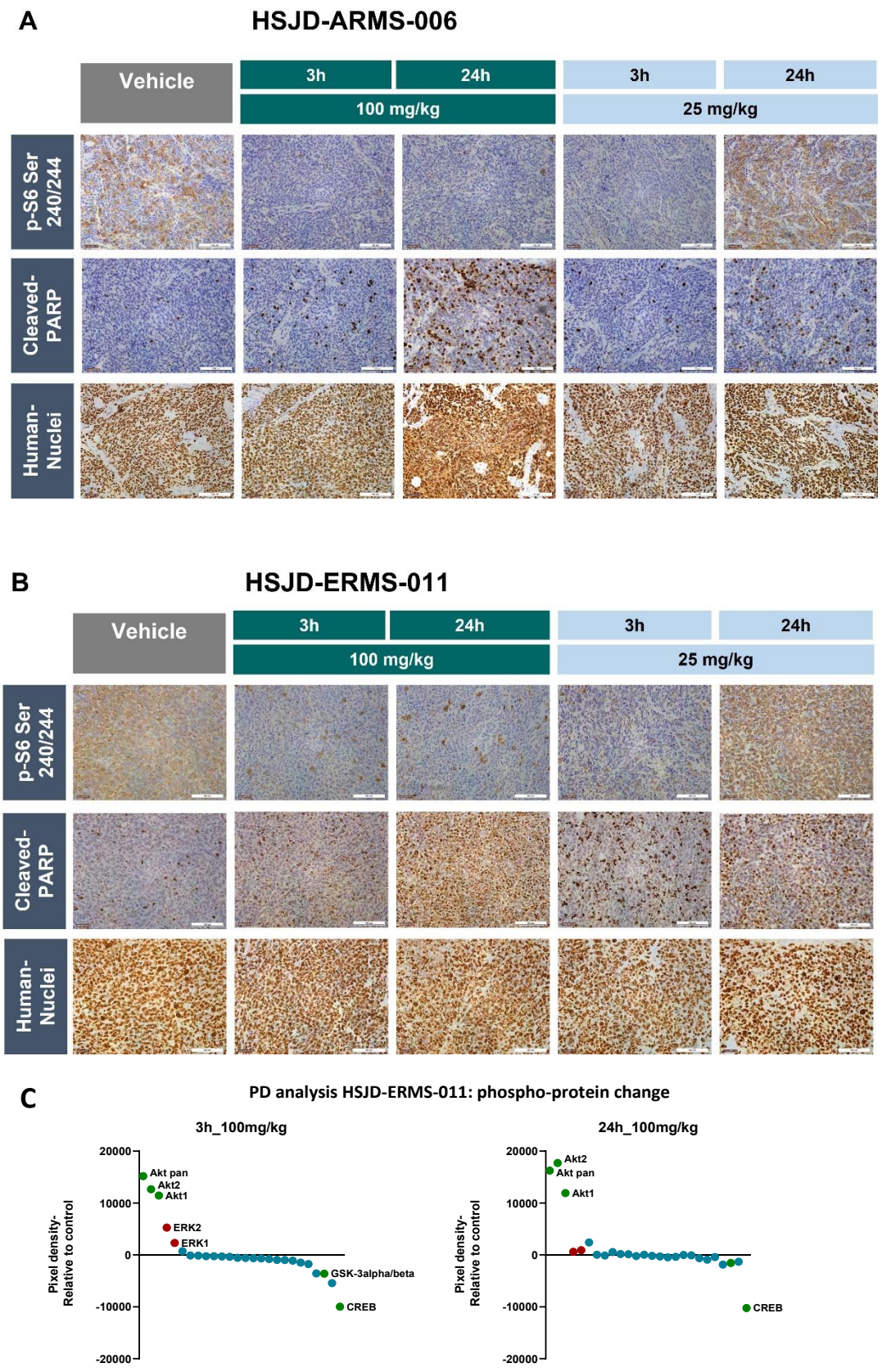

Figure IV. 19. Pharmacodynamic changes at 3 h and 24 h after a single ipatasertib dose. A) and **B)** Immunohistochemistry for p-S6(240/244), Cleaved-PARP and human nuclei in control and treated tumors in HSJD-ARMS-006 and HSJD-ERMS-011 at 100 mg/kg and 25 mg/kg. One representative

tumor for each condition is shown. Pictures, 20× magnification. **C)** Protein phosphorylation levels (measured by a proteome profiler phospho-MAPK array) in tumors from 100 mg/kg ipatasertib-treated mice. Data represent phosphorylated proteins in tumors from ipatasertib-treated mice referred to tumors from vehicle-treated mice. Note the initial increased in ERK1/2 phosphorylation 3 h after treatment, but restoration to baseline values at 24 h. Accordingly to ipatasertib mechanism of action, AKT phosphorylation was detected, but phospho-CREB, the most significantly inhibited target, was drastically reduced at the two time points evaluated.

Taken together, 25 mg/kg as well as 100 mg/kg doses were sufficient to achieve effective Ipatasertib intratumoral concentrations and to fully inhibit the AKT/mTOR pathway and cause cell death. However, only the 100 mg/kg dose sustained drug concentration enough to fully inhibit the AKT pathway at 24 h. Our data suggests that the 25 mg/kg dosing would require ipatasertib administration every day, whereas the 100 mg/kg dosing administration could be spaced out at least every other day since S6 inactivation was persistent and the intratumoral concentration of the active drug remained over 1 μM for more than 24 h.

3.4 Dual blockade of the AKT/mTOR and MEK/ERK signaling in *in vitro* RMS culture models.

These *in vitro* and *in vivo* data suggested the existence of two different RMS subgroups on the basis of AKT or MEK functional dependency. In order to identify these, we analyzed RMS selective sensitivities to specific AKT and MEK drug inhibitors. RMS cell lines and primary models were treated with the AKT inhibitor ipatasertib (1 μM) alone or in combination with the MEK inhibitor trametinib (0.1μM or 1 μM), and protein extracts were collected 24 h after treatment. To assess drug specificity and effective inhibition of downstream cascades, phosphorylation of surrogate proteins for each pathway was analyzed by western blot. Phosphorylation of AKT at S473 and T308 was used as readout for AKT activity, ERK phosphorylation for MEK activity, and phosphorylation of PRAS40 and S6 ribosomal protein as surrogate readouts for mTOR activity.

As observed previously, RMS cell lines displayed constitutive phosphorylation of PRAS40 and S6 ribosomal protein (**Figure IV. 20A**). In addition, different profiles

of response to the inhibitors, especially among cell lines, could be observed. Accordingly, to the reported drug inhibitory mechanism, cell exposure to ipatasertib increased phospho-AKT levels in the three cell lines tested [178]. Ipatasertib monotherapy fully inhibited PRAS40 and S6 in RH4 cells, while partially reduced or did not affect the phosphorylation levels of these proteins in CW9019 and RD cells, respectively. On the other side, trametinib monotherapy did not affect PRAS40 nor S6 phosphorylation in any RMS cell line. However, ipatasertib and trametinib combined resulted in reduced S6 and PRAS40 phosphorylation levels in the three RMS cell lines, highlighting the universal and critical crosstalk of AKT and ERK pathways in RMS. Inhibition of the activation of mTOR surrogate markers was paralleled by an increase in cleaved PARP in RD cells, suggesting an apoptotic effect. Inhibition of ERK phosphorylation was only achieved when trametinib was added, confirming the selectivity of the drugs (**Figure IV. 20A**).

Ipatasertib effect in RMS primary cells was similar to RH4 cells, and inhibited S6, PRAS40 and GSK3 phosphorylation, while trametinib did not affect their activation. Interestingly, although cleaved PARP could be detected in both primary culture models upon single ipatasertib treatment, ipatasertib and trametinib combination further increased c-PARP levels in A006-s and A001_S cells, as observed in the cell lines (**Figure IV. 20B**).

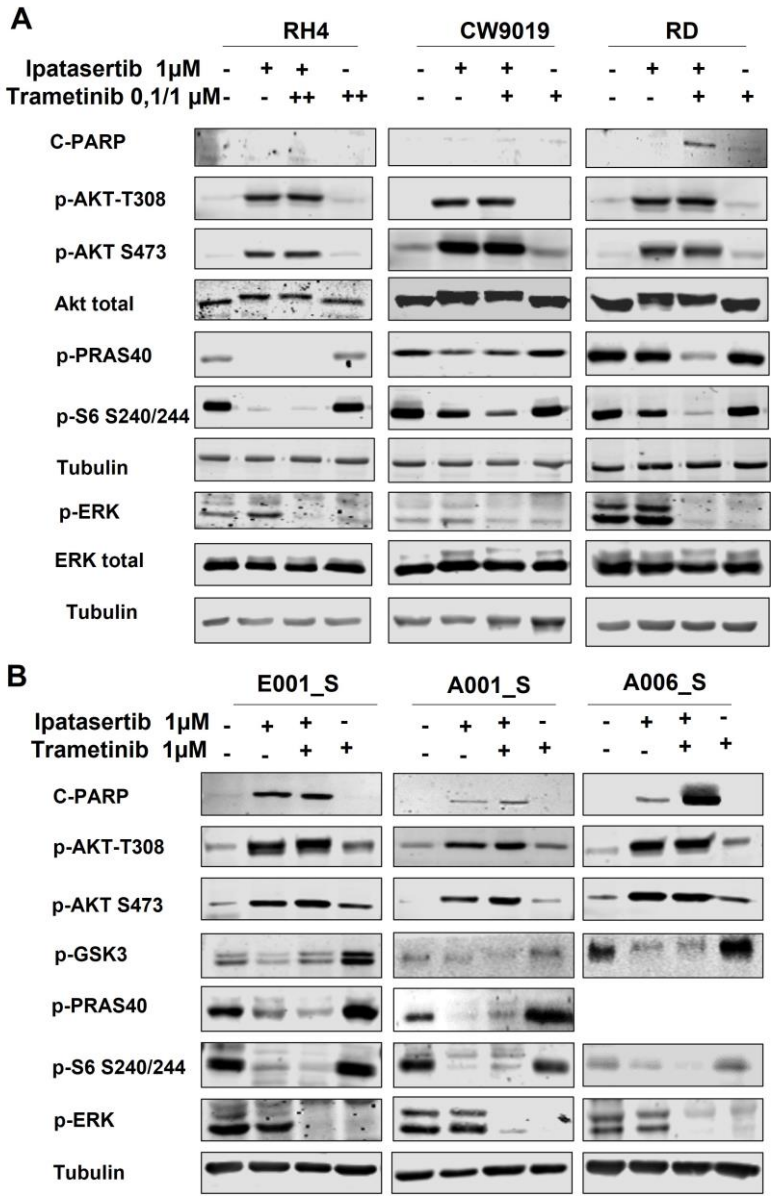

Figure IV. 20. Phosphorylation of proteins in the AKT and MEK pathways and c-PARP in RMS cultures treated with ipatasertib (AKT inhibitor) and trametinib (MEK inhibitor). Western blot of phospho-proteins in RMS cell lines **(A)** and primary cultures **(B)** treated with ipatasertib and trametinib for 24 h. Tubulin was used as loading control.

Functionally, inhibition of AKT and MEK revealed two RMS subgroups on the basis of their differential sensitivity to ipatasertib or to trametinib. The ipatasertib sensitive subgroup included RH4, A001_S, A006_S and E001_S cells, which displayed ipatasertib IC50 values ranging from 0.52μM in RH4 to 0.17 μM in E001_S (**Table 2 Section 2.1**). Trametinib IC50 values differed nearly three orders of magnitude among RMS cells lines (**Table IV. 5**), ranging from

micromolar concentrations in RH30 and RH4 cells to nanomolar range in RD and CW9019. In the latest, cultures treated with nanomolar concentrations of trametinib resulted in substantial amounts of dead cells. In contrast, trametinib resistant models such as RH4, RH30, A001_S and E001_S tolerated concentrations higher than 1 µM for 72 h without any significant cell viability effect. Interestingly, the ipatasertib-sensitive RMS models corresponded to the trametinib-resistant models.

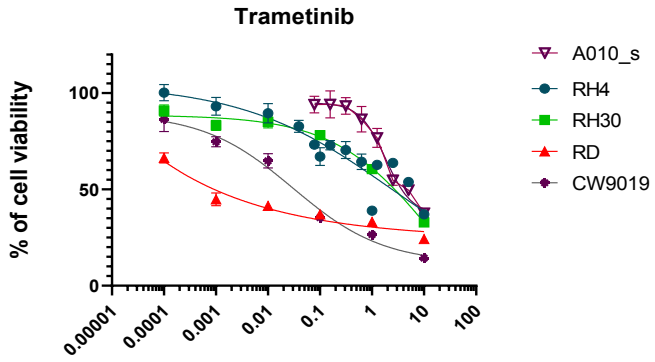

Cell line	Trametinib IC50
RH4	2,33 µM
RH30	2,29 µM
RD	17,55nM
CW9019	33,40 nM
A010_s	1,81 µM

Figure IV. 21. Anti-proliferative effects of trametinib in RMS cell lines and A010_S primary culture. Cell viability was measured at 72 h by MTS assay and IC50s were calculated using Graphpad Prism version 7. **Table IV. 5. Trametinib IC50 values in RMS models** (micromolar range).

To determine whether the dual blockade of both the AKT and MEK pathways sensitizes ipatasertib-resistant cells or whether trametinib had a synergic effect in ipatasertib-sensitive cells, both inhibitors were combined. **Figure IV. 22A** shows cell viability data for RMS cell lines treated with low or high concentrations of trametinib as single agent (light and dark red) or combined (light and dark grey) with 0.625 µM ipatasertib (blue bars). In these experiments, ipatasertib was fixed at a suboptimal concentration, lower than that required to achieve the best inhibitory effect, in order to evaluate potential synergism in the anti-proliferative response after adding trametinib at different concentrations. In RMS cell lines, combined treatment with trametinib/ipatasertib caused a higher cell viability reduction than each drug individually. Moreover, this combination drastically decreased RD cell viability when compared to the effect of single agents. Indeed, in these cells, highly resistant to ipatasertib (83% cell viability), the addition of trametinib at doses as low as 1nM reduced cell viability to 16%, while the effect of trametinib alone was 48%. This data suggested a synergistic effect of AKT and

MEK inhibitors for RD cells. Treatments with increasing concentrations of ipatasertib combined with fixed doses of trametinib in RMS primary cells further confirmed the synergistic effect of AKT plus MEK inhibitors. Primary RMS cells responded to ipatasertib as single agent in a dose dependent manner, which was enhanced when combined with trametinib at a dose that did not affect cell viability when used as single agent (1 μM) (**Figure IV. 22B**).

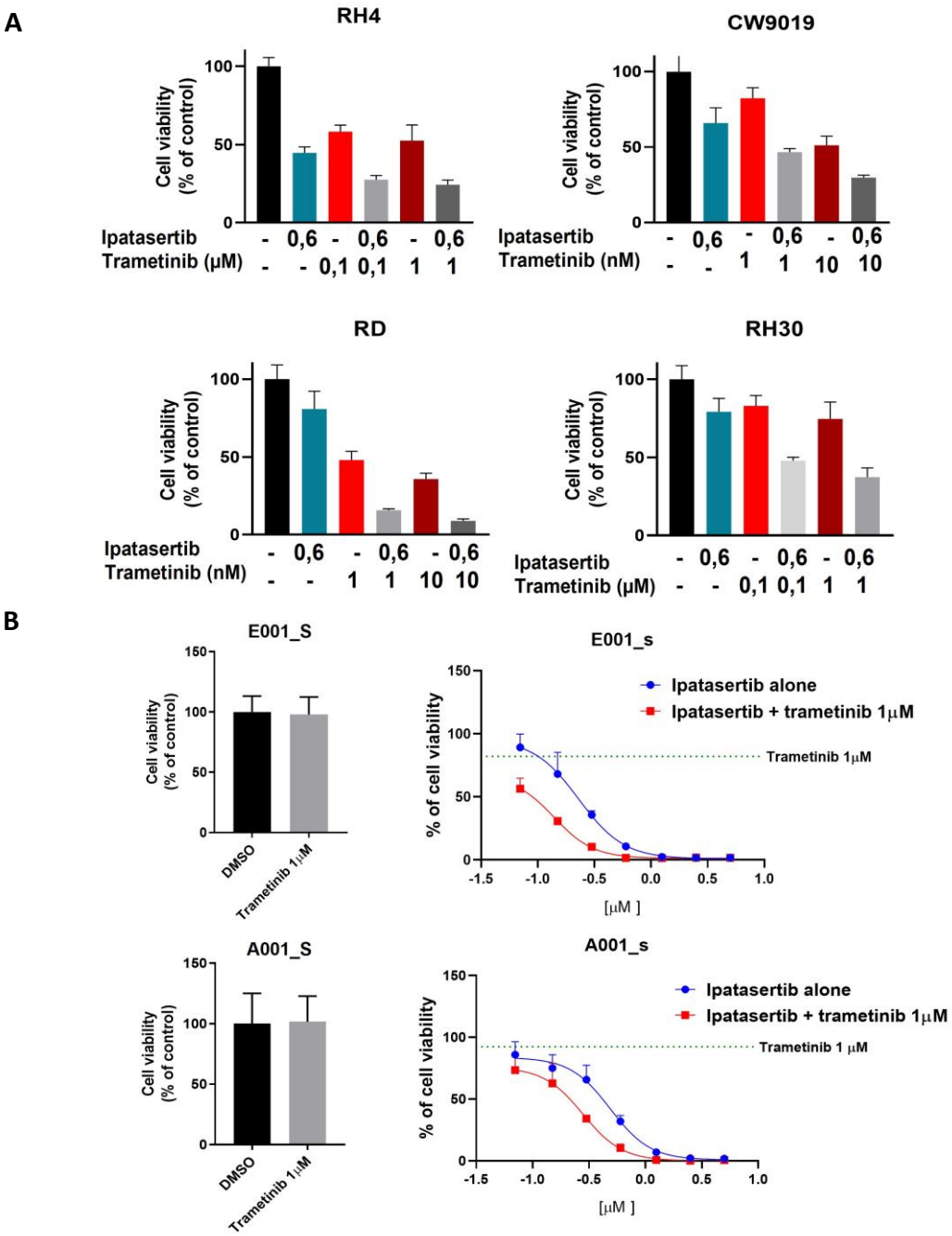

Figure IV. 22. Effect of combined ipatasertib and trametinib treatments for 72 h on RMS cell viability. A) Comparative analysis of ipatasertib (blue) and trametinib (red) effects on RMS cell line viability, determined by MTS assays. Fixed ipatasertib dose (0.625 μM) was combined with 0.1 or

1μM trametinib (RH4 and RH30 cells) and 1 or 10nM trametinib (RD and CW9019 cells) (mean+/-s.d. from two biological replicates). **B)** Cell viability assay with increasing concentrations of ipatasertib, 1μM trametinib and combined treatment in RMS primary cultures. Observe the shift in cell viability of those cultures treated with both ipatasertib and trametinib when compared to ipatasertib alone.

3.5 Dual pharmacological inhibition of the AKT/mTOR and MEK/ERK pathways in RMS models *in vivo*.

These preliminary *in vitro* results prompted us to analyze the combinatorial effects of AKT and MEK inhibition *in vivo*. To this end, the RMS primary A006_S cells were selected since they displayed high sensitivity to low doses of ipatasertib and resistance to trametinib. Moreover, combined ipatasertib/trametinib treatment showed synergistic effects in A006_S cells *in vitro*. In addition, but not less important, we confirmed the capacity of A006_S primary cells to grow *in vivo*, expressing the characteristic RMS markers.

A006_S cells were subcutaneously inoculated and when tumors had reached a volume of 100-350mm^3, mice were divided into 4 groups: vehicle; 3 mg/kg trametinib; 100 mg/kg ipatasertib; and the combination of both drugs administered 5 days a week at the maximal tolerated dose (MTD). Mice carrying A006_S xenografts received treatment for 3 weeks. ipatasertib consistently led to decreases in tumor volume reaching complete response in 100% of tumors, thus combination with trametinib did not synergistically improve the responses (**Figure IV. 23A**). The A006_S EFS-KM curves showed that ipatasertib significantly increased mice survival (p= 0,0042; Log-rank corrected by Bonferroni), trametinib did not affect mice survival (p=0,4164 Log-rank corrected by Bonferroni)(**Figure IV. 23B**), and the group treated with ipatasertib/trametinib displayed an EFS curve that overlapped with that of the ipatasertib group (p= 0,6684). Of note, more than 20% of weight loss was observed in mice treated with the drug combination. Initially, ipatasertib at 100mg/kg also induced weight reduction but animals rapidly recovered (**Figure IV. 23C**). ipatasertib in combination with trametinib led to progressive weight reduction that limited the use of the combination treatment.

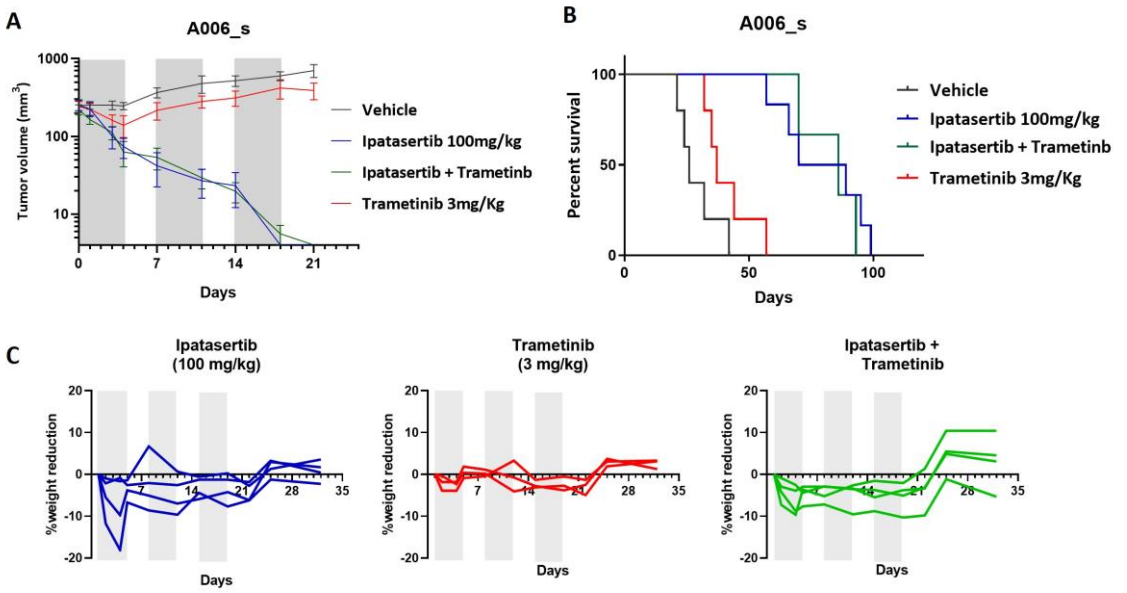

Figure IV. 23. Effect of ipatasertib and trametinib in the tumoral growth of RMS primary model *in vivo*. A) Tumor growth of A006_S subcutaneous xenografts in mice treated with 100 mg/kg per day of ipatasertib (blue), 3 mg/kg per day of trametinib (red) or the combination of the two drugs (green) or vehicle control (grey). A006_S mice received drug administration for 3 weeks (15 doses). Gray shadow depicts treatment time frame (5 days) for three cycles. Mean ± sem; control, ipatasertib, and combination $n = 4$ mice; trametinib, $n = 3$ mice; two-way ANOVA for each paired comparison. **B)** Kaplan–Mayer curves for mice survival for A006-S tumors (Log rank Mantel-Cox test corrected by Bonferroni). **C)** Percentage of weigh reduction of each animal treated for A006_S model.

In summary, our data support that downstream inhibition of the IGF pathway, either in a subgroup of AKT-dependent RMS or in the MEK-dependent subgroup, is an effective pharmacological approach to inhibit RMS tumor growth *in vitro* and *in vivo*. We provide data that distinguish two functional subgroups of RMS based on the response to the clinical grade AKT and MEK inhibitor drugs ipatasertib and trametinib, respectively. Since AKT and MEK are critical nodes of highly interconnected signaling pathways in RMS, co-administration of targeted therapies was expected to show synergistic effects. However, the *in vivo* data showed that trametinib did not improve ipatasertib single agent activity in the A006_S primary model tested. Interestingly a common feature between the primary cultures and the RH4 cell line is their exquisite sensitivity to the AKT-inhibitor ipatasertib.

One limitation of the study is the dose of ipatasertib tested. To optimize combination studies with trametinib, a lower dose of ipatasertib should be evaluated. In addition, whether trametinib treatment is able to sensitize RMS initially resistant to ipatasertib remains to be studied. Nevertheless, the toxicities encountered along with the clinical experience of similar combinations prevent the translation potential of the combination of MEK and AKT inhibitors for humans [220].

4 The AKT inhibitors ipatasertib (GDC-0068) and miransertib (ARQ-092): different anti-tumor activity against RMS.

4.1 Antiproliferative effects of two different AKT inhibitors

To further investigate the mechanism of AKT inhibition as a therapeutic strategy for RMS, the effect of ipatasertib (which is an ATP-competitive AKT inhibitor) was compared to that of miransertib (an allosteric AKT inhibitor) in *in vitro* and *in vivo* experiments. The experiments unexpectedly revealed that the two drugs displayed different cytotoxicity activity *in vitro* (**Figure IV. 24**). Indeed, in RH4 cell cultures, miransertib IC50 value was higher than ipatasertib (0.84 µM *vs.* 0.45 µM), indicating less sensitivity of these cells to miransertib. More importantly, miransertib showed a very limited activity over primary RMS models sensitive to ipatasertib. Miransertib IC50 was 700 nM for A010_S, while ipatasertib IC50 values were much lower (99nM). Exception for this behavior is the E024_S model, in which miransertib IC50 value was lower than Ipatasertib IC50s (0.24 µM vs 0.72 µM). This data suggested that therapeutic targeting of AKT with the ATP-competitive inhibitor ipatasertib is more effective than the allosteric inhibitor miransertib in a subgroup of RMS PDX.

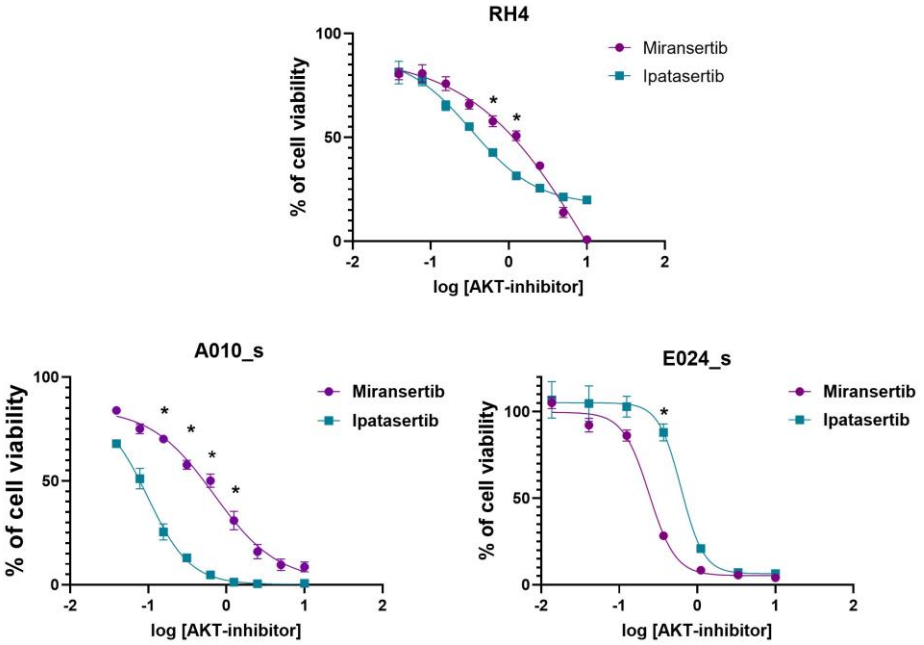

Figure IV. 24. Comparison of miransertib and ipatasertib activities in RMS cell lines and primary culture models. Cytotoxic activity of Miransertib (purple) and Ipatasertib (blue) in a panel of RMS cell lines and primary cultures. Each point represents mean ± SEM. Cell were seeded and treated simultaneously in similar conditions for both treatments. Multiple comparison two-way anova for statistics significances at each point concentration *p value <0.001

4.2 Inactivation of the AKT/mTOR pathway in RH4 cells by subcytotoxic concentrations of miransertib or ipatasertib.

To dissect the differential cytotoxic effect of miransertib and ipatasertib we analyzed the status of the AKT/mTOR pathway. To this end, we selected the RH4 cell line due to its high dependency on the IGF1R-AKT pathway. RH4 cells were treated for 24 hours with either ipatasertib or miransertib, and the status of the AKT pathway was analyzed by western blot. Again, according to their respective action mechanism, ipatasertib increased pAKT levels, while miransertib reduced AKT phosphorylation levels. S6 phosphorylation was reduced with both treatments, while S6 total levels remained unchanged (**Figure IV. 25A)**. Higher doses of ipatasertib or miransertib did not further reduce S6 phosphorylation levels, suggesting that residual p-S6 is AKT-independent. Then, RH4 cells were treated at different time points with increasing concentrations of miransertib or ipatasertib (from 0.2 to 10 µM). In parallel, RH4 cells treated with the IGF1R

inhibitor m708.5 (from 2 to 50 µg/ml) were included in the analysis for comparative purposes. As shown in **Figure IV. 25B**, miransertib and ipatasertib effectively reduced not only the phosphorylation of AKT, but also direct substrates of mTORC1, such as S6 and PRAS40, and phosphorylation levels of FOXO1/3 (which is also an AKT target) were also reduced in a dose dependent manner. Apoptotic effects, evaluated by cleaved PARP levels, were observed, as expected, in RH4 cells treated with m708.5 at 10 to 50 µg/ml dose, and in cells treated with 5 µM ipatasertib or miransertib **(Figure IV. 25C).** To compare the transcriptomic effects of each AKT inhibitor on RMS, a gene expression array was performed with mRNA extracted from ipatasertib and miransertib treated cells. The transcriptional spectrum observed in ipatasertib-treated cells was broader than in cells cultured with miransertib, suggesting that ipatasertib could act inhibiting more kinases, in addition to AKT, than miransertib. Gene expression analysis resulted in 1829 differentially expressed genes (DEGs) in ipatasertib-treated cells for 24h, in contrast to 799 DEGs upon 24h of miransertib treatment. According to the inhibitory nature of both drugs, the number of downregulated genes was superior to the upregulated. The intersection of DEGs for each drug demonstrated that miransertib shared more than 88% DEGs with ipatasertib, while only 40% DEGs in ipatasertib-treated cells were shared with miransertib. Indeed, 60% DEGs were uniquely found in ipatasertib-treated cells, revealing the wide plethora of ipatasertib-inhibited targets reflected at the transcriptional level **(Figure IV. 25D)**. Consistent with their described mechanism of action, the most significantly depleted genes in RH4 cells treated with 1 µM of each AKT inhibitor showed enrichment in the expression of genes involved in mTORC1 signaling pathway, confirming the downregulation of the pathway. Furthermore, regarding the proliferation gene sets, MYC target gene set and E2F target genes were inhibited by both drugs **(Figure IV. 25E)**. On the other hand, energy metabolism in mitochondria and oxidative phosphorylation were also similarly inhibited by both drugs. Within the subgroup of genes upregulated after treatment with ipatasertib or miransertib, enrichment in FOXO targets were found. Therefore, FOXO signaling was reactivated after AKT blockade with both inhibitors, which would favor pro-myogenic (differentiation) effects in RMS.

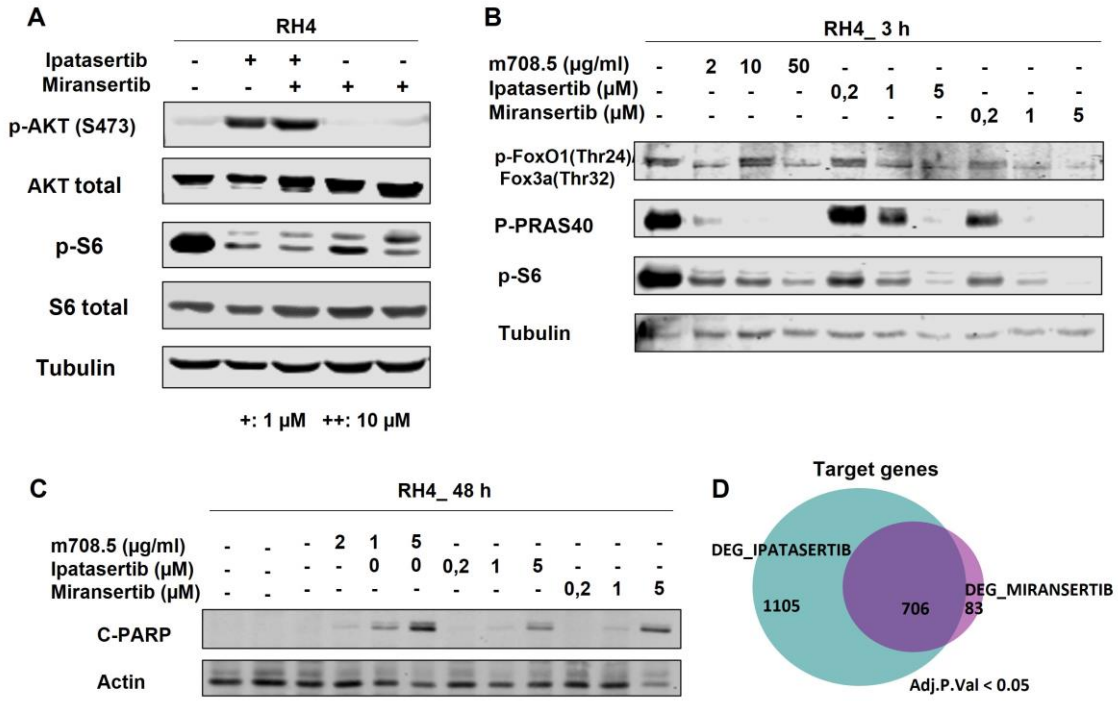

E

Most Significantly enriched terms, p.adjust<0.05	IPATASERTIB		MIRANSERTIB	
Downregulated genes	NES	p.adjust	NES	p.adjust
Hallmark MTORC1 SIGNALING	-2,60	1,E-09	-2,47	1E-09
Hallmark MYC TARGETS V1	-2,75	1,E-09	-2,76	1E-09
Hallmark MYC TARGETS V2	-2,67	1,E-09	-2,59	1E-09
Hallmark OXIDATIVE PHOSPHORYLATION	-2,51	1,E-09	-2,52	1E-09
Hallmark UNFOLDED PROTEIN RESPONSE	-2,42	1,E-09	-2,42	1E-09
Upregulated genes	NES	p.adjust	NES	p.adjust
Hallmark KRAS SIGNALING DN	1,94	2,E-07	1,55	3,E-03
Hallmark UV RESPONSE DN	1,68	6,E-04	2,02	1,E-06
Hallmark EPITHELIAL MESENCHYMAL TRANSITION	1,51	3,E-03	1,55	3,E-03
Hallmark MYOGENESIS	1,32	3,E-02	*not significant*	
Hallmark WNT BETA CATENIN SIGNALING	*not significant*		1,77	6,E-03

Figure IV. 25. AKT signaling inhibition and transcriptional changes in ipatasertib and miransertib RH4-treated cells. A) RH4 cells were treated with 1 or 10 µM concentrations of ipatasertib or miransertib for 24 hours, and pAKT (S473) and pS6 (S240/244) and their corresponding total protein levels were assessed by western blot analysis. **B)** RH4 control and cells treated for 3 h with increasing concentrations of m708.5, ipatasertib or miransertib were analyzed for pFOXO1 (T24) /FOX3a (T32), pPRAS40 (T246) and pS6 (S240/244) levels. Tubulin was used as loading control. **C)** RH4 control and cells treated for 48 h with increasing doses of m708.5, ipatasertib and miransertib were analyzed for Cleaved PARP levels. Actin was used as loading control. **D)** Venn diagrams for ipatasertib and miransertib DEGs in RH4 cells upon 24 h treatment of ipatasertib or miransertib (using Adj.P.Val < 0.05 cut-off; FDR method). Common genes are represented in dark shading. Each diagram contains the number of genes represented. **E)** Table of most significantly enriched terms (p.adjusted <0.05) in RH4 treated for 24 h with ipatasertib or with miransertib when compared with vehicle-treated cells. Blue color indicates downregulated gene set (NES negative) and purple upregulated gene sets.

The parallelisms found between miransertib and ipatasertib inhibition of AKT downstream signaling and at the transcriptional level did not explain the differences observed in cell viability studies.

4.3 Antitumoral activity of miransertib and ipatasertib *in vivo*

To test whether ipatasertib and miransertib display different activity in RMS models *in vivo*, as observed *in vitro*, mice bearing the HSJD-ERMS-011 PDX were selected given the high sensitivity of these tumors to ipatasertib. Ipatasertib and miransertib were daily administered at 100 mg/kg by oral gavage. Of note, the vehicle for miransertib is a phosphoric acid solution, which ensures proper drug absorption (see Material and Methods for details).

Initially, the same posology schedule was stablished for miransertib and ipatasertib in our prospective experiments, that is, five days with drug administration followed by two resting days per week. However, this schedule had to be modified due to the loss of body weight (about 15% of the initial weight) during miransertib administration. Therefore, miransertib protocol schedule was reformulated and set to four days of administration followed by three days' rest. On this schedule, tumor volumes in miransertib-treated mice were initially reduced when compared to vehicle-treated control group but eventually they all grew to similar size as the controls (**Figure IV. 26A** and **Figure IV. 26B)**. Ipatasertib showed more potent tumor growth reduction at both 25 mg/kg (blue line) and 100 mg/kg (green line) doses. Indeed, tumor volumes in the ipatasertib group reached undetectable tumor volumes. Taken together, ipatasertib, but not miransertib, displayed evident tumor inhibitory capacity in ERMS-011-PDX. As shown in **Figure IV. 26C**, both the miransertib and ipatasertib groups showed regaining of body weight during the off days. In this study one animal in the miransertib group and one animal in the 100 mg/kg ipatasertib group were eliminated from the study due to toxicity. Altogether, and consistent with the *in vitro* data, miransertib did not recapitulate the antitumor effectiveness of ipatasertib in RMS models.

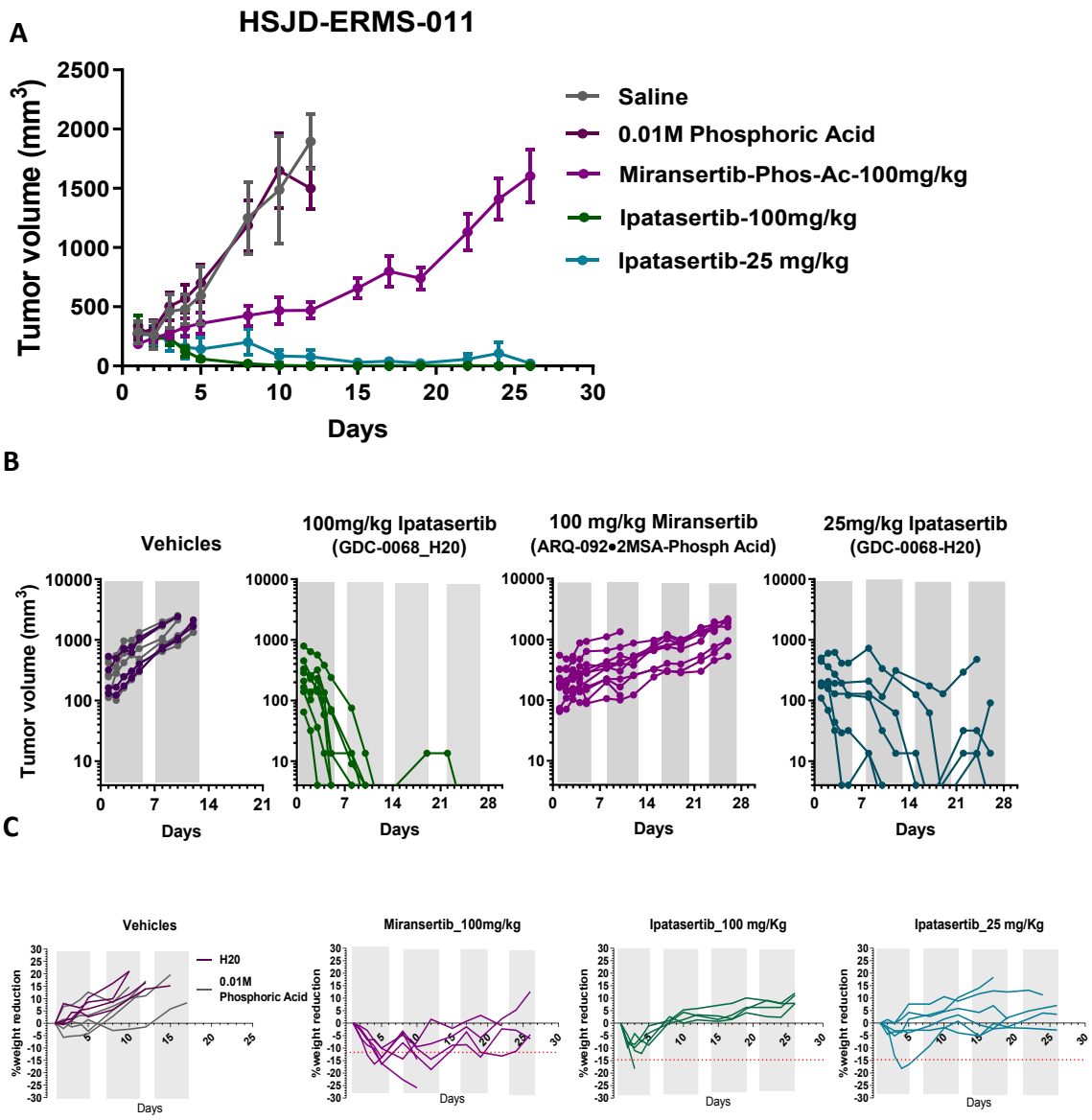

Figure IV. 26. Antitumoral effectiveness of miransertib and ipatasertib *in vivo*. A) Tumor growth of RMS-ERMS-011 PDX in mice under ipatasertib or miransertib treatments. Mean ± sem. N = 6 mice in the miransertib group: n = 4 and n = 5 in 100 and 25 mg/kg ipatasertib groups, respectively. Statistical analysis was performed by two-way ANOVA; p value<0.0001. **B)** Plots of individual tumor size for each group. **C)** Percentage of body weight variation during treatment and follow-up of each individual tumor. Highlighted in grey, administration days. Red line, 15% of weight loss, indicative of toxicity.

5 Ipatasertib targets PRKG1 in RMS.

5.1 Ipatasertib-sensitive RMSs express high PRKG1 levels.

The subtle differential transcriptional profiles of ipatasertib and miransertib treated cells plus the striking differences of these AKT inhibitors against RMS led us to hypothesize that ipatasertib might be targeting other relevant kinases for RMS biology besides AKT. Although both drugs were designed to specifically inhibit AKT, *in silico* data indicates that the target spectrum of ipatasertib is broader than that of miransertib (https://clue.io/repurposing-app). After AKT, the cGMP-dependent protein kinase PRKG1 is the most potently inhibited protein by nanomolar concentrations of ipatasertib, while miransertib do not affect PRKG1 protein (**Figure IV. 27A, Table I. 7**). Two different references documented the ipatasertib inhibition of PRKG1 by kinome selectivity profiles [178, 221]. Importantly, in our transcriptomic data of AKT inhibitors, we found interactors of PRKG1 among the genes downregulated by ipatasertib but not significantly affected by miransertib. We found PPP1R12B, also called Myosin Phosphatase Target Subunit 2 (MYPT2) (**Figure IV. 27B**), among the genes selectively regulated by ipatasertib. Two isoforms of myosin phosphatase target (MYPT) have been identified: MYPT1 (gene *PPP1R12A*) and MYPT2 (gene *PPP1R12B*). Unlike MYPT1, which is widely expressed, MYPT2 is specific to heart, skeletal muscle and brain. Both MYPT1 and MYPT2 interact with PRKG1 (BioGRID) in the regulation of actin-myosin contractile dynamics [222, 223]. Also, MYPT1 is a cyclin A/CDK1 substrate, acting as molecular link between CDK1 and PLK1 [224].

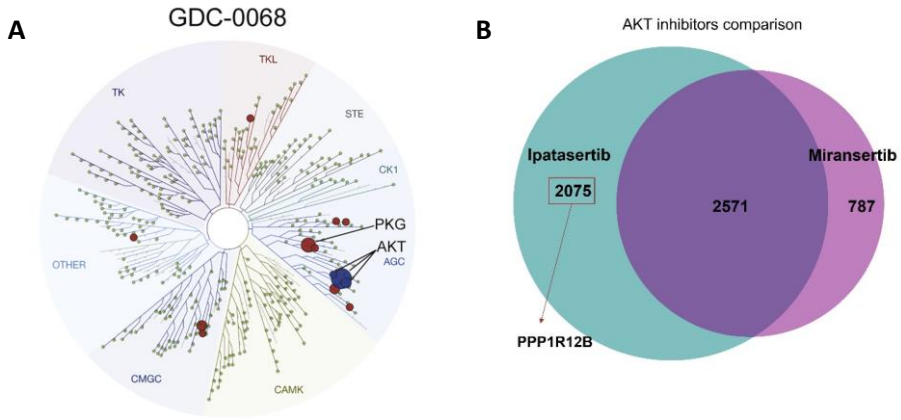

Figure IV. 27. Ipatasertib, but not Miransertib, affects PRKG1 activity. A) TREEspot visualization of the biochemical kinome selectivity profile of Ipatasertib (1 µM). Inhibited kinases are highlighted. In red, PRKG1; in blue, AKT. Figure taken from [221]. **B)** Venn diagrams for Ipatasertib and Miransertib DEGs in RH4 cells upon 24 h treatment of ipatasertib or miransertib (using as a cut-off p value < 0.05). Common genes are represented in dark shading. Each diagram contains the number of genes represented. Observe that PPP1R12B (MYPT2) is among those selective ipatasertib target genes.

The above data led us to focus our study on PRKG1. PRKG1 is a cyclic GMP-dependent protein kinase that has two different isoforms, PRKG1α and PRKG1β. These isoforms are important components of many signal transduction processes in diverse cell types and are involved in vascular smooth muscle contraction (https://www.genecards.org).

Data on the role of PRKG1 in tumor cells is scarce and contradictory, and PRKG1 expression or function in RMS has not been explored. Therefore, we first analyzed the protein levels of PRKG1 in three experimental models: in RH4 cells and in the primary cell cultures A006_S (sensitive to ipatasertib but not to miransertib) and E024_S (sensitive to miransertib and refractory to ipatasertib). PRKG1 was expressed in the two ipatasertib-sensitive models RH4 and A006_S, but not in E024_S cells. Of note, neither ipatasertib nor miransertib treatments affected PRKG1 levels (**Figure IV. 28**).

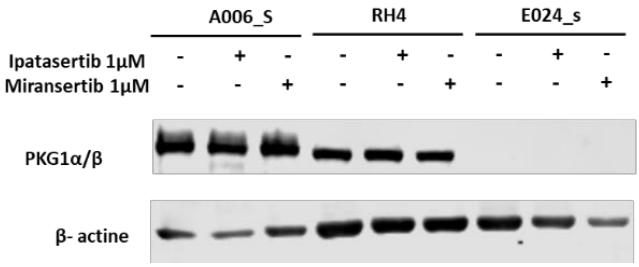

Figure IV. 28. PRKG1 levels in A006_S, RH4 and E024_S cells in basal culture conditions or upon 1 µM ipatasertib or miransertib treatments for 24 h, assessed by western blot analysis. Image shows one representative experiment detecting PKG1α/β protein levels. Actin was used as loading control.

This preliminary result encouraged us to further explore the relationship between ipatasertib sensitivity and PRKG1 levels. To this end, we carried out a transcriptional analysis in five cell lines, four primary cell cultures, and seven primary RMS tumors and their corresponding PDXs, by using the Human Genome U219 Array (Affymetrix, Thermo Fisher). Unsupervised principal component analysis (PCA) and unsupervised hierarchical clustering of the RMS transcriptomes primarily segregated the established cell lines from the primary samples, likely reflecting the long selection processes underwent by the former (**Figure IV. 29A**). Of the primary tumor samples, heatmap representation showed that each primary cell culture clustered with its primary tumor, exception made for E001_S and MO10 cultures, whose transcriptional profiles differed from their primary tumor or PDX, respectively (**Figure IV. 29**). These differences could be attributed to different origins or cell heterogeneity of the samples. Indeed, the MO10 sample corresponded to bone marrow infiltrated with tumor cells, from which the corresponding PDX was generated. With respect to E001_S, this cell culture was originated from a tumor biopsy without a previous tumor expansion step *in vivo*.

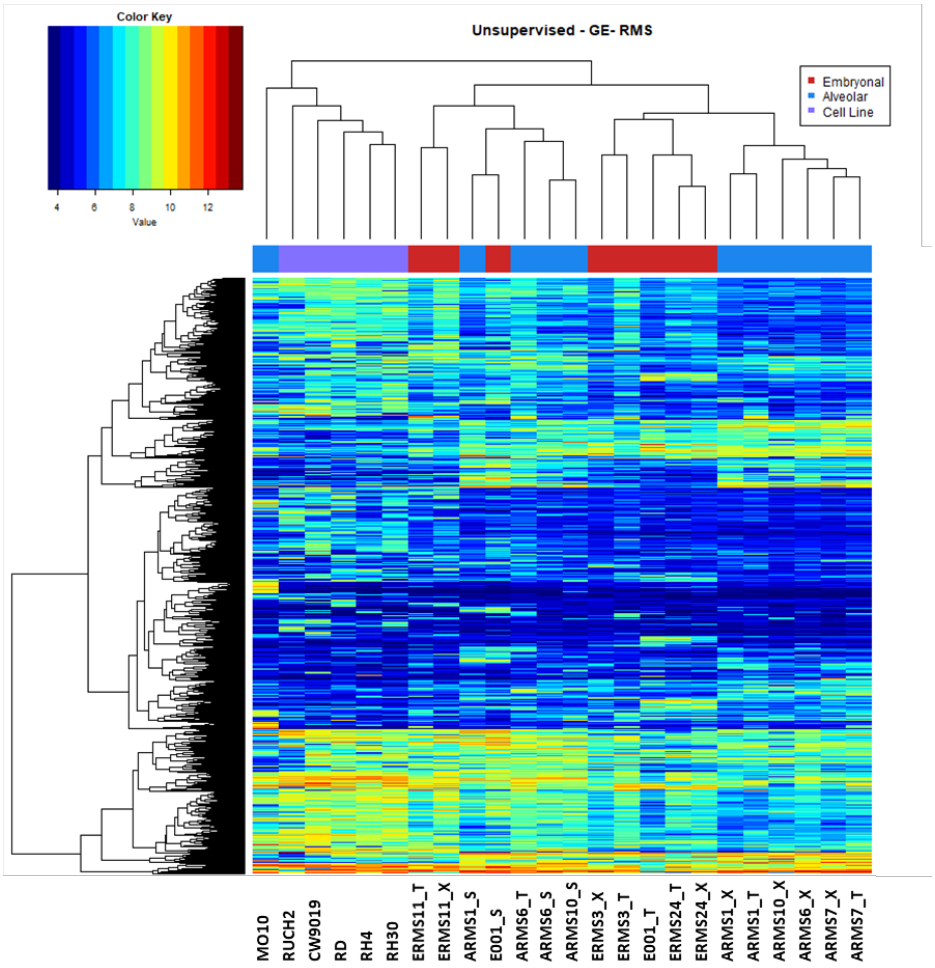

Figure IV. 29. Gene expression analysis of the RMS samples included in the study. Hierarchical clustering of gene expression data (SD ≥ 1) in primary RMS tumors (_T), their corresponding PDXs (_X) and primary cultures growing as spheres (_S) (SD ≥ 1). Samples were colored in red (RMS embryonal), in blue (RMS alveolar) or in purple (cell lines) in the graph to facilitate group identification.

Unsupervised clustering showed that RMS PDXs and primary cells cluster together with their corresponding primary tumors at transcriptomic level, while RMS cell lines cluster separately. Of RMS tumors, PDX and primary cells, we discriminated two distinct groups based on *PRKG1* expression levels. According to the array probe corresponding to PRKG1, RMS primary samples exhibited high variability in PRKG1 levels, and two different groups could be discriminated: high-PRKG1-RMS and low-PRKG1-RMS (**Figure IV. 30A**). Correlation analysis revealed the direct relationship between *PRKG1* mRNA levels in PDX and primary tumors and *in vivo* ipatasertib efficacy: the stronger the tumor regression is, the higher the levels of PRKG1 mRNA are (**Figure IV. 30B**). Indeed, the most

sensitive RMS tumors to ipatasertib were found to express the highest levels of PRKG1. This data identified PRKG1 as a potential biomarker for ipatasertib-response in RMS tumors. By contrast, none of the AKT mRNAs (AKT1, AKT2 and AKT3) were among the differentially expressed genes in the unsupervised clustering analysis (SD>1), nor correlated with the ipatasertib effects observed in RMS, ruling out AKT as the kinase responsible for the ipatasertib differential effects in RMS (**Figure IV. 30C)**.

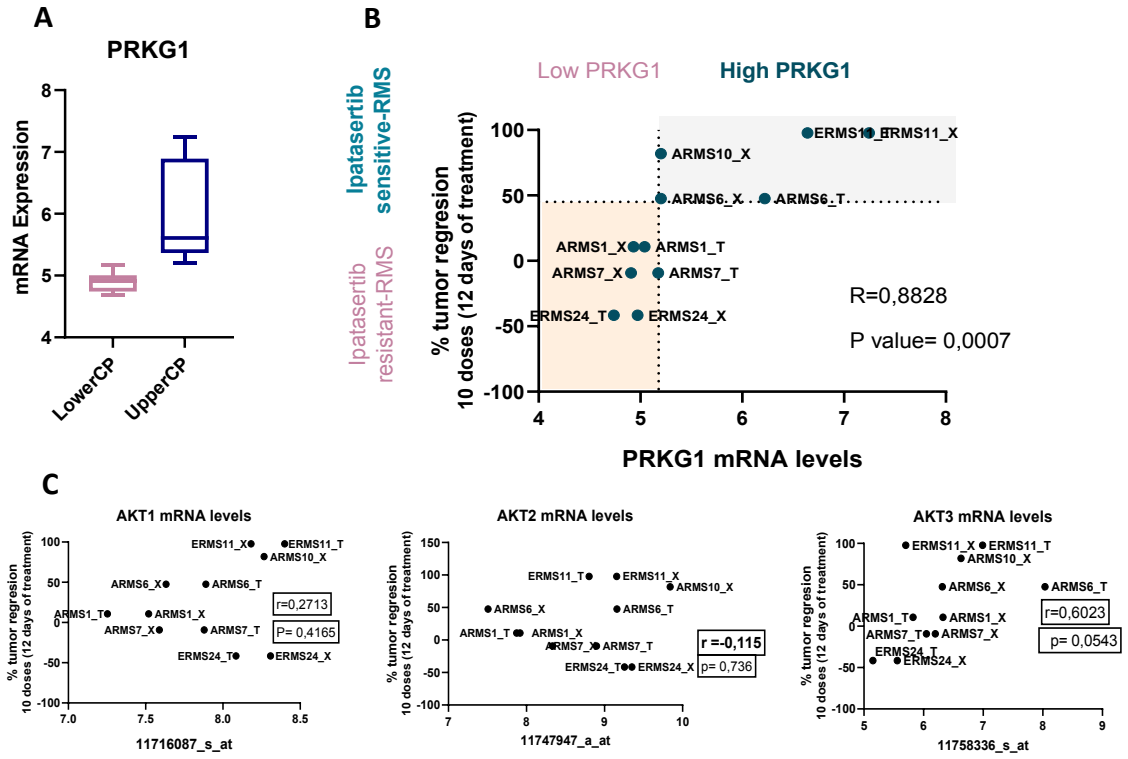

Figure IV. 30. PRKG1 mRNA levels correlate with RMS responsiveness to ipatasertib *in vivo*. A) Box plot representing PRKG1 mRNA levels from RMS_T/_X/_S. Unsupervised analysis revealed the existence of two groups according to high (ERMSE_S, ARMS1_S ARMS6_T, ARMS6_X, ARMS6_S, ARMS10_X, ARMS10_S, ERMS11_T, and ERMS11_X) or low (ERMSE_T, ARMS1_T, ARMS1_X, ERMS3_T, ERMS3_X, ARMS7_T, ARMS7_X, ERMS24_T, ERMS24_X) expression of PRKG1 (cut-off= 5.187; Median). MO_010 model was excluded from the analysis due to technical issues. **B)** Scatterplot of PRKG1 mRNA levels (11740294_a_at probe) showing the positive correlation with tumor regression after ten doses of ipatasertib in different RMS experimental models. **C)** Scatterplot of AKT1/2/3 mRNA levels (X probes respectively) and tumor regression after ipatasertib treatment, as indicated above.

5.2 The transcriptional profiles of RMS with high PRKG1 expression levels are enriched in cell cycle and impoverished in myogenic genes.

To identify molecular hallmarks associated to high PRKG1 expression levels, we performed a supervised analysis based on PRKG1 expression levels in the primary RMS models (cut-off = 5.187). Of note, the MO_010 model was excluded from this analysis due to inconclusive data regarding ipatasertib response *in vivo*.

As shown in **Figure IV. 31A,** the established cut-off for PRKG1 levels cleanly segregated RMS models with complete response to ipatasertib *in vivo* from those resistant, with the only exceptions of ARMS-001_X and ARMS-010_X, at the interface of the hierarchical classification. Levels for both PRKG1 α and β mRNAs were validated by RT-qPCR (**Figure IV. 31B**). Overall, RMS models with complete response to ipatasertib treatment corresponded to those with higher PRKG1 levels (High_PRKG1), while RMS models with stable or progressive disease displayed low mRNA *PRKG1* levels (Low_PRKG1). Therefore, the cut-off point established was a useful tool to cluster both groups for subsequent analysis.

Differential expression analysis of High_PRKG1 versus Low_PRKG1 samples identified 408 DEGs (FDR <0.05) (**Figure IV. 31C**). Of these, 104 genes were, at least 1.5 times more expressed in High_PRKG1 than in Low_PRKG1. *SIX1, EYA4, PLK2*, and *CDK6* are some examples. SIX1 and EYA4 are implicated in early normal muscle development (see Introduction). PLK2 and CDK6 are involved in the G1/S phase transition of the cell cycle, but their expression falls with differentiation [225, 226], suggesting that high PRKG1 levels may be related to the regulation of the proliferation and differentiation balance of the developmental myogenic cell. Also, genes involved in negative regulation of ERK1, ERK2 and MAP kinase activity, such as *SPRED1/2* and *SPRY1/2* were found highly expressed in the High_PRKG1 subgroup. This enrichment could explain trametinib inefficiency in ipatasertib-sensitive RMS models.

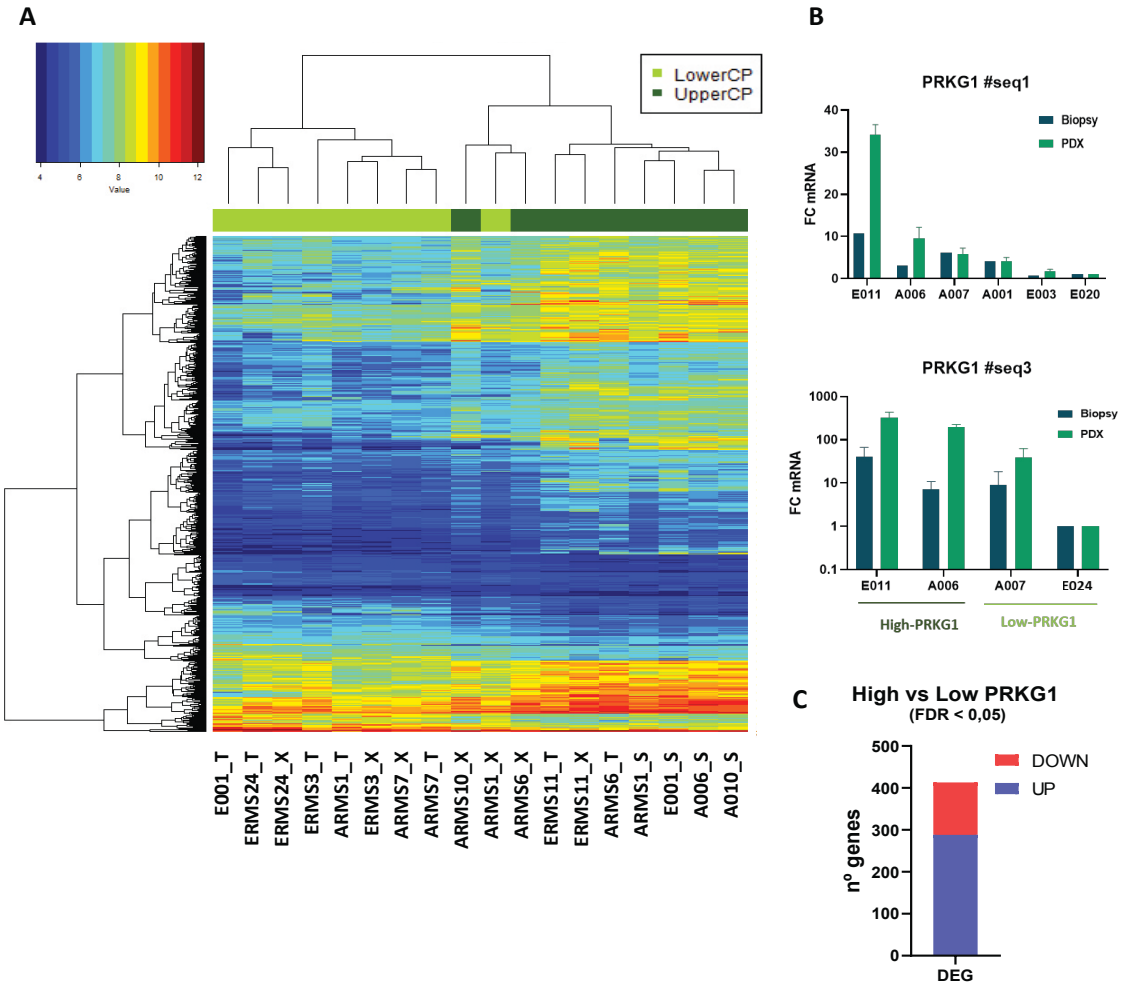

Figure IV. 31. Supervised analysis of gene expression in RMS experimental models. A) Hierarchical clustering of the supervised analysis performed on the bases of a cut-off point=5.1875 for PRKG1 mRNA levels (FDR<0.05). This analysis identified 408 DEGs. Dark green labeled samples (on the right) correspond to ipatasertib-sensible RMS models, while light green corresponds to ipatasertib-resistant RMS models. **B)** ΔΔCt values from RT-qPCR for PRKG1 α and β (sequences 1 and 3, respectively) in xenografts and primary tumors included in the microarray analysis. **C)** Number of DEGs overexpressed and underrepresented in High_PRKG1 RMS.

Gene ontology (GO) analysis of DEGs in the High_PRKG1 group was performed, in an attempt to identify specific gene functions associated to the high expression of this kinase. We initially performed gene set enrichment analysis (GSEA) to investigate the representation of general hallmark gene sets in the High_PRKG1 group. This analysis revealed that the upregulated genes in the High_PRKG1 subgroup were enriched in functions involving pathways of the E2F targets, G2M checkpoints, MYC targets, and mTORC1 signaling (**Figure IV. 32).** In contrast,

the expression of genes involved in myogenesis and KRAS signaling pathways were underrepresented in this subgroup. In sum, this analysis showed that high PRKG1 levels are associated with increased cell cycling activity and activation of the mTOR pathway in the ipatasertib-responsive models (High_PRKG1), whereas genes regulating the myogenesis process and KRAS signaling activity are underrepresented in these RMSs. In **Figure IV. 32**, the most significant core enrichment genes are shown for each gene set.

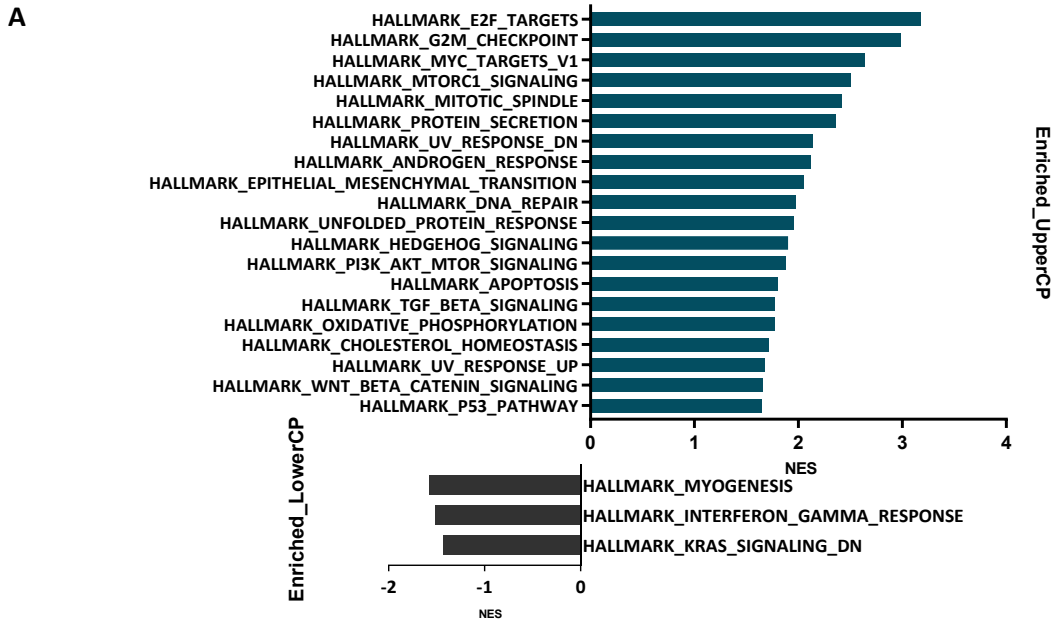

Figure IV. 32. Functional pathways associated with high PRKG1 levels in RMS. A) GSEA enrichment analysis of hallmark gene sets significantly enriched in High_PRKG1 *vs.* Low_PRKG1 samples. Normalized enrichment scores (NES) are shown in the X-axis, and the Y-axis shows the Hallmarks. (*follow in next page*)

B

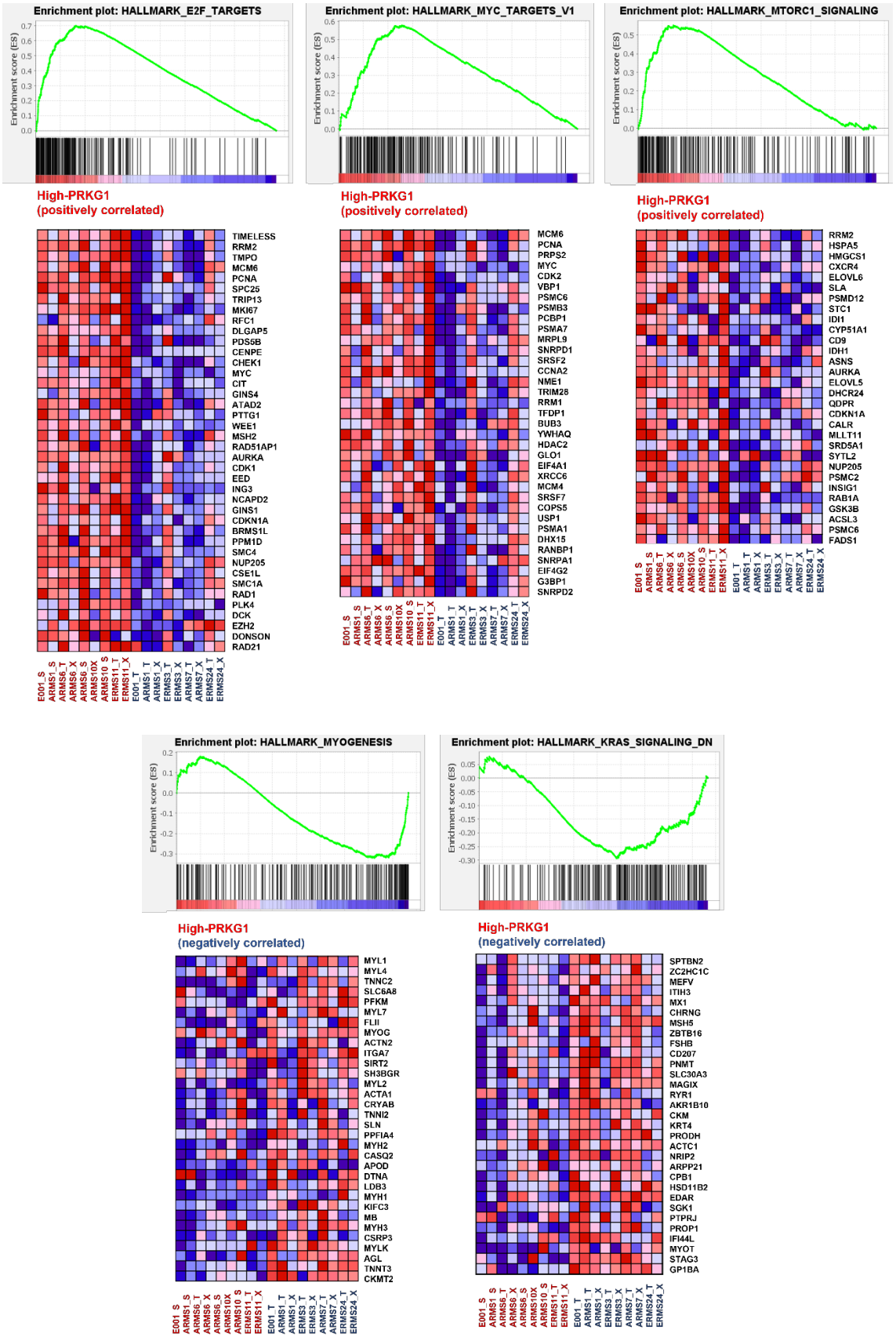

Figure IV. 32. Functional pathways associated with high PRKG1 levels in RMS. (*Continuation*) **B)** GSEA enrichment plots and the corresponding heatmaps of the core enrichment genes in High_PRKG1 versus Low_PRKG1 samples. Genes whose expression levels are most closely associated

with the High_PRKG1 group get the highest metric scores with positive or negative sign, located at the left or right edge of the list, respectively. The score at the peak of the plot is the enrichment score (ES) for this gene set and those genes displayed before or at the peak are defined as core enrichment genes for this gene set. Next to GSEA plot, heatmap illustrating gene expression levels for each gene in the core enrichment subset. Range of colors (red to blue) shows the range of expression values (high to low). Between the 30 and 40 most significant genes are shown in each gene set.

Taken together, high levels of PRKG1 are transcriptionally associated with a proliferative phenotype and poor differentiation, as indicated by the downsize of myogenic markers. In addition, as previously demonstrated, high PRKG1 expression is associated with a favorable response to ipatasertib. We hypothesize that PRKG1 expression levels play a role in the myogenic differentiation dynamics of RMS. Since there is no information available on the role of PRKG1 in developmental tumors, we next focused on defining the function of this gene.

5.3 PRKG1 silencing induces a transcriptional myogenic pattern and cell cycle arrest in RMS.

To identify genes regulated by PRKG1 in RMS, PRKG1 gene silencing using RNA interference (RNAi) was carried out by oligofection of RH4 cells with four different PRKG1 siRNAs that target different exons common for both α and β isoforms. PRKG1 depletion at the protein level was confirmed for all the siRNAs (**Figure IV. 33A**). Sequence #J14 was selected for genome-wide studies since it was the most effective sequence in reducing PRKG1 levels (**Figure IV. 33AB**). Of note, three different primers were used to determine the levels of PRKG1 isoforms by RT-qPCR: primers #1 and #2 detect the PRKG1α isoform, while primer #3 mainly detects the PRKG1β isoform (**Figure IV. 33AB**; see M&M).

PRKG1 knockdown in RH4 cells resulted in the differential expression of 1469 genes (p value <0.05), with 796 upregulated and 673 downregulated. To further study the function of PRKG1 as regulator of RMS differentiation, we analyzed the upregulated gene signature after PRKG1 depletion. Numerous muscle-specification genes such MYL1, MEF2C, and MSTN were identified as significantly upregulated. Indeed, GSEA revealed a positive enrichment of

muscle cell differentiation and contractile muscle gene signatures in PRKG1 depleted cells (**Figure IV. 33C**). In contrast, genes known to regulate metabolism and proliferation such as CDK5 and PPARGC1A were significantly downregulated.

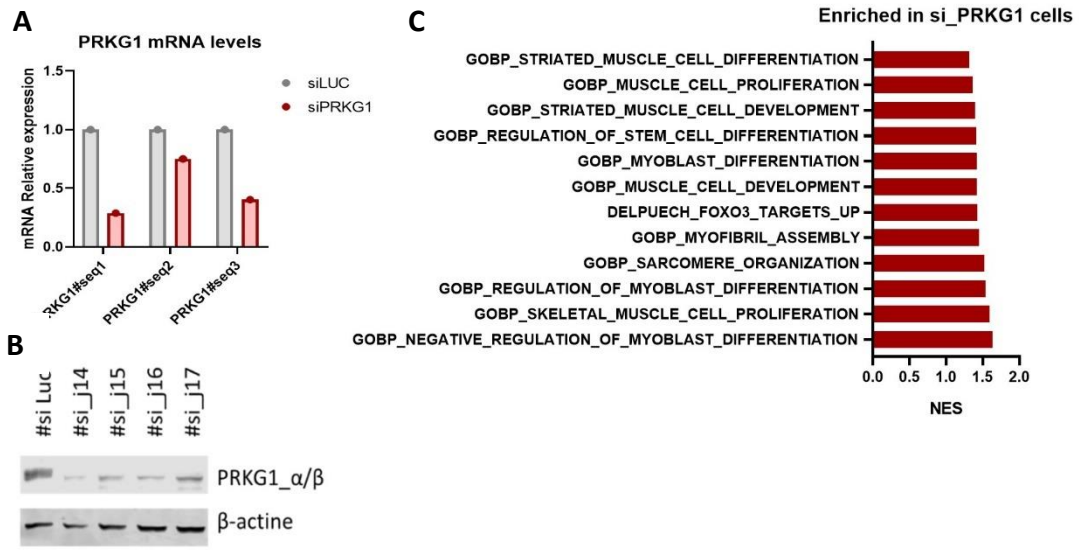

Figure IV. 33. Transcriptional changes upon PRKG1 knockdown in RH4 cells. **A)** Representative immunoblots showing PRKG1 levels in RH4 cells oligofected with four different PRKG1 siRNA sequences: #J14, #J15, #J16, #J17. siRNA targeting luciferase was used as negative control. **B)** Levels of PRKG1 mRNA in RH4 cells oligofected with siRNAs, and relative to RH4 cells expressing luciferase siRNA, detected by RT-qPCR. PRKG1 mRNA levels were validated with three different pairs of primers. **C)** Bar chart showing GSEA (p value <0.05) (PRKG1 siRNA *vs.* luciferase siRNA), which revealed positive enrichment for curated muscle cell differentiation and skeletal muscle contraction gene signatures.

To deeply characterize PRKG1 targets in RMS, we used the CRISPR/Cas9 technology to knock-out endogenous PRKG1 in RH4 cells. In contrast to the siRNA #J14, our CRISRP/CAS9 system consisted of a pull of three different sgRNA sequences targeting exon 1 of *PRKG1* gene (**M&M**). Protein levels of PRKG1 in two knock out (KO) clones (8D and 9D) were reduced when compared to mock control clones (5G and 6D), although knockdown efficiency was incomplete (**Figure IV. 34A**), likely due to the alternative splicing of exon 1 in the PRKG1 isoform β. We selected clone 9D for further studies since DNA sequencing confirmed the homozygous deletion of PRKG1 in that particular clone (**Figure IV. 34B**). Of note, clone 9D cells proliferated slower than control cells (**Figure IV. 34C**).

Our working hypothesis postulated that ipatasertib sensitivity relies on PRKG1 levels. Accordingly, KO-PRKG1 cells should be less sensitive to the drug than parental cells. Indeed, ipatasertib treatment of KO-PRKG1 cells was less effective in reducing cell viability (IC50: 0.79; 95%CI: 0.68 to 0.93) than the same treatment in the parental RH4 cells (IC50: 0.57; 95%CI: 0.49 to 0.65) (**Figure IV. 34D**).

Genome wide expression analysis of the KO-PRKG1 clone 9D revealed a total of 259 DEGs (Adj. p value <0.05 and |logFC|> 1) compared to RH4 parental cells (**Figure IV. 34E**). Of these, 202 were upregulated and 57 downregulated DEGs. At the functional level, the myogenesis hallmark gene set was statistically enriched in KO-PRKG1 cells, while genes of the mTORC1 signaling and MYC targets were impoverished in the transcriptional profile of KO-PRKG1 cells (**Figure IV. 34F**). Of the genes of the myogenesis cluster, TNNI1 and MYL1 were among the genes transcriptionally enriched in KO-PRKG1 cells, while genes known to regulate cell cycle and proliferation such as EIF4EBP1 and CDK4 were significantly downregulated (**Figure IV. 34F**). These results indicate that PRKG1 depletion impairs cell proliferation and induces differentiation, recapitulating the physiologic myogenic differentiation process.

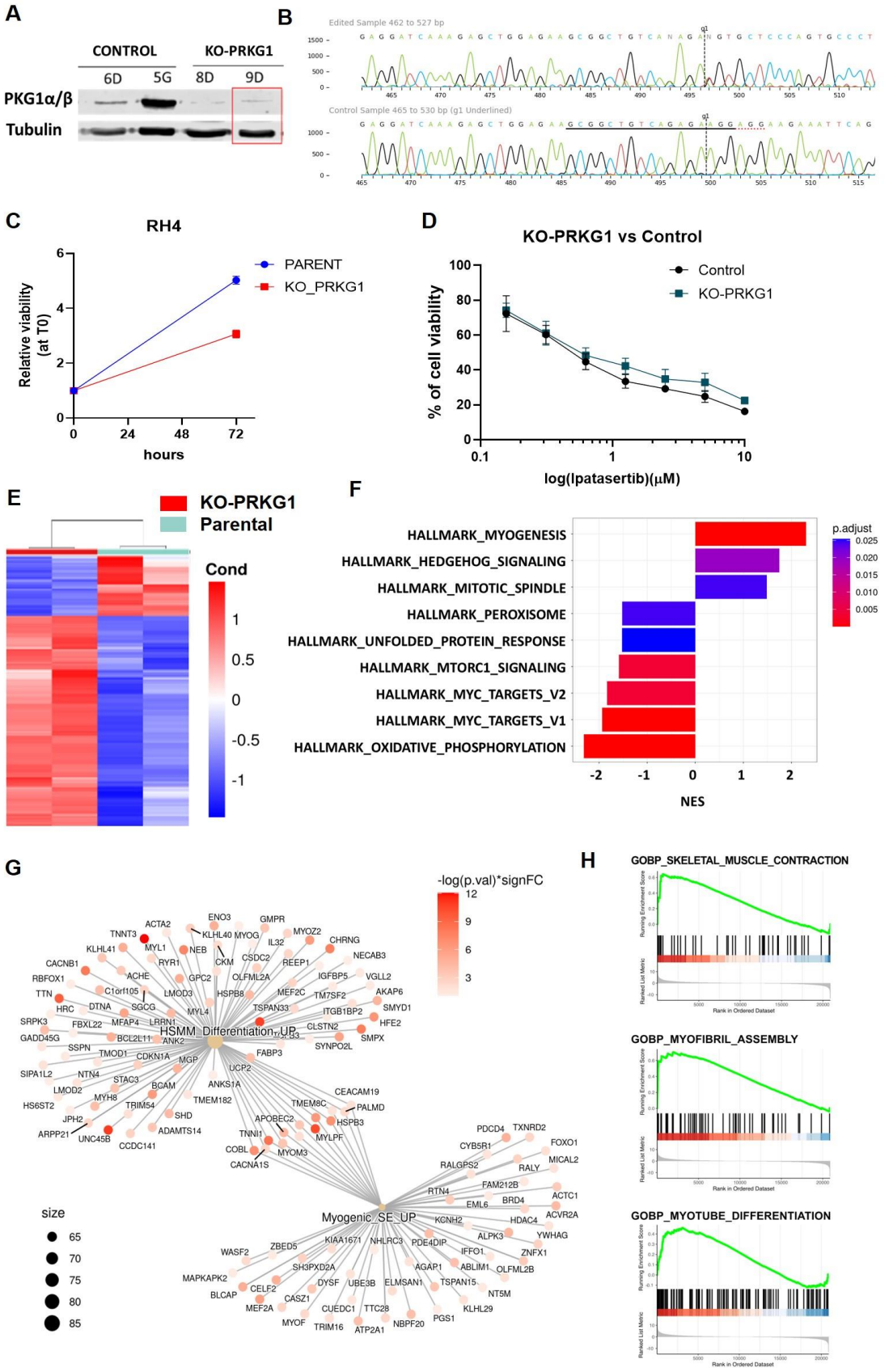

Figure IV. 34. Transcriptional effects of PRKG1 knock-out in RH4 cells. A) PRKG1 expression in RH4 clones generated from mock and PRKG1 sgRNA, after CRISP/CAS9 technology, assessed by western

blot, confirming PKG1α/β silencing. **B)** Sanger sequencing of clones 9D (KO-PRKG1) and 6D (PRKG1 wild type). Track for sgRNA guide#1 is shown. **C)** Proliferation of parental and KO-PRKG1 RH4 cells, measured 72 h after seeding. Graph shows a reduced proliferative capacity of KO-PRKG1 cells. **D)** MTS cell proliferation curves, expressing percentage of viable cells in parental (in blue) and KO-PRKG1 (red) RH4 cells after treatments with diferent concentrations of ipatasertib for 72h. Observe that ipatasertib effectiveness in reducing cell viability is lower in the KO-PRKG1 clone than in the parental cells. **E)** Heatmaps generated with DEGs in KO-PRKG1 cells (|logFC|> 1 and Adj.P.Val < 0.05). **F)** Barplot of significantly enriched terms in KO-PRKG1 cells (NES positive) *vs.* parental cells (NES negative) (p.adjust<0.05). **G)** Gene-concept networks of the significantly enriched terms in KO-PRKG1 cells. Observe the enrichment in hSMM_differentiation_UP (human Skeletal Mucle Myoblast) and Myogenic_SE_UP (Super Enhancers) gene sets defined by Yoeh et al in 2018. **H)** GSEA plots of DEGs in PRKG-KO versus parental cells show positive enrichment for skeletal muscle contraction, myofibril assembly and myotube differentiation gene signatures. Genes whose expression levels are most closely associated with the KO-PRKG1 condition get the highest metric scores with positive sign, located at the left edge of the list.

Next, the two genetic signatures of pediatric RMS described by Dr. J. Khan's team (Yohe ME et al, 2018) were studied in PRKG1 depleted cells. The expression of genes belonging to these two signatures, the human myogenic differentiation gene signature (hSMM_diff_UP), and the signature of myogenic super-enhancers induced genes (MYO_SE_UP), were enriched in the PRKG1-KO transcriptome (**Figure IV. 34G**). Moreover, the GSEA plot nicely showed a positive enrichment in the gene expression of muscle cell differentiation program and contractile muscle gene signatures in PRKG1-KO cells compared to the parental cell line. On the other hand, the transcriptional profile of PRKG1-KO cells displayed an impoverishment in the expression of genes involved in oxidative phosphorylation.

Taken together, PRKG1 depletion in RH4 cells resulted in transcriptional profiles similar to those found in Low_PRKG1 RMS models, suggesting that PRKG1 expression levels contribute, at least in part, to the proliferative phenotype and the repressed myogenic differentiation of the High_PRKG1 RMS. For the first time we provide evidence that PRKG1 levels closely link ipatasertib anti-tumoral activity with the myogenic differentiation status in RMS tumors. The two experimental approaches reducing PRKG1 levels in RMS indicate that PRKG1 plays a central role in the balance between a more proliferative tumor cell with a transcriptome depleted in myogenic markers versus a less proliferative cell but enriched in terminal differentiation markers of the myogenic program.

Binding of MYOD1 to the *PRKG1* gene in RMS

To date, the putative role of PRKG1 in the skeletal muscle development induced by MRFs has not been reported. Based on our data, we hypothesized that the regulation of PRKG1 might depend on the myogenic master regulator MYOD1. To approach this question, we investigated the status of chromatin marks associated to active transcription of the *PRKG1* gene as well as the MYOD1 binding to this genomic region. As shown in **Figure IV. 35**, *in silico* extraction of publicly available data from sequencing of chromatin immunoprecipitations (ChIP-seq) corresponding to this region revealed that MYOD1 binds to the *PRKG1* gene at the transcription stat site (TSS), decorated with mono- and tri-methylated lysine 4 at histone 3, in RH4 cells. In contrast, PAX3-FOXO1 binding was not present in this genomic region, suggesting that PRKG1 may act as an effector of MYOD1-regulated myogenic differentiation blockade in both FN and FP RMS.

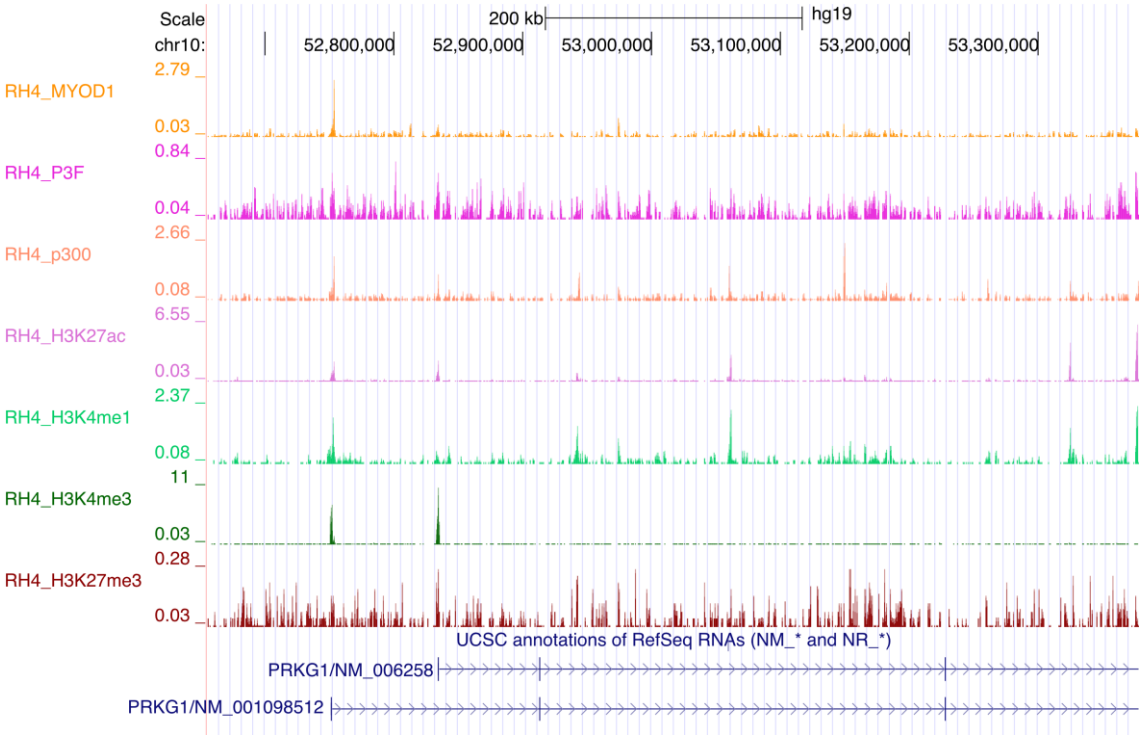

Figure IV. 35. Histone covalent marks associated with transcription are present at PRKG1 transcription start site, and MYOD1 binds to the *PRKG1* gene in RH4 cells. Genome browser visualization of MYOD1 and PAX3-FOXO1 ChIP-seq tracks at the PRKG1 gene promoter in RH4 cells. Four tracks corresponding to four histone marks: H3K4me3, H3K4me1, and H3K27ac, and H3K27me3 (the latter, associated to transcriptional repression) in RH4 cells were included. The y axis represents normalized read density in reads per million (rpm). ChIP-seq tracks are publicly available from Gryder et al [7].

In this thesis we have shown evidence of the role of PRKG1 in both FN and FP RMS in response to ipatasertib. Furthermore, in a FP-RMS model such as the RH4 cell line we were able to describe at the transcriptomic level the shift from a more proliferative to a more differentiated phenotype by modulating PRKG1 levels. Although more data, particularly in FN-RMS models, are needed to confirm the mechanism, we here propose that PRKG1 has a role in the maintenance of the undifferentiated and proliferative phenotype in FP and FN-RMS.

6 Expression and prognostic value of PRKG1 in RMS

6.1 PRKG1 is highly expressed in RMS tumors

The correlation analysis of PRKG1 expression and ipatasertib-sensitive RMS encouraged us to analyze PRKG1 expression levels in an *in silico* compilation of 783 developmental tumors. This data set included representation of the most relevant solid tumors in the pediatric age: central nervous system tumors (DIPG, LGG, HGG, EP, PA, MB and ATRT), sarcomas (RMS, ES, OS, and SS) and NB. We also included gene expression data from human mesenchymal and embryonic stem cells (hMSC and hESC, respectively) and differentiated tissues, to check whether PRKG1 expression could be related to cell differentiation stages. As shown in **Figure IV. 36A**, RMS can be distinguished from any other developmental tumor or normal tissue by their high and disperse PRKG1 levels. Importantly, RMS segregation on the bases of their genetic features revealed that PRKG1 levels were independent of the fusion status (PAX-FOXO1 positive or negative), in agreement with our previous data (**Figure IV. 36B**).

The broad dispersion in PRKG1 levels in RMS tumors was of particular interest, feature even more relevant as far as it was neither due nor related to the presence of the oncogenic fusion. In addition, the existence of RMS subtypes with different degrees of PRKG1 mRNA levels agreed with our data showing that PRKG1 protein levels were highly expressed by ipatasertib-sensitive, but not in resistant, cells *in vitro*.

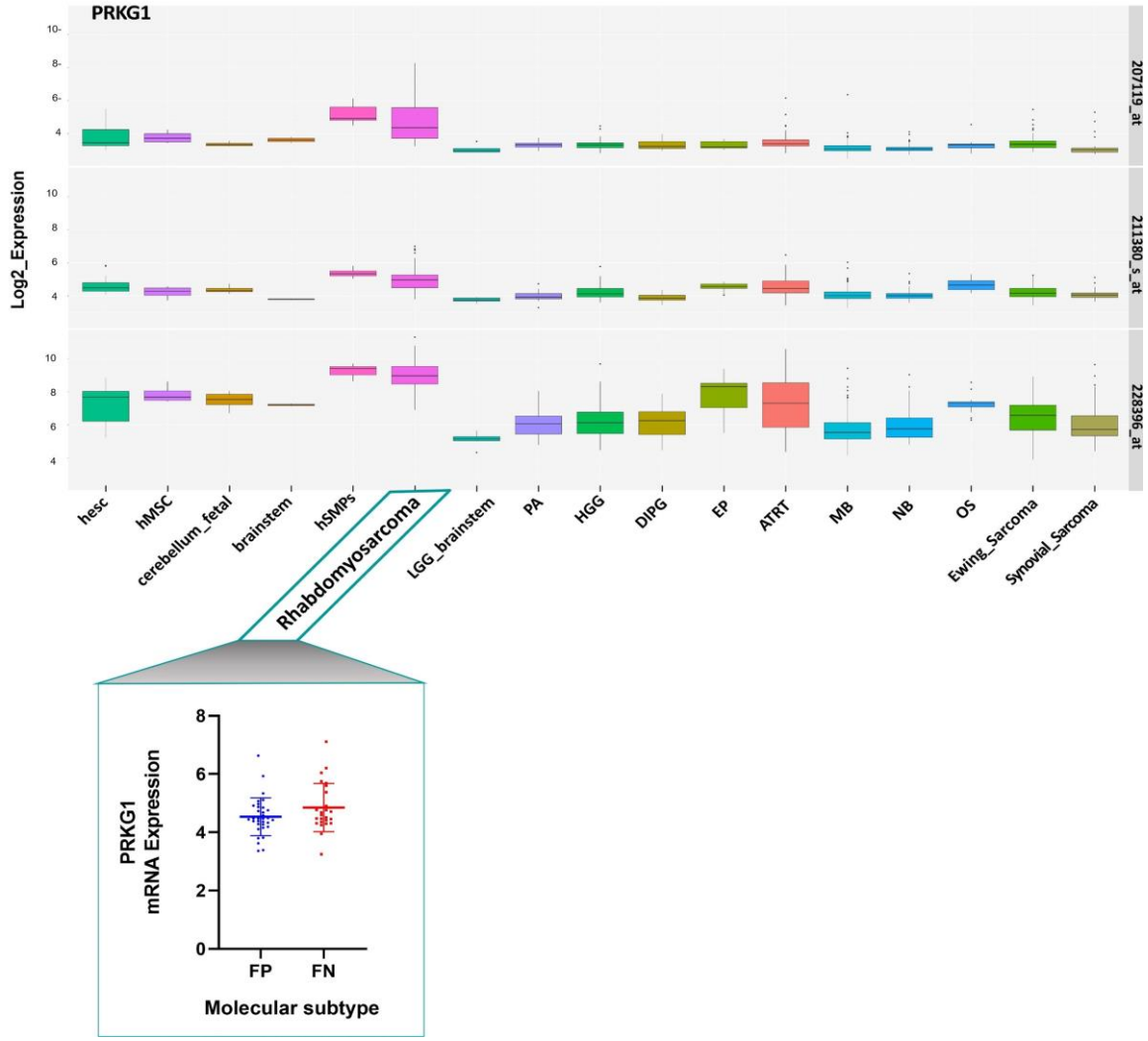

Figure IV. 36. PRKG1 expression levels in developmental tumors, from *in silico* databases. A) PRKG1 mRNA expression, extracted from GEO databases for pediatric tumors (array probe PRKG1_207119_at, PRKG1_211380_s_at and 228396_at in Affymetrix U133plus2.0). Tumors represented are low-grade glioma (LGG), pilocytic astrocytoma (PA), high-grade glioma or glioblastoma (HGG or GBM), diffuse intrinsic pontine glioma (DIPG), ependymoma (EP), atypical teratoid/rhabdoid tumors (ATRT), medulloblastoma (MB), neuroblastoma (NB), osteosarcoma (OS), Ewing sarcoma (EW), synovial sarcoma (SS), human skeletal muscle precursor cells (hSMPs) and RMS. Stem cells represented are human mesenchymal and embryonic stem cells (hMSC and hESC, respectively). Embryonal tissues are fetal brainstem and cerebellum. **B)** Box plot representing PRKG1 mRNA levels from 58 RMS patients in GSE66533, dissociated in two groups according to their fusion oncogene status.

6.2 PRKG1 prognostic value in RMS tumors

The biological function of PRKG1 in RMS is unknown, and the potential prognostic value has not been explored. In order to address this issue, overall

survival analysis of RMS patients was performed by using the E-TABM-1202 database (European Bioinformatics Institute (EBI) array-express repository) [23]. This database includes a 10-year follow-up data of RMS patients. All patients included were treated with multi-agent chemotherapy and surgery, with or without radiotherapy, according to the SIOP (International Society of Paediatric Oncology) protocols. Williamson and colleagues determined the presence of PAX3-FOXO1 or PAX7-FOXO1 in this cohort by multiplex RT-PCR [23].

To determine the optimal cut-off point to separate two PRKG1 gene expression groups, with high and low PRKG1 expression, the Contal-O'Quigley method was used [217]. The overall survival curves were calculated by the Kaplan-Meier method and the log-rank test. High PRKG1 expression levels were significantly associated with favorable patient outcome (log-rank, p=0.013). However, as shown in **Figure IV. 37A,** patients with better survival (red line) are mostly comprised by RMS-FN. We hypothesized that the presence, or absence, of the fusion gene could be acting as a confounding variable. To illustrate how the fusion gene affects this database, we performed the overall survival analysis with the same parameters used for PRKG1 (**Figure IV. 37B)**. We replicated the already published data [25]: the PAX3/7-FOXO1 fusion gene (green line) has prognostic implication on disease survival compared to its absence.

In order to determine the impact of PRKG1 levels in each molecular RMS subgroup (FP- or FN-RMS), we integrated both variables. The optimal cut-off point of 3.05 was calculated. Despite the fact that the two-by-two comparison in each molecular subgroup was not statistically significant (in PAX3/7-FOXO1 RMSs, PRKG1 <3.05 *vs.* PRKG1 >3.05: p = 0.47; in FN-RMS, PRKG1 <3.05 *vs.* PRKG1 >=3.05: p = 1), patients with high PRKG1 levels displayed a trend towards an increased survival in both molecular RMS subgroups. Particularly remarkable was the clinical evolution of the four FP-RMS patients with high PRKG1 levels, in contrast to their low PRKG1 counterparts (**Figure IV. 37C)**. Although the low prevalence of RMS limits the size of publicly available cohorts recording PRKG1 levels and patient survival data, this data suggests that statistical significance could be reached by increasing the cohort of each

subgroup. These data indicate (pending validation with an external cohort) that high PRKG1 levels are associated with increased survival.

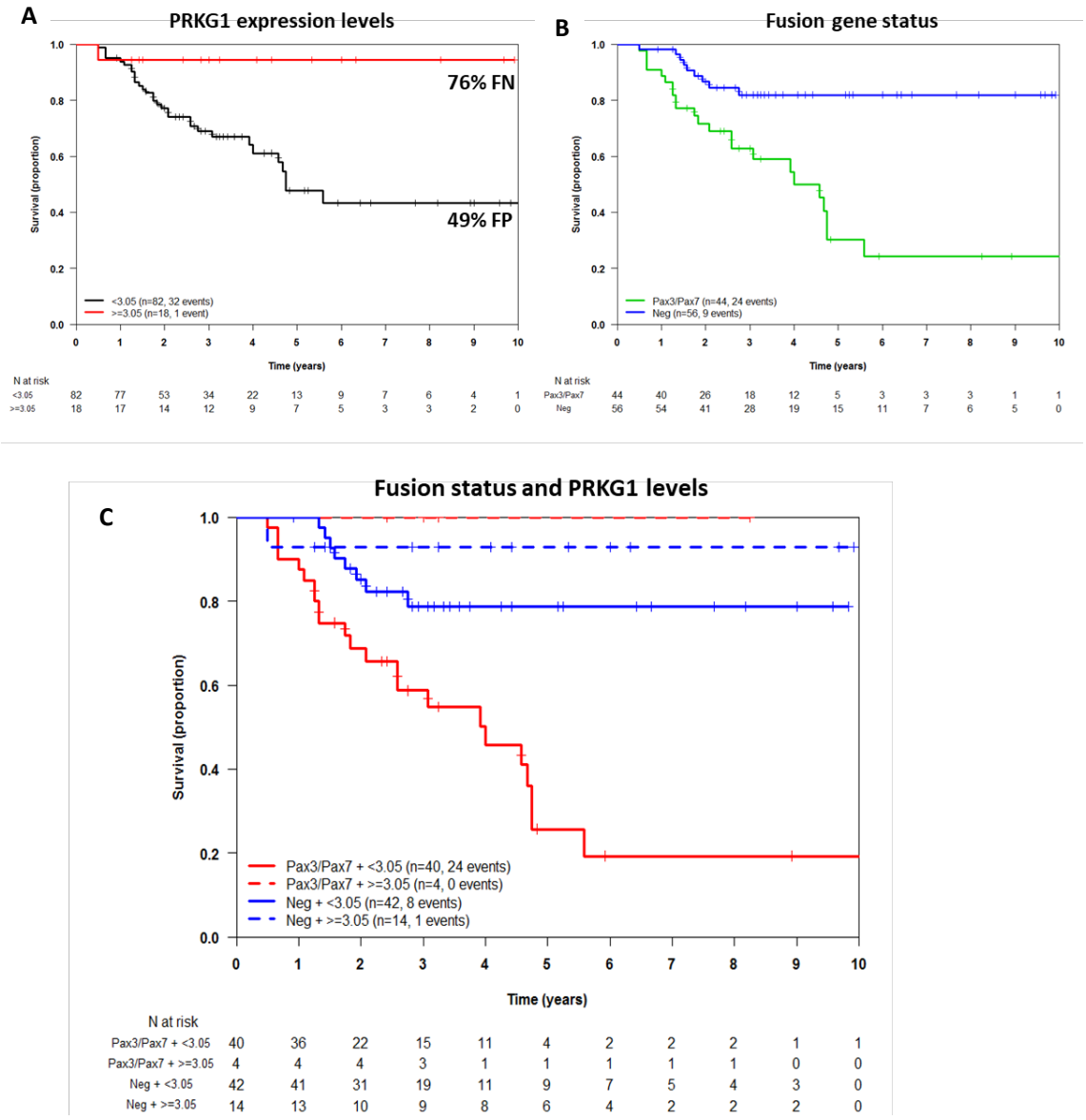

Figure IV.37. High PRKG1 expression levels predict enhanced overall survival in RMS patients. A) Kaplan–Meier survival analysis of 100 RMS patients grouped by PRKG1 expression. High PRKG1 expression (red line) *vs.* low PRKG1 expression (black line). The cut-off point for PRKG1 levels was determined using the Contal-O'Quigley method. **B)** Kaplan–Meier survival analysis of 101 RMS patients grouped by fusion status. **C)** Kaplan–Meier survival analysis of FP- or FN-RMS and high or low PRKG1 expression subgroups. PAX3/7-FOXO1-positive RMS patients (n = 44) (red line); FN-RMS (n = 56) (black line). Discontinued lines, high PRKG1 levels; continuous lines, low PRKG1 levels.

In summary, PRKG1 gene expression is higher in RMS than in any other developmental tumor. In addition, the broad dispersion of PRKG1 levels in RMS tumors indicates the existence of RMS subtypes with different degrees of PRKG1 expression, and high PRKG1 levels are associated with increased survival. Correlation analysis revealed the relationship between high PRKG1 levels and *in vivo* sensitivity to ipatasertib, indicating that PRKG1 constitutes a bona fide marker to identify ipatasertib-sensitive RMS. Transcriptional analysis showed that RMS samples with the highest levels of PRKG1 are enriched in genes involved in the mTOR pathway and in cell cycle hyperactivity, while display reduced expression of myogenic markers. Taken together, these data suggest a role of PRKG1 in the balance between proliferation and myogenic differentiation, and its association with early stages of the myogenic blockade that occurs in RMS cells.

V. DISCUSSION

RMS is the most common soft tissue in children. Despite our significant advances in understanding molecular mechanisms driving RMS, the prospect for curing children with metastatic and recurrent RMS is still very low [14, 22, 227, 228]. Indeed, the backbone of RMS treatment has remained unchanged over the last thirty years, and the standard treatment requires months of intense chemotherapy, surgery, and radiotherapy. The aggressiveness of these treatments leads to late morbidities in children who, in principle, tolerate these therapies better than adults, but they have to deal with a longer life expectancy with after-effects.

To date, the pharmaceutical efforts have not been specifically addressed to target the particular vulnerabilities of pediatric tumors. Rather, they are oriented towards mutations and alterations frequently found in adult tumors that are otherwise rarely present in pediatric tumors. This reality results in the lack of specific drugs targeting pediatric tumors, which represent only 1-2% of the global cancer burden, very far away from the numbers required to substantiate a profitable investment for companies. In addition, the low prevalence of the pediatric tumors determines the access to clinical trials that, most of the time, occurs in metastatic and refractory situations, at which stage the curative options are already very low. The development of new, more effective and selective therapies targeting rhabdomyosarcoma cell peculiarities is urgent, especially for high-risk RMS patients. Therefore, this thesis research responds to the necessity of identifying specific RMS vulnerabilities and designing personalized drug strategies.

Pediatric tumors, including RMS, are characterized by a low mutational rate shift in favor of driver epigenetic alterations [229]. The pharmacological approach based on small-molecule inhibitors or biological compounds blocking key signaling pathways for tumor cell survival is essential and promising for translational clinical research.

Two main limitations for the clinical application of signaling-targeted therapies are: 1) the necessity to refine the selection of patients with potential to benefit from specific therapies by the identification of appropriate biomarkers [230]; and 2) the escape mechanisms that, either by adaptive means or by selection pressure, develop in tumors that override the cytotoxicity induced by these

treatments. Thus, tumor drug-dependencies experience continuous shifts to new ones.

Our project started from an initial dissection of the most relevant RTK signaling cascade in RMS cells, the IGF1R triggered pathway, and the effect of blocking this cascade with the antibody m708.5. However, the wide variety of responses observed to m708.5 treatment in RMS cells, the adaptive mechanisms involving AKT activation, and the compensation among different RTKs made it necessary to first understand the diversity of downstream elements in the IGF1R signaling in RMS models. Thus, and as others have stated (see [208]), we stress the relevance of generating *in vitro* and *in vivo* tumor models from patient samples to identify potential biomarkers and to define RMS subsets of drug-dependency.

Upon IGF1R activation, the intracellular signaling pathways PI3K/AKT and Ras/MEK/ERK lead to tumor proliferation, survival, and metastasis in tumor cells. The contribution of these two pathways to RMS is heterogeneous, and the dependency of certain RMSs on AKT signaling has been reported previously [122]. Manzella et al. [208] used *in vitro* drug screening to identify a subgroup of RMS including both FP- and FN-RMS particularly sensitive to AKT inhibitors. However, the identification of a biomarker to predict the sensitivity to AKT inhibitors is lacking. Here, we have identified a RMS subgroup of FP and FN tumors that depend on the AKT/mTOR pathway and display a particular sensitivity to the pan-AKT inhibitor ipatasertib. Importantly, we identified PRKG1 as a biomarker to predict RMS sensitivity to ipatasertib. In addition, we described the role of PRKG1 in the pathophysiology of RMS.

The present work identifies: (i) Ipatasertib as an effective pharmacological treatment for pediatric RMS tumors with high *PRKG1* expression levels; (ii) PRKG1 levels as a prognostic biomarker independent of the fusion oncogene; and (iii) PRKG1 involved in the deregulation of the myogenic program in RMS.

1 Therapies targeting IGF1R and AKT in combination with MEK/ERK inhibition in pediatric RMS

RMS is an IGF2-dependent tumor, and the exploration of targeted therapies in RMS has historically involved IGF1R signaling. IGF1R activation is probably the most pursued therapeutic target in recent years both in preclinical and clinical studies for pediatric RMS. However, diverse compensatory mechanisms that prevent tumor cell response to therapies blocking the IGF pathway have been described [101, 133, 144]. In addition, the IGF1R signaling is a central node for the RMS cell after an insult. As new targets develop, either based on genetic mechanisms [231], epigenetics [202], or even immunogenic mechanisms [232], the combination with IGF1R inhibitors appears necessary to achieve an effective tumor growth inhibition. With this notion in mind, we started with the inhibition of the autocrine or/and paracrine IGF1/2 signaling in RMS cells and to explore how pharmacological inhibition of this cascade affects tumor viability.

1.1 The dual specific anti-IGF1/IGF2 human monoclonal antibody m708.5 in pediatric RMS

During the last two decades, IGF1R was considered a very promising therapeutic target for the treatment of pediatric sarcomas [142, 233], and for developmental tumors in general. Despite the demonstrated dependency of pediatric sarcomas on the IGF1R, pharmaceutical companies discontinued the studies to block IGF1R signaling due to discouraging results in clinical trials for adult patients [95, 234]. In this work, we evaluated in-depth the anti-tumoral activity of the antibody m708.5, targeting the ligands IGF1 and 2, in RMS models. We hypothesized that blockade of ligand binding to the receptor, rather than receptor targeting, could resolve some of the limitations found in previous anti-IGF1R studies.

We initiated our studies by using commercially available RMS cell lines, as they have been well characterized previously. Of the four RMS cell lines tested, the fusion positive RH4 cell line displayed the greatest cell viability inhibition upon m708.5 treatment. This decrease in viability was accompanied by a trend of G_0/G_1 cell-cycle arrest and induction of apoptosis. The high dependency of this cell line

on the IGF1R signaling contrasted with the other three cell lines analyzed (which included embryonic and alveolar RMS), with minimal or null dependency on the IGF1R pathway.

Diverse cellular and molecular mechanisms could account for the divergent responses seen to m708.5 treatments in RMS cells. Comparative studies of IGF1R subcellular distribution in RH4 versus CW9010 by confocal microscopy revealed that IGF1R was localized at the cell membrane in RH4 cells, while CW9019 cells displayed low IGF1R cell membrane levels and a scattered cytoplasmic IGF1R distribution. This difference could explain, at least in part, the diverse sensitivities to anti-IGF1R treatment in RMS cell lines. Presumably, the small-molecule BMS-754807, a potent inhibitor of IGF1R/IR, has an advantage over m708.5 antibody in this respect, as it probably inhibits receptor kinase activities regardless of the receptor subcellular distribution [131]. The unexpected sensitivity of CW9019 to submicromolar doses of BMS-754807 can be explained by the expression of the receptor not only in the plasma membrane but also in the cytoplasmic or nuclear compartments, where it likely also can effectively trigger the pathway.

At the molecular level, m708.5 functional activity on RMS cells viability correlated with its effects on IGF signaling: in the responding RH4 cells, IGF1R phosphorylation and AKT downstream signaling were downregulated; in the non-responding CW9019, RD, and RH30 cells, m708.5 did not inhibit the activation of IGF downstream signaling. IGF signaling is initiated by ligand binding to the receptor, and both IGF1 and IGF2 induce IGF1R phosphorylation in tyrosine residues critical for receptor autophosphorylation and activation. In RMS cells, IGF2 is secreted in higher quantities than IGF1, due to autocrine overexpression [123]. Taken together, the particular sensitivity of RH4 cells to IGF1/2 depletion by m708.5 can be explained by the IGF1R membrane distribution, and probably also by a high IGF2 autocrine production in these cells [235].

Other mechanisms that could account for the lack of response in CW9019 cells to m708.5 are their dependency on RTKs other than IGF1R. Indeed, the activation of alternative RTKs to bypass the blockade of the IGF1R signaling has already been described [236, 237]. In this respect, we found that even RH4 cells

eventually developed resistance to m708.5 by AKT activation, a mechanism previously described to be triggered in RMS cells exposed to IGF1R inhibitors [133, 238]. The activation of ligand-independent signaling pathways pointed to the inhibition of proteins downstream of RTK signaling as an interesting approach for RMS.

1.2 Combination of AKT and MEK inhibitors

Our results led us to explore RMS pharmacological dependencies on convergent signaling pathways essential for both FP-RMS and FN-RMS: the AKT/mTOR and MEK/ERK pathways. Several MEK inhibitors, such as cobimetinib, AZD6244 or trametinib have already been tested in preclinical RMS models. The interest in MEK targeting in RMS increased after two major publications: that describing the landscape of RMS alterations [14], which reported RAS pathway mutations in 22% of the RMS, and the work from Yohe and colleagues [202] describing the epigenetic mechanism whereby trametinib induces differentiation in RAS-mutated RMS. However, MEK inhibitors used as single agents decrease pro-apoptotic proteins and increase anti-apoptotic proteins such as MCL1 in RMS. Therefore, combined inhibition of MEK and MCL1 was demonstrated to be an effective mechanism to overcome tumor adaptation [239]. Despite these findings, MEK inhibition as a monotherapy resulted inefficient in inhibiting tumor growth in RD xenograft model [195, 202].

Two research articles have shown that the combination of PI3K/AKT and MEK/ERK inhibition is required to effectively achieve tumor growth inhibition *in vivo* [195, 240]. Moreover, they also showed that 60% and 29% of primary ARMS and ERMS tumors, respectively, expressed phospho-AKT in the absence of phospho-ERK. This strong relationship between MEK and AKT/mTOR pathways supports the rational for combining MEK and AKT inhibitors, particularly in RAS mutant RMSs. Also, due to the concomitant activation of the PI3K/AKT/mTOR and the RAS/MEK/ERK pathways, co-administration of inhibitors for both pathways induced mitochondrial apoptosis in RMS [196, 240]. However, clinical trials with trametinib in combination with temsirolimus (mTOR inhibitor) or uprosertib (AKT inhibitor) were discontinued due to excessive toxicity [241, 242]. Also, combinations of MEK inhibition with AKT inhibition using cobimetinib and

ipatasertib showed limited tolerability and efficacy when tested in a phase I clinical trial [220].

Our results in primary models and cell lines showed, in agreement with Manzella *et al.* [208], the existence of a subset of RMSs that is particularly sensitive to ipatasertib, and another subgroup especially sensitive to trametinib. Interestingly, ipatasertib-sensitive RMS models corresponded to trametinib-resistant tumors. Also, trametinib-sensitive cell lines are m708.5-resistant as well as ipatasertib-resistant. Our data showed basal ERK and AKT activation in all the tested RMS models, which led us to carry out trametinib and ipatasertib combination studies in RMS. Combined administration of both drugs resulted in the inhibition of the mTOR activity only in RAS mutated RD cells, supporting the role of mTORC1 as central node for integrating the cross-talk between AKT and MEK pathways [243].

In contrast, in RMS models that mostly depend on AKT signaling, treatment with ipatasertib initially enhanced ERK phosphorylation, but basal phosphorylation levels were restored after prolonged exposure to ipatasertib. In addition, trametinib did not enhance ipatasertib activity *in vivo*. In summary, ipatasertib-sensitive RMSs did not activate the MEK/ERK pathway to overcome AKT blockade.

2 Ipatasertib as effective treatment in RMS tumors with high PRKG1 levels

2.1 Ipatasertib activity in RMS models

The association between active AKT/mTOR pathway and poor survival in childhood RMS patients was described in 2007. Since then, the relevance of mTOR activation for ERMS and ARMS tumorigenesis has been well established. Currently, temsirolimus (mTOR inhibitor) is included in the COG phase 3 clinical trial open for RMS patients in combination with VAC (vincristine, dactinomycin, cyclophosphamide) alternating with VI (vincristine and irinotecan) (clinical trial identifier: NCT02567435).

In contrast, few advances have occurred in AKT targeting for RMS treatment. A broad plethora of AKT inhibitors have been developed for adult tumors driven by

PIK3CA mutations. However, data regarding the use of these inhibitors in pediatric tumors are scanty. One of the main goals in this thesis was to investigate AKT targeting in *in vitro* and *in vivo* RMS models with the intend to initiate translation to the clinic for RMS patients. We selected two orally bioavailable AKT inhibitors that are currently being studied in humans for different malignancies [183, 192]: ipatasertib and miransertib.

The *in vitro* screening performed with patient-derived RMS models was crucial to characterize ipatasertib signaling and viability cell effects, given the small and heterogeneous set of commercially available cell lines. We established new primary cell cultures from primary tumors (E001_s) or from RMS-derived xenografts (A006_s, A001_s, A010_s). All *in vitro* cultures were generated following standard protocols, since the influence of different culture conditions was beyond the objective of this thesis. However, it should be noted that not all PDX or biopsies were able to generate a stable cell culture. There were models such as ARMS007_s or E011_s, whose cell cultures were unable to be perpetuated, observing differentiation or proliferation arrest after the second passage, which constituted a limitation of the study. Recently Manzella et al. have described new conditions to improve the efficiency of cell culture establishment [208].

In contrast to cell lines from other pediatric tumors evaluated in our laboratory (data not shown), ipatasertib showed selective anti-tumoral activity in *in vitro* RMS models, suggesting that its antiproliferative effect might be related to specific RMS molecular features. We extended these observations to *in vivo* studies with patient-derived RMS models by using the Response Evaluation Criteria in Solid Tumors (RECIST). Following these criteria, ipatasertib was evaluated using ten doses of the maximal tolerated dose (100 mg/Kg/day, oral administration) in mice carrying patient-derived RMS xenografts. With this schedule, complete tumor regression was achieved in four out of eight different models, and we defined as ipatasertib-sensitive models these four RMS-PDX that achieved complete response in at least 50% of treated mice. Most of these ipatasertib-sensitive models were generated from relapsed patients who had already received many rounds of cytotoxic therapy (chemo and radiation). It is noteworthy that even in

RMS models that did not completely regress, the maximal ipatasertib doses significantly increased mice survival when treated for four weeks. Different ipatasertib doses were tested in animals harboring RMS PDX and, in line with adult cancer data, ipatasertib presented an anti-tumor dose-dependent effect in RMS models. We would like to especially stress the fact that ipatasertib effectiveness was independent of the oncogenic fusion status.

In contrast to other oncology drug studies, our data shows that using ipatasertib as a monotherapy resulted in tumor volume reduction of less than 2 mm^3 in mice harboring aggressive PDX-RMS. The major limitation of these *in vivo* studies was tumor regrowth after discontinuation of ipatasertib treatment. However, ipatasertib re-administration to mice with incipient tumor recurrences inhibited tumor regrowth of the most sensitive model (HSJD-ERMS-011). Taken together, our preclinical studies clearly demonstrated the efficacy of ipatasertib in blocking the growth of PDX-RMS established from chemorefractory patients. Our data also suggested that metronomic maintenance treatment could be an alternative to prolong tumor remission in patients.

To evaluate drug bioavailability parameters, one fusion-positive and one fusion-negative RMS-PDX highly sensitive to ipatasertib were tested for a 25 or 100 mg/kg dose. Ipatasertib presented a favorable oral absorption and distribution from plasma to tissues. The rapid distribution from plasma to tissues agreed with high free-drug fraction in plasma described for both human and mouse (39% plasma protein binding in human, and 56% in mouse) [180]. These data correlated with the relatively short half-life (T1/2) of ipatasertib observed in our data. The pharmacodynamic effects were demonstrated by the inhibition of S6 phosphorylation and induction of PARP cleavage in HSJD-ARMS-006 and HSJD-ERMS-011 tumors, confirming the ability of ipatasertib to inhibit tumor growth by blocking mTOR signaling and causing tumor cell death in RMS models. The efficacy associated with favorable biodistribution and limited toxicity reinforced further exploration of ipatasertib in RMS.

Ipatasertib achieved intratumoral concentrations higher than required to induce apoptosis, according with the tumor regression, in the two models and the two doses tested. A relevant finding was that the intratumoral concentration of the

drug 24 h at the lower ipatasertib dose (25 mg/kg) was still higher than the Cmax. These data suggest that the posology could be reconsidered for the 100 mg/Kg dosing with an alternative every other day schedule, instead of the tested daily administration. For translation efforts and based on the pharmacokinetic data, it would be worth exploring 48-h administrations rather than reducing the dose of ipatasertib, since drug concentrations in the blood and tumor greatly condition the response. In this regard, ipatasertib was administered to a 12-year-old patient with a fusion oncogene that involved AKT. The patient received 300 mg/day and showed objective tumor shrinkage by imaging [188]. This dosing is consistent with our PK data. However, in younger children that dose might turn toxic, and therefore further studies with lower and spaced doses should be performed to evaluate the efficacy observed at 25 mg/kg.

The *in vivo* efficacy studies of ipatasertib in the primary tumor model from the first relapse of a 3-year-old ERMS patient (E001_s) supported the compassionate use of ipatasertib in the context of an extremely aggressive second relapse in the central nervous system. Just before starting ipatasertib treatment, a tumor sample from the second relapse (E024) was obtained, and *in vivo* efficacy studies were performed in parallel with the ipatasertib administration to the patient. Ipatasertib was equally ineffective in the PDX model and in the patient, who had tumor progression. Many reasons explain this lack of response. First, the dose: since there is no previous experience with this drug in children, and in order to reduce potential toxicities, the dose approved by the ethical committee informed by the data from the company providing the drug was reduced five times from the dose we had proposed on the basis of preclinical data. Second, the tumor was in the CNS and ipatasertib appears to have a reduced blood-brain barrier passage. Third, between the first and second relapses, the patient was treated for one year with temsirolimus plus irinotecan and temozolomide. Patient-derived xenografts, from both first and second relapses, showed MYCN amplification and low PRKG1 levels. According to our most current understanding of the role of PRKG1 as a biomarker of response to ipatasertib in RMS, we now could have predicted the lack of response beforehand.

2.2 Antitumoral effects of ipatasertib in RMS in comparison to other AKT inhibitors

Miransertib is an allosteric AKT inhibitor that appears to be a more potent antitumoral agent in cancer cells harboring AKT-E17K mutation [190], PI3K mutations [191], and overgrowth syndromes in children driven by AKT and PI3K mutations [192]. In striking contrast, our *in vitro* data showed that miransertib display limited activity over most ipatasertib-sensitive RMS primary cell models. *In vivo*, miransertib was orally administrated at MTD 100 mg/kg per day for 5 days per week. Of note, the solubility of miransertib was pH-dependent, and therefore, drug vehicle for oral administration was according to previously published conditions. Despite being a potent pan-AKT inhibitor, miransertib did not induce tumor regression in HSJD-ERMS-011, in contrast to ipatasertib treatment. In addition, mice that received miransertib were unable to complete the four weeks of administration with five doses per week because of severe decrease in body weight.

From the discrepant activity of both anti-AKT drugs in RMS models and cells, the following questions emerged: Why are the two AKT inhibitors ipatasertib and miransertib different with respect to anti-tumor activity against RMS? Why are some RMS particularly sensitive to ipatasertib? Is there a biomarker to predict RMS response to ipatasertib?

We first analyzed the different mechanism of action between ipatasertib and miransertib that could account for the striking and unexpected differences in the antitumoral activity displayed by the two AKT inhibitors against RMS. ipatasertib is an ATP-competitive inhibitor, while miransertib is an allosteric inhibitor. The antitumoral effect of ipatasertib was unlikely related to the inhibition of the AKT pathway since both inhibitors were equally effective in their inhibitory effect of the AKT/mTOR signaling as evaluated by the phosphoprotein levels in ipatasertib and miransertib treated cells [178, 179]. In addition, analysis of the transcriptional changes induced by each inhibitor in the most ipatasertib-sensitive RMS cell line RH4 showed that most significantly inhibited target genes were shared by both drugs (MYC targets, oxidative phosphorylation and mTOR signaling genes) as expected for any potent AKT inhibitor. Similarly, upregulation of FOXO targets

inducing myogenic differentiation and cell arrest was also observed with both drugs. According to the effects described for other AKT inhibitors in RMS, whereas AKT silencing was shown to rescue RMS cell differentiation arrest [244], we found enrichment in the myogenic gene signature with both AKT inhibitors.

It is worth noting that there were broader changes in the transcriptome of ipatasertib treated cells as compared to miransertib, which likely reflect the different mechanism of AKT inhibition. As an ATP-competitive (or conformation-selective) AKT inhibitor, ipatasertib can influence the global conformation of other kinases, misnamed “off-targets”, that have a similar regulatory architecture as AKT, in agreement with our data showing a broader target spectrum by ipatasertib than miransertib. In contrast, AKT allosteric inhibitors such as miransertib exhibit a high degree of specificity towards AKT, and drug concentrations resulting in inhibition of off-targets are much higher to those corresponding to the IC50 values for any AKT isoform.

Focusing on kinase inhibition, ipatasertib, but not miransertib, potently inhibits PRKG1α and PRKG1β [178, 221]. Moreover, similar ATP-competitive AKT inhibitors, such as afuresertib and uprosertib, are also described to potently inhibit PRKG1. However, the functional consequences of PRKG1 inhibition have not been studied [245], and there are no mentions of PRKG1 involvement in the antitumoral effect of these AKT inhibitors [246]. At the transcriptomic level, we observed not only targets that are the most significantly ipatasertib-modulated ones within the AKT/mTOR pathway (which are likewise targets of miransertib) but also others that were exclusively targets of ipatasertib, such as *PPP1R12B* gene. These weaker, but unique, ipatasertib-targetted, differentially expressed genes supported a role of PRKG1 in the ipatasertib response against RMS. More data are needed to describe the downstream targets of PRKG1 when treated with ipatasertib.

2.3 PRKG1 expression and role in RMS

PRKG1 is a cGMP-dependent kinase that, like AKT, belongs to the AGC kinase family of proteins [247, 248]. This family is named after protein kinases A, G, and

C (PKA, PKC, PKG), which are cytoplasmic serine/threonine kinases regulated by secondary messengers, such as cyclic AMP or lipids [249]. PRKG1 is expressed in a wide range of tissues and plays functional roles in organs with smooth muscle, among other roles [247]. In cardiomyocytes PRKG1 phosphorylates TSC2, the GTPase regulatory subunit of mTORC1 [250]. Also, PRKG1 signaling pathway mediates osteoblast differentiation [251-253].

Few and contradictory information is available on the role of PRKG1 in cancer. Two different PRKG1 isoforms, PRKG1α and PRKG1β, are expressed based on alternative splicing; however, their activities have not been well distinguished. In high-grade ovarian cancer, PRKG1 enhances SRC activation, DNA synthesis and cell proliferation [254], and its expression is a predictive factor of therapy response [255]. The scarce literature also includes that PRKG1 stimulation reduces cell viability in glioma neurospheres [256], and contradictory roles in apoptosis in breast cancer [257] and non-small cell lung carcinoma (NSCLC) [258]. A thorough search of relevant literature did not result in any article describing PRKG1 in pediatric cancers.

2.3.1 PRKG1 is differentially expressed in RMS

We analyzed PRKG1 expression in a collection of embryonic healthy tissues and different developmental tumor types including sarcomas, neuroblastoma, and CNS tumors, among others. Unexpectedly, **PRKG1 was highly and differentially expressed in RMS, with levels only comparable to fetal skeletal muscle**. Importantly, PRKG1 levels were independent of the oncogenic fusion, the most determinant molecular feature in RMS tumorigenesis. This finding encouraged us to delve further into the role of PRKG1 in RMS.

2.3.2 High PRKG1 expression identifies ipatasertib-sensitive RMS

The transcriptomic analysis of RMS-derived xenografts together with their corresponding human primary samples identified a subset of RMS with the highest PRKG1 levels enriched in ipatasertib-sensitive tumors. Indeed, we could

establish a positive correlation between ipatasertib response and PRKG1 mRNA levels. These results revealed PRKG1 as *a bona fide* biomarker for ipatasertib response in RMS where no genetic alterations in the AKT/mTOR pathway occur.

Functional analysis of the **transcriptome in RMS primary samples, xenografts and primary cultures** revealed enrichment in two main proliferation gene sets including targets of cell cycle regulators such as E2F and MYC, and mTORC1 signaling in ipatasertib sensitive (high PRKG1) RMS. In contrast, these transcriptomes displayed a relative loss of MAPK activity and myogenesis hallmark gene sets. The enrichment in mTORC1 signaling and downregulation of the MAPK pathway are consistent with tumor sensitivity to AKT inhibitors such as ipatasertib. However, cell cycle and myogenic differences were not anticipated. To the best of our knowledge, this is the first report correlating ipatasertib response with developmental myogenesis and, more importantly, identifying PRKG1 as an ipatasertib response biomarker.

In organism development, and in particular, in skeletal muscle–committed cells, the **balance** between **proliferating progenitor** and **differentiation** is fundamental [259]. Muscle specific proteins of the MYOD family activate muscle differentiation and inhibit proliferation in the core control circuit that balances differentiation and proliferation [260]. In RMS, our transcriptomic data indicate that high PRKG1 samples are positively enriched in genes such as *MYC, CHEK1, WEE1* and *PLK4*, all of which were associated with proliferation, as well as with E2F and MYC target gene signatures. The E2F transcription factors are critical regulators of cell cycle progression, and the top transcription factor binding sites in the *PRKG1* promoter correspond to *E2F, E2F-1 E2F-2 E2F-3a* and *E2F-4* (genecards.org), suggesting feedback mechanisms ensuring E2F and PRKG1 coordinated expression. MYC target signatures describe functions related to RNA processing and cell-cycle progression in cancer and stem cells [261, 262]. c-MYC expression is reduced throughout myogenic differentiation from myoblast to myotubes, and MYC oncogenic program overexpression induce cell proliferation [263, 264]. mTOR and MYC converge to regulate the expression of genes involved in nucleotide synthesis and the glycolytic cycle [264].

Regarding the mTORC1 signaling enrichment seen in high PRKG1 RMS samples, it has been reported that mTOR knockdown in myoblasts activates the transcription of MYOD-driven skeletal muscle promoters [265]. The enrichment in mTORC1 target genes in these tumors, together with a high proliferative index, might explain in part the ipatasertib response. Some particular examples of genes upregulated in the mTORC1 signature in high PRKG1 samples include SLA (Src-adaptor protein), IGFBP5, GSK3B, and IDH1 (isocitrate dehydrogenase 1 soluble), all downstream of the IGF1R signaling pathway.

Other genes that have already been described with a well-established role in this balance between proliferation and differentiation such as *BMP4, CDK6* or *CCND2* were also enriched in RMS samples with high PRKG1. Bone morphogenic proteins (BMPs) such as BMP4 are involved in the balance between proliferation and differentiation of embryonic muscle cells [266]. The cyclin D2 (CCND2) is a CDK4/6-associated cyclin regulated by MYOD with roles in cell cycle regulation and myogenic cell fate [267]. Of particular interest is the homeobox protein SIX1, which is one of the most uniformly and highly expressed genes in samples with the highest PRKG1 levels and best ipatasertib responses. SIX1 has recently been described as a master regulator in the repression of RMS differentiation [268]. All these data point to high levels of PRKG1 associated to RMS cells blocked in a muscle progenitor-like state with an enhanced proliferative potential.

2.3.3 Depletion of PRKG1 in RMS cells induces myogenic differentiation

The transcriptome of cells **genetically depleted of PRKG1** showed a relative loss of genes of the mTORC1 signaling pathway, MYC targets, and of the oxidative phosphorylation signature. The same general transcriptomic signature was found in cells treated with any of the AKT inhibitors tested, ipatasertib or miransertib. However, some differential genes were affected by ipatasertib but not by miransertib. The *PRKG1* CRISPR/CAS9 knockout in RMS cells resulted in a significant enrichment in gene expression of the myogenic hallmark gene set. Specifically, the PRKG1 knockout displayed enhanced expression of gene signatures related to skeletal muscle contraction within the myogenic

differentiation program. Therefore, PRKG1 expression is associated and functionally involved with the deregulated myogenic program in RMS tumorigenesis.

Both PRKG1 knock-down by small interference RNA and PRKG knock-out (KO) by the CRISPR/CAS9 method resulted in reduced cell proliferation coupled with activation of a myogenic signature including increased expression of MYL1, TNNI1, and MEF2 family of genes. MYL1 is a marker of terminal differentiation, and it is upregulated upon JARID2 knockdown. JARID2 is a component of the Polycomb Repressive Complex 2 (PRC2), with central roles in multi-lineage differentiation in embryonic stem cells. TNNI1 (troponin I, Slow Skeletal Muscle) is a contractile muscle protein associated with terminal differentiation in RMS samples. The *TNNI1* and *MEF2* genes are under the transcriptional control of a MYOD-regulated enhancer [269]. SIX4 overexpression was also associated with PRKG1 knockdown. SIX4 acts synergistically with SIX1 to specifically activate fast-type muscle genes [270]. All of these genes are overexpressed in PRKG1 KO cells, likely contributing to RMS differentiation. More studies are needed to describe the precise mechanisms involved. It could be that PRKG1 repressed differentiation-related genes and, therefore, PRKG1 KO resulted in their transcriptional release. Alternatively, it could involve indirect mechanisms, such as increased stability or decreased degradation of the mRNA of those targets.

In summary, our data revealed a transcriptional phenotype enriched in proliferation related genes and depletion of myogenic-inducing factors in the RMS subgroup with high PRKG1 levels, which correspond to the RMS that better respond to ipatasertib. Furthermore, the transcriptome of RMS cells genetically depleted for PRKG1 showed the role of this protein in repressing myogenic gene expression, and favoring gene signatures corresponding to mTOR signaling, MYC target genes, and OX-PHO gene marks. Further supporting this notion, the transcriptional profile of ipatasertib-treated cells paralleled that of PRKG1 depleted cells and, therefore, its therapeutic effect is likely mediated by inhibition of PRKG1. Taken together, our data demonstrate that genetic inhibition of PRKG1 predominantly associates with upregulation of the myogenic transcriptional program in RMS cells.

2.3.4 Prognostic value of PRKG1

Currently, the **risk stratification** of RMS is based on the location of the primary tumor, histology, extent of residual disease after surgery, and the presence or absence of metastases [19]. The only molecular marker with prognostic impact currently available is the presence of FOXO1 rearrangements, which are being incorporated into the management of RMS. However, biomarkers with prognostic value for treatment decision in RMS are not yet available in the clinical practice.

Different preclinical studies have investigated gene expression signatures that may have prognostic value, especially in RMS-FN. In 2010, a collection of 34 genes with predictive value in the outcome of patients with RMS was reported [271]. Subsequently, the European cooperative group defined a signature of five key genes for RMS, called "metagenes", which the COG subsequently reduced to three genes [272]. However, these metagenes have not yet been evaluated in prospective clinical trials. The development of new biomarkers that could predict the response to targeted therapy and help in risk stratification is critical for the consolidation of precision pharmacology.

We have analyzed the relationship between PRKG1 expression and patient survival, considering FOXO1 rearrangement status, in a collection of one hundred RMS patients. Kaplan–Meier analysis based on PRKG1 expression levels discriminated each molecular subtype into two subgroups. In both FP- and FN-RMS, high PRKG1 levels were associated to increased patient survival, suggesting that high PRKG1 levels are predictive of favorable prognosis.

PRKG1 levels are associated with a more proliferative and less differentiated stage of RMS. Although one possible interpretation is that elevated PRKG1 levels would confer responsiveness to current RMS therapies, given that efficacy of cytotoxic therapies is higher in highly proliferative cells, another possibility is that PRKG1 might reflect a stage of molecular differentiation in RMS with better sensitivity to cytotoxic treatments.

3 Open questions for future research

Based on the existence of RMS with different PRKG1 levels, we now must understand what molecular mechanism regulates *PRKG1* expression during myogenic differentiation. We speculate that regulation of PRKG1 expression might mediate some of the functions driven by the MYOD1 transcription factor in RMS cells. Indeed, most of the RMS relevant studies have been focused on describing the synergy mechanisms between MYOD1 and PAX3-FOXO1 in FP-RMS [7], or MYOD-MYOG and the RAS oncogene in FN-RMS [202], while the mechanisms by which MYOD1 exerts its transcriptional repression are not fully understood in RMS. Regardless of the fusion oncogene or the mutational status, repression of MYOD1-driven differentiation pathways in FN or FP RMS results in cells blocked in a myoblast-like proliferative phase.

Importantly, in FN-RMS models, PRKG1 appeared as one of the DEGs in HDAC3 KO cells, when exploring the interaction of NCOR/HDAC3 complex with MYOD1 to block the expression of myogenic markers [273]. Briefly, using an inducible system to knockout HDAC3, PRKG1 expression was downregulated at short times and then induced at a later stage. On the other hand, although the relationship between PRKG1 and the PAX3-FOXO1 fusion gene has not been specifically addressed, PRKG1 was included in the list of genes associated to PAX3-FOXO1 binding sites [73]. In addition, PAX3-FOXO1 binds to enhancers of the *PRKG1* gene in RMS cells, and its expression drops in PAX3-FOXO1 depleted cells [7]. These data, together with the presence of MYOD1 at the *PRKG1* transcription start site in RH4 cells identified in ChIP-seq public databases, suggest that PRKG1 acts as an effector of the MYOD1-regulated myogenic differentiation blockade in both FN- and FP-RMS.

Further open questions are the relevance of each PRKG1 protein isoform in RMS tumorigenesis, their role as markers of myogenic stage of differentiation, and the role of the kinase activity in tumor growth. We cannot exclude that both PRKG1 isoforms have different functions in the context of RMS. Since ipatasertib inhibits both isoforms, here we have worked indistinctively with both. Moreover, we present data using two different techniques to silence PRKG1: siRNA and CRISPR/CAS9. Mechanistically they are different: while the siRNA-PRKG1

targets exon 14, the sgRNA used to guide CAS9 activity removed nucleotides at exon 1, a region only found in the alpha isoform. Therefore, we did not expect to see the complete overlap of PRKG1-regulated genes using the different techniques. In addition, although both technologies drastically reduced PRKG1 protein levels, none of these resulted in complete depletion of PRKG1 protein, probably because not all PRKG1 transcripts were targeted by these techniques. It is important to note that all the approaches that succeeded in silencing or knocking-out PRKG1 included in this thesis were carried out in the RH4 cell line; future steps will be aimed to effectively silence PRKG1 expression in embryonal RMS models and primary cultures. Future efforts will be addressed to discriminate the role of each PRKG1 isoform in the blockade of myogenesis differentiation, as well as their role in muscle precursor cells.

Also related to PRKG1 function, the PRKG1 kinase activity was described to function in cardiac protection against pressure overload [250]. In this report, PRKG1 was demonstrated to phosphorylate TSC2 and thereby regulate mTORC1 activity. Therefore, new experiments are required to define the relationship between mTORC1 and PRKG1 in cancer, and particularly in RMS.

Lastly, we demonstrated that PRKG1 expression level is a biomarker that can predict ipatasertib sensitivity in RMS. This suggests that AKT/mTOR-dependent RMS, characterized by an undifferentiated transcriptomic profile, might be sensitive to ATP-competitive AKT inhibitors. Whether or not other AKT inhibitors besides ipatasertib that also target PRKG1 could be of use in RMS needs to be evaluated. While the precise contribution of the antitumoral effect of ipatasertib depends on the inhibition of PRKG1 is still unclear, the importance of ensuring that AKT remains inhibited for tumor growth inhibition in RMS is clear. Therefore, which targets regulate PRKG1 to sensitize RMS to ipatasertib should be explored in future approaches. We can speculate that mitochondrial metabolism of anti-apoptotic proteins might play a key role on how ipatasertib modulates PRKG1 to cause cell death in RMS [274].

Main Thesis Achievements

My thesis study was born from the determination of the family of Cristina Casanovas, who was a patient in our institution who suffered from, and eventually died from, FN-RMS. Together with the leadership of Dr. Jaume Mora, they pushed to establish a new research line in our group focused on generating the basis for a new therapeutic approach designed for pediatric RMS patients that could reach the clinic. Under the supervision of Dr. Jaume Mora and Dra. Inmaculada Hernandez, I joined this challenge.

This project began with the characterization of the molecular heterogeneity and drug variability dependency defining each RMS subgroup. The initial objective was the characterization of the IGF pathway and its therapeutic targeting with the monoclonal antibody m708.5. These results conducted us to explore pharmacological sensitivities downstream IGF1R, in the RMS models.

The three most relevant achievements in my thesis are: (i) the demonstration that, unlike other AKT inhibitors, ipatasertib is efficient in patient-derived RMS models; (ii) the identification of a new biomarker—PRKG1—that predicts ipatasertib response in RMS patients; and (iii) the fusion-independent prognostic value of PRKG1 levels in RMS.

With such discoveries, we have placed PRKG1, for the first time, in the molecular picture of pediatric RMS.

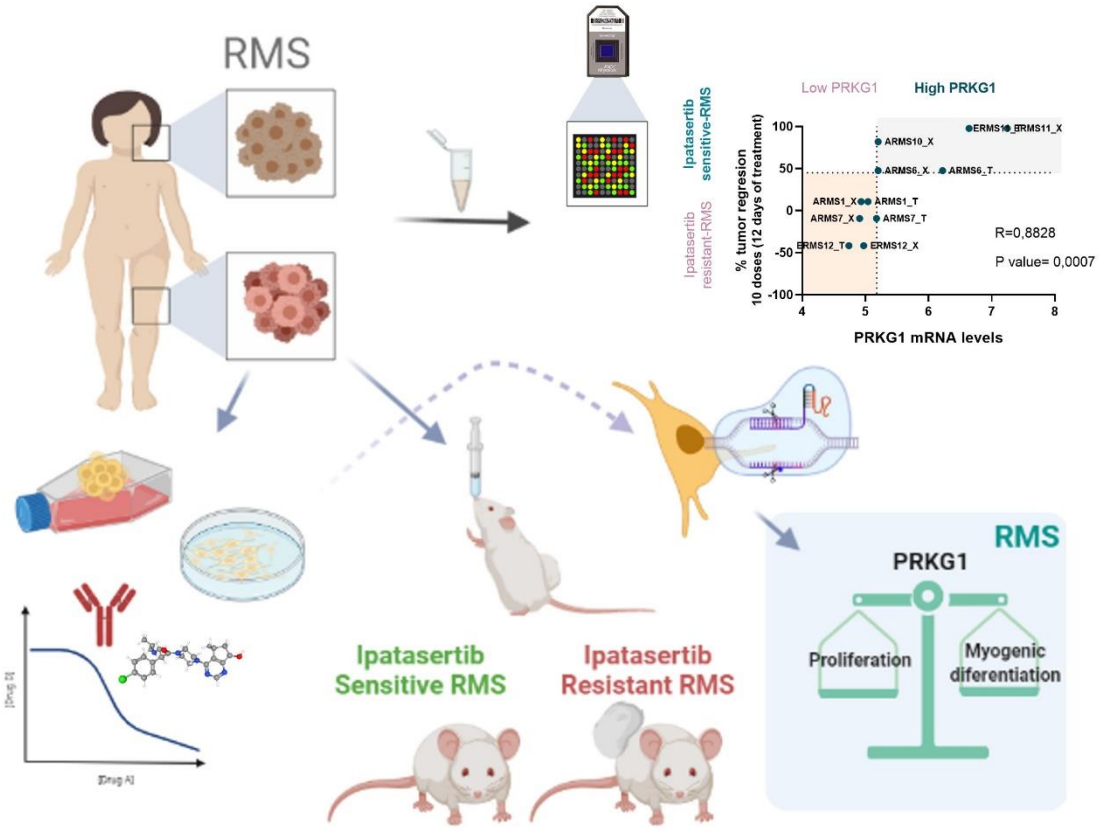

Overview of the main findings of the present thesis. The first aim of this project was to characterize IGF signaling pathway in RMS cell by describing the effects of pharmacological inhibition by the monoclonal antibody m708.5 *in vitro*. In addition to commercial cell lines, PDXs, and tumor spheres models from RMS primary samples were generated to evaluate AKT and MEK target therapies. Responses to ipatasertib were correlated to PRKG1 mRNA levels in RMS samples. Finally, we identified the role of PRKG1 in keeping the balance between proliferation and differentiation in RMS cells.

VI. CONCLUSIONS

The main conclusions of the study are:

1. Pharmacologic depletion of IGF1/2 with the human monoclonal antibody m708.5 downregulated the IGF1R signaling cascade but did not uniformly affect cell viability in the four cell lines tested (including FP and FN RMS models).
2. The elevated IGF1R expression at the cell membrane correlated with the exquisite sensitivity of the RH4 cell line among the RMS cell lines to m708.5 treatment.
3. Ipatasertib antitumoral efficacy *in vivo* correlated with its IC50 values *in vitro*.
4. Ipatasertib clearly demonstrated effectiveness in blocking the growth of PDX-RMS in a dose-dependent manner *in vivo*. To avoid tumoral recurrence, metronomic treatment should be used.
5. Clinically feasible doses achieved effective micromolar concentrations at intratumoral and plasma compartments. Such concentrations are sufficient to induce PD parameters, including phospho-S6 downregulation and cell death.
6. A subgroup of RMS, including FP and FN-RMS, can be discriminated that is especially sensitive to ipatasertib treatment but resistant to trametinib.
7. The AKT allosteric inhibitor miransertib did not recapitulates ipatasertib antitumoral effectiveness in most ipatasertib-sensible PDX.
8. The PRKG1 mRNA levels in PDXs and primary RMS tumors positively correlated with ipatasertib efficacy *in vivo*.
9. RMS primary tumors, PDXs, and primary cultures with high PRKG1 mRNA levels associated with a proliferative and poorly myogenic transcriptional phenotype.
10. Genetic silencing of PRKG1 in a FP-RMS cell line showed a positive enrichment in myogenic differentiation gene signature.
11. High and disperse levels of PRKG1 distinguished RMS from any other developmental tumor.

VII. BIBLIOGRAPHY

Bibliography

1. Skapek, S.X., et al., *Rhabdomyosarcoma.* Nat Rev Dis Primers, 2019. **5**(1): p. 1.
2. Shern, J.F., M.E. Yohe, and J. Khan, *Pediatric Rhabdomyosarcoma.* Crit Rev Oncog, 2015. **20**(3-4): p. 227-43.
3. Kashi, V.P., M.E. Hatley, and R.L. Galindo, *Probing for a deeper understanding of rhabdomyosarcoma: insights from complementary model systems.* Nat Rev Cancer, 2015. **15**(7): p. 426-39.
4. *<MARIS_Develoment tumor.pdf>.*
5. J., M., *What is a pediatric tumor?* 2012.
6. MacQuarrie, K.L., et al., *Comparison of Genome-Wide Binding of MyoD in Normal Human Myogenic Cells and Rhabdomyosarcomas Identifies Regional and Local Suppression of Promyogenic Transcription Factors.* Molecular and Cellular Biology, 2013. **33**(4): p. 773-784.
7. Gryder, B.E., et al., *PAX3-FOXO1 Establishes Myogenic Super Enhancers and Confers BET Bromodomain Vulnerability.* Cancer Discov, 2017. **7**(8): p. 884-899.
8. Kumar, S., et al., *Myogenin is a specific marker for rhabdomyosarcoma: An immunohistochemical study in paraffin-embedded tissues.* Modern Pathology, 2000. **13**(9): p. 988-993.
9. Rudzinski, E.R., et al., *The World Health Organization Classification of Skeletal Muscle Tumors in Pediatric Rhabdomyosarcoma: A Report From the Children's Oncology Group.* Arch Pathol Lab Med, 2015. **139**(10): p. 1281-7.
10. Ries LAG, S.M., Gurney JG, Linet M, Tamra T, Young JL, Bunin GR *Cancer Incidence and Survival among Children and Adolescents: United States SEER Program 1975-1995.* 1999.
11. Ognjanovic, S., et al., *Trends in childhood rhabdomyosarcoma incidence and survival in the United States, 1975-2005.* Cancer, 2009. **115**(18): p. 4218-26.
12. Jawad, N. and K. McHugh, *The clinical and radiologic features of paediatric rhabdomyosarcoma.* Pediatr Radiol, 2019. **49**(11): p. 1516-1523.
13. Inarejos Clemente, E.J., et al., *MRI of Rhabdomyosarcoma and Other Soft-Tissue Sarcomas in Children.* Radiographics, 2020. **40**(3): p. 791-814.
14. Hawkins, D.S., et al., *Children's Oncology Group's 2013 blueprint for research: Soft tissue sarcomas.* Pediatr Blood Cancer, 2013. **60**(6): p. 1001-8.
15. Oberlin, O., et al., *Prognostic factors in metastatic rhabdomyosarcomas: results of a pooled analysis from United States and European cooperative groups.* J Clin Oncol, 2008. **26**(14): p. 2384-9.
16. Diller, L., et al., *Germline p53 mutations are frequently detected in young children with rhabdomyosarcoma.* J Clin Invest, 1995. **95**(4): p. 1606-11.
17. Yang, P., et al., *Association of childhood rhabdomyosarcoma with neurofibromatosis type I and birth defects.* Genet Epidemiol, 1995. **12**(5): p. 467-74.
18. Doros, L., et al., *DICER1 Mutations in embryonal rhabdomyosarcomas from children with and without familial PPB-tumor predisposition syndrome.* Pediatric Blood & Cancer, 2012. **59**(3): p. 558-560.
19. Estep, A.L., et al., *HRAS mutations in Costello syndrome: Detection of constitutional activating mutations in codon 12 and 13 and loss of wild-type allele in malignancy.* American Journal of Medical Genetics Part A, 2006. **140a**(1): p. 8-16.
20. Kratz, C.P., et al., *Cancer in Noonan, Costello, Cardiofaciocutaneous and LEOPARD Syndromes.* American Journal of Medical Genetics Part C-Seminars in Medical Genetics, 2011. **157c**(2): p. 83-89.
21. Weksberg, R., C. Shuman, and J.B. Beckwith, *Beckwith-Wiedemann syndrome.* European Journal of Human Genetics, 2010. **18**(1): p. 8-14.
22. *Rhabdomyosarcoma.* Nat Rev Dis Primers, 2019. **5**(1): p. 2.

23. Williamson, D., et al., *Fusion gene-negative alveolar rhabdomyosarcoma is clinically and molecularly indistinguishable from embryonal rhabdomyosarcoma.* J Clin Oncol, 2010. **28**(13): p. 2151-8.
24. Hibbitts, E., et al., *Refinement of risk stratification for childhood rhabdomyosarcoma using FOXO1 fusion status in addition to established clinical outcome predictors: A report from the Children's Oncology Group.* Cancer Med, 2019. **8**(14): p. 6437-6448.
25. Missiaglia, E., et al., *PAX3/FOXO1 fusion gene status is the key prognostic molecular marker in rhabdomyosarcoma and significantly improves current risk stratification.* J Clin Oncol, 2012. **30**(14): p. 1670-7.
26. Skapek, S.X., et al., *PAX-FOXO1 fusion status drives unfavorable outcome for children with rhabdomyosarcoma: a children's oncology group report.* Pediatr Blood Cancer, 2013. **60**(9): p. 1411-7.
27. Ahmed, A.A., et al., *MYOD1 as a prognostic indicator in rhabdomyosarcoma.* Pediatr Blood Cancer, 2021. **68**(9): p. e29085.
28. Heyn, R.M., et al., *The role of combined chemotherapy in the treatment of rhabdomyosarcoma in children.* Cancer, 1974. **34**(6): p. 2128-42.
29. Stevens, M.C., et al., *Treatment of nonmetastatic rhabdomyosarcoma in childhood and adolescence: third study of the International Society of Paediatric Oncology--SIOP Malignant Mesenchymal Tumor 89.* J Clin Oncol, 2005. **23**(12): p. 2618-28.
30. Donaldson, S.S. and J.R. Anderson, *Rhabdomyosarcoma: many similarities, a few philosophical differences.* J Clin Oncol, 2005. **23**(12): p. 2586-7.
31. Crist, W.M., et al., *Intergroup rhabdomyosarcoma study-IV: results for patients with nonmetastatic disease.* J Clin Oncol, 2001. **19**(12): p. 3091-102.
32. Walterhouse, D.O., et al., *Shorter-duration therapy using vincristine, dactinomycin, and lower-dose cyclophosphamide with or without radiotherapy for patients with newly diagnosed low-risk rhabdomyosarcoma: a report from the Soft Tissue Sarcoma Committee of the Children's Oncology Group.* J Clin Oncol, 2014. **32**(31): p. 3547-52.
33. Bisogno, G., et al., *Addition of dose-intensified doxorubicin to standard chemotherapy for rhabdomyosarcoma (EpSSG RMS 2005): a multicentre, open-label, randomised controlled, phase 3 trial.* Lancet Oncol, 2018. **19**(8): p. 1061-1071.
34. Arndt, C.A.S., et al., *Vincristine, Actinomycin, and Cyclophosphamide Compared With Vincristine, Actinomycin, and Cyclophosphamide Alternating With Vincristine, Topotecan, and Cyclophosphamide for Intermediate-Risk Rhabdomyosarcoma: Children's Oncology Group Study D9803.* Journal of Clinical Oncology, 2009. **27**(31): p. 5182-5188.
35. Pappo, A.S., et al., *Two consecutive phase II window trials of irinotecan alone or in combination with vincristine for the treatment of metastatic rhabdomyosarcoma: the Children's Oncology Group.* J Clin Oncol, 2007. **25**(4): p. 362-9.
36. Casey, D.L., et al., *Increased local failure for patients with intermediate-risk rhabdomyosarcoma on ARST0531: A report from the Children's Oncology Group.* Cancer, 2019. **125**(18): p. 3242-3248.
37. Donaldson, S.S., et al., *Results from the IRS-IV randomized trial of hyperfractionated radiotherapy in children with rhabdomyosarcoma--a report from the IRSG.* Int J Radiat Oncol Biol Phys, 2001. **51**(3): p. 718-28.
38. Weigel, B.J., et al., *Intensive Multiagent Therapy, Including Dose-Compressed Cycles of Ifosfamide/Etoposide and Vincristine/Doxorubicin/Cyclophosphamide, Irinotecan, and Radiation, in Patients With High-Risk Rhabdomyosarcoma: A Report From the Children's Oncology Group.* J Clin Oncol, 2016. **34**(2): p. 117-22.
39. Malempati, S., et al., *The addition of cixutumumab or temozolomide to intensive multiagent chemotherapy is feasible but does not improve outcome for patients with*

metastatic rhabdomyosarcoma: A report from the Children's Oncology Group. Cancer, 2019. **125**(2): p. 290-297.

40. Defachelles, A.S., et al., *Randomized Phase II Trial of Vincristine-Irinotecan With or Without Temozolomide, in Children and Adults With Relapsed or Refractory Rhabdomyosarcoma: A European Paediatric Soft tissue Sarcoma Study Group and Innovative Therapies for Children With Cancer Trial.* J Clin Oncol, 2021: p. JCO2100124.
41. Mora, J., et al., *Treatment of relapsed/refractory pediatric sarcomas with gemcitabine and docetaxel.* J Pediatr Hematol Oncol, 2009. **31**(10): p. 723-9.
42. Weigel, B.J., et al., *Role of high-dose chemotherapy with hematopoietic stem cell rescue in the treatment of metastatic or recurrent rhabdomyosarcoma.* J Pediatr Hematol Oncol, 2001. **23**(5): p. 272-6.
43. Klingebiel, T., et al., *Treatment of children with metastatic soft tissue sarcoma with oral maintenance compared to high dose chemotherapy: report of the HD CWS-96 trial.* Pediatr Blood Cancer, 2008. **50**(4): p. 739-45.
44. Bisogno, G., et al., *Vinorelbine and continuous low-dose cyclophosphamide as maintenance chemotherapy in patients with high-risk rhabdomyosarcoma (RMS 2005): a multicentre, open-label, randomised, phase 3 trial.* Lancet Oncol, 2019. **20**(11): p. 1566-1575.
45. Mok, G.F. and D. Sweetman, *Many routes to the same destination: lessons from skeletal muscle development.* Reproduction, 2011. **141**(3): p. 301-12.
46. Robson, E.J., S.J. He, and M.R. Eccles, *A PANorama of PAX genes in cancer and development.* Nat Rev Cancer, 2006. **6**(1): p. 52-62.
47. Hatina, J., et al., *Sarcoma Stem Cell Heterogeneity.* Adv Exp Med Biol, 2019. **1123**: p. 95-118.
48. Braun, T. and M. Gautel, *Transcriptional mechanisms regulating skeletal muscle differentiation, growth and homeostasis.* Nat Rev Mol Cell Biol, 2011. **12**(6): p. 349-61.
49. Shih, H.P., M.K. Gross, and C. Kioussi, *Muscle development: forming the head and trunk muscles.* Acta Histochem, 2008. **110**(2): p. 97-108.
50. Bentzinger, C.F., Y.X. Wang, and M.A. Rudnicki, *Building muscle: molecular regulation of myogenesis.* Cold Spring Harb Perspect Biol, 2012. **4**(2).
51. Rios, A.C. and C. Marcelle, *Head Muscles: Aliens Who Came in from the Cold?* Developmental Cell, 2009. **16**(6): p. 779-780.
52. Chen, A.E., D.D. Ginty, and C.M. Fan, *Protein kinase A signalling via CREB controls myogenesis induced by Wnt proteins.* Nature, 2005. **433**(7023): p. 317-22.
53. Borello, U., et al., *The Wnt/beta-catenin pathway regulates Gli-mediated Myf5 expression during somitogenesis.* Development, 2006. **133**(18): p. 3723-3732.
54. Lagha, M., et al., *Pax3 regulation of FGF signaling affects the progression of embryonic progenitor cells into the myogenic program.* Genes Dev, 2008. **22**(13): p. 1828-37.
55. Reshef, R., M. Maroto, and A.B. Lassar, *Regulation of dorsal somitic cell fates: BMPs and Noggin control the timing and pattern of myogenic regulator expression.* Genes Dev, 1998. **12**(3): p. 290-303.
56. Drummond, C.J., et al., *Hedgehog Pathway Drives Fusion-Negative Rhabdomyosarcoma Initiated From Non-myogenic Endothelial Progenitors.* Cancer Cell, 2018. **33**(1): p. 108-124 e5.
57. Keller, C., et al., *Alveolar rhabdomyosarcomas in conditional Pax3:Fkhr mice: cooperativity of Ink4a/ARF and Trp53 loss of function.* Genes Dev, 2004. **18**(21): p. 2614-26.
58. Linardic, C.M., et al., *The PAX3-FKHR fusion gene of rhabdomyosarcoma cooperates with loss of p16(INK4A) to promote bypass of cellular senescence.* Cancer Research, 2007. **67**(14): p. 6691-6699.

59. Ren, Y.X., et al., *Mouse mesenchymal stem cells expressing PAX-FKHR form alveolar rhabdomyosarcomas by cooperating with secondary mutations.* Cancer Research, 2008. **68**(16): p. 6587-6597.
60. Abraham, J., et al., *Lineage of origin in rhabdomyosarcoma informs pharmacological response.* Genes Dev, 2014. **28**(14): p. 1578-91.
61. Hettmer, S., et al., *Sarcomas induced in discrete subsets of prospectively isolated skeletal muscle cells.* Proceedings of the National Academy of Sciences of the United States of America, 2011. **108**(50): p. 20002-20007.
62. Linardic, C.M., et al., *Genetic modeling of human rhabdomyosarcoma.* Cancer Res, 2005. **65**(11): p. 4490-5.
63. Langenau, D.M., et al., *Effects of RAS on the genesis of embryonal rhabdomyosarcoma.* Genes & Development, 2007. **21**(11): p. 1382-1395.
64. Hatley, M.E., et al., *A Mouse Model of Rhabdomyosarcoma Originating from the Adipocyte Lineage.* Cancer Cell, 2012. **22**(4): p. 536-546.
65. Galili, N., et al., *Fusion of a Fork Head Domain Gene to Pax3 in the Solid Tumor Alveolar Rhabdomyosarcoma.* Nature Genetics, 1993. **5**(3): p. 230-235.
66. Sorensen, P.H.B., et al., *PAX3-FKHR and PAX7-FKHR gene fusions are prognostic indicators in alveolar rhabdomyosarcoma: A report from the children's oncology group.* Journal of Clinical Oncology, 2002. **20**(11): p. 2672-2679.
67. Fredericks, W.J., et al., *The Pax3-Fkhr Fusion Protein Created by the T(2/13) Translocation in Alveolar Rhabdomyosarcomas Is a More Potent Transcriptional Activator Than Pax3.* Molecular and Cellular Biology, 1995. **15**(3): p. 1522-1535.
68. Boudjadi, S., et al., *The expression and function of PAX3 in development and disease.* Gene, 2018. **666**: p. 145-157.
69. Barr, F.G., *Gene fusions involving PAX and FOX family members in alveolar rhabdomyosarcoma.* Oncogene, 2001. **20**(40): p. 5736-5746.
70. Davis, R.J. and F.G. Barr, *Fusion genes resulting from alternative chromosomal translocations are overexpressed by gene-specific mechanisms in alveolar rhabdomyosarcoma.* Proceedings of the National Academy of Sciences of the United States of America, 1997. **94**(15): p. 8047-8051.
71. Bharathy, N., et al., *P/CAF mediates PAX3-FOXO1-dependent oncogenesis in alveolar rhabdomyosarcoma.* Journal of Pathology, 2016. **240**(3): p. 269-281.
72. Thalhammer, V., et al., *PLK1 Phosphorylates PAX3-FOXO1, the Inhibition of Which Triggers Regression of Alveolar Rhabdomyosarcoma.* Cancer Research, 2015. **75**(1): p. 98-110.
73. Cao, L., et al., *Genome-wide identification of PAX3-FKHR binding sites in rhabdomyosarcoma reveals candidate target genes important for development and cancer.* Cancer Res, 2010. **70**(16): p. 6497-508.
74. Shklover, J., et al., *MyoD uses overlapping but distinct elements to bind E-box and tetraplex structures of regulatory sequences of muscle-specific genes.* Nucleic Acids Research, 2007. **35**(21): p. 7087-7095.
75. Davicioni, E., et al., *Identification of a PAX-FKHR gene expression signature that defines molecular classes and determines the prognosis of alveolar rhabdomyosarcomas.* Cancer Research, 2006. **66**(14): p. 6936-6946.
76. Taulli, R., et al., *Validation of met as a therapeutic target in alveolar and embryonal rhabdomyosarcoma.* Cancer Research, 2006. **66**(9): p. 4742-4749.
77. van Gaal, J.C., et al., *Anaplastic lymphoma kinase aberrations in rhabdomyosarcoma: clinical and prognostic implications.* J Clin Oncol, 2012. **30**(3): p. 308-15.
78. Alijaj, N., et al., *Novel FGFR4-Targeting Single-Domain Antibodies for Multiple Targeted Therapies against Rhabdomyosarcoma.* Cancers (Basel), 2020. **12**(11).

79. Boudjadi, S., et al., *A Fusion Transcription Factor-Driven Cancer Progresses to a Fusion-Independent Relapse via Constitutive Activation of a Downstream Transcriptional Target.* Cancer Res, 2021. **81**(11): p. 2930-2942.
80. Milewski, D., et al., *FOXF1 is required for the oncogenic properties of PAX3-FOXO1 in rhabdomyosarcoma.* Oncogene, 2021.
81. Blevins, M.A., et al., *The SIX1-EYA transcriptional complex as a therapeutic target in cancer.* Expert Opinion on Therapeutic Targets, 2015. **19**(2): p. 213-225.
82. Stewart, E., et al., *Identification of Therapeutic Targets in Rhabdomyosarcoma through Integrated Genomic, Epigenomic, and Proteomic Analyses.* Cancer Cell, 2018. **34**(3): p. 411-+.
83. Shern, J.F., et al., *Comprehensive genomic analysis of rhabdomyosarcoma reveals a landscape of alterations affecting a common genetic axis in fusion-positive and fusion-negative tumors.* Cancer Discov, 2014. **4**(2): p. 216-31.
84. Williamson, D., et al., *Relationship between MYCN copy number and expression in rhabdomyosarcomas and correlation with adverse prognosis in the alveolar subtype.* Journal of Clinical Oncology, 2005. **23**(4): p. 880-888.
85. Barr, F.G., et al., *Genomic and clinical analyses of 2p24 and 12q13-q14 amplification in alveolar rhabdomyosarcoma: a report from the Children's Oncology Group.* Genes Chromosomes Cancer, 2009. **48**(8): p. 661-72.
86. Zhan, S., D.N. Shapiro, and L.J. Helman, *Activation of an imprinted allele of the insulin-like growth factor II gene implicated in rhabdomyosarcoma.* J Clin Invest, 1994. **94**(1): p. 445-8.
87. Martins, A.S., et al., *Targeting the insulin-like growth factor pathway in rhabdomyosarcomas: rationale and future perspectives.* Sarcoma, 2011. **2011**: p. 209736.
88. Taylor, A.C., et al., *p53 mutation and MDM2 amplification frequency in pediatric rhabdomyosarcoma tumors and cell lines.* Medical and Pediatric Oncology, 2000. **35**(2): p. 96-103.
89. Shern, J.F., et al., *Targeted resequencing of pediatric rhabdomyosarcoma: report from the Children's Oncology Group, the Children's Cancer and Leukaemia Group, The Institute of Cancer Research UK, and the National Cancer Institute.* Journal of Clinical Oncology, 2018. **36**(15).
90. Marics, I., et al., *FGFR4 signaling is a necessary step in limb muscle differentiation.* Development, 2002. **129**(19): p. 4559-4569.
91. Taylor, J.G., et al., *Identification of FGFR4-activating mutations in human rhabdomyosarcomas that promote metastasis in xenotransplanted models.* Journal of Clinical Investigation, 2009. **119**(11): p. 3395-3407.
92. Kohsaka, S., et al., *A recurrent neomorphic mutation in MYOD1 defines a clinically aggressive subset of embryonal rhabdomyosarcoma associated with PI3K-AKT pathway mutations.* Nat Genet, 2014. **46**(6): p. 595-600.
93. Shern, J.F., et al., *Genomic Classification and Clinical Outcome in Rhabdomyosarcoma: A Report From an International Consortium.* J Clin Oncol, 2021. **39**(26): p. 2859-2871.
94. Monti, E. and A. Fanzani, *Uncovering metabolism in rhabdomyosarcoma.* Cell Cycle, 2016. **15**(2): p. 184-95.
95. Wagner, L.M., et al., *Phase II study of cixutumumab in combination with temsirolimus in pediatric patients and young adults with recurrent or refractory sarcoma: a report from the Children's Oncology Group.* Pediatr Blood Cancer, 2015. **62**(3): p. 440-4.
96. Merker, M., et al., *Haploidentical allogeneic hematopoietic stem cell transplantation in patients with high-risk soft tissue sarcomas: results of a single-center prospective trial.* Bone Marrow Transplant, 2018. **53**(7): p. 891-894.

97. Chen, C., et al., *Current and Future Treatment Strategies for Rhabdomyosarcoma.* Front Oncol, 2019. **9**: p. 1458.
98. McClure, J.J., X.Y. Li, and C.J. Chou, *Advances and Challenges of HDAC Inhibitors in Cancer Therapeutics.* Advances in Cancer Research, Vol 138, 2018. **138**: p. 183-211.
99. McKinnon, T., et al., *Functional screening of FGFR4-driven tumorigenesis identifies PI3K/mTOR inhibition as a therapeutic strategy in rhabdomyosarcoma.* Oncogene, 2018. **37**(20): p. 2630-2644.
100. Liao, Z.C., et al., *Phase II trial of VEGFR2 inhibitor apatinib for metastatic sarcoma: focus on efficacy and safety.* Experimental and Molecular Medicine, 2019. **51**.
101. Wan, X.L., et al., *IGF-1R Inhibition Activates a YES/SFK Bypass Resistance Pathway: Rational Basis for Co-Targeting IGF-1R and Yes/SFK Kinase in Rhabdomyosarcoma.* Neoplasia, 2015. **17**(4): p. 358-366.
102. Zibat, A., et al., *Activation of the hedgehog pathway confers a poor prognosis in embryonal and fusion gene-negative alveolar rhabdomyosarcoma.* Oncogene, 2010. **29**(48): p. 6323-6330.
103. LoRusso, P.M., et al., *Phase I trial of hedgehog pathway inhibitor vismodegib (GDC-0449) in patients with refractory, locally advanced or metastatic solid tumors.* Clin Cancer Res, 2011. **17**(8): p. 2502-11.
104. Yan, C., et al., *Visualizing Engrafted Human Cancer and Therapy Responses in Immunodeficient Zebrafish.* Cell, 2019. **177**(7): p. 1903-+.
105. Kotschy, A., et al., *The MCL1 inhibitor S63845 is tolerable and effective in diverse cancer models.* Nature, 2016. **538**(7626): p. 477-+.
106. Place, A.E., et al., *Accelerating drug development in pediatric cancer: a novel Phase I study design of venetoclax in relapsed/refractory malignancies.* Future Oncology, 2018. **14**(21): p. 2115-2129.
107. Alcon, C., et al., *Sequential combinations of chemotherapeutic agents with BH3 mimetics to treat rhabdomyosarcoma and avoid resistance.* Cell Death & Disease, 2020. **11**(8).
108. Desantes, K., et al., *A phase 1, open-label, dose escalation study of enoblituzumab (MGA271) in pediatric patients with B7-H3-expressing relapsed or refractory solid tumors.* Journal of Clinical Oncology, 2017. **35**.
109. Boone, D.N. and A.V. Lee, *Targeting the insulin-like growth factor receptor: developing biomarkers from gene expression profiling.* Crit Rev Oncog, 2012. **17**(2): p. 161-73.
110. Andersen, M., et al., *IGF1 and IGF2 specificities to the two insulin receptor isoforms are determined by insulin receptor amino acid 718.* PLoS One, 2017. **12**(6): p. e0178885.
111. Mourkioti, F. and N. Rosenthal, *IGF-1, inflammation and stem cells: interactions during muscle regeneration.* Trends in Immunology, 2005. **26**(10): p. 535-542.
112. Ratajczak, M.Z., et al., *Parental imprinting regulates insulin-like growth factor signaling: a Rosetta Stone for understanding the biology of pluripotent stem cells, aging and cancerogenesis.* Leukemia, 2013. **27**(4): p. 773-9.
113. Kim, S.Y., et al., *The role of IGF-1R in pediatric malignancies.* Oncologist, 2009. **14**(1): p. 83-91.
114. Girnita, L., et al., *Something old, something new and something borrowed: emerging paradigm of insulin-like growth factor type 1 receptor (IGF-1R) signaling regulation.* Cell Mol Life Sci, 2014. **71**(13): p. 2403-27.
115. Massoner, P., et al., *Insulin-like growth factors and insulin control a multifunctional signalling network of significant importance in cancer.* Br J Cancer, 2010. **103**(10): p. 1479-84.
116. Larsson, O., A. Girnita, and L. Girnita, *Role of insulin-like growth factor 1 receptor signalling in cancer.* British Journal of Cancer, 2005. **92**(12): p. 2097-2101.
117. Pollak, M.N., E.S. Schernhammer, and S.E. Hankinson, *Insulin-like growth factors and neoplasia.* Nat Rev Cancer, 2004. **4**(7): p. 505-18.

118. Baserga, R., *The insulin-like growth factor-1 receptor as a target for cancer therapy.* Expert Opinion on Therapeutic Targets, 2005. **9**(4): p. 753-768.
119. Furstenberger, G. and H.J. Senn, *Insulin-like growth factors and cancer.* Lancet Oncology, 2002. **3**(5): p. 298-302.
120. Morgillo, F., et al., *Heterodimerization of insulin-like growth factor receptor/epidermal growth factor receptor and induction of survivin expression counteract the antitumor action of erlotinib.* Cancer Research, 2006. **66**(20): p. 10100-10111.
121. Li, J., et al., *Structural basis of the activation of type 1 insulin-like growth factor receptor.* Nature Communications, 2019. **10**.
122. Petricoin, E.F., 3rd, et al., *Phosphoprotein pathway mapping: Akt/mammalian target of rapamycin activation is negatively associated with childhood rhabdomyosarcoma survival.* Cancer Res, 2007. **67**(7): p. 3431-40.
123. Zhong, H., et al., *MEDI-573, alone or in combination with mammalian target of rapamycin inhibitors, targets the insulin-like growth factor pathway in sarcomas.* Mol Cancer Ther, 2014. **13**(11): p. 2662-73.
124. Minniti, C.P. and L.J. Helman, *IGF-II in the pathogenesis of rhabdomyosarcoma: a prototype of IGFs involvement in human tumorigenesis.* Adv Exp Med Biol, 1993. **343**: p. 327-43.
125. El-Badry, O.M., et al., *Insulin-like growth factor II acts as an autocrine growth and motility factor in human rhabdomyosarcoma tumors.* Cell Growth Differ, 1990. **1**(7): p. 325-31.
126. Khan, J., et al., *cDNA microarrays detect activation of a myogenic transcription program by the PAX3-FKHR fusion oncogene.* Proceedings of the National Academy of Sciences of the United States of America, 1999. **96**(23): p. 13264-13269.
127. Wang, W., et al., *Insulin-like growth factor II and PAX3-FKHR cooperate in the oncogenesis of rhabdomyosarcoma.* Cancer Res, 1998. **58**(19): p. 4426-33.
128. Marshall, A.D. and G.C. Grosveld, *Alveolar rhabdomyosarcoma - The molecular drivers of PAX3/7-FOXO1-induced tumorigenesis.* Skeletal Muscle, 2012. **2**.
129. Rikhof, B., et al., *The insulin-like growth factor system and sarcomas.* J Pathol, 2009. **217**(4): p. 469-82.
130. Ayalon, D., T. Glaser, and H. Werner, *Transcriptional regulation of IGF-I receptor gene expression by the PAX3-FKHR oncoprotein.* Growth Horm IGF Res, 2001. **11**(5): p. 289-97.
131. Aslam, M.I., et al., *Dynamic and nuclear expression of PDGFRalpha and IGF-1R in alveolar Rhabdomyosarcoma.* Mol Cancer Res, 2013. **11**(11): p. 1303-13.
132. Makawita, S., et al., *Expression of insulin-like growth factor pathway proteins in rhabdomyosarcoma: IGF-2 expression is associated with translocation-negative tumors.* Pediatr Dev Pathol, 2009. **12**(2): p. 127-35.
133. Cao, L., et al., *Addiction to elevated insulin-like growth factor I receptor and initial modulation of the AKT pathway define the responsiveness of rhabdomyosarcoma to the targeting antibody.* Cancer Res, 2008. **68**(19): p. 8039-48.
134. Shapiro, D.N., et al., *Antisense-mediated reduction in insulin-like growth factor-I receptor expression suppresses the malignant phenotype of a human alveolar rhabdomyosarcoma.* J Clin Invest, 1994. **94**(3): p. 1235-42.
135. Tsuchiya, K., et al., *Insulin-like growth factor-I has different effects on myogenin induction and cell cycle progression in human alveolar and embryonal rhabdomyosarcoma cells.* Int J Oncol, 2007. **31**(1): p. 41-7.
136. Missiaglia, E., et al., *Genomic imbalances in rhabdomyosarcoma cell lines affect expression of genes frequently altered in primary tumors: an approach to identify candidate genes involved in tumor development.* Genes Chromosomes Cancer, 2009. **48**(6): p. 455-67.

137. Kang, Z., et al., *Downregulation of IGFBP2 is associated with resistance to IGF1R therapy in rhabdomyosarcoma.* Oncogene, 2014. **33**(50): p. 5697-705.
138. Davicioni, E., et al., *Molecular classification of rhabdomyosarcoma--genotypic and phenotypic determinants of diagnosis: a report from the Children's Oncology Group.* Am J Pathol, 2009. **174**(2): p. 550-64.
139. Houghton, P.J., et al., *Initial testing of a monoclonal antibody (IMC-A12) against IGF-1R by the Pediatric Preclinical Testing Program.* Pediatr Blood Cancer, 2010. **54**(7): p. 921-6.
140. Sokolowski, E., et al., *Proof-of-concept rare cancers in drug development: the case for rhabdomyosarcoma.* Oncogene, 2014. **33**(15): p. 1877-89.
141. van Erp, A.E.M., et al., *Targeted Therapy-based Combination Treatment in Rhabdomyosarcoma.* Mol Cancer Ther, 2018. **17**(7): p. 1365-1380.
142. Pappo, A.S., et al., *A phase 2 trial of R1507, a monoclonal antibody to the insulin-like growth factor-1 receptor (IGF-1R), in patients with recurrent or refractory rhabdomyosarcoma, osteosarcoma, synovial sarcoma, and other soft tissue sarcomas: results of a Sarcoma Alliance for Research Through Collaboration study.* Cancer, 2014. **120**(16): p. 2448-56.
143. Cao, J. and D. Yee, *Disrupting Insulin and IGF Receptor Function in Cancer.* Int J Mol Sci, 2021. **22**(2).
144. Abraham, J., et al., *Evasion mechanisms to Igf1r inhibition in rhabdomyosarcoma.* Mol Cancer Ther, 2011. **10**(4): p. 697-707.
145. Zhao, Q., et al., *Human monoclonal antibody fragments binding to insulin-like growth factors I and II with picomolar affinity.* Mol Cancer Ther, 2011. **10**(9): p. 1677-85.
146. Zhao, Q., et al., *A dual-specific anti-IGF-1/IGF-2 human monoclonal antibody alone and in combination with temsirolimus for therapy of neuroblastoma.* Int J Cancer, 2015. **137**(9): p. 2243-52.
147. Gao, J., et al., *Dual IGF-I/II-neutralizing antibody MEDI-573 potently inhibits IGF signaling and tumor growth.* Cancer Res, 2011. **71**(3): p. 1029-40.
148. Lazaro, G., E. Kostaras, and I. Vivanco, *Inhibitors in AKTion: ATP-competitive vs allosteric.* Biochem Soc Trans, 2020. **48**(3): p. 933-943.
149. Manning, B.D. and A. Toker, *AKT/PKB Signaling: Navigating the Network.* Cell, 2017. **169**(3): p. 381-405.
150. Thorpe, L.M., H. Yuzugullu, and J.J. Zhao, *PI3K in cancer: divergent roles of isoforms, modes of activation and therapeutic targeting.* Nat Rev Cancer, 2015. **15**(1): p. 7-24.
151. Sarbassov, D.D., et al., *Phosphorylation and regulation of Akt/PKB by the rictor-mTOR complex.* Science, 2005. **307**(5712): p. 1098-101.
152. Fruman, D.A., et al., *The PI3K Pathway in Human Disease.* Cell, 2017. **170**(4): p. 605-635.
153. Matheny, R.W., Jr. and M.L. Adamo, *Current perspectives on Akt Akt-ivation and Akt-ions.* Exp Biol Med (Maywood), 2009. **234**(11): p. 1264-70.
154. Melotte, V., et al., *The N-myc downstream regulated gene (NDRG) family: diverse functions, multiple applications.* FASEB J, 2010. **24**(11): p. 4153-66.
155. Sommer, E.M., et al., *Elevated SGK1 predicts resistance of breast cancer cells to Akt inhibitors.* Biochem J, 2013. **452**(3): p. 499-508.
156. Murray, J.T., et al., *Exploitation of KESTREL to identify NDRG family members as physiological substrates for SGK1 and GSK3.* Biochem J, 2004. **384**(Pt 3): p. 477-88.
157. Garcia-Martinez, J.M. and D.R. Alessi, *mTOR complex 2 (mTORC2) controls hydrophobic motif phosphorylation and activation of serum- and glucocorticoid-induced protein kinase 1 (SGK1).* Biochem J, 2008. **416**(3): p. 375-85.
158. Liu, G.Y. and D.M. Sabatini, *mTOR at the nexus of nutrition, growth, ageing and disease (vol 29, pg 145, 2020).* Nature Reviews Molecular Cell Biology, 2020. **21**(4): p. 246-246.

159. Kim, L.C., R.S. Cook, and J. Chen, *mTORC1 and mTORC2 in cancer and the tumor microenvironment.* Oncogene, 2017. **36**(16): p. 2191-2201.
160. Gonzalez, E. and T.E. McGraw, *The Akt kinases: isoform specificity in metabolism and cancer.* Cell Cycle, 2009. **8**(16): p. 2502-8.
161. Cybulski, N. and M.N. Hall, *TOR complex 2: a signaling pathway of its own.* Trends Biochem Sci, 2009. **34**(12): p. 620-7.
162. Rozengurt, E., H.P. Soares, and J. Sinnet-Smith, *Suppression of feedback loops mediated by PI3K/mTOR induces multiple overactivation of compensatory pathways: an unintended consequence leading to drug resistance.* Mol Cancer Ther, 2014. **13**(11): p. 2477-88.
163. Hribal, M.L., et al., *Regulation of insulin-like growth factor-dependent myoblast differentiation by Foxo forkhead transcription factors.* J Cell Biol, 2003. **162**(4): p. 535-41.
164. Stitt, T.N., et al., *The IGF-1/PI3K/Akt pathway prevents expression of muscle atrophy-induced ubiquitin ligases by inhibiting FOXO transcription factors.* Mol Cell, 2004. **14**(3): p. 395-403.
165. Bois, P.R. and G.C. Grosveld, *FKHR (FOXO1a) is required for myotube fusion of primary mouse myoblasts.* EMBO J, 2003. **22**(5): p. 1147-57.
166. Xu, M., et al., *FoxO1: a novel insight into its molecular mechanisms in the regulation of skeletal muscle differentiation and fiber type specification.* Oncotarget, 2017. **8**(6): p. 10662-10674.
167. Maurer, U., et al., *Glycogen synthase kinase-3 regulates mitochondrial outer membrane permeabilization and apoptosis by destabilization of MCL-1.* Mol Cell, 2006. **21**(6): p. 749-60.
168. Koo, J., et al., *mTOR Complex 2 Stabilizes Mcl-1 Protein by Suppressing Its Glycogen Synthase Kinase 3-Dependent and SCF-FBXW7-Mediated Degradation.* Mol Cell Biol, 2015. **35**(13): p. 2344-55.
169. Faqar-Uz-Zaman, S.F., et al., *BCL-xL-selective BH3 mimetic sensitizes rhabdomyosarcoma cells to chemotherapeutics by activation of the mitochondrial pathway of apoptosis.* Cancer Lett, 2018. **412**: p. 131-142.
170. Kehr, S., et al., *Targeting BCL-2 proteins in pediatric cancer: Dual inhibition of BCL-XL and MCL-1 leads to rapid induction of intrinsic apoptosis.* Cancer Lett, 2020. **482**: p. 19-32.
171. Chen, G., et al., *Mcl-1 Interacts with Akt to Promote Lung Cancer Progression.* Cancer Res, 2019. **79**(24): p. 6126-6138.
172. van der Vos, K.E. and P.J. Coffer, *The extending network of FOXO transcriptional target genes.* Antioxid Redox Signal, 2011. **14**(4): p. 579-92.
173. Jothi, M., et al., *AKT and PAX3-FKHR cooperation enforces myogenic differentiation blockade in alveolar rhabdomyosarcoma cell.* Cell Cycle, 2012. **11**(5): p. 895-908.
174. Kostaras, E., et al., *A systematic molecular and pharmacologic evaluation of AKT inhibitors reveals new insight into their biological activity.* Br J Cancer, 2020. **123**(4): p. 542-555.
175. Martorana, F., et al., *AKT Inhibitors: New Weapons in the Fight Against Breast Cancer?* Front Pharmacol, 2021. **12**: p. 662232.
176. Lin, K., et al., *An ATP-site on-off switch that restricts phosphatase accessibility of Akt.* Sci Signal, 2012. **5**(223): p. ra37.
177. Chan, T.O., et al., *Resistance of Akt kinases to dephosphorylation through ATP-dependent conformational plasticity.* Proc Natl Acad Sci U S A, 2011. **108**(46): p. E1120-7.
178. Blake, J.F., et al., *Discovery and preclinical pharmacology of a selective ATP-competitive Akt inhibitor (GDC-0068) for the treatment of human tumors.* J Med Chem, 2012. **55**(18): p. 8110-27.

179. Yan, Y., et al., *Evaluation and clinical analyses of downstream targets of the Akt inhibitor GDC-0068.* Clin Cancer Res, 2013. **19**(24): p. 6976-86.
180. Lin, J., et al., *Targeting activated Akt with GDC-0068, a novel selective Akt inhibitor that is efficacious in multiple tumor models.* Clin Cancer Res, 2013. **19**(7): p. 1760-72.
181. Gris-Oliver, A., et al., *Genetic Alterations in the PI3K/AKT Pathway and Baseline AKT Activity Define AKT Inhibitor Sensitivity in Breast Cancer Patient-derived Xenografts.* Clin Cancer Res, 2020. **26**(14): p. 3720-3731.
182. Saura, C., et al., *A First-in-Human Phase I Study of the ATP-Competitive AKT Inhibitor Ipatasertib Demonstrates Robust and Safe Targeting of AKT in Patients with Solid Tumors.* Cancer Discov, 2017. **7**(1): p. 102-113.
183. Isakoff, S.J., et al., *Antitumor activity of ipatasertib combined with chemotherapy: results from a phase Ib study in solid tumors.* Ann Oncol, 2020. **31**(5): p. 626-633.
184. Kim, S.B., et al., *Ipatasertib plus paclitaxel versus placebo plus paclitaxel as first-line therapy for metastatic triple-negative breast cancer (LOTUS): a multicentre, randomised, double-blind, placebo-controlled, phase 2 trial.* Lancet Oncol, 2017. **18**(10): p. 1360-1372.
185. Dent, R., et al., *Final results of the double-blind placebo-controlled randomized phase 2 LOTUS trial of first-line ipatasertib plus paclitaxel for inoperable locally advanced/metastatic triple-negative breast cancer.* Breast Cancer Res Treat, 2021. **189**(2): p. 377-386.
186. Oliveira, M., et al., *FAIRLANE, a double-blind placebo-controlled randomized phase II trial of neoadjuvant ipatasertib plus paclitaxel for early triple-negative breast cancer.* Ann Oncol, 2019. **30**(8): p. 1289-1297.
187. Sweeney, C., et al., *Ipatasertib plus abiraterone and prednisolone in metastatic castration-resistant prostate cancer (IPATential150): a multicentre, randomised, double-blind, phase 3 trial.* Lancet, 2021. **398**(10295): p. 131-142.
188. Slotkin, E.K., et al., *Patient-Driven Discovery, Therapeutic Targeting, and Post-Clinical Validation of a Novel AKT1 Fusion-Driven Cancer.* Cancer Discov, 2019. **9**(5): p. 605-616.
189. Lapierre, J.M., et al., *Discovery of 3-(3-(4-(1-Aminocyclobutyl)phenyl)-5-phenyl-3H-imidazo[4,5-b]pyridin-2-yl)pyridin -2-amine (ARQ 092): An Orally Bioavailable, Selective, and Potent Allosteric AKT Inhibitor.* J Med Chem, 2016. **59**(13): p. 6455-69.
190. Yu, Y., et al., *Targeting AKT1-E17K and the PI3K/AKT Pathway with an Allosteric AKT Inhibitor, ARQ 092.* PLoS One, 2015. **10**(10): p. e0140479.
191. Yu, Y., et al., *In-vitro and in-vivo combined effect of ARQ 092, an AKT inhibitor, with ARQ 087, a FGFR inhibitor.* Anticancer Drugs, 2017. **28**(5): p. 503-513.
192. Forde, K., et al., *Clinical experience with the AKT1 inhibitor miransertib in two children with PIK3CA-related overgrowth syndrome.* Orphanet J Rare Dis, 2021. **16**(1): p. 109.
193. Lakhani N, T.A., Rasco DW, et al, *Results of a phase Ib study of ARQ 092 in combination with carboplatin (C) plus paclitaxel (P), or with P in patients (pts) with solid tumors.* 2017.
194. Mendoza, M.C., E.E. Er, and J. Blenis, *The Ras-ERK and PI3K-mTOR pathways: cross-talk and compensation.* Trends Biochem Sci, 2011. **36**(6): p. 320-8.
195. Renshaw, J., et al., *Dual blockade of the PI3K/AKT/mTOR (AZD8055) and RAS/MEK/ERK (AZD6244) pathways synergistically inhibits rhabdomyosarcoma cell growth in vitro and in vivo.* Clin Cancer Res, 2013. **19**(21): p. 5940-51.
196. Dolgikh, N., et al., *NRAS-Mutated Rhabdomyosarcoma Cells Are Vulnerable to Mitochondrial Apoptosis Induced by Coinhibition of MEK and PI3Kalpha.* Cancer Res, 2018. **78**(8): p. 2000-2013.
197. Perreault, S., et al., *A phase 2 study of trametinib for patients with pediatric glioma or plexiform neurofibroma with refractory tumor and activation of the MAPK/ERK pathway: TRAM-01.* BMC Cancer, 2019. **19**(1): p. 1250.

198. Gilmartin, A.G., et al., *GSK1120212 (JTP-74057) is an inhibitor of MEK activity and activation with favorable pharmacokinetic properties for sustained in vivo pathway inhibition.* Clin Cancer Res, 2011. **17**(5): p. 989-1000.
199. Zeiser, R., H. Andrlova, and F. Meiss, *Trametinib (GSK1120212).* Recent Results Cancer Res, 2018. **211**: p. 91-100.
200. Michailovici, I., et al., *Nuclear to cytoplasmic shuttling of ERK promotes differentiation of muscle stem/progenitor cells.* Development, 2014. **141**(13): p. 2611-20.
201. Perry, R.L., M.H. Parker, and M.A. Rudnicki, *Activated MEK1 binds the nuclear MyoD transcriptional complex to repress transactivation.* Mol Cell, 2001. **8**(2): p. 291-301.
202. Yohe, M.E., et al., *MEK inhibition induces MYOG and remodels super-enhancers in RAS-driven rhabdomyosarcoma.* Sci Transl Med, 2018. **10**(448).
203. Chen, X., et al., *Targeting oxidative stress in embryonal rhabdomyosarcoma.* Cancer Cell, 2013. **24**(6): p. 710-24.
204. Marampon, F., et al., *MEK/ERK inhibitor U0126 affects in vitro and in vivo growth of embryonal rhabdomyosarcoma.* Mol Cancer Ther, 2009. **8**(3): p. 543-51.
205. Hinson, A.R., et al., *Human rhabdomyosarcoma cell lines for rhabdomyosarcoma research: utility and pitfalls.* Front Oncol, 2013. **3**: p. 183.
206. Meel, M.H., et al., *Culture methods of diffuse intrinsic pontine glioma cells determine response to targeted therapies.* Exp Cell Res, 2017. **360**(2): p. 397-403.
207. Monje, M., et al., *Hedgehog-responsive candidate cell of origin for diffuse intrinsic pontine glioma.* Proc Natl Acad Sci U S A, 2011. **108**(11): p. 4453-8.
208. Manzella, G., et al., *Phenotypic profiling with a living biobank of primary rhabdomyosarcoma unravels disease heterogeneity and AKT sensitivity.* Nat Commun, 2020. **11**(1): p. 4629.
209. Gentleman, R.C., et al., *Bioconductor: open software development for computational biology and bioinformatics.* Genome Biol, 2004. **5**(10): p. R80.
210. Irizarry, R.A., et al., *Exploration, normalization, and summaries of high density oligonucleotide array probe level data.* Biostatistics, 2003. **4**(2): p. 249-64.
211. Ritchie, M.E., et al., *limma powers differential expression analyses for RNA-sequencing and microarray studies.* Nucleic Acids Res, 2015. **43**(7): p. e47.
212. Benjamini, Y. and Y. Hochberg, *Controlling the False Discovery Rate: A Practical and Powerful Approach to Multiple Testing.* Journal of the Royal Statistical Society. Series B (Methodological), 1995. **57**(1): p. 289-300.
213. Subramanian, A., et al., *Gene set enrichment analysis: a knowledge-based approach for interpreting genome-wide expression profiles.* Proc Natl Acad Sci U S A, 2005. **102**(43): p. 15545-50.
214. Yu, G., et al., *clusterProfiler: an R package for comparing biological themes among gene clusters.* Omics, 2012. **16**(5): p. 284-7.
215. Irizarry, R.A., et al., *Use of mixture models in a microarray-based screening procedure for detecting differentially represented yeast mutants.* Stat Appl Genet Mol Biol, 2003. **2**: p. Article1.
216. Kaplan, E.L. and P. Meier, *Nonparametric Estimation from Incomplete Observations.* Journal of the American Statistical Association, 1958. **53**(282): p. 457-481.
217. Contal, C. and J. O'Quigley, *An application of changepoint methods in studying the effect of age on survival in breast cancer.* Computational Statistics & Data Analysis, 1999. **30**(3): p. 253-270.
218. Martinelli, S., et al., *RAS signaling dysregulation in human embryonal Rhabdomyosarcoma.* Genes Chromosomes Cancer, 2009. **48**(11): p. 975-82.
219. Castillo-Ecija, H., et al., *Prognostic value of patient-derived xenograft engraftment in pediatric sarcomas.* J Pathol Clin Res, 2021. **7**(4): p. 338-349.

220. Shapiro, G.I., et al., *A phase Ib open-label dose escalation study of the safety, pharmacokinetics, and pharmacodynamics of cobimetinib (GDC-0973) and ipatasertib (GDC-0068) in patients with locally advanced or metastatic solid tumors.* Invest New Drugs, 2021. **39**(1): p. 163-174.
221. You, I., et al., *Discovery of an AKT Degrader with Prolonged Inhibition of Downstream Signaling.* Cell Chem Biol, 2020. **27**(1): p. 66-73 e7.
222. Surks, H.K., et al., *Regulation of myosin phosphatase by a specific interaction with cGMP-dependent protein kinase Ialpha.* Science, 1999. **286**(5444): p. 1583-7.
223. Dippold, R.P. and S.A. Fisher, *A bioinformatic and computational study of myosin phosphatase subunit diversity.* Am J Physiol Regul Integr Comp Physiol, 2014. **307**(3): p. R256-70.
224. Dumitru, A.M.G., et al., *Cyclin A/Cdk1 modulates Plk1 activity in prometaphase to regulate kinetochore-microtubule attachment stability.* Elife, 2017. **6**.
225. Mochizuki, M., et al., *Polo-Like Kinase 2 is Dynamically Regulated to Coordinate Proliferation and Early Lineage Specification Downstream of Yes-Associated Protein 1 in Cardiac Progenitor Cells.* J Am Heart Assoc, 2017. **6**(10).
226. Knight, J.D. and R. Kothary, *The myogenic kinome: protein kinases critical to mammalian skeletal myogenesis.* Skelet Muscle, 2011. **1**: p. 29.
227. Dantonello, T.M., et al., *Survival following disease recurrence of primary localized alveolar rhabdomyosarcoma.* Pediatr Blood Cancer, 2013. **60**(8): p. 1267-73.
228. Bisogno, G., et al., *Sequential high-dose chemotherapy for children with metastatic rhabdomyosarcoma.* Eur J Cancer, 2009. **45**(17): p. 3035-41.
229. Grobner, S.N., et al., *The landscape of genomic alterations across childhood cancers.* Nature, 2018. **555**(7696): p. 321-327.
230. Schwartz, G.K., et al., *Cixutumumab and temsirolimus for patients with bone and soft-tissue sarcoma: a multicentre, open-label, phase 2 trial.* Lancet Oncol, 2013. **14**(4): p. 371-82.
231. Guenther, L.M., et al., *A Combination CDK4/6 and IGF1R Inhibitor Strategy for Ewing Sarcoma.* Clinical Cancer Research, 2019. **25**(4): p. 1343-1357.
232. Wu, Q., et al., *IGF1 receptor inhibition amplifies the effects of cancer drugs by autophagy and immune-dependent mechanisms.* J Immunother Cancer, 2021. **9**(6).
233. Malempati, S., et al., *Phase I/II trial and pharmacokinetic study of cixutumumab in pediatric patients with refractory solid tumors and Ewing sarcoma: a report from the Children's Oncology Group.* J Clin Oncol, 2012. **30**(3): p. 256-62.
234. Fidler, M.J., et al., *Targeting the insulin-like growth factor receptor pathway in lung cancer: problems and pitfalls.* Ther Adv Med Oncol, 2012. **4**(2): p. 51-60.
235. Rezvani, G., et al., *A set of imprinted genes required for normal body growth also promotes growth of rhabdomyosarcoma cells.* Pediatric Research, 2012. **71**(1): p. 32-38.
236. Harbinski, F., et al., *Rescue screens with secreted proteins reveal compensatory potential of receptor tyrosine kinases in driving cancer growth.* Cancer Discov, 2012. **2**(10): p. 948-59.
237. Wilson, T.R., et al., *Widespread potential for growth-factor-driven resistance to anticancer kinase inhibitors.* Nature, 2012. **487**(7408): p. 505-9.
238. Wan, X., et al., *Rapamycin induces feedback activation of Akt signaling through an IGF-1R-dependent mechanism.* Oncogene, 2007. **26**(13): p. 1932-1940.
239. Clara Alcon, F.M., Estela Prada, Jaume Mora, Aroa Soriano, Gabriela Guillén, Soledad Gallego, Josep Roma, Josep Samitier, Alberto Villanueva, Joan Montero, *Sequential combination of trametinib and an MCL-1 inhibitor as a 1 novel therapy to treat rhabdomyosarcoma.* 2021.

240. Guenther, M.K., U. Graab, and S. Fulda, *Synthetic lethal interaction between PI3K/Akt/mTOR and Ras/MEK/ERK pathway inhibition in rhabdomyosarcoma.* Cancer Lett, 2013. **337**(2): p. 200-9.
241. Tolcher, A.W., et al., *A phase IB trial of the oral MEK inhibitor trametinib (GSK1120212) in combination with everolimus in patients with advanced solid tumors.* Annals of Oncology, 2015. **26**(1): p. 58-64.
242. Tolcher, A.W., et al., *Phase I dose-escalation trial of the oral AKT inhibitor uprosertib in combination with the oral MEK1/MEK2 inhibitor trametinib in patients with solid tumors.* Cancer Chemotherapy and Pharmacology, 2020. **85**(4): p. 673-683.
243. Saxton, R.A. and D.M. Sabatini, *mTOR Signaling in Growth, Metabolism, and Disease (vol 168, pg 960, 2017).* Cell, 2017. **169**(2): p. 362-362.
244. Granados, V.A., et al., *Selective Targeting of Myoblast Fusogenic Signaling and Differentiation-Arrest Antagonizes Rhabdomyosarcoma Cells.* Cancer Res, 2019. **79**(18): p. 4585-4591.
245. Dumble, M., et al., *Discovery of novel AKT inhibitors with enhanced anti-tumor effects in combination with the MEK inhibitor.* PLoS One, 2014. **9**(6): p. e100880.
246. Pachl, F., et al., *Characterization of a chemical affinity probe targeting Akt kinases.* J Proteome Res, 2013. **12**(8): p. 3792-800.
247. Wolfertstetter, S., J.P. Huettner, and J. Schlossmann, *cGMP-Dependent Protein Kinase Inhibitors in Health and Disease.* Pharmaceuticals (Basel), 2013. **6**(2): p. 269-86.
248. Hofmann, F., *The biology of cyclic GMP-dependent protein kinases.* Journal of Biological Chemistry, 2005. **280**(1): p. 1-4.
249. Pearce, L.R., D. Komander, and D.R. Alessi, *The nuts and bolts of AGC protein kinases.* Nat Rev Mol Cell Biol, 2010. **11**(1): p. 9-22.
250. Ranek, M.J., et al., *PKG1-modified TSC2 regulates mTORC1 activity to counter adverse cardiac stress.* Nature, 2019. **566**(7743): p. 264-269.
251. Schall, N., et al., *Protein kinase G1 regulates bone regeneration and rescues diabetic fracture healing.* JCI Insight, 2020. **5**(9).
252. Jafari, A., et al., *Pharmacological Inhibition of Protein Kinase G1 Enhances Bone Formation by Human Skeletal Stem Cells Through Activation of RhoA-Akt Signaling.* Stem Cells, 2015. **33**(7): p. 2219-31.
253. Wong, J.C. and R.R. Fiscus, *Essential roles of the nitric oxide (no)/cGMP/protein kinase G type-Ialpha (PKG-Ialpha) signaling pathway and the atrial natriuretic peptide (ANP)/cGMP/PKG-Ialpha autocrine loop in promoting proliferation and cell survival of OP9 bone marrow stromal cells.* J Cell Biochem, 2011. **112**(3): p. 829-39.
254. Leung, E.L., et al., *Protein Kinase G Type I alpha Activity in Human Ovarian Cancer Cells Significantly Contributes to Enhanced Src Activation and DNA Synthesis/Cell Proliferation.* Molecular Cancer Research, 2010. **8**(4): p. 578-591.
255. Benvenuto, G., et al., *Expression profiles of PRKG1, SDF2L1 and PPP1R12A are predictive and prognostic factors for therapy response and survival in high-grade serous ovarian cancer.* International Journal of Cancer, 2020. **147**(2): p. 565-574.
256. Wilson, T.J., et al., *Reversibility of glioma stem cells' phenotypes explains their complex in vitro and in vivo behavior. Discovery of a novel neurosphere-specific enzyme, cGMP-dependent protein kinase 1, using the genomic landscape of human glioma stem cells as a discovery tool.* Oncotarget, 2016. **7**(39): p. 63020-63041.
257. Fallahian, F., et al., *Cyclic GMP induced apoptosis via protein kinase G in oestrogen receptor-positive and -negative breast cancer cell lines.* Febs Journal, 2011. **278**(18): p. 3360-3369.
258. Wong, J.C., M. Bathina, and R.R. Fiscus, *Cyclic GMP/protein kinase G type-I alpha (PKG-I alpha) signaling pathway promotes CREB phosphorylation and maintains higher c-IAP1, livin, survivin, and Mcl-1 expression and the inhibition of PKG-I alpha kinase activity*

synergizes with cisplatin in non-small cell lung cancer cells. Journal of Cellular Biochemistry, 2012. **113**(11): p. 3587-3598.
259. Wilson, R.A., et al., *Negative regulation of initial steps in skeletal myogenesis by mTOR and other kinases.* Sci Rep, 2016. **6**: p. 20376.
260. Olson, E.N., *Interplay between Proliferation and Differentiation within the Myogenic Lineage.* Developmental Biology, 1992. **154**(2): p. 261-272.
261. Lin, C.Y., et al., *Transcriptional Amplification in Tumor Cells with Elevated c-Myc.* Cell, 2012. **151**(1): p. 56-67.
262. Grandori, C. and R.N. Eisenman, *Myc target genes.* Trends in Biochemical Sciences, 1997. **22**(5): p. 177-181.
263. Conacci-Sorrell, M., C. Ngouenet, and R.N. Eisenman, *Myc-Nick: A Cytoplasmic Cleavage Product of Myc that Promotes alpha-Tubulin Acetylation and Cell Differentiation.* Cell, 2010. **142**(3): p. 480-493.
264. Pourdehnada, M., et al., *Myc and mTOR converge on a common node in protein synthesis control that confers synthetic lethality in Myc-driven cancers.* Proceedings of the National Academy of Sciences of the United States of America, 2013. **110**(29): p. 11988-11993.
265. Wilson, R.A., et al., *Negative regulation of initial steps in skeletal myogenesis by mTOR and other kinases.* Scientific Reports, 2016. **6**.
266. Friedrichs, M., et al., *BMP signaling balances proliferation and differentiation of muscle satellite cell descendants.* BMC Cell Biol, 2011. **12**: p. 26.
267. Tenente, I.M., et al., *Myogenic regulatory transcription factors regulate growth in rhabdomyosarcoma.* Elife, 2017. **6**.
268. Hsu, J., et al., *SIX1 is a master regulator of the Rhabdomyosarcoma undifferentiated state*. 2021.
269. Pomella, S., et al., *Interaction between SNAI2 and MYOD enhances oncogenesis and suppresses differentiation in Fusion Negative Rhabdomyosarcoma.* Nature Communications, 2021. **12**(1).
270. Niro, C., et al., *Six1 and Six4 gene expression is necessary to activate the fast-type muscle gene program in the mouse primary myotome.* Developmental Biology, 2010. **338**(2): p. 168-182.
271. Davicioni, E., et al., *Gene Expression Profiling for Survival Prediction in Pediatric Rhabdomyosarcomas: A Report From the Children's Oncology Group.* Journal of Clinical Oncology, 2010. **28**(7): p. 1240-1246.
272. Hingorani, P., et al., *Clinical Application of Prognostic Gene Expression Signature in Fusion Gene-Negative Rhabdomyosarcoma: A Report from the Children's Oncology Group.* Clinical Cancer Research, 2015. **21**(20): p. 4733-4739.
273. Phelps, M.P., et al., *CRISPR screen identifies the NCOR/HDAC3 complex as a major suppressor of differentiation in rhabdomyosarcoma.* Proc Natl Acad Sci U S A, 2016. **113**(52): p. 15090-15095.
274. Alcon, C., et al., *ER+ Breast Cancer Strongly Depends on MCL-1 and BCL-xL Anti-Apoptotic Proteins.* Cells, 2021. **10**(7).